DNA Nanotechnology and Supramolecular Chemistry in Biomedical Therapy Applications

Peter James Cail

A thesis submitted to the University of Birmingham for the degree of Doctor of Philosophy

School of Chemistry

University of Birmingham

September 2017

UNIVERSITY^{OF} BIRMINGHAM

University of Birmingham Research Archive

e-theses repository

Acknowledgements

On completing this thesis, I would firstly like to thank my supervisor Professor Mike Hannon for giving me the PhD opportunity and for all his support and help over the four years. My time would also have been much harder had it not been for all the friends made in the Hannon group. To past members, for making me feel welcome when I first started I would like to thank Jeni, Ashleigh and Lois for all their advice and jokes, making work fun from the start and for never minding when I forgot to bring cake in on my cake week. To current members, I would like to thank Lucia, Callum and Rich for great chats and lunches, on top of all the help and time they gave me.

This thesis would also not be complete without help and valuable training. I would like to thanks Dr Nik Hodges from School of Biosciences, University of Birmingham for all his training with flow cytometry and advice presenting biological data, as well as the use of his facilities on the 4^{Th} floor of the bioscience building. Thanks also go to Dr Luke Williams from cancer science unit, University of Birmingham for his time taken to train me to culture cells professionally. The confocal microscopy images presented here would not have been possible without the training of Dr Alessio di Maio from the BALM institute, University of Birmingham, on the use of a confocal microscope. Thanks also go to Dr Doug Browning from the IMI, University of Birmingham, for the advice handling radioactive material and for the use of the groups hot lab facility.

Collaborations were integral to this thesis, and credit must go to Dr Wang Liying and Professor Shao Fangwei from the Institute of Chemical Biology, Nanyang Technological University, Singapore, for performing the AFM experiments found in this thesis. Thanks also go to Dr Lucia Cardo from the Hannon group, University of Birmingham, for the opportunity to work

with her on her exciting project which is outlined in chapter 5. I would also like to thank Jamie Webster from the Protein Expression Facility for his help producing the EGFP mentioned in chapter 6

Finally I would like to thank all my friends and family for all their support throughout my lengthy student career. I would never have made it this far without all of them and for this reason I dedicate this thesis to my family and friends.

Declaration

The experimental work, observations and recommendations reported in this thesis are the author's unless specifically stated and have not previously been submitted as part of a degree at the University of Birmingham or any other institution.

Peter Cail

September 2017

List of Papers Published From this Thesis

1. P. J. Cail, W. Liying, A. Mucha, S. Phongtongpasuk, S. Fangwei and M. J. Hannon, Cellular Delivery of a Supramolecular anti-cancer agent using a DNA Tetrahedron. (Manuscript to be submitted)

2. L. Cardo, I. Nawroth, P.J. Cail, J.A. McKeating and M.J. Hannon, Metallo supramolecular cylinders inhibit HIV-1 TAR-TAT complex formation and viral replication *in cellulo*. (Manuscript under review)

Contents

Abbreviations

μL	Micro litre
μM	Micro molar
3D	Three Dimensions
3WJ	Three way junction
A	Adenine
AFM	Atomic force microscopy
ATP	Adenosine tri phosphate
Bp	Base pair
C	Cytosine
CD	Circular Dichroism
Cy5	Cyanine 5
d	doublet
dd	doublet of doublets
DLS	Dynamic Light Scattering
DMEM	Dulbecco's Modified Eagle's medium
DNA	Deoxyribonucleic acid
dsDNA	Double stranded DNA
ESI	Electrospray Ionisation

FeCy	Iron cylinder
G	Guanine
HIV-1	Human immunodeficiency virus-1
HPLC	High Performance Liquid Chromatography
IC_{50}	Half maximal inhibitory concentration
ICP-MS	Inductively coupled plasma mass spectrometry
K	Kelvin
M	Left handed helicate (minus)
MeOD	Deuterated methanol
MeOH	Methanol
MTT	3-(4,5-Dimethylthiazol-2-yl)-2,5-Diphenyltetrazolium Bromide
MW	Molecular weight
MWCO	Molecular weight cut off
NiCy	Nickel cylinder
nM	Nano molar
NMR	Nuclear Magnetic Resonance
Oligo	Oligonucleotide
P	Right handed helicate (plus)
^{32}P	Phosphorus isotope 32

PAGE	Polyacrylamide gel electrophoresis
PDI	Poly dispersity Index
PDT	Photodynamic Therapy
ppb	Parts per billion
RNA	Ribonucleic acid
rpm	Revolutions per minute
RPMI	Roswell Park Memorial Institute medium
RuCy	Ruthenium cylinder
s	Singlet
ssDNA	Single stranded DNA
T	Thymine
TAR	Trans Activator Response region
TAT	Transactivator protein
td	triple of doublets
TEMED	Tetramethylethylenediamine
Tet	Tetrahedron
TM Buffer	Tris Magnesium Chloride Buffer
UV-Vis	Ultraviolet-visible spectroscopy

Abstract

The overall aim of this thesis is to investigate the combination of supramolecular cylinders with DNA nanotechnology and assess any effects that can occur through binding and any applications this could have in biomedical therapy applications. From this base it is hoped that insight can be gained as to whether supramolecular chemistry can be used to create DNA nano-machines, capable of triggered release of cargo.

The thesis begins with a review of DNA discovery, structure and binding by small molecules, followed by a review of the field of DNA nanotechnology. By expanding on the field of DNA nanotechnology recognition, chapters 2 and 3 will highlight the advantages of supramolecular chemistry when combined with DNA nanotechnology in both nano-machines and inside cell systems with a focus on DNA tetrahedral nanostructures. Chapter 4 researches the photocleavage capabilities of a ruthenium cylinder and the possibilities of selective release and photodynamic therapy using a DNA tetrahedron. Chapter 5 illustrates a new class of anti-viral agents capable of structure recognition regardless of RNA sequence. The chapter focuses on the inhibition of binding between the TAR RNA and ADP-1 peptide found in the HIV-1 virus.

Chapter 1

Introduction

1.1 DNA – An Introduction

1.1.1 Discovery of DNA

DNA was first isolated by Friedrich Miescher in 1869. The Swiss chemist discovered what he called nuclein inside human white blood cells obtained from pus-coated bandages. By separating this phosphorus rich nuclein from the surrounding proteins, he realised he had discovered a new substance which started the track towards understanding DNA fully.[1]

Following on from this initial discovery many years later in 1919 Phoebus Levene, a Russian biochemist put forward his polynucleotide theory, discovered through analysing hydrolysis products of nucleic acids. He stated that nucleic acids were in fact long chains of nucleotides, which turned out to be correct.[2] Although the theory stated that nucleotides were long identical repeats of the nucleotides, the idea however, aided further research.[3]

In 1950, a vital stepping stone was reported by Erwin Chargaff, he found from separating DNA samples with paper chromatography, the ratios of nucleic acids were different depending on the sample being analysed.[4] From this he concluded that Phoebus Levene cannot be correct and that DNA has varying sequences. He also found that the ratio between the purines and the pyrimidines was 1:1 regardless of the sample source. Specifically he found that adenine and thymine were in equal proportions and the same was true of guanine and cytosine.[4] This became known as 'Chargaff's rules' and was instrumental in the eventual final elucidation of the structure of DNA.[5]

Following from this, two English chemists, Rosalind Franklin and Raymond Gosling managed to produce the X-ray diffraction pattern of DNA in 1953 (Figure 1.1).[6] This X structure shown in the picture suggested that the structure of DNA must be a repeating
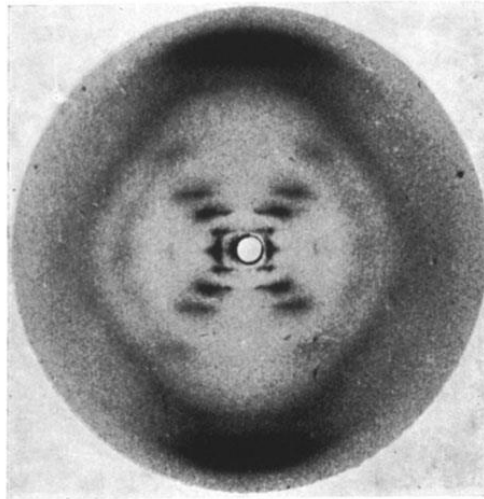
Figure 1.1 - X-ray diffraction pattern of DNA produced by Franklin and Gosling.
Taken from 6.

structure which is uniform in nature. The crystallography also gave measurements for the width of DNA and therefore distances between the bases which would prove vital in discovering the final structure. Finally, with these initial pieces of evidence in place, Watson and Crick were able to propose their model of DNA in 1953.[7] They proposed a right-handed double helical structure, with the nucleotide bases hydrogen bonded down the centre, surrounded by the phosphate-sugar backbone on the outside. Chargaff's rule were also followed by correctly pairing A to T and G to C, resulting in the observed ratios of 1:1 between the bases. Figure 1.2 shows the structure of DNA proposed by Watson and Crick in 1953.
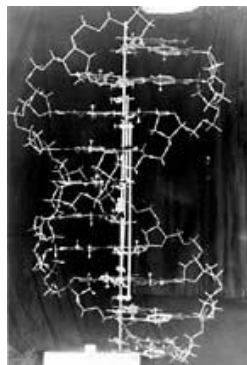
Figure 1.2 – Original model of Watson and Cricks structure of DNA. Photo from the Archives at Cold Spring Harbor Laboratory.

1.1.2 Different Structures of DNA

1.1.2.1 Helical DNA

DNA has a huge variety of structures, but they mainly follow what is known as Watson-Crick base-pairing. As discussed earlier, this is the pairing between A and T and between G and C. This pairing is composed of hydrogen bonds between NH groups on one base and oxygen on an adjacent base. Figure 1.3 illustrates this hydrogen bond pairing between these bases.[8]
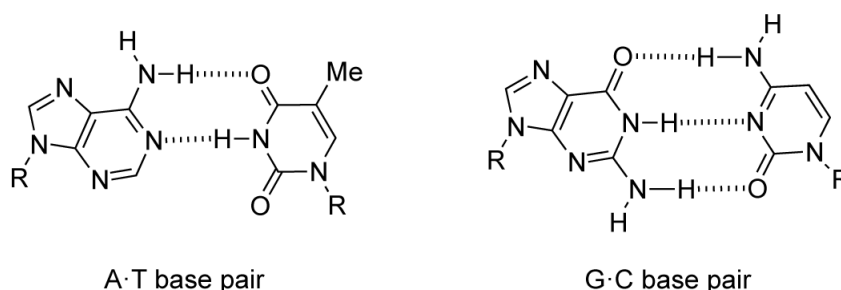
Figure 1.3 – Drawing illustrating Watson-Crick base pairing between DNA nucleotides. Taken From 8.

The main form of helical DNA is known as B-DNA. Here, the bases shown above are bound to a deoxyribose unit to form what is known as a nucleotide. These nucleotides are then linked by a phosphate group to form long strands of nucleotides called an oligonucleotide. Two complimentary strands (with regard to the above Watson-Crick base pairing) are hydrogen bonded together as illustrated, with each base pair in the chains stacked with one above and one below and stabilised further by favourable π interactions from the aromatic groups in the bases. The bases are centralised due to their hydrophobicity and the stacking results in a double helix structure. As the helix turns, a major groove and a minor groove is created, with one of each per full turn of B-DNA. This full turn occurs across about 10-11 base pairs of helix.[9] *In vivo* this form of DNA is by far the most common, carrying the genetic information

for organisms.   There is another form of right handed double helical DNA possible known as A-DNA. This generally occurs in dehydrated samples of DNA and is estimated to form when relative humidity drops below around 75%.[10] This is because with less H_2O molecules available, the ribose sugars bend in a different fashion, causing the base pairs to bend away from the helical axis by a 19° angle meaning the phosphate groups can bind less H_2O molecules.[10] A-DNA as a result is shorter and wider than the B form of DNA. Biologically, the A form is thought to exist as protection against bacterial dehydration.[11] It has also been proposed that due to the shorter conformation compared to B-DNA, the transition to A-form can drive the mechanism for genome packing in bacteriophages.[12]

The final form of helical DNA found in biology differs from the other two as it is left-handed, meaning the double helix winds to the left. The phosphate groups in the backbone zig-zag in an alternating fashion, hence coining the Z name.[13] The helix is thinner and more elongated than in B-DNA with around 12 bp per turn and a diameter reduced from 2 nm to 1.8 nm. The major and minor grooves have little difference in size and the structure as a whole is considered to be unfavourable.[14] It is rarely formed *in vivo* as it is higher energy than B DNA and is thought to form briefly due to biological activity such as during transcription to relieve torsional strain in supercoiled DNA.[15] All three helical DNA forms are visually represented in figure 1.4.

A-DNA   B-DNA   Z-DNA
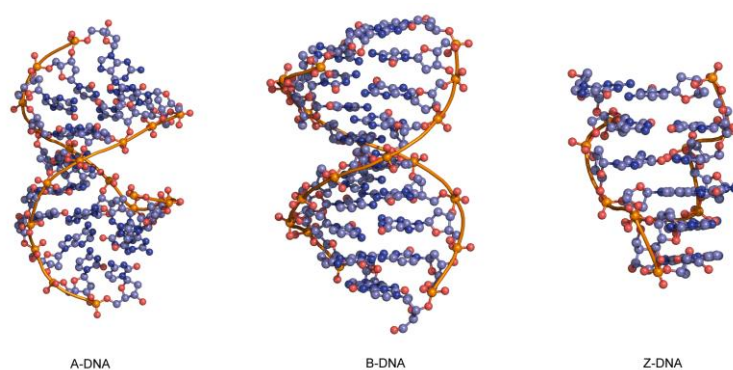
Figure 1.4 – Left: A-DNA, Centre: B-DNA, Right: Z-DNA. Taken from 8.

1.1.2.2 DNA Junctions

There are two types of DNA junctions that can form *in vivo*. The first is the three way junction (3WJ) of which the replication fork is one example. These occur as the name suggests during cell replication as the DNA is split and copied by enzymes such as DNA polymerase. Figure 1.5a shows the structure of a 3WJ, which consists of helical DNA which is then split into single strands which then form a template for complimentary bases to be added to each emerging single strand to produce two final helical pieces of DNA.[16]

A Holliday junction (named after the discovering scientist Robin Holliday) is a DNA four way junction (4WJ) (figure 1.5b). It consists of four double stranded pieces of helical DNA joined together in one junction. These form *in vivo* in repair mechanisms and in biology the junction is not stationary and can slide up and down each strand by breaking and pairing bases as it moves.

Both of these structures have been replicated *in vitro* with short synthetic oligonucleotides, resulting in further studies on their structure.[17, 18] These structures are have been more recently utilised in the field of DNA nanotechnology as a means to build up structures comprised of DNA.[19] This area will be covered in depth later on in the chapter.
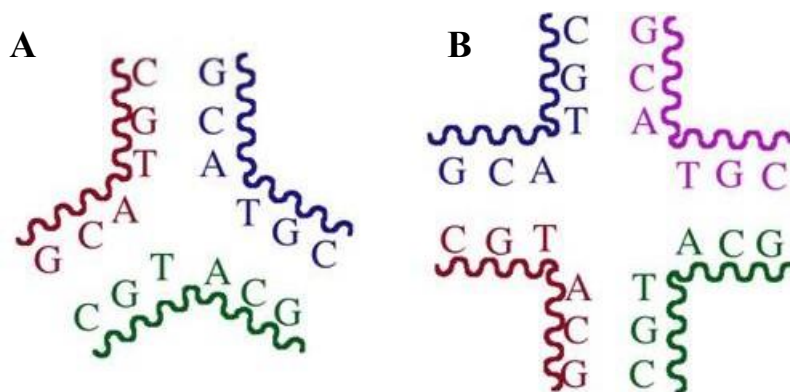
Figure 1.5 – A) Representation of a DNA 3WJ. B) Representation of a DNA 4WJ. Taken from 18.

1.1.2.3 Guanine Quadruplex

The guanine quadruplex (G4 DNA) is a DNA secondary structure which does not follow traditional Watson-Crick base pairing. Instead it exhibits 'Hoogsteen' binding between 4 guanine molecules to form a G-quartet with a central metal cation such as sodium or potassium. (Figure 1.6a). Because of this, the structure can only form in guanine rich sequences. These G-quartets then stack upon one another through π-interactions to form a guanine quadruplex (figure 1.6b).[20]
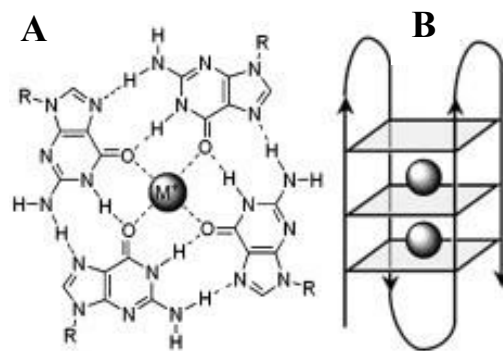
Figure 1.6 – A) G quartet exhibiting four guanine bases with Hoogsteen binding and stabilising central metal cation. B) Representation of stacking G quartets to form a G-quadruplex. Taken from 21

These structures are found at the end of the chromosomes and protect the ends of a subset of some genes during replication.[20] They have also been found to have significant roles in biological systems, such as formation in the telomeric regions in cells to reduce the action of telomerase, which lengthens the telomeres and increases cell lifetime. Overexpression of telomerase can lead to immortalised cells which replicate indefinitely and as such is thought to be involved in around 80-85% of all types of cancer.[22] The potential presence of G-quadruplex structures has also been discovered in oncogene promotor regions.[23] G-quadruplexes of varying topologies, specific to mutated genes relating to a number of cancers,

have been reported such as human c-MYC[24] and human c-KIT[25] (figure 1.7)[26]. Formation of G-quadruplex in these genomic DNA sequences can alter protein output by blocking transcription mechanisms. As each of these quadruplex topologies vary, they have attracted great interest as targets for selective chemotherapy drugs, some of which will be explored later.
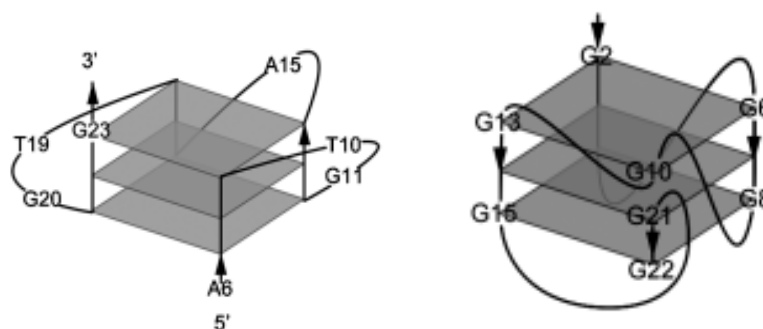
Figure 1.7 – Left: G-quadruplex topology found in the promoter region of the c-MYC oncogene. Right: G-quadruplex topology found in the promoter region of the c-KIT oncogene. Taken from 26.

1.1.3 Targeting DNA structures with small molecules

DNA has long been a very attractive target for drug design as biological outputs start at the DNA level. This means that many diseases such as cancer have their roots in DNA changes and mutations. Alterations in the genetic code of a cell can lead to differing transcriptions of RNA which ultimately leads to altered expression of proteins or enzymes which leads to uncontrolled cell proliferation and function. An example of cancer being caused by changes in protein expression is the well-known simultaneous over expression of the proteins Bcl-2 (an anti-apoptic protein)[27] and Myc (a gene expression regulator)[28], which are characteristic in B-cell lymphoma and cause uncontrollable cell proliferation.[29] Targeting these DNA genes which causes these expressions could offer selective therapy for many cancers. Cancer isn't

the only disease with interesting DNA targets which could have therapeutic effects; Viruses such as HIV work by integrating genetic material in the form of DNA or RNA into host cells. In the case of HIV this infection allows for virus proliferation and cell death in the host T-lymphocytes, leading to loss of immune system for the patient.[30]

This section aims to review the significant developments in drug and small molecule designs for targeting DNA for applications in the clinic, discussing and providing examples of the main modes of DNA binding exhibited by each.

1.1.3.1 Cisplatin and Derivatives

Cisplatin or *cis*-diamminedichloroplatinum(II) (Figure 1.8a) is a square planar Pt(II) compound with two chloride and two ammine ligands in a *cis* arrangement. As part of the alkylating agent drug family, the biological effects of cisplatin were first reported in 1965 by Rosenberg who noticed that cisplatin could inhibit proliferation of *E.coli* bacteria.[31] Its anti-cancer properties were then studied and in 1978 it became the first anti-cancer metallo-drug to become licensed.[32] Since then it has been used to treat a huge range of cancers including bladder, testicular, cervical, head, neck, ovarian, small cell lung, germ cell cancers as well as sarcomas and lymphoma.[33, 34]

Cisplatin's action results from its DNA binding ability. Once in the cell, the chloride ligands are hydrolysed and the platinum is free to bind directly the N7 reactive centre on purine DNA bases (typically guanine). It binds directly to two adjacent purines and this interaction leads to DNA kinking which makes DNA replication impossible while the adduct remains in place (Figure 1.8b).[35] The DNA damage activates various apoptotic factors which lead to cell apoptosis.[36] The DNA binding is a metal-ligand bind and opened up research into thousands of other coordination and covalent DNA binders.[36] This is important because cellular

mechanisms can develop to form resistance to cisplatin action. Many mechanisms have been

identified and once cells have been exposed to cisplatin, they begin to develop. Some main

examples of these are decreases in cellular uptake and increases in efflux to reduce overall

accumulation[37], increases in DNA repair proteins such as topoisomerase II which can remove

cisplatin from the DNA adducts by double stranded excision to reform undamaged DNA.[38]

A **B**
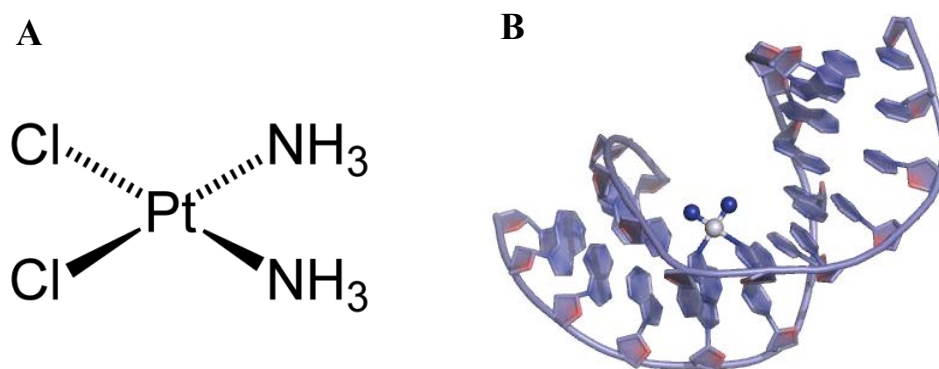
Figure 1.8 – A) Molecular structure of cisplatin. B) Three-dimensional illustration of
a cisplatin-DNA adduct. Platinum shown as a white sphere with the two amine ligands
as blue spheres. Taken from 35.

It is also worth noting that cisplatin does not discriminate between cancerous cells and the

patient's healthy cells. This causes tissue damage throughout the body and significant side

effects which create a narrow therapeutic window and limit its clinical use. Major side effects

are neurotoxicity, nephrotoxicity, ototoxicity, haemolytic anaemia, cardiotoxicity and severe

nausea.[36] It is these side effects and resistance which inspired a generation of Pt(II) drugs

which act in a similar fashion but have varying ligands to reduce toxicity and circumvent drug

resistance. Figure 1.9[39] shows the structures and names of a range of cisplatin derivatives that

have been developed and subsequently been licensed for use in the clinic. Briefly, carboplatin

has been the most successful of these, gaining worldwide approval. Its replacement of the

chloride ligands with one bidentate 1,1-cyclobutanedicarboxylic acid led to significantly

reduced organ toxicity[40], although the mechanism of action and the DNA lesion remains the

same so cisplatin resistant cells are often also carboplatin resistant.[41] Some progress has been

achieved in overcoming resistance with other agents such as oxaliplatin which by replacing

the amines (and thus changing the DNA lesion) has been shown to be effective against some

cisplatin resistant cell lines.[42] None of these, however, can specifically target certain cancers,

but are an excellent example of the class of clinical "alkylating agents" with respect to DNA

targeting and binding.
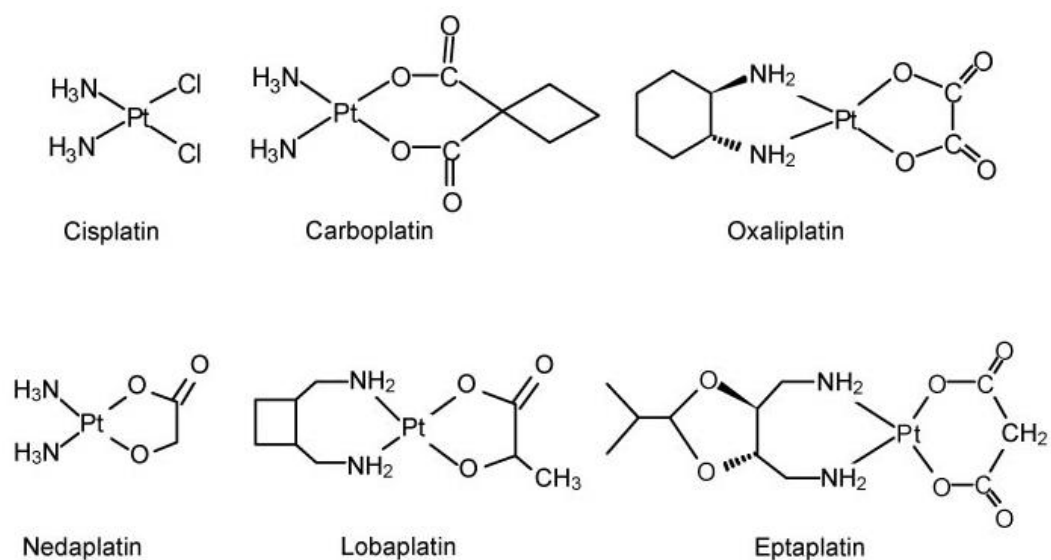
Figure 1.9 – Cisplatin and its second generation derivatives. Taken from 39.

1.1.3.2 Intercalators

DNA intercalation is the insertion of planar small molecules in-between the spaces separating

the DNA base pairs in the helix.[43] For this to be possible, the drugs designed are usually

polycyclic, aromatic and therefore planar which allows the molecule to stack by π-interactions with the base pairs (Figure 1.10).[44] Ionic interactions between the intercalator and the negative charge on the phosphate backbone are also key to adduct stabilisation. The planar characteristic means that the base pairs will not be pushed out of plane which would make binding energetically unfavourable. The intercalation does however, have an effect on the helix. A gap must be made to make space and so the base pairs in which the drug will intercalate lengthen by about 3.5Å per drug molecule.[45] To account for this extra length, the turn of the helix must relax and therefore the DNA unwinds to some extent. Due to the strain on the helix, only 1 intercalator can fit per 2 nucleotide groups, this is known as the neighbouring pair effect. This unwinding is completely dependent on the intercalating molecule and the overall action of the drug will be based on this also. This is because the unwinding causes problems with the action of topoisomerases; enzymes responsible for unwinding the helix before the DNA can undergo transcription.[45]
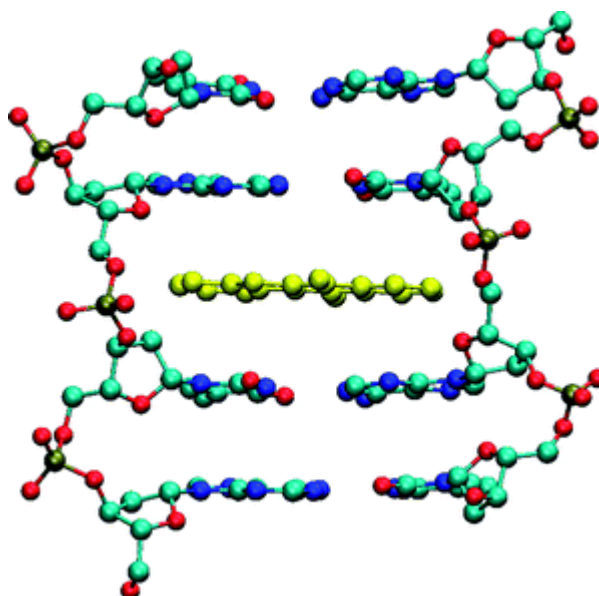
Figure 1.10 – Intercalation of a small molecule (in this case ethidium bromide), illustrating the gap formed between DNA bases and the lengthening of the phosphate backbone. Taken from 44.

It is proposed that as the mode of action of anti-cancer intercalators is to poison the action of topoisomerases, specifically topoisomerase II (TOP2), that these drugs can exhibit selectivity towards cancer cells as TOP2 is active during cell proliferation, which is much more abundant in tumours than in healthy tissue.[46] There is much evidence for the action of the most successful anti-cancer intercalators to be based on enzyme based damage due to TOP2 inactivation.[47, 48] Anthracycline antitumor antibiotics, specifically doxorubicin and daunorubicin (figure 1.11) are a very important family of drugs discovered that intercalate into DNA, forming ionic bonds with the phosphate backbone through the protonated amino group on the sugar and inhibiting TOP2 activity.

doxorubicin (adriamycin)   daunorubicin (daunomycin)
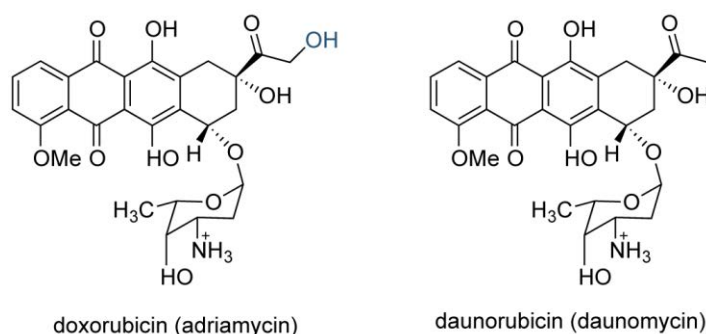
Figure 1.11 – Chemical structure of doxorubicin (left) and daunorubicin (right). Difference between the two molecules highlighted by blue hydroxyl group on doxorubicin. Taken from 34

It is worth pointing out that the activities of these two drugs are quite different, as daunorubicin is only active against leukaemias whilst doxorubicin has a wide range of anti-cancer activity due to the addition of one hydroxyl group. It is thought this is due to the differences of lipophilicity, with doxorubicin with lower lipophilicity able to form electrostatic interactions more readily in the cellular environment.[49] Although it could also be

due to daunorubicin being less able to access solid tumours and therefore more suitable for blood cancers. Figure 1.12 illustrates a doxorubicin-DNA adduct.[50]
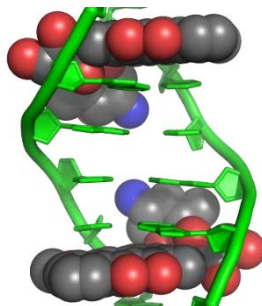
Figure 1.12 – Structure of two doxorubicin molecules intercalated into a DNA helix. Taken from 50.

1.1.3.3 DNA Groove Binders

By exploiting the major and minor grooves in the DNA helix, it is possible to design small molecules to target these areas for therapeutic effect. The first to be considered are minor groove binders. These drugs are designed to possess certain key features that make them suitable for this type of binding. Short chains of heterocyclic or aromatic hydrocarbons with freedom of rotation are characteristic to allow them to stabilise the DNA structure in the minor groove through displacement of water from the hydration layer surrounding DNA through π-interactions.[35] Another important feature usually included in design is cationic groups at the end of the heterocyclic/aromatic chains. These serve to form hydrogen bonds
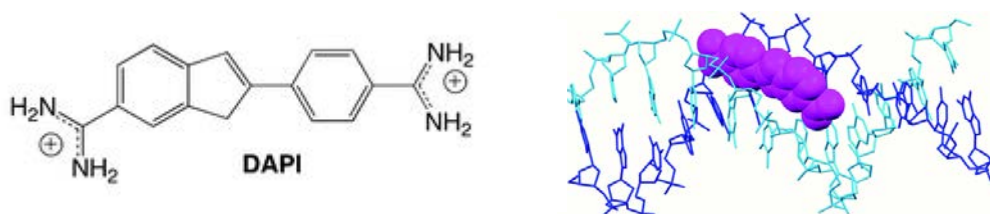
Figure 1.13 – Left) Chemical structure of DAPI. Right) DNA minor groove binding of DAPI. Taken from 52.

14

directly to the DNA bases as well as to interact electrostatically with the anionic phosphate backbone. All of these are an important factor in this form of DNA binding.[51] They tend to have a binding preference for AT over GC rich sequences as these provide a smaller minor groove which offers better binding sites for the molecule.[52] Figure 1.13 illustrates the binding of DAPI (4',6-diamidino-2-phenylindole), a minor groove binder commonly used in fluorescence microscopy as a stain for DNA.

In the clinic, many minor groove binders have been investigated as this type of binding can inhibit the activity of polymerases, providing useful biological activity which has been utilised in anti-parasitic, antibiotic and antiviral applications.[53] One key example is that of distamycin (figure 1.19), a polyamide antibiotic containing many of the key features discussed earlier. This minor groove binder also has binding preference at AT rich regions. Its main action is through inhibiting DNA transcription.[54] Many derivatives and combination treatments from this natural product have found use in anti-cancer therapy, acting as antineoplastic agents.[55, 56]
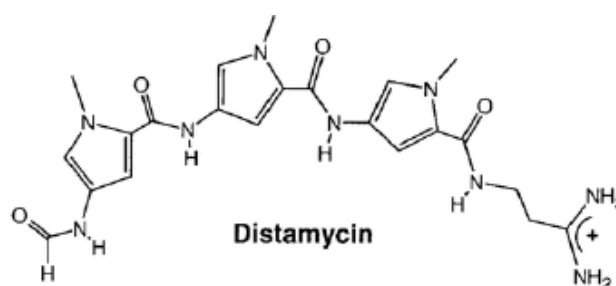
Figure 1.14 – Chemical structure of distamycin. Taken from 56.

The second form of groove binding targets the other groove structure in DNA, the major groove. This structure is much larger than the minor groove and also has great variety in

shape and binding sites due to differing base pair sequences. The interactions between the molecule and DNA are often specific hydrogen bonds directly to the DNA bases.[52] Features characteristic of major groove binders are that firstly they are too bulky to bind to the minor groove. Molecules employing an alpha helical peptide structure that match the turn of the DNA are also characteristic. Strong examples of these are protein motifs such as a zinc finger which can form base pair specific hydrogen bonds to the bases and the cylindrical shape can fit perfectly into a major groove.[52] This type of recognition is often found naturally in the
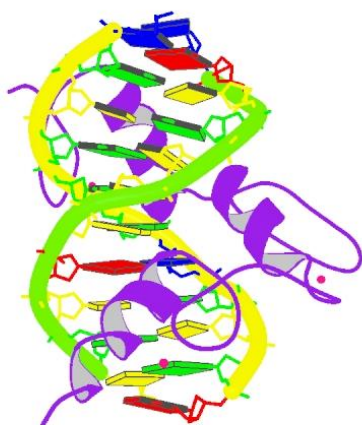
Figure 1.15 – X-ray crystal structure of a zinc finger – DNA complex, the protein involved is a transcription protein derived from *e.coli* bacteria. Protein data bank number: PDT039. Taken from 57

body in protein mediated biological activity (Figure 1.15). By mimicking some of these established proteins, some success has been found in designing proteins that can recognise specific DNA sequences[57, 58], but the complexity and unpredictability of the hydrogen bonding involved make it very difficult to design novel therapeutic peptides that target these structures.[59]   Success was also found by Hannon *et al* by synthesising a di-nuclear supramolecular iron helicate[60], roughly the same size as a zinc finger and capable of binding inside a major groove. This helicate will be discussed in full later on in the chapter.

By exploiting hydrogen bonding in similar, single stranded pieces of DNA or oligonucleotides are also able to bind to the major groove through Hoogsteen or reverse Hoogsteen base pairing on the exposed side of the purine bases. Both protonated cytosine and guanine can bind a guanine base and both adenine and thymine can bind an adenine through this fashion (figure 1.16).[52] This binding is sequence specific to sections of purine bases and when bound, forms what is known as triplex DNA – 3 strands of DNA in the helix. This sort of binding has been found to interfere with gene expression and its sequence specific nature has attracted some research attention. Notably the drug Fomivirsen is an antiviral oligonucleotide with the sequence GCG TTT GCT CTT CTT CTT GCG (5'-3'). It blocks viral action by binding to viral mRNA, halting vital protein expression.[61]
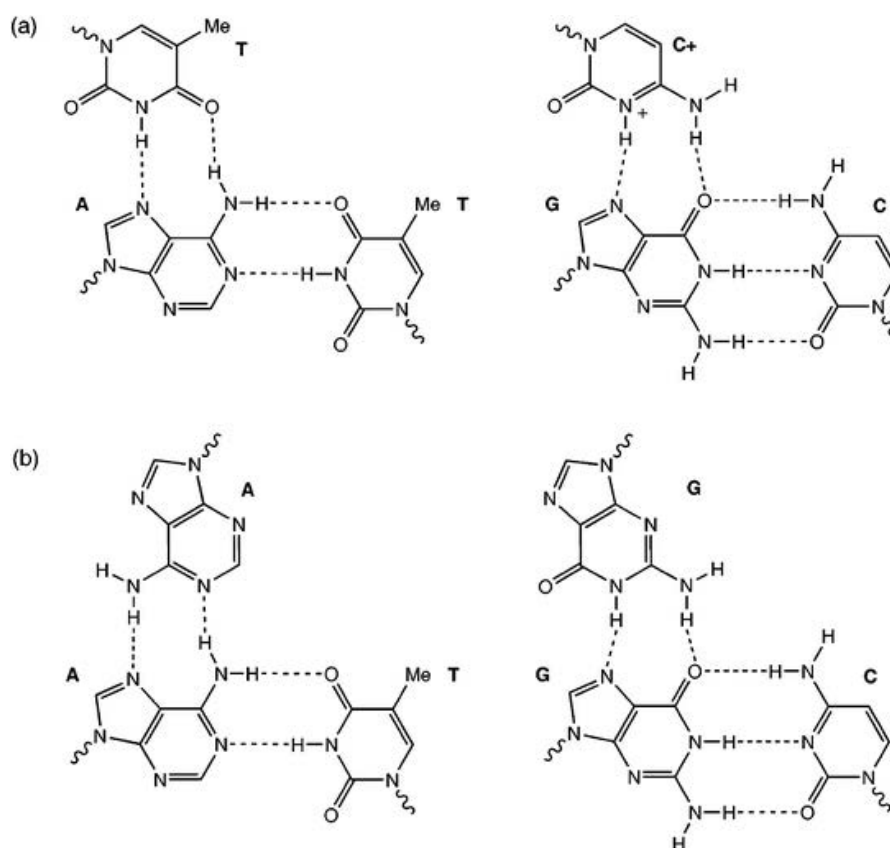
Figure 1.16 – A) Chemical structures of Hoogsteen base pairing in triplex DNA, B) Reverse Hoogsteen base pairing. Taken from 52

1.1.3.4 G-Quadruplex Binders

As discussed earlier, G-quadruplexes form in guanine rich areas of the genome which have been found to have strong biological significance such as the telomeres and gene promotor regions of key oncogenes. They are also unusual DNA structures with strong characteristic features whose topologies vary widely. For these reasons, they have been a target of wide interest in recent years.[62, 63] They are considered to be druggable due to their role in the majority of human cancers, whether it be inhibiting the action of telomerase which has a key role in cell immortalisation and transformation[64] or in the gene promoter regions of key oncogenes such as c-MYC, controlling expression of proliferation enzymes.[28] Hundreds of small molecules have been synthesised in recent years which have been shown to interact with G-quadruplexes with certain characteristic molecule designs becoming apparent.[65] Figure 1.17 shows some examples of proven G-quadruplex binding compounds that have

Telomestatin

(a)

TMPyP4

(b)
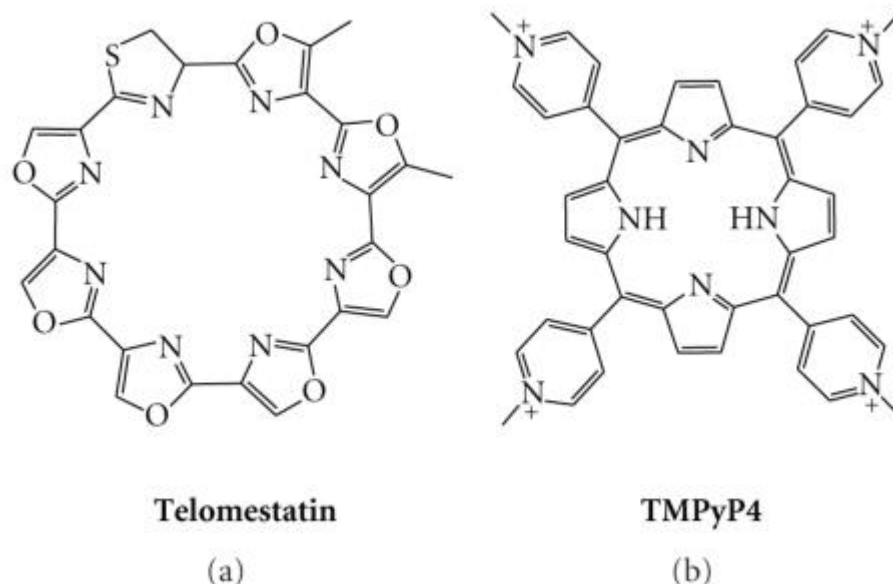
Figure 1.17 – A) telomestatin, a known G-quadruplex binder and telomerase inhibitor. B) TMPyP4, a strong quadruplex binder with potent anti-cancer activity. Taken from 66.

made it to clinical trials. Both the molecules shown exhibit a large amount of planar aromatic groups for stacking on top of the upper or lower most G-tetrad in the quadruplex.[66] Square planar complexes with central metal cations such as Pt(II) or Pd(II) have also been suggested as the metal ions help co-ordinate ligands in the square planar fashion required for stacking.[67] The positive central charge can also stabilise the quadruplex by substituting the central cation Na^+ or K^+ usually found inside the quadruplex.[67]

1.1.3.5 Cylinder DNA binding

The focus of this thesis will be a metallosupramolecular iron cylinder (FeCy) and its enantiomers, first designed and synthesised by Hannon *et al* in 1997 (figure 1.18b).[60]
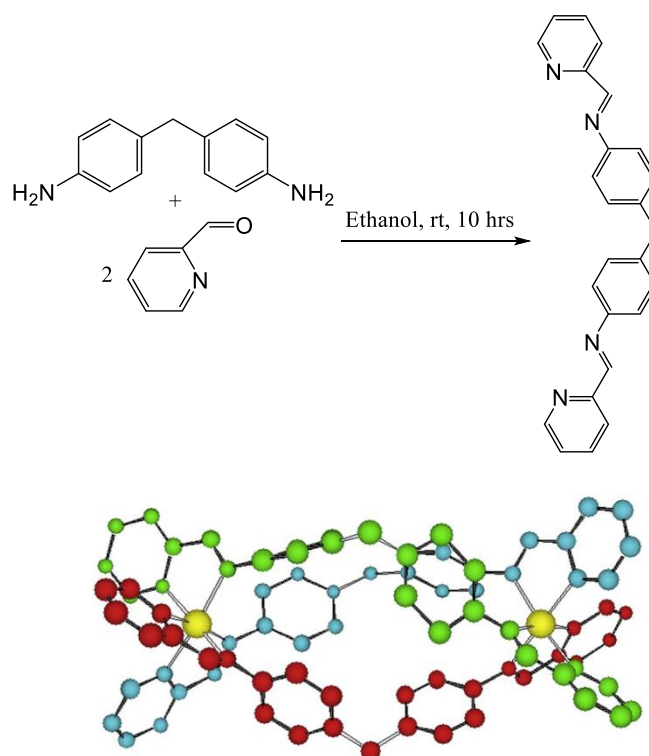
Figure 1.18 - A) top: Synthetic scheme of the reaction step to form the cylinder ligand. B) 3D diagram of the cylinder, each of the three ligands shown in red, blue and green with the two central iron ions as yellow spheres, bottom figure taken from 60.

Two other cylinders, containing Ni and Ru (NiCy and RuCy) as centres in place of iron will also be explored. The iron cylinder is so named due to its cylindrical 3D shape. It is roughly 2 nm in length and 1 nm in width which gives it similar dimensions to that of a zinc finger protein which is able to bind major grooves in DNA. The FeCy compound is synthesised in a simple one pot reaction (Figure 1.18a)[68]. Firstly the pyridylimine ligand is formed before complexation of 3 equivalents of the ligand to 2 equivalents of $FeCl_2$ to form the iron cylinder as a racemic mixture of two enantiomers. These two enantiomers exist due to the inherent helical structure of the ligands leading to either a left-handed helicate, known as the M enantiomer, or the right handed helicate, known as the P enantiomer (Figure 1.19a). These enantiomers were first separated in 2001 using filter paper as a cellulose chiral stationary phase.[69] Since then, cellulose powder column protocols have been developed to allow easy and clear separation of the enantiomers (Figure 1.19b). The cylinder is tetracationic, which helps in its strong binding to DNA and a variety of counter ions are available to the structure, most notably Cl^- which allows the cylinder to be water soluble and so very useful in biological experiments.
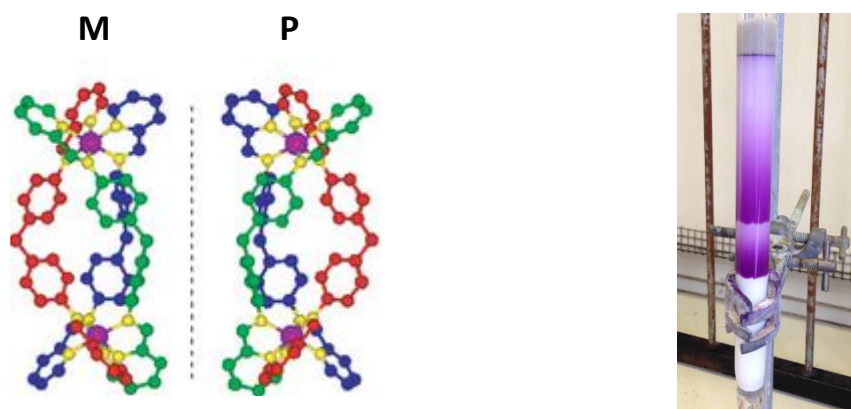
Figure 1.19 – A) Left: Crystal structures of both the M (left) enantiomer and P (right) enantiomer. Taken from 69. B) Right: Cellulose column showing separation of enantiomers, eluting M enantiomer first followed by the P.

The DNA binding activity of the cylinder has been studied in some depth. To begin with, the cylinder was shown to bind inside the major groove of DNA (Figure 1.20).[70]
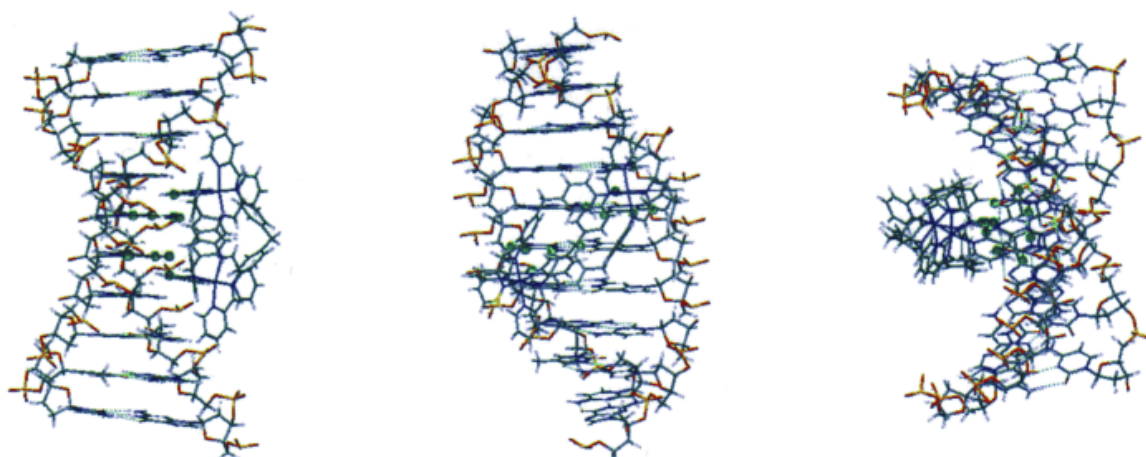
Figure 1.20 – Structures of confirming cylinder binding inside a DNA major groove synthetically formed in solution by the oligonucleotide [5′-d(GACGGCCGTC)]2. Resolved by NMR experiments. Figure taken from 70.

The high cationic charge of the cylinder allows binding of the polyanionic DNA and as such has a number of dramatic effects on the DNA. By binding across about 5 bp in the duplex, the cylinder causes the DNA to 'wrap-up' and coil intramolecularly which has been illustrated by AFM (Figure 1.21).[70] As discussed earlier, major groove binding proteins tend to match the helical turn of B-DNA and this is also true of the cylinder. As it has two enantiomers, however, they have been shown to have different binding modes to DNA.[71] The M enantiomer induces much more coiling in DNA than the P. Further experimentation here showed that while the M enantiomer can be proven to bind to the major groove, P enantiomer binding was found to be unlikely to be here, and the most likely binding area was bridging 2 phosphate groups in the backbone across the minor groove. This is a less perfect fit and thus can explain the discrepancy in binding strength and coiling.[71]
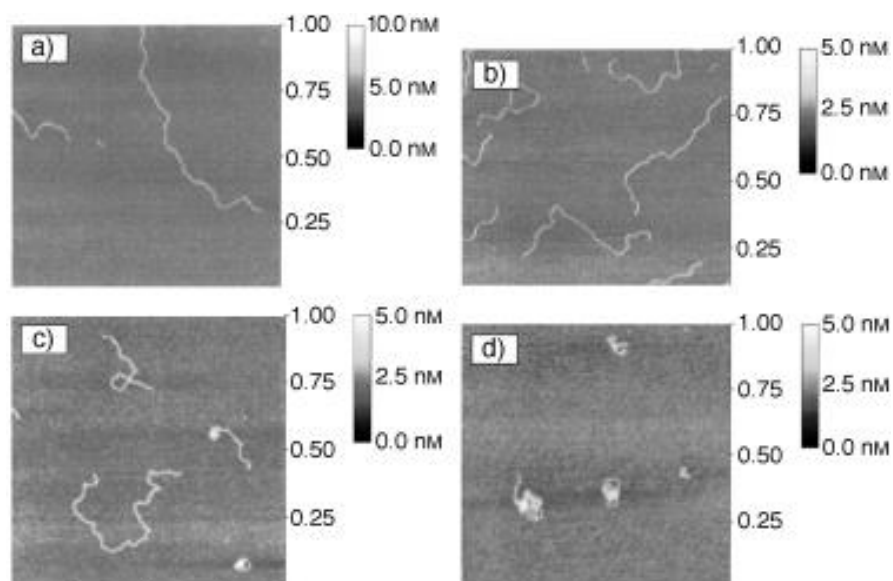
Figure 1.21 – AFM images of the linearised plasmid pBR322, 4361 bp, diameter of 475 nm, cleaved with Pst I and Sal I enzymes to give two linear fragments of 1401 bp and 2962 bp. A) linear plasmid fragments alone, B) Low concentration of FeCy with plasmid, C) Medium concentration of FeCy with plasmid, D) High concentration of FeCy with plasmid. Taken from ref 70

The iron cylinder has also been shown to bind another DNA structure which is unprecedented in small molecule DNA recognition. It can recognise, bind and stabilise a DNA three way junction (3WJ) (figure 1.22).[72] 3WJ structures, as discussed earlier, form in DNA strands during replication, where a topoisomerase unwinds the DNA and polymerase can start to duplicate the strand. With regards to cancer therapy, 3WJ are an attractive target as cancer cells proliferate at a much accelerated rate compared to a healthy cell and so will have a higher proportion of 3WJ and so could offer some form of drug selectivity.

The cylinder has been shown to have a preference for 3WJ structures over B-DNA[72]. It is also possible that the cylinder will preferentially bind to other DNA structures, the degree of which will be explained and discussed further in Chapter 2. Interestingly, the crystal structure of the

cylinder binding inside the 3WJ in figure 1.22 universally showed the M enantiomer bound inside the 3WJ despite the fact the DNA was incubated with a racemic mixture.[72] This result is not an exhaustive study of the enantiomer interactions with the 3WJ and cannot conclude that the P enantiomer does not bind. It does, however, suggest that the M enantiomer does bind more effectively than the P enantiomer.
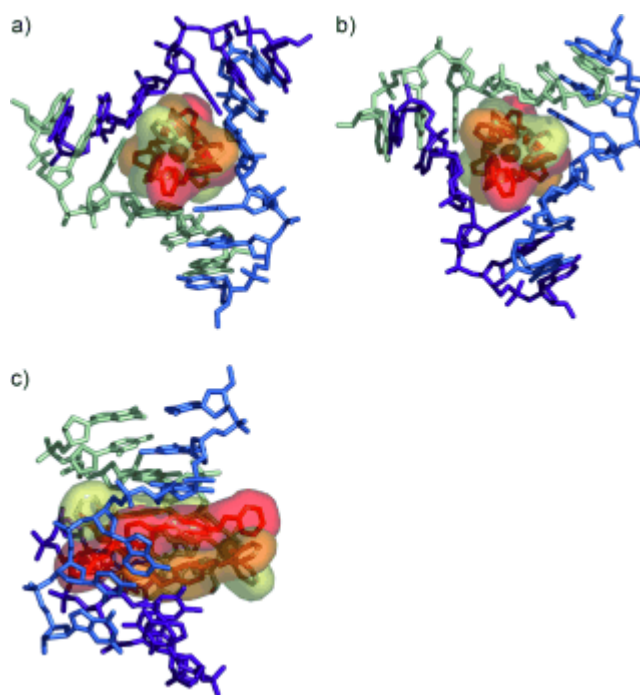
Figure 1.22 – A) 'major groove' side of the 3WJ with cylinder bound inside the centre. B) 'minor groove' side of the 3WJ with cylinder bound inside. C) Side on view of the cylinder bound 3WJ, showing the ligands on the major groove side sticks out further than the minor groove side. Taken from 72.

The binding of the cylinder also causes distortion, the result of which leads to bases stacking out of plane and the backbone bending.[72] This is important biologically as it is less likely that enzymes will be able to initiate transcriptions when cylinder and thus gene protein expression can be altered.

In this regard, the biological activity of the iron cylinder has been studied in some depth due to its unique and powerful DNA binding capabilities. Against cancer cells, the cylinder has been shown to have potent cytotoxicity against numerous cell lines whilst proving not to be genotoxic or mutagenic in comet assays or the AMES test.[68]

1.2 DNA Nanotechnology

1.2.1 Origins and methods of structural DNA Nanotechnology

The concept of DNA nanotechnology was first publicised by Professor Nadrian Seeman at New York University in 1982 [73], where, taking inspiration from a repeating unit picture in a local pub, noticed similar interactions could be translated to synthetic ssDNA. By definition, DNA nanotechnology is a branch of nanotechnology concerned with the design, study and application of synthetic structures based on DNA. DNA nanotechnology takes advantage of the physical and chemical properties of DNA rather than the genetic information it carries. Specifically Seeman outlined that designed synthetic oligonucleotide strands could self-assemble into predetermined DNA structures.[73,74] This was based on maximising well known Watson-Crick base pairing interactions and minimising symmetry which would lead to linear duplexes of DNA. Seeman provided proof of this concept when he synthesised a 3D cube structure starting with specifically designed oligonucleotides.[19] Figure 1.23 illustrates the scheme starting with cyclised ssDNA leading finally to the fully formed 3D cube over a multi-step synthesis. This initial bottom-up approach, whilst providing proof of concept for Seeman, proved to be a laborious synthesis which provided just a 1 % yield.

The general synthetic approach for this bottom-up scheme begins with ssDNA. These strands are designed specifically and synthetically made so they can hybridise to the most favourable Watson-Crick base pairing and give predictably positioned double stranded DNA. To allow these oligonucleotides to cyclise with themselves or ligate end to end with other
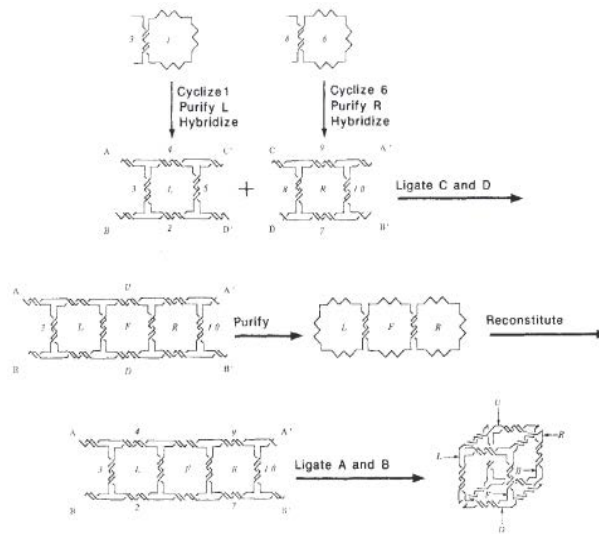
Figure 1.23 – Schematic diagram illustrating Prof. Seeman' first synthesis of the 3D DNA cube. Taken from 19.

oligonucleotides, they must first be phosphorylated.[75] This is the process of attaching an ATP group to the 5' or 3' end of an oligonucleotide, generally using a kinase enzyme in the presence of ATP to facilitate the reaction. Once phosphorylated, the strands can be hybridised together to form duplex DNA strands. In Seeman's synthetic scheme a process known as annealing is employed. This simple step involves heating the strands together in stoichiometric quantities in buffer beyond the DNA melting point at which all hydrogen bonds are dissociated. Once left to cool, the strands form hydrogen bonds together according to the most thermodynamically favourable Watson-Crick base pairing and form the pre-meditated duplex structure desired. Ligase enzymes can then be used to ligate the additional ATP groups into the formed structure.

Another key DNA nanotechnology method is also known as 'sticky-ended cohesion'[76] which is a key technique in all genetic microbiology and can be illustrated more clearly in figure 1.24.[77] Here, two complimentary ssDNA overlaps at the end of two pieces of helical DNA can be annealed together with great affinity. This is because the sequence specific affinity for each

is known and will be highly specific as long as any competing species have altered overlapping sequences that provide less favourable hydrogen bonding. This concept is central to the majority of DNA nanostructures produced in the last 35 years which rely on sequence specific and sequential structural motifs.[78]
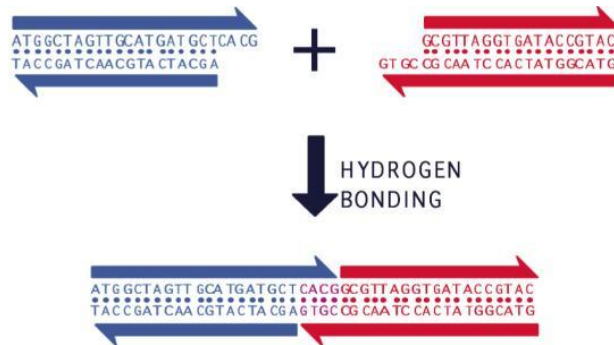
Figure 1.24 – Schematic diagram, illustrating the single stranded overhangs of the duplex DNA hydrogen bonding together to form a single duplex. Taken from 77.

As discussed early, branched junctions of DNA occur throughout the genomic DNA in the cell. To create small DNA structures, such as the cube, it is imperative that rigid and stable junctions can be assembled.[73] In biology the strands involved in the earlier discussed three and four way junctions, have symmetry with each other. This allows junction migration which is key to the biological process as the strands move through the enzymes, which involves breaking and reforming the hydrogen bonds between each nucleotide as the junction moves down the duplex.[79] However, in DNA nanostructures, junction migration is undesirable. To avoid this, junctions must be designed to minimise symmetry between all single strands involved in the junction.[80] This is illustrated clearly in figure 1.25, which shows that by eliminating symmetry in the strands involved in the junction, only 1 stable form of junction is

synthesised and junction migration is impossible as there is no complimentary nucleotides for the boxed tetrad of nucleotides in the junction. This method works for junctions with few arms such as the Holliday junction, but more complicated and imaginative approaches have been developed to synthesise junctions with higher numbers of arms, as symmetry is difficult to eliminate here across the junction.[81]
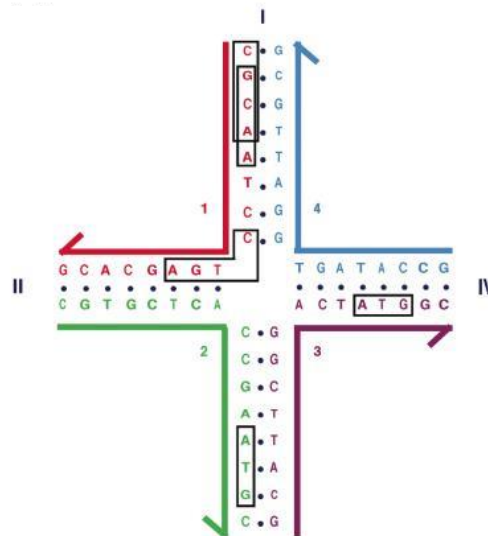
Figure 1.25 - Sequence model for a synthetic 4-way junction. The sequences are of 13 overlapping tetramers. The first two are boxed at the top of the model. The second boxed tetramer (AGTC) illustrates there is no complimentary tetramer anywhere in the model to ensure no pairing across the junction. The boxed trimers (ATG) clearly could compete here but the free energy difference between the desired junction and the trimer prevents this. Taken from 81.

These basic methods form the basis of designing and synthesising a small DNA nanostructure. There are more methods and a whole other branch of DNA nanotechnology has developed known as DNA origami which will be discussed in depth later in the review.

Before this, various examples of structures originating from these methods and their impacts will be discussed.

1.2.2 Small 3D DNA structures

By exploiting the design and construction techniques discussed above, numerous research groups have reported synthesis of a wide variety of small 3D DNA structures. Notable examples building on from Seeman's initial cube, include a truncated octahedron[82], reported by Zhang and Seeman in 1994. The structure, shown in figure 1.26 shows each vertex is separated by 2 helical DNA turns, this structure was a step up in terms of complexity from the cube, and like the cube, it was flexible due to all nicks in the duplex being ligated. The structures were never able to be resolved microscopically and so, gel electrophoresis had to be relied upon for structure elucidation. It is also worth noting that the synthesis involved many steps and purifications and thus, took around 2 years to complete start to finish and had a low yield of less than 1%.[82]
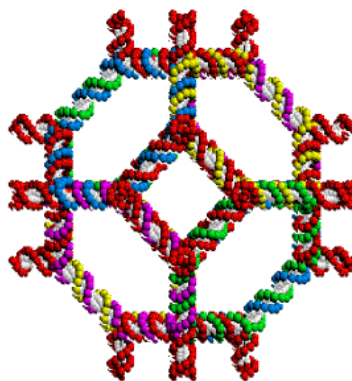
Figure 1.26 – Proposed structure of a DNA octahedron. Taken from 82.

An advance was made on this labour intensive synthetic method by Shih et al in designing a truncated octahedron out of a 1.7 Kb strand which was designed to be folded into an octahedron by a simple annealing step.[83] The structure was able to be resolved with cryo-electron microscopy and provided some of the first microscopy images of small 3D DNA nanostructures. Figure 1.27 shows the microscopy images obtained here, interestingly AFM images were not reported in this publication and this could be due to the structures inherent flexibility, which wouldn't allow the structure to resist the pressures involved in AFM analysis to provide images that would accurately reflect the overall structure.
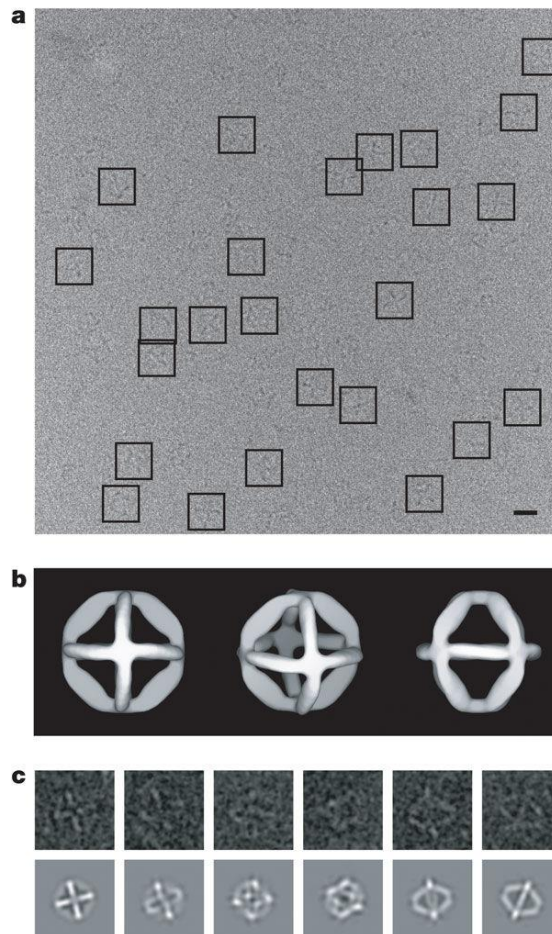
Figure 1.27 – A) Raw Cryo-EM images of Octahedron. B) Projections of expected image. C) Raw images of each expected orientation. Taken from 83.

1.2.2.1 DNA Tetrahedron

A DNA tetrahedron structure reported in 2004 by Turberfield *et al* was a revolutionary single step self-assembled 3D DNA structure, synthesised at a yield of over 95%, depending on concentration.[75] This structure attracted a lot of interest and many variants have been synthesised and the structure very well characterised.[84] The tetrahedron is also a major focus in this thesis and so research surrounding it will be reviewed in some depth.

The revolutionary one-step self-assembly employs four oligonucleotides which are then annealed together in buffer. On cooling, diastereomeric tetrahedra are formed as the thermodynamic product in high yield.[75] Figure 1.28 illustrates this step and shows the overall structure of the first tetrahedron structure synthesised by Turberfield *et al.*
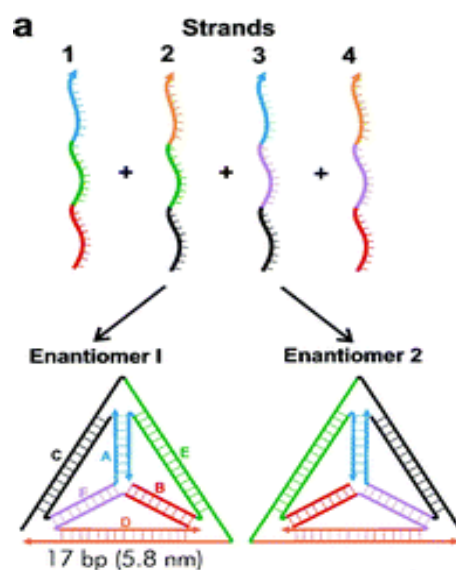
Figure 1.28 – Diagram illustrating the 1 step synthesis of the DNA tetrahedron. Taken from 75.

Following on from this discovery, a variety of tetrahedron structures were reported by Goodman *et al.*[85] These involved varying the side lengths to demonstrate the versatility of the assembly step. Dimers were also reported, by leaving a complimentary sticky-ended overlap on one edge to allow 2 tetrahedra to hydrogen bond to one another. Figure 1.29 demonstrates some examples of this family of tetrahedra visually.
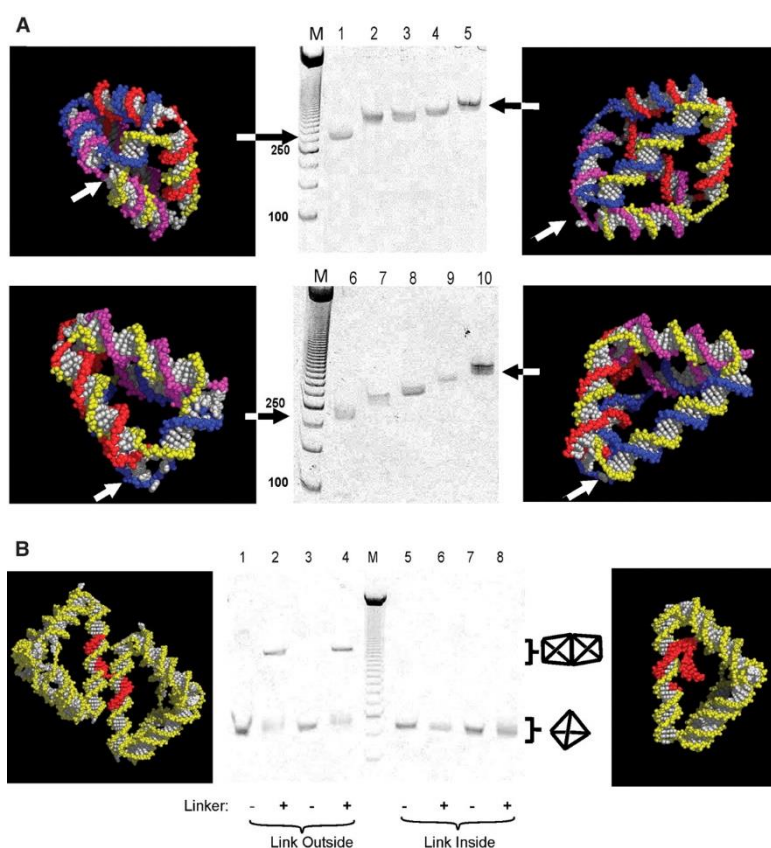
Figure 1.29 - (A) Tetrahedra with five 20-bp edges and one edge of 10 bp (lane 1), 15 bp (lane 2), 20 bp (lane 3), 25 bp (lane 4), or 30 bp (lane 5). Tetrahedra with four 20-bp edges, one 10-bp edge, and an opposite edge of 10 bp (lane 6), 15 bp (lane 7), 20 bp (lane 8), 25 bp (lane 9), or 30 bp (lane 10). For both series the tetrahedra in the first and last lanes are illustrated by 3D models; the edge that is varied is marked with an arrow. (B) Linking experiments demonstrating stereoselectivity. A linking strand may join two 5×20/1×30-bp tetrahedra by hybridizing in 10-bp single-stranded gaps in both long edges.[83] Figure taken from 85

These tetrahedra have a wide scope for functionality and variety. The hollow cavity also represents a clear opportunity to encapsulate a cargo. Research initially focused on filling this internal cavity with a protein. The first attempt by Erben *et al* involved covalently binding a small recombinant protein inside the tetrahedron.[86] The central cavity was estimated to be able to encapsulate a sphere of a radius of 2.6 nm, equivalent to a folded protein of around 60 kDa. Cytochrome C protein (12.4 kDa) was selected and conjugated to one of the four construction strands of the tetrahedron through a surface amine at the 5' end of the oligonucleotide. The tetrahedron could then be constructed by combining the other three strands. By controlling the design of the tetrahedron, the position of the protein attachment can be adjusted as the turn of the duplex rotates about 13° per nucleotide down the turn.[86] Figure 1.30 illustrates the structure of the formed tetrahedron and outlines the control over the pitch and positioning of the attached protein, with each possible base position tested by gel electrophoresis.
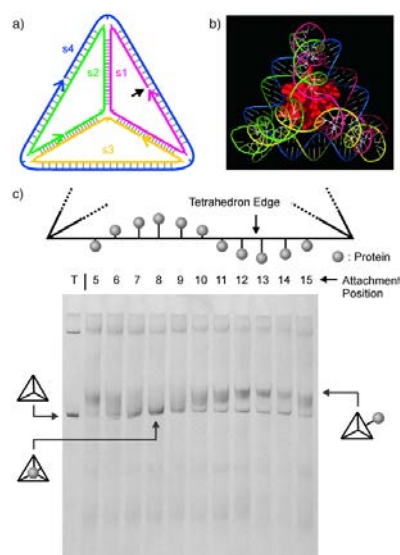
Figure 1.30 – A) structure of formed tetrahedron with nicks located on the vertices. B) Model of final product. C) Diagram demonstrating effect of the rotation of the duplex on protein attachment point and gel electrophoresis experiment. Taken from 86

This publication only covered the encapsulation of the cargo and didn't highlight any methods for subsequently releasing the cargo. As the surface amine attachment is a covalent bond, the bond would be very difficult to break without denaturing the protein. Various other covalent strategies for combining DNA with proteins have been reported including bifunctional crosslinkers[87], click chemistry[88] and disulphide bonds[89]. A reversible, non-covalent attachment between cargo and DNA structure became the challenge and this challenge began to be addressed when Goodman *et al* reported a reversible non-covalent coupling between proteins and oligonucleotides via a nickel mediated co-ordination bond involving Histidine tags on the protein and NTA (nitrilotriacetic acid) groups on the oligonucleotide.[90] Once the coupling was initiated, the central Ni cation could be sequestered via use of a chelating agent, breaking the coupling.

This coupling was then used by Bermudez *et al.* in 2012 in a tetrahedron-like structure and enhanced green fluorescent protein (EGFP) was internalised inside a DNA tetrahedron with i-motif functionalities on the edges.[91] The reversibility and subsequent release of the internalised EGFP was achieved through lowering the pH of the buffer to hydrolyse the Ni co-ordination bonds and form i-motifs in the vertexes which causes the tetrahedron to collapse in shape, subsequently releasing the protein from the structure. Unfortunately the low pH required for this denatured much of the protein activity.

Another cargo encapsulation example involving the tetrahedron was reported by Crawford *et al.* in 2013.[92] In this publication, catabolite activator protein (CAP), a transcription factor, was encapsulated inside a DNA tetrahedron. CAP intracellularly regulates up to 100 genes in the body and so was an interesting target as transcription factors activity can be blocked whilst inside a DNA cage as it cannot bind cellular DNA.[92] If an external trigger was found that

could release the protein whilst inside a cell, this would be a way to elegantly regulate gene expression.

Encapsulation was achieved by incorporating a 22 bp sequence that matches the 22 bp recognition site on CAP into a DNA tetrahedron. This would then allow the CAP to recognise the site on the tetrahedron and bind inside (figure 1.31).
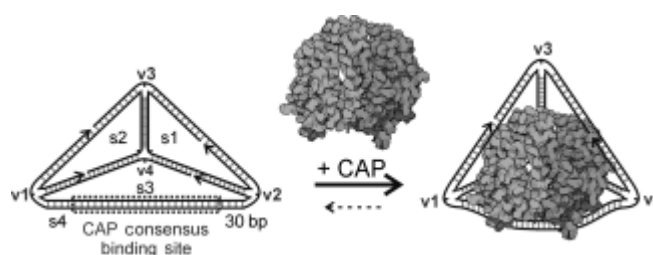
Figure 1.31 – Model diagram of the DNA tetrahedron possessing the binding site for CAP and the subsequent encapsulation of CAP inside the central cavity. Taken from 92.

The subsequent release of the CAP was demonstrated by addition of a nuclease to remove the DNA (effectively, if unselectively). However, it is reasonable to theorise any deformation of the binding site by an external factor would result in protein release such as DNA binding of a small molecule.

The potential of the DNA tetrahedron as a strong candidate for cellular delivery of cargo has been discussed in depth and further literature reports of biological compatibility will be discussed further later in this introduction.

1.2.3 DNA Origami

A large branch of DNA nanotechnology that must be mentioned has become known as DNA origami. DNA origami was first reported in 2006 by Paul Rothemund at the California Institute of Technology.[93] It involves using a 'construction strand' which is an oligonucleotide of around 7kb. This construction strand is then manipulated with designed smaller 'staple' strands. These smaller oligonucleotides bind to the construction strand in a single step process to form the most energetically favourable formation. By carefully designing the staple strands, one is able to form controllable shapes of up to 100 nm in diameter.[93] This technique allowed for a wide variety of recognisable shapes and structures to be synthesised and observed by AFM (figure 1.32).
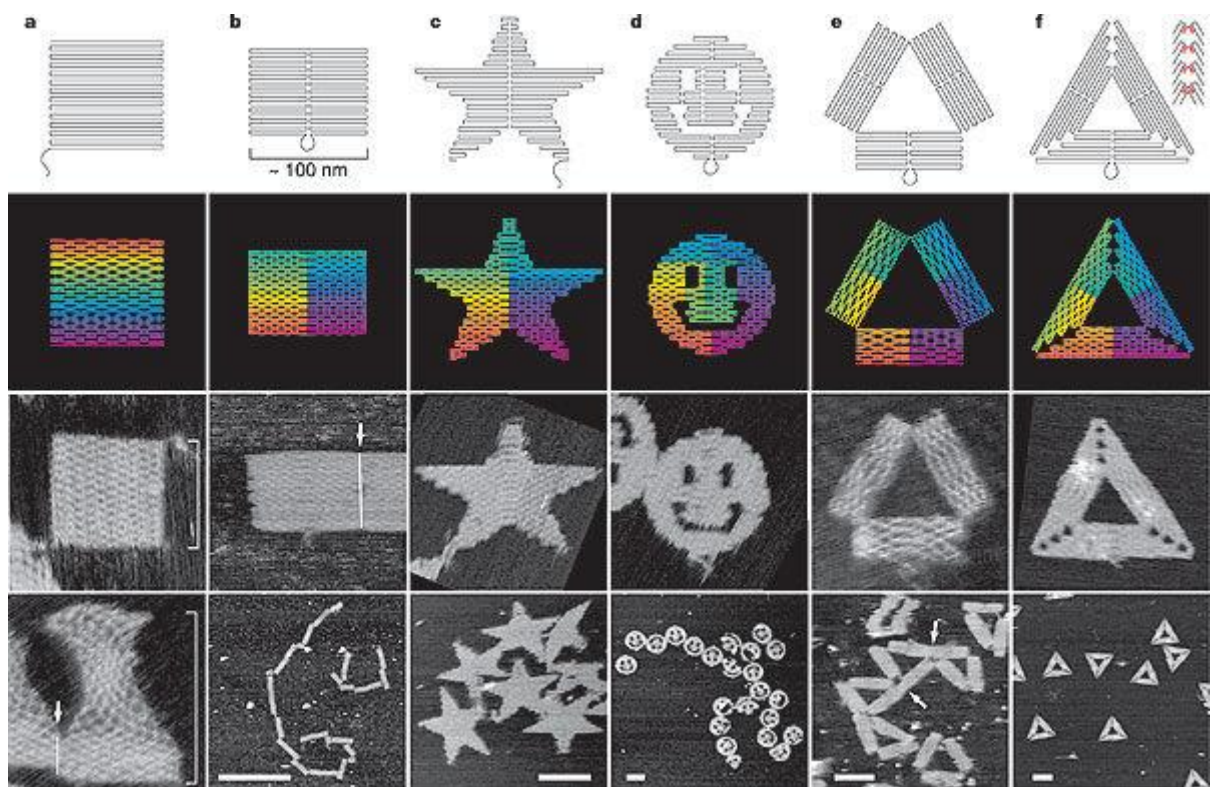
Figure 1.32 – Wide variety of shapes of folded DNA to form a) a square, b) a rectangle, c) a star, d) a smiley face, e) a pyramid of rectangles, f) a hollow triangle. All imaged by AFM. Taken from 93.

This revolutionary work opened up many research opportunities to expand, not only on these 2D arrays, but to form 3D structures out of folded DNA origami.[94] The first and one of the most notable examples was by Gothelf *et al.* in 2009, synthesising a 3D box which possessed an openable lid which could be opened selectively on addition of an oligonucleotide or 'key'(figure 1.33).[95]
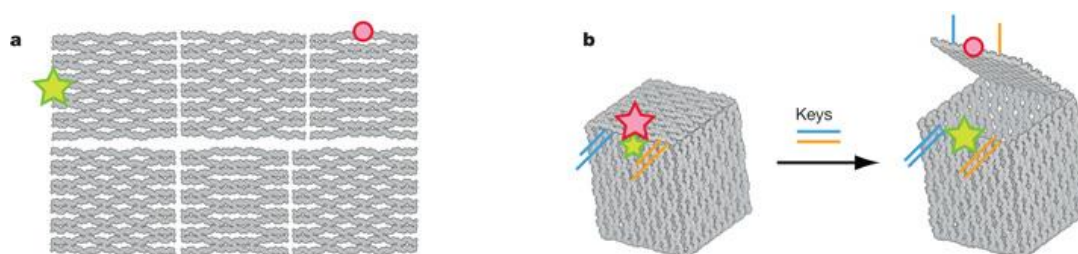
Figure 1.33 – Model illustration of a) the origami construction square sections of folded DNA, functionalised with FRET pair (yellow star and red circle), b) fully constructed box with lid closed, allowing FRET to occur between the FRET pair. On addition of competing oligonucleotides (keys), the box is opened and halts FRET. Taken from 95.

Rigid enough to be characterised by AFM, cryo-EM and confirming the control of the lid through FRET experiments, this box certainly had an impact on the research area. The box has a few advantages over previously reported 3D DNA proposed cargo carriers as it can be opened by a specific trigger of any ssDNA or ssRNA, which could be tuned to specific

cellular sequences. It also occurs under native conditions[95] and unlike low pH conditions seen earlier[91], biological cargo is unlikely to be damaged by the triggered release.

Many groups reported similar boxes of differing size and shape to this original box, including a very similar box synthesised through closing a single open origami motif.[96] Sugiyama *et al.* reported triangular, square and octahedral hollow prisms of DNA origami in simple 1 pot folding of a motif.[97] A hollow DNA origami tetrahedron (figure 1.34) was also reported by Yan *et al.* in 2009 which attempted to address potential problems with the hollow sides to Turberfield's tetrahedron.[98]
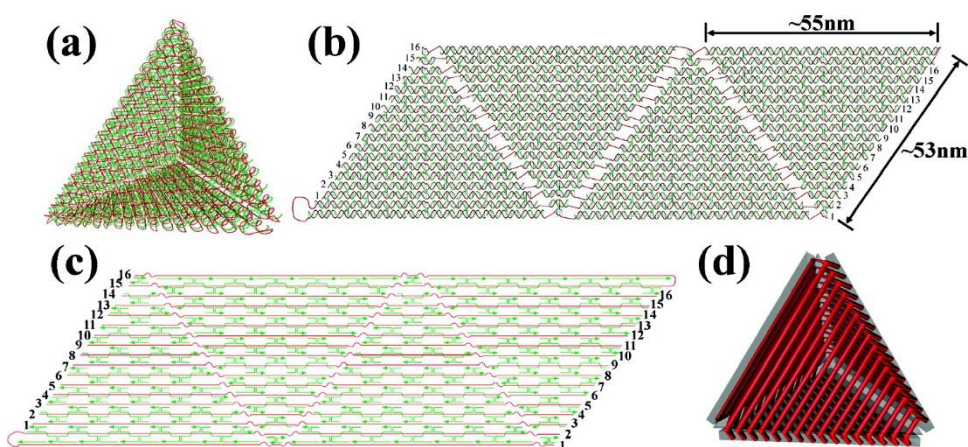
Figure 1.34 – A) Model drawing of completed origami tetrahedron. B) 2D drawing of the unfolded motif constructed. C) 2D drawing illustrating the folding of the construction strand. D) Model illustrating construction features of the tetrahedron. Taken from 98.

Yet another approach to using DNA origami to construct 3D structures was reported by Shih *et al.*[99] Here, the hollow cavity of the structures were replaced by honeycomb rods of DNA

nanotubes. This pleated helical construction approach was aimed more at nanoscale device bearing applications rather than a cargo carrier. This was made possible by the much more rigid and solid structure of the design (figure 1.35).
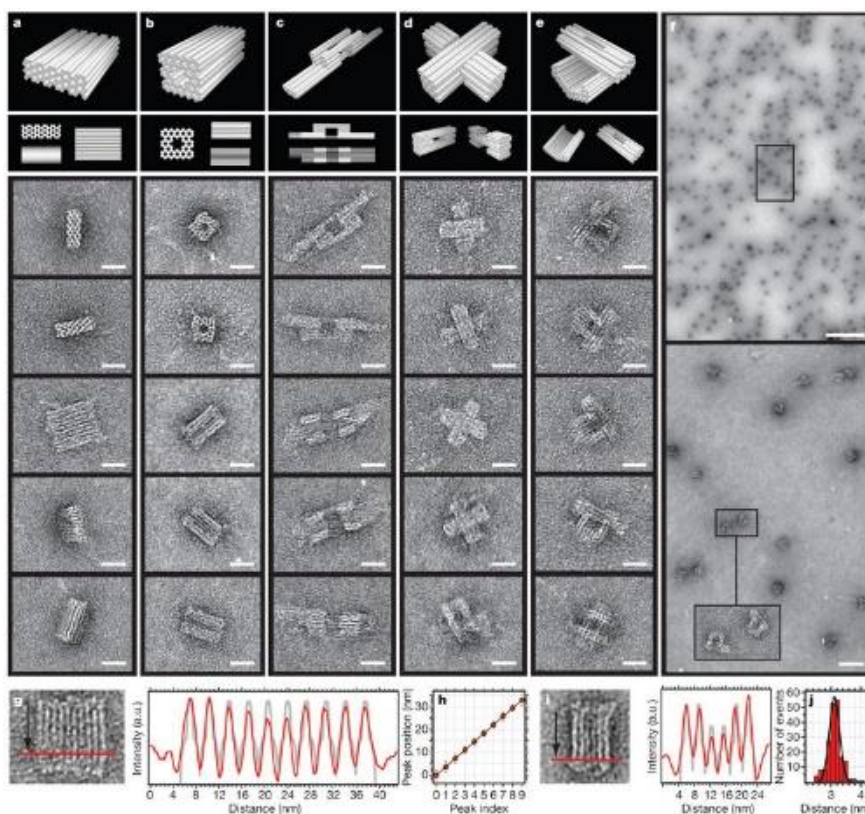
Figure 1.35 – TEM images of a variety of synthesised honeycomb DNA origami structures. Taken from 99.

Overall, DNA origami was shown to be a very versatile method within DNA nanotechnology to achieve a wide variety of structural targets. With this versatility, and DNA being a biocompatible substance, it is no surprise it has gained so much interest as a capable cargo delivery medium to cellular systems. Research resulting from combining DNA nanotechnology with biological systems will now be reviewed.

1.3 DNA nanotechnology in Biological Applications

1.3.1 DNA tetrahedron in cellular systems

The DNA tetrahedron was first reported to be able to enter cells by Walsh *et al.* in 2011 following its discovery in 2004.[100] This is particularly interesting as the polyanionic nature of DNA makes cell membranes impermeable for dsDNA and ssDNA.[101] Here, Turberfield's original tetrahedron was fluorescently labelled with a fluorescent tag and incubated with human embryonic kidney cells (HEK line). The uptake and localisation was observed and measured with and without transfection agents by confocal microscopy. It was found that even in the absence of transfection agents, the tetrahedron was readily taken up by the cells. It was also found through FRET experiments that the tetrahedron remains intact for over 48 hours inside the cells.[100]

However, the article does not detail the mechanism by which the structure enters the cells. Instead it speculates on theories consistent with other nanoparticle uptake studies,[102] suggesting macropinocytosis, clathrin-mediated endocytosis, and caveolae-mediated endocytosis as possible entry mechanisms.[103] All these suggestions are reasonable; because of the anionic nature of DNA and cell membranes, an active uptake mechanism seems the most likely as opposed to passive diffusion (due to electrostatic repulsions.)

It wasn't until 2014 that studies were reported that could begin to shed light on the most likely mechanism. Liang *et al.* reported that the DNA tetrahedron was taken up via caveolae mediated endocytosis.[104] By utilising total internal reflection fluorescence microscopy (TIRFM) (figure 1.36) and tracking single fluorescently labelled tetrahedra, they were able to accurately assess the uptake pathway and subsequent intracellular transportation pathways.
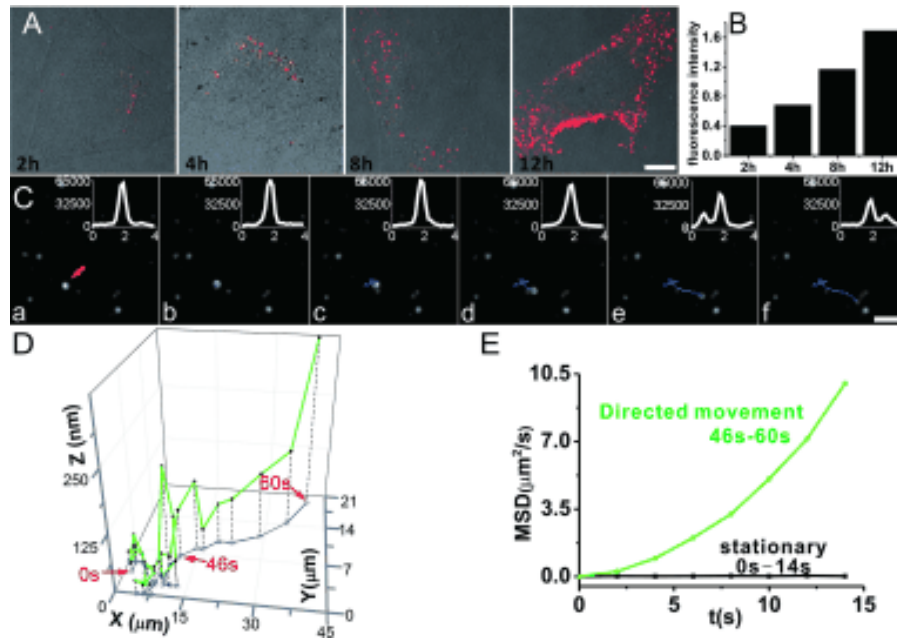
Figure 1.36 – A) confocal images of cy3 labelled tetrahedron uptake from 2-12 hours. C) TIRFM images a to f showing one tetrahedron (indicated by arrow in frame a) and its uptake movements over time, highlighted by the blue arrow. D + E) 3D graphical presentation illustrating tetrahedron movement over time. Taken from 104

The article managed to exclude other uptake pathways by creating conditions that would make other options impossible and by a process of elimination left only the caveolae dependent pathway possible. The major step came between attempting to differentiate between clathrin and caveolae dependent pathways. By treating the HeLa cells with methyl-β-cyclodextrin (MβCD), which depletes cholesterol and disrupts caveolae and subsequently caveolae dependent endocytosis, the group were able to observe a decrease of approximately 54%.[104, 105] Conversely, by treating with sucrose to inhibit the effectiveness of the clathrin mediated pathway[106], no change in uptake was observed, allowing the group to conclude the uptake mechanism reported.

Also following on from the reported cellular compatibility of the tetrahedron, delivery of the known chemotherapy drug doxorubicin with and without the DNA tetrahedron was reported to the breast cancer lines MCF-7 and MCF-7/ADR (doxorubicin resistant) in 2013.[107] This exploited the DNA intercalating abilities of doxorubicin discussed earlier to combine the drug and the tetrahedron prior to cellular treatment (Figure 1.37).
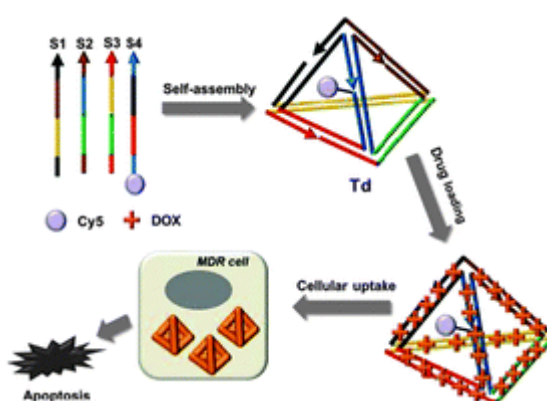
Figure 1.37 – Model diagram illustrating the construction of the doxorubicin loaded tetrahedron via intercalation, followed by cellular treatment with the formed conjugate. Taken from 107.

Not only was cytotoxic activity reported when the doxorubicin was delivered via the tetrahedron, most interestingly, it was able to by-pass doxorubicin resistance.[107] It is well known that after repeated exposure to certain drugs, cancer cells can develop resistance mechanisms, one of which involves altering membrane proteins which regulate drug uptake to increase the efflux of the drug.[108] As the DNA tetrahedron has been shown to be taken up by caveolae dependant endocytosis[104], it will bypass any membrane protein based resistance built up against certain drugs. It was observed that by delivering doxorubicin via DNA tetrahedron,

not only was total cellular doxorubicin content increased in doxorubicin resistant cells, but cell viability was significantly decreased when compared to treating with free doxorubicin.[107] Whilst this wasn't the first report of using nanoparticles to deliver therapeutics to overcome drug resistance via altered uptake pathway, for instance, liposomal doxorubicin (marketed as Doxil) has been used in the clinic for over 25 years[109, 110], it was one of the first instances of using a DNA nanostructure to overcome this type of resistance against a common therapeutic agent.

Aside from delivery of classic chemotherapy drugs, the delivery of more novel therapies such as siRNAs (small interfering RNA) via DNA tetrahedron have been reported.[111,112] The vast amount of options of functionality was neatly demonstrated in this report as a variety of gene silencing ligands were attached to the tetrahedron to produce promising results in the resulting cell testing. The conjugate was formed by synthesising a DNA tetrahedron from 6 oligonucleotides to furnish a single stranded overhang to which a siRNA with the corresponding overhang could be attached (figure 1.38).[111] This method of delivery not only demonstrated great versatility in gene selection, but also exhibited enhanced lifetimes of the siRNA in blood flow in mouse models from 6 mins with free siRNA to 24 mins when delivered by the tetrahedron. This gives a good indication that the DNA tetrahedron can help protect vulnerable or unstable cargo in cellular environments.

Overall, the DNA tetrahedron has shown great promise as a drug delivery medium, with successful reports demonstrating great advantages.[113] However, there has not been a reported example of a triggered cargo release following an external trigger inside cells.
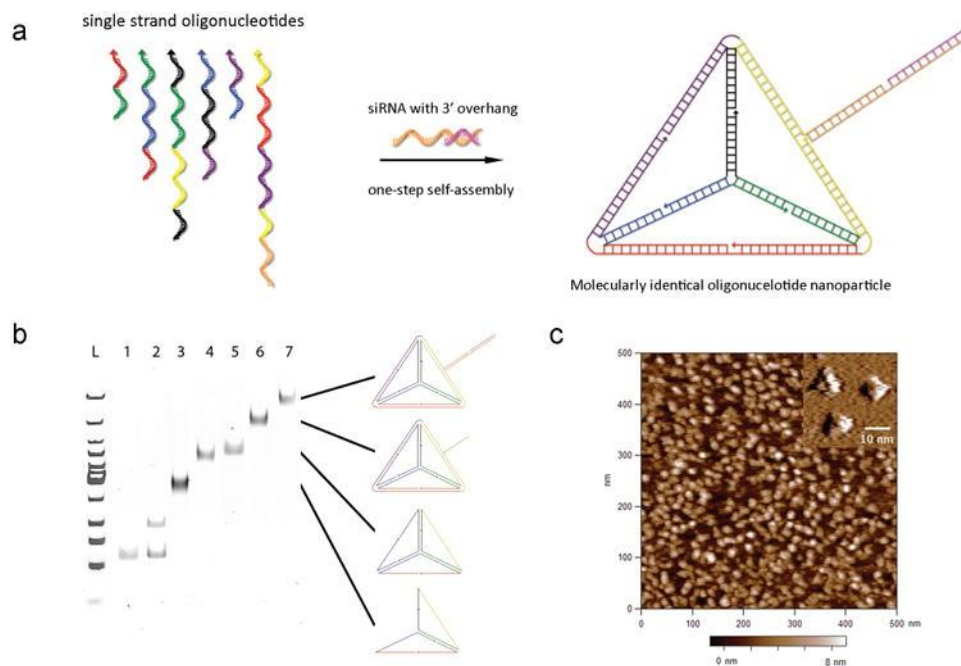
Figure 1.38 – A) model illustrating construction of the tetrahedron from 6 oligonucleotides and the subsequent self-assembly of the siRNA functionality. B) gel electrophoresis experiment confirming construction of tetrahedron. C) AFM images of tetrahedron on a surface. Taken from 111.

1.3.2 Biological Applications of Other Types of DNA Nanostructures

The DNA tetrahedron is not the only DNA structure reported to have applications in cellular delivery. DNA origami in the form of triangular origami nanotubes has shown to be compatible with cell systems and was reported to successfully deliver doxorubicin and bypass drug resistance mechanisms much in the same way as previously discussed.[114] It is not clear whether the much larger DNA structures reported here are internalised via the same mechanism as the smaller tetrahedron, but high levels of drug loading due to sheer amount of DNA bases carrying the drugs such as doxorubicin. It will be interesting to see in years to

come, with the ever decreasing cost of synthetic DNA, which method will be more cost effective when treating *in vivo*. It is also worth noting that these publications do not discuss whether some of the cytotoxicity of the doxorubicin is diminished when delivered by DNA.

DNA nanotubes are also capable of entering cells and were reported to be able to deliver integrated CpG-oligonucleotides.[115] CpG-oligonucleotides are short ssDNA containing sequences of the nucleotide cysteine followed by guanine, separated by a phosphodiester group. They are active when unmethylated as they are recognised in cellular environments by receptors which initiate an immune response from the cell.[116] They have been shown to stimulate immune responses against tumour antigens.[116] However, they are vulnerable to nucleases and as ssDNA alone, cannot enter cells alone as their polyanionic nature leads to repulsion from cell membranes. By conjugating them inside DNA nanotube structures (figure 1.39), the CpG oligonucleotides are protected and reported to enter cells *in vivo* within minutes. In mouse models, treatment with the conjugate resulted in increased levels of leukocytes; implicit of an immune response. Nanotubes alone did not result in immune response and as with other DNA structures, did not show cytotoxicity due to its high biocompatibility.[115]
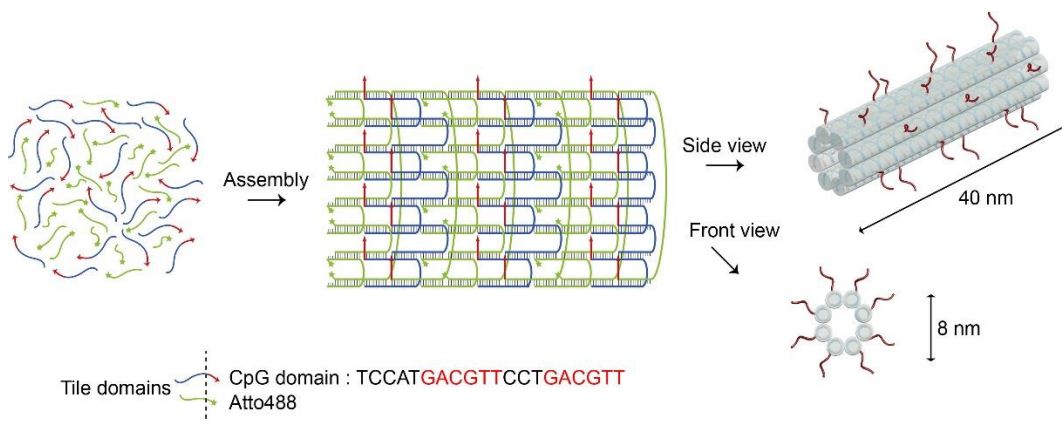
Figure 1.39 – Model illustrating the design and structure of the CpG-oligonucleotide integrated DNA nanotubes. Taken from 115.

Finally, it is worth noting the most widely studied nanocarrier for targeted drug delivery as a means of comparison to DNA nanostructures: Liposomes.[117] Liposomes are phospholipid vesicles, made up of one or more lipid bilayers surrounding an aqueous central space. Their success can be attributed to a number of key attributes, the first being that they are capable of encapsulating both hydrophobic and hydrophilic molecules.[118] The large aqueous center also allows encapsulation of large macromolecules such as DNA and proteins.[119] This allows easy compatibility with a wide range of drugs. As phospholipids, they are biocompatible and have a wide range of physicochemical and biophysical properties that can be manipulated to control their characteristics in biomedical applications and targeting.[120] Unlike DNA nanocarriers, some liposomal pharmaceuticals have become clinically approved. The most successful example of this is PEG conjugated liposomal doxorubicin.[121] Encapsulating in this way has a number of advantages, the most notable being that it increases the half-life of doxorubicin in the blood while decreasing the peak levels of free drug in the blood. This increases accumulation in tumour tissue while decreasing cardiac muscle cell toxicity by reducing exposure here.[122]

Despite the plethora of research, liposomal delivery modes have had a multitude of issues surrounding them, leading to dampened success in the clinic. Some of the main reasons for this are scaling up the manufacture of them is often problematic leading to unreliable product. Changes in manufacturing processes can also lead to broken down or denatured encapsulated compound.[123] This highlights the importance of pursuing other nanocarriers such as DNA nanostructures.

1.4 Overview of Thesis

This thesis aims to explore the effects of metallosupramolecular cylinders binding to different nucleic acid structures, with a particular focus on the DNA tetrahedron. The interaction between the cylinder and tetrahedron will be fully explored, examining any interactions for potential applications, along with possible biological compatibility. This research aims to set up findings that will plug the gap of externally triggered cargo release using DNA nanotechnology inside cellular systems.

Chapter 2 will begin to investigate the iron-supramolecular cylinder's affinity to a variety of DNA structures. It will then discuss the affinity to the DNA tetrahedron and explore any effects binding has to this structure. The enantiomers of the iron cylinder will also be explored and any differing binding behaviours to the tetrahedron investigated.

Chapter 3 will investigate the biological activity of the cylinder-tetrahedron conjugate in cellular systems through established biological assays and microscopy. The potential effects of free tetrahedron and free cylinder when compared to conjugate will be investigated and following from this, the future applications of the complexes will be discussed.

Chapter 4 explores a ruthenium cylinders ability to absorb light and induce DNA cleavage when bound to DNA. Activity at different wavelengths will be experimented and reported. Ruthenium cylinder photocleavage will be applied to the DNA tetrahedron with a view to trigger breaking open the tetrahedron with an external trigger. Finally, initial experiments on the potential application of the ruthenium cylinder as a photodynamic therapeutic agent in cells and the possible use of the tetrahedron in this setting are described.

Chapter 5 investigates the binding of iron, nickel and ruthenium cylinders to a looped region of HIV RNA, significant to the virus' growth cycle. The effectiveness of inhibition and the anti-retro viral activity will also be discussed.

1.5 References

1.   R. Dahm, *Friedrich Miescher and the discovery of DNA.* Developmental Biology, 2005. **278**(2): p. 274-288.

2.   P.A. Levene, *THE STRUCTURE OF YEAST NUCLEIC ACID: IV. AMMONIA HYDROLYSIS.* Journal of Biological Chemistry, 1919. **40**(2): p. 415-424.

3.   L. Pray, *Discovery of DNA structure and function: Watson and Crick. .* Nature Education, 2008. **1**((1)): p. 100.

4.   E. Chargaff, B. Magasanik, E. Vischer, C. Green, R. Doniger, and D. Elson, *Nucleotide composition of pentose nucleic acids from yeast and mammalian tissues.* J Biol Chem, 1950. **186**(1): p. 51-67.

5.   N. Kresge, R.D. Simoni, and R.L. Hill, *Chargaff's Rules: the Work of Erwin Chargaff.* Journal of Biological Chemistry, 2005. **280**(24): p. e21.

6.   R.E. Franklin and R.G. Gosling, *MOLECULAR CONFIGURATION IN SODIUM THYMONUCLEATE.* Nature, 1953. **171**(4356): p. 740-741.

7.   J.D. Watson and F.H. Crick, *Molecular structure of nucleic acids; a structure for deoxyribose nucleic acid.* Nature, 1953. **171**(4356): p. 737-8.

8.   atdbio, *Nucleic Acid Structure* atdbio.com/content/5/Nucleic-acid-structure.

9.   J.C. Wang, *Helical repeat of DNA in solution.* Proceedings of the National Academy of Sciences, 1979. **76**(1): p. 200-203.

10.   T.J. Berg JM, Stryer L, *DNA Can Assume a Variety of Structural Forms.* Biochemistry. **5th edition**.

11.   D.R. Whelan, T.J. Hiscox, J.I. Rood, K.R. Bambery, D. McNaughton, and B.R. Wood, *Detection of an en masse and reversible B- to A-DNA conformational transition in prokaryotes in response to desiccation.* Journal of The Royal Society Interface, 2014. **11**(97).

12.   S.C. Harvey, *The scrunchworm hypothesis: Transitions between A-DNA and B-DNA provide the driving force for genome packaging in double-stranded DNA bacteriophages.* Journal of Structural Biology, 2015. **189**(1): p. 1-8.

13.   A. Herbert and A. Rich, *The Biology of Left-handed Z-DNA.* Journal of Biological Chemistry, 1996. **271**(20): p. 11595-11598.

14.   A Rich, a. A Nordheim, and A.H.J. Wang, *The Chemistry and Biology of Left-Handed Z-DNA.* Annual Review of Biochemistry, 1984. **53**(1): p. 791-846.

15.   J. Klysik, S.M. Stirdivant, J.E. Larson, P.A. Hart, and R.D. Wells, *Left-handed DNA in restriction fragments and a recombinant plasmid.* Nature, 1981. **290**(5808): p. 672-677.

16.   A. Kuzminov, *DNA replication meets genetic exchange: Chromosomal damage and its repair by homologous recombination.* Proceedings of the National Academy of Sciences of the United States of America, 2001. **98**(15): p. 8461-8468.

17.   J. Lee, Y. Voziyanov, S. Pathania, and M. Jayaram, *Structural Alterations and Conformational Dynamics in Holliday Junctions Induced by Binding of a Site-Specific Recombinase.* Molecular Cell, 1998. **1**(4): p. 483-493.

18.   M.J. Hannon, *DNA recognition Press release.* University of Birmingham, 2006. **1**(1): p. 4.

19.   J. Chen and N.C. Seeman, *Synthesis from DNA of a molecule with the connectivity of a cube.* Nature, 1991. **350**(6319): p. 631-633.

20.   M.L. Bochman, K. Paeschke, and V.A. Zakian, *DNA secondary structures: stability and function of G-quadruplex structures.* Nat Rev Genet, 2012. **13**(11): p. 770-780.

21.   Y. Hong, M. Häußler, J.W.Y. Lam, Z. Li, K.K. Sin, Y. Dong, H. Tong, J. Liu, A. Qin, R. Renneberg, and B.Z. Tang, *Label-Free Fluorescent Probing of G-Quadruplex Formation and Real-Time*

Monitoring of DNA Folding by a Quaternized Tetraphenylethene Salt with Aggregation-Induced Emission Characteristics. Chemistry – A European Journal, 2008. **14**(21): p. 6428-6437.

22.   D. Yang and K. Okamoto, *Structural insights into G-quadruplexes: towards new anticancer drugs.* Future medicinal chemistry, 2010. **2**(4): p. 619-646.

23.   A. Rustighi, M.A. Tessari, F. Vascotto, R. Sgarra, V. Giancotti, and G. Manfioletti, *A polypyrimidine/polypurine tract within the Hmga2 minimal promoter: a common feature of many growth-related genes.* Biochemistry, 2002. **41**(4): p. 1229-40.

24.   T. Simonsson, P. Pecinka, and M. Kubista, *DNA tetraplex formation in the control region of c-myc.* Nucleic Acids Res, 1998. **26**(5): p. 1167-72.

25.   S. Rankin, A.P. Reszka, J. Huppert, M. Zloh, G.N. Parkinson, A.K. Todd, S. Ladame, S. Balasubramanian, and S. Neidle, *Putative DNA quadruplex formation within the human c-kit oncogene.* J Am Chem Soc, 2005. **127**(30): p. 10584-9.

26.   T.M. Ou, Y.J. Lu, J.H. Tan, Z.S. Huang, K.Y. Wong, and L.Q. Gu, *G-quadruplexes: Targets in anticancer drug design.* Chemmedchem, 2008. **3**(5): p. 690-713.

27.   J.M. Hardwick and L. Soane, *Multiple Functions of BCL-2 Family Proteins.* Cold Spring Harbor Perspectives in Biology, 2013. **5**(2).

28.   D. Dominguez-Sola, C.Y. Ying, C. Grandori, L. Ruggiero, B. Chen, M. Li, D.A. Galloway, W. Gu, J. Gautier, and R. Dalla-Favera, *Non-transcriptional control of DNA replication by c-Myc.* Nature, 2007. **448**(7152): p. 445-451.

29.   I.M. de Alboran, R.C. O'Hagan, F. Gärtner, B. Malynn, L. Davidson, R. Rickert, K. Rajewsky, R.A. DePinho, and F.W. Alt, *Analysis of C-MYC Function in Normal Cells via Conditional Gene-Targeted Mutation.* Immunity. **14**(1): p. 45-55.

30.   G. Maartens, C. Celum, and S.R. Lewin, *HIV infection: epidemiology, pathogenesis, treatment, and prevention.* The Lancet. **384**(9939): p. 258-271.

31.   B. Rosenberg, L. Vancamp, and T. Krigas, *INHIBITION OF CELL DIVISION IN ESCHERICHIA COLI BY ELECTROLYSIS PRODUCTS FROM A PLATINUM ELECTRODE.* Nature, 1965. **205**: p. 698-9.

32.   L. Kelland, *The resurgence of platinum-based cancer chemotherapy.* Nat Rev Cancer, 2007. **7**(8): p. 573-84.

33.   P.J. Loehrer and L.H. Einhorn, *CIsplatin.* Annals of Internal Medicine, 1984. **100**(5): p. 704-713.

34.   T.C. Johnstone, K. Suntharalingam, and S.J. Lippard, *The Next Generation of Platinum Drugs: Targeted Pt(II) Agents, Nanoparticle Delivery, and Pt(IV) Prodrugs.* Chemical Reviews, 2016. **116**(5): p. 3436-3486.

35.   atdbio, *Nucleic Acid-Drug Interactions.* Atdbio.com/content/16/Nucleic Acid-Drug Interactions.

36.   S. Dasari and P.B. Tchounwou, *Cisplatin in cancer therapy: molecular mechanisms of action.* European journal of pharmacology, 2014. **0**: p. 364-378.

37.   L.R. Kelland, S.Y. Sharp, C.F. O'Neill, F.I. Raynaud, P.J. Beale, and I.R. Judson, *Mini-review: discovery and development of platinum complexes designed to circumvent cisplatin resistance.* J Inorg Biochem, 1999. **77**(1-2): p. 111-5.

38.   J.G. Hengstler, J. Lange, A. Kett, N. Dornhofer, R. Meinert, M. Arand, P.G. Knapstein, R. Becker, F. Oesch, and B. Tanner, *Contribution of c-erbB-2 and topoisomerase IIalpha to chemoresistance in ovarian cancer.* Cancer Res, 1999. **59**(13): p. 3206-14.

39.   W.P. Liu, Q.S. Ye, Y. Yu, X.Z. Chen, S.Q. Hou, L.G. Lou, Y.P. Yang, Y.M. Wang, and Q. Su, *Novel Lipophilic Platinum(II) Compounds of Salicylate Derivatives RESEARCH, DEVELOPMENT AND LIPOSOMAL FORMULATION.* Platinum Metals Review, 2008. **52**(3): p. 163-171.

40.   Y.-P. Ho, S.C.F. Au-Yeung, and K.K.W. To, *Platinum-based anticancer agents: Innovative design strategies and biological perspectives.* Medicinal Research Reviews, 2003. **23**(5): p. 633-655.

41.   M.A. Jakupec, M. Galanski, and B.K. Keppler, *Tumour-inhibiting platinum complexes—state of the art and future perspectives*, in *Reviews of Physiology, Biochemistry and Pharmacology*. 2003, Springer Berlin Heidelberg: Berlin, Heidelberg. p. 1-53.

42.   S.v. Zutphen and J. Reedijk, *Targeting platinum anti-tumour drugs: Overview of strategies employed to reduce systemic toxicity.* Coordination Chemistry Reviews, 2005. **249**(24): p. 2845-2853.

43.   N.J. Wheate, C.R. Brodie, J.G. Collins, S. Kemp, and J.R. Aldrich-Wright, *DNA intercalators in cancer therapy: organic and inorganic drugs and their spectroscopic tools of analysis.* Mini Rev Med Chem, 2007. **7**(6): p. 627-48.

44.   J. Cerny and P. Hobza, *Non-covalent interactions in biomacromolecules.* Physical Chemistry Chemical Physics, 2007. **9**(39): p. 5291-5303.

45.   A. Mukherjee and W.D. Sasikala, *Drug-DNA Intercalation: From Discovery to the Molecular Mechanism*, in *Dynamics of Proteins and Nucleic Acids*, T. KarabenchevaChristova, Editor. 2013. p. 1-62.

46.   J.L. Nitiss, *Targeting DNA topoisomerase II in cancer chemotherapy.* Nature Reviews Cancer, 2009. **9**(5): p. 338-350.

47.   Y. Pommier, R.E. Schwartz, L.A. Zwelling, and K.W. Kohn, *Effects of DNA intercalating agents on topoisomerase II induced DNA strand cleavage in isolated mammalian cell nuclei.* Biochemistry, 1985. **24**(23): p. 6406-10.

48.   K.M. Tewey, T.C. Rowe, L. Yang, B.D. Halligan, and L.F. Liu, *Adriamycin-induced DNA damage mediated by mammalian DNA topoisomerase II.* Science, 1984. **226**(4673): p. 466-8.

49.   L. Gallois, M. Fiallo, and A. Garnier-Suillerot, *Comparison of the interaction of doxorubicin, daunorubicin, idarubicin and idarubicinol with large unilamellar vesicles: Circular dichroism study.* Biochimica et Biophysica Acta (BBA) - Biomembranes, 1998. **1370**(1): p. 31-40.

50. C.A. Frederick, L.D. Williams, G. Ughetto, G.A. Van der Marel, J.H. Van Boom, A. Rich, and A.H.J. Wang, *Structural comparison of anticancer drug-DNA complexes: adriamycin and daunomycin.* Biochemistry, 1990. **29**(10): p. 2538-2549.

51. T.A. Larsen, D.S. Goodsell, D. Cascio, K. Grzeskowiak, and R.E. Dickerson, *The structure of DAPI bound to DNA.* J Biomol Struct Dyn, 1989. **7**(3): p. 477-91.

52. M.J. Hannon, *Supramolecular DNA recognition.* Chemical Society Reviews, 2007. **36**(2): p. 280-295.

53. P.G. Baraldi, A. Bovero, F. Fruttarolo, D. Preti, M.A. Tabrizi, M.G. Pavani, and R. Romagnoli, *DNA minor groove binders as potential antitumor and antimicrobial agents.* Medicinal Research Reviews, 2004. **24**(4): p. 475-528.

54. P. Majumder, A. Banerjee, J. Shandilya, P. Senapati, S. Chatterjee, T.K. Kundu, and D. Dasgupta, *Minor Groove Binder Distamycin Remodels Chromatin but Inhibits Transcription.* PLOS ONE, 2013. **8**(2): p. e57693.

55. P.G. Baraldi, D. Preti, F. Fruttarolo, M.A. Tabrizi, and R. Romagnoli, *Hybrid molecules between distamycin A and active moieties of antitumor agents.* Bioorganic & Medicinal Chemistry, 2007. **15**(1): p. 17-35.

56. D.E. Wemmer, *Designed sequence-specific minor groove ligands.* Annu Rev Biophys Biomol Struct, 2000. **29**: p. 439-61.

57. D. Jantz, B.T. Amann, G.J. Gatto, and J.M. Berg, *The Design of Functional DNA-Binding Proteins Based on Zinc Finger Domains.* Chemical Reviews, 2004. **104**(2): p. 789-800.

58. M. Elrod-Erickson, M.A. Rould, L. Nekludova, and C.O. Pabo, *Zif268 protein-DNA complex refined at 1.6 A: a model system for understanding zinc finger-DNA interactions.* Structure, 1996. **4**(10): p. 1171-80.

59. A. Sarai and H. Kono, *Protein-DNA Recognition Patterns and Predictions.* Annual Review of Biophysics and Biomolecular Structure, 2005. **34**(1): p. 379-398.

60. M. J. Hannon, C. L. Painting, A. Jackson, J. Hamblin, and W. Errington, *An inexpensive approach to supramolecular architecture.* Chemical Communications, 1997(18): p. 1807-1808.

61. B. Roehr, *Fomivirsen approved for CMV retinitis.* J Int Assoc Physicians AIDS Care, 1998. **4**(10): p. 14-6.

62. S. Balasubramanian, L.H. Hurley, and S. Neidle, *Targeting G-quadruplexes in gene promoters: a novel anticancer strategy?* Nature reviews. Drug discovery, 2011. **10**(4): p. 261-275.

63. V.S. Chambers, G. Marsico, J.M. Boutell, M. Di Antonio, G.P. Smith, and S. Balasubramanian, *High-throughput sequencing of DNA G-quadruplex structures in the human genome.* Nat Biotech, 2015. **33**(8): p. 877-881.

64. D. Hanahan and R.A. Weinberg, *The hallmarks of cancer.* Cell, 2000. **100**(1): p. 57-70.

65. D. Monchaud and M.P. Teulade-Fichou, *A hitchhiker's guide to G-quadruplex ligands.* Org Biomol Chem, 2008. **6**(4): p. 627-36.

66. D. Monchaud, A. Granzhan, N. Saettel, A. Guedin, J.L. Mergny, and M.P. Teulade-Fichou, *"One ring to bind them all"-part I: the efficiency of the macrocyclic scaffold for g-quadruplex DNA recognition.* J Nucleic Acids, 2010. **2010**.

67. S.N. Georgiades, N.H. Abd Karim, K. Suntharalingam, and R. Vilar, *Interaction of Metal Complexes with G-Quadruplex DNA.* Angewandte Chemie International Edition, 2010. **49**(24): p. 4020-4034.

68. A.C.G. Hotze, N.J. Hodges, R.E. Hayden, C. Sanchez-Cano, C. Paines, N. Male, M.-K. Tse, C.M. Bunce, J.K. Chipman, and M.J. Hannon, *Supramolecular Iron Cylinder with Unprecedented DNA Binding Is a Potent Cytostatic and Apoptotic Agent without Exhibiting Genotoxicity.* Chemistry & Biology, 2008. **15**(12): p. 1258-1267.

69. M.J. Hannon, I. Meistermann, C.J. Isaac, C. Blomme, J.R. Aldrich-Wright, and A. Rodger, *Paper: a cheap yet effective chiral stationary phase for chromatographic resolution of metallo-supramolecular helicates.* Chemical Communications, 2001(12): p. 1078-1079.

70. M. Hannon, I. Meistermann, C.J. Isaac, A. Rodger, V. Moreno, M.J. Prieto, E. Sletten, and E. Moldrheim, *Intramolecular DNA coiling mediated by a metallo-supramolecular cylinder that targets the major groove.* Journal of Inorganic Biochemistry, 2001. **86**(1): p. 56-56.

71. I. Meistermann, V. Moreno, M.J. Prieto, E. Moldrheim, E. Sletten, S. Khalid, P.M. Rodger, J.C. Peberdy, C.J. Isaac, A. Rodger, and M.J. Hannon, *Intramolecular DNA coiling mediated by metallosupramolecular cylinders: Differential binding of P and M helical enantiomers.* Proceedings of the National Academy of Sciences of the United States of America, 2002. **99**(8): p. 5069-5074.

72. A. Oleksi, A.G. Blanco, R. Boer, I. Uson, J. Aymami, A. Rodger, M.J. Hannon, and M. Coll, *Molecular recognition of a three-way DNA junction by a metallosupramolecular helicate.* Angewandte Chemie-International Edition, 2006. **45**(8): p. 1227-1231.

73. N.C. Seeman, *Nucleic acid junctions and lattices.* Journal of Theoretical Biology, 1982. **99**(2): p. 237-247.

74. N.C. Seeman and H.F. Sleiman, *DNA nanotechnology.* Nature Reviews Materials, 2017. **3**: p. 17068.

75. R.P. Goodman, R.M. Berry, and A.J. Turberfield, *The single-step synthesis of a DNA tetrahedron.* Chemical Communications, 2004(12): p. 1372-1373.

76. S.N. Cohen, A.C. Chang, H.W. Boyer, and R.B. Helling, *Construction of biologically functional bacterial plasmids in vitro.* Proc Natl Acad Sci U S A, 1973. **70**(11): p. 3240-4.

77. N.C. Seeman, *Nanomaterials Based on DNA.* Annual review of biochemistry, 2010. **79**: p. 65-87.

78.   P. Yin, H.M. Choi, C.R. Calvert, and N.A. Pierce, *Programming biomolecular self-assembly pathways.* Nature, 2008. **451**(7176): p. 318-22.

79.   P. Hsieh and I.G. Panyutin, *DNA Branch Migration*, in *Nucleic Acids and Molecular Biology*, F. Eckstein and D.M.J. Lilley, Editors. 1995, Springer Berlin Heidelberg: Berlin, Heidelberg. p. 42-65.

80.   N.C. Seeman, *De Novo Design of Sequences for Nucleic Acid Structural Engineering.* Journal of Biomolecular Structure and Dynamics, 1990. **8**(3): p. 573-581.

81.   X. Wang and N.C. Seeman, *Assembly and Characterization of 8-Arm and 12-Arm DNA Branched Junctions.* Journal of the American Chemical Society, 2007. **129**(26): p. 8169-8176.

82.   Y. Zhang and N.C. Seeman, *Construction of a DNA-Truncated Octahedron.* Journal of the American Chemical Society, 1994. **116**(5): p. 1661-1669.

83.   W.M. Shih, J.D. Quispe, and G.F. Joyce, *A 1.7-kilobase single-stranded DNA that folds into a nanoscale octahedron.* Nature, 2004. **427**(6975): p. 618-21.

84.   R.P. Goodman, I.A. Schaap, C.F. Tardin, C.M. Erben, R.M. Berry, C.F. Schmidt, and A.J. Turberfield, *Rapid chiral assembly of rigid DNA building blocks for molecular nanofabrication.* Science, 2005. **310**(5754): p. 1661-5.

85.   R.P. Goodman, I.A.T. Schaap, C.F. Tardin, C.M. Erben, R.M. Berry, C.F. Schmidt, and A.J. Turberfield, *Rapid Chiral Assembly of Rigid DNA Building Blocks for Molecular Nanofabrication.* Science, 2005. **310**(5754): p. 1661-1665.

86.   C.M. Erben, R.P. Goodman, and A.J. Turberfield, *Single-molecule protein encapsulation in a rigid DNA cage.* Angew Chem Int Ed Engl, 2006. **45**(44): p. 7414-7.

87.   S.S. Ghosh, P.M. Kao, A.W. McCue, and H.L. Chappelle, *Use of maleimide-thiol coupling chemistry for efficient syntheses of oligonucleotide-enzyme conjugate hybridization probes.* Bioconjugate Chemistry, 1990. **1**(1): p. 71-76.

88.   B.P. Duckworth, Y. Chen, J.W. Wollack, Y. Sham, J.D. Mueller, T.A. Taton, and M.D. Distefano, *A Universal Method for the Preparation of Covalent Protein–DNA Conjugates for Use in Creating Protein Nanostructures.* Angewandte Chemie International Edition, 2007. **46**(46): p. 8819-8822.

89.   D. Corey and P. Schultz, *Generation of a hybrid sequence-specific single-stranded deoxyribonuclease.* Science, 1987. **238**(4832): p. 1401-1403.

90.   R.P. Goodman, C.M. Erben, J. Malo, W.M. Ho, M.L. McKee, A.N. Kapanidis, and A.J. Turberfield, *A Facile Method for Reversibly Linking a Recombinant Protein to DNA.* ChemBioChem, 2009. **10**(9): p. 1551-1557.

91.   J.-W. Keum and H. Bermudez, *DNA-based delivery vehicles: pH-controlled disassembly and cargo release.* Chemical Communications, 2012. **48**(99): p. 12118-12120.

92.   R. Crawford, C.M. Erben, J. Periz, L.M. Hall, T. Brown, A.J. Turberfield, and A.N. Kapanidis, *Non-covalent Single Transcription Factor Encapsulation Inside a DNA Cage.* Angewandte Chemie-International Edition, 2013. **52**(8): p. 2284-2288.

93.   P.W.K. Rothemund, *Folding DNA to create nanoscale shapes and patterns.* Nature, 2006. **440**(7082): p. 297-302.

94.   F.C. Simmel, *Three-Dimensional Nanoconstruction with DNA.* Angewandte Chemie International Edition, 2008. **47**(32): p. 5884-5887.

95.   E.S. Andersen, M. Dong, M.M. Nielsen, K. Jahn, R. Subramani, W. Mamdouh, M.M. Golas, B. Sander, H. Stark, C.L.P. Oliveira, J.S. Pedersen, V. Birkedal, F. Besenbacher, K.V. Gothelf, and J. Kjems, *Self-assembly of a nanoscale DNA box with a controllable lid.* Nature, 2009. **459**(7243): p. 73-76.

96.   A. Kuzuya and M. Komiyama, *Design and construction of a box-shaped 3D-DNA origami.* Chemical Communications, 2009(28): p. 4182-4184.

97. M. Endo, K. Hidaka, T. Kato, K. Namba, and H. Sugiyama, *DNA Prism Structures Constructed by Folding of Multiple Rectangular Arms.* Journal of the American Chemical Society, 2009. **131**(43): p. 15570-15571.

98. Y.G. Ke, J. Sharma, M.H. Liu, K. Jahn, Y. Liu, and H. Yan, *Scaffolded DNA Origami of a DNA Tetrahedron Molecular Container.* Nano Letters, 2009. **9**(6): p. 2445-2447.

99. S.M. Douglas, H. Dietz, T. Liedl, B. Hogberg, F. Graf, and W.M. Shih, *Self-assembly of DNA into nanoscale three-dimensional shapes.* Nature, 2009. **459**(7245): p. 414-418.

100. A.S. Walsh, H. Yin, C.M. Erben, M.J.A. Wood, and A.J. Turberfield, *DNA Cage Delivery to Mammalian Cells.* ACS Nano, 2011. **5**(7): p. 5427-5432.

101. J. Li, H. Pei, B. Zhu, L. Liang, M. Wei, Y. He, N. Chen, D. Li, Q. Huang, and C. Fan, *Self-Assembled Multivalent DNA Nanostructures for Noninvasive Intracellular Delivery of Immunostimulatory CpG Oligonucleotides.* ACS Nano, 2011. **5**(11): p. 8783-8789.

102. H. Gao, W. Shi, and L.B. Freund, *Mechanics of receptor-mediated endocytosis.* Proceedings of the National Academy of Sciences of the United States of America, 2005. **102**(27): p. 9469-9474.

103. H. Hillaireau and P. Couvreur, *Nanocarriers' entry into the cell: relevance to drug delivery.* Cellular and Molecular Life Sciences, 2009. **66**(17): p. 2873-2896.

104. L. Liang, J. Li, Q. Li, Q. Huang, J.Y. Shi, H. Yan, and C.H. Fan, *Single-Particle Tracking and Modulation of Cell Entry Pathways of a Tetrahedral DNA Nanostructure in Live Cells.* Angewandte Chemie-International Edition, 2014. **53**(30): p. 7745-7750.

105. M.G. Qaddoumi, H.J. Gukasyan, J. Davda, V. Labhasetwar, K.J. Kim, and V.H. Lee, *Clathrin and caveolin-1 expression in primary pigmented rabbit conjunctival epithelial cells: role in PLGA nanoparticle endocytosis.* Mol Vis, 2003. **9**: p. 559-68.

106. J.E. Heuser and R.G. Anderson, *Hypertonic media inhibit receptor-mediated endocytosis by blocking clathrin-coated pit formation.* The Journal of Cell Biology, 1989. **108**(2): p. 389-400.

107.   K.R. Kim, D.R. Kim, T. Lee, J.Y. Yhee, B.S. Kim, I.C. Kwon, and D.R. Ahn, *Drug delivery by a self-assembled DNA tetrahedron for overcoming drug resistance in breast cancer cells.* Chem Commun (Camb), 2013. **49**(20): p. 2010-2.

108.   E. Borowski, M.M. Bontemps-Gracz, and A. Piwkowska, *Strategies for overcoming ABC-transporters-mediated multidrug resistance (MDR) of tumor cells.* Acta Biochimica Polonica, 2005. **52**(3): p. 609-627.

109.   M.E. Davis, Z. Chen, and D.M. Shin, *Nanoparticle therapeutics: an emerging treatment modality for cancer.* Nat Rev Drug Discov, 2008. **7**(9): p. 771-782.

110.   G. Szakacs, J.K. Paterson, J.A. Ludwig, C. Booth-Genthe, and M.M. Gottesman, *Targeting multidrug resistance in cancer.* Nat Rev Drug Discov, 2006. **5**(3): p. 219-234.

111.   H. Lee, A.K.R. Lytton-Jean, Y. Chen, K.T. Love, A.I. Park, E.D. Karagiannis, A. Sehgal, W. Querbes, C.S. Zurenko, M. Jayaraman, C.G. Peng, K. Charisse, A. Borodovsky, M. Manoharan, J.S. Donahoe, J. Truelove, M. Nahrendorf, R. Langer, and D.G. Anderson, *Molecularly Self-Assembled Nucleic Acid Nanoparticles for Targeted In Vivo siRNA Delivery.* Nature nanotechnology, 2012. **7**(6): p. 389-393.

112.   L. Li, X. Hu, M. Zhang, S. Ma, F. Yu, S. Zhao, N. Liu, Z. Wang, Y. Wang, H. Guan, X. Pan, Y. Gao, Y. Zhang, Y. Liu, Y. Yang, X. Tang, M. Li, C. Liu, Z. Li, and X. Mei, *Dual Tumor-Targeting Nanocarrier System for siRNA Delivery Based on pRNA and Modified Chitosan.* Molecular Therapy - Nucleic Acids, 2017. **8**: p. 169-183.

113.   D. Wu, L. Wang, W. Li, X. Xu, and W. Jiang, *DNA nanostructure-based drug delivery nanosystems in cancer therapy.* Int J Pharm, 2017. **533**(1): p. 169-178.

114.   Q. Jiang, C. Song, J. Nangreave, X. Liu, L. Lin, D. Qiu, Z.-G. Wang, G. Zou, X. Liang, H. Yan, and B. Ding, *DNA Origami as a Carrier for Circumvention of Drug Resistance.* Journal of the American Chemical Society, 2012. **134**(32): p. 13396-13403.

115.   S. Sellner, S. Kocabey, K. Nekolla, F. Krombach, T. Liedl, and M. Rehberg, *DNA nanotubes as intracellular delivery vehicles in vivo.* Biomaterials, 2015. **53**: p. 453-463.

116.   G.J. Weiner, H.-M. Liu, J.E. Wooldridge, C.E. Dahle, and A.M. Krieg, *Immunostimulatory oligodeoxynucleotides containing the CpG motif are effective as immune adjuvants in tumor antigen immunization.* Proceedings of the National Academy of Sciences, 1997. **94**(20): p. 10833-10837.

117.   L. Sercombe, T. Veerati, F. Moheimani, S.Y. Wu, A.K. Sood, and S. Hua, *Advances and Challenges of Liposome Assisted Drug Delivery.* Front Pharmacol, 2015. **6**: p. 286.

118.   B.-S. Ding, T. Dziubla, V. V Shuvaev, S. Muro, and V. Muzykantov, *Advanced Drug Delivery Systems That Target The Vascular Endothelium*. Vol. 6. 2006. 98-112.

119.   N. Monteiro, A. Martins, R.L. Reis, and N.M. Neves, *Liposomes in tissue engineering and regenerative medicine.* Journal of The Royal Society Interface, 2014. **11**(101).

120.   S. Hua and S. Wu, *The use of lipid-based nanocarriers for targeted pain therapies.* Frontiers in Pharmacology, 2013. **4**(143).

121.   Y.M. Ning, K. He, R. Dagher, R. Sridhara, A.T. Farrell, R. Justice, and R. Pazdur, *Liposomal doxorubicin in combination with bortezomib for relapsed or refractory multiple myeloma.* Oncology (Williston Park), 2007. **21**(12): p. 1503-8; discussion 1511, 1513, 1516 passim.

122.   A.M. Rahman, S.W. Yusuf, and M.S. Ewer, *Anthracycline-induced cardiotoxicity and the cardiac-sparing effect of liposomal formulation.* Int J Nanomedicine, 2007. **2**(4): p. 567-83.

123.   A.S. Narang, R.K. Chang, and M.A. Hussain, *Pharmaceutical Development and Regulatory Considerations for Nanoparticles and Nanoparticulate Drug Delivery Systems.* Journal of Pharmaceutical Sciences, 2013. **102**(11): p. 3867-3882.

Chapter 2

Interaction of an Iron supramolecular Cylinder with a DNA Tetrahedron and a Three Way Junction

2.1 Introduction

Metallosupramolecular cylinders have shown unprecedented DNA binding to a wide variety of DNA structures including the major groove[1] and most notably binding to and stabilising DNA Y-shaped replication forks or 3-way-junctions (3WJ).[2] The binding is such that it causes bending and supercoiling of DNA (Figure 2.1).[3, 4]
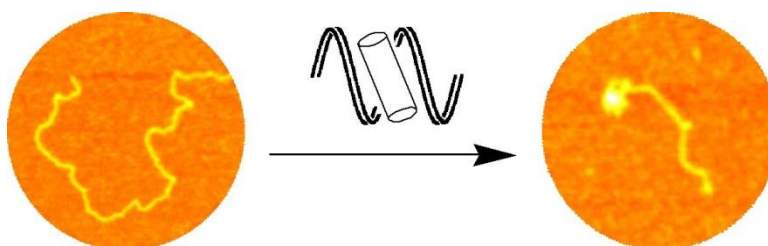
Figure 2.1 - AFM images illustrating the effect of cylinder induced supercoiling of DNA. Taken from reference 4

A wide variety of cylinders have exhibited similar behaviour, although none have shown the binding strength of the "parent" iron cylinder which has been previously synthesised within the group.[3, 5-8]
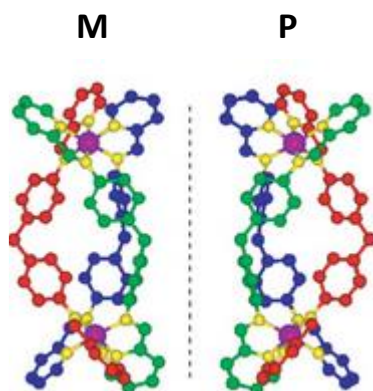
Figure 2.2 – Crystal structures of both the M (left) enantiomer and P (right) enantiomer. Taken from reference 10

Being a di-nuclear triple helicate, it is inherently chiral and has two enantiomers (M and P) which can be separated using cellulose as a chiral stationary phase (Figure 2.2).[9, 10]

As the DNA interactions of the cylinders are influenced by π-stacking interactions, shape and orientation are key to the cylinders' behaviour. As such, the two enantiomers exhibit slightly different characteristics in their binding.[11] Most interestingly, in crystallographic experiments involving a racemic mixture of the cylinder and a synthetic DNA 3WJ, only the M enantiomer was found to bind inside the 3WJ.[12] In the field of DNA nanotechnology, this recognition and strength of binding would be of great interest as the characteristics can be used to develop triggered changes in conformational structure, release of cargo or quite simply delivery of the cylinder itself.

The DNA tetrahedron synthesised by Turberfield is the first rigid 3D DNA nanostructure that has been synthesised in one, high yield simple step synthesis.[13] The structure of this tetrahedron contains 3WJs at each apex and 17 bp of duplex DNA at the sides (Figure 2.3).
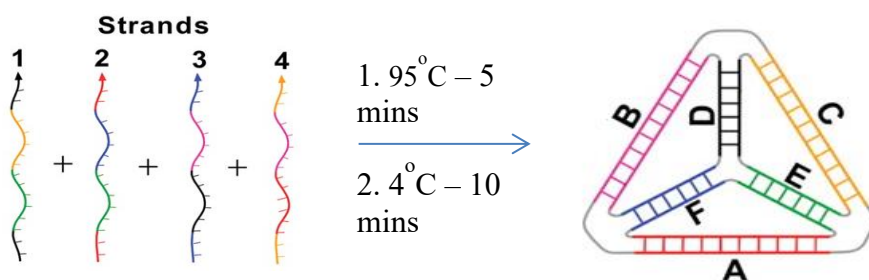
Figure 2.3 - Schematic diagram illustrating the formation of the tetrahedron. Taken from reference 13

Therefore, the parent cylinder should not only be able to bind to the structures involved here, but its binding strength could distort or trigger conformation changes. The tetrahedron is very rigid with a hollow cavity which could contain a cargo of a radius of up to 2.6 nm.[14] Binding

events of the cylinder to the tetrahedron in the major groove and at the apex 3WJ could cause structure changes in the tetrahedron itself. Also the conjugate formed would itself be of biological interest due to the cytotoxicity of the cylinder and the inherent bio-compatibility of the tetrahedron due to its DNA building blocks and proven cellular uptake.[15]

This chapter initially investigates the cylinders' binding affinity to the DNA 3WJ when in competition with other DNA structures. Investigation then moves on to assess the cylinder – tetrahedron interaction, building on initial work completed by Siriporn Phongtongpasuk previously in the Hannon group. This is studied mainly by gel electrophoresis experiments to observe any possible band shifts which would confirm the presence of a conjugate. Further characterisation of the nature of this interaction is then attempted by different methods. Part two of the chapter aims to explore the possible differences between the cylinders two M and P enantiomers with regard to tetrahedron interaction. Any possible differences could shed more light on the nature of the overall interaction and whether site specific binding is possible to ascertain.

2.2 Results and Discussion

2.2.1 Part 1 – Cylinder 3WJ Binding

Competition Gel Electrophoresis Assays

The ability of the iron cylinder to bind inside a DNA 3WJ has been firmly established and discussed earlier.[16] With so many other DNA structures involved inside cells, it is important to establish the binding preferences and to what extent the iron cylinder will preferentially bind to a 3WJ over another structure. To study this, a series of polyacrylamide gel electrophoresis (PAGE) experiments were undertaken.

PAGE is a widely used and very useful method in biochemistry for tracking and characterising protein or DNA samples as a function of their electrophoretic mobility.[17] Electrophoretic mobility depends on the bio-molecule's size, shape and overall negative charge and refers to the speed of the migration through the gel.[18] The experiment is performed by applying a potential difference across the gel (negative to positive) – effectively pulling the negatively charged sample through the gel. PAGE can be a native or denaturing experiment, depending on the conditions. Native refers to examining the samples in their stable (folded) biological state, for example, duplex DNA as it would be in solution. Denaturing refers to unfolding and breaking the biomolecule down to constituent parts, for example, down to single stranded DNA. In these experiments, a synthetic 3WJ was employed under native conditions. It consists of three 14-mer oligonucleotides containing unpaired bases in the centre to form the 3WJ (Figure 2.4).[16] The small amount of bases in the duplex arms means that this 3WJ will be stable as a 3WJ below 4°C, but will dissociate into single strands at higher temperatures.[19] This provides a perfect model as at room temperature, no 3WJ is formed unless it is stabilised by, in this case, the cylinder binding inside.
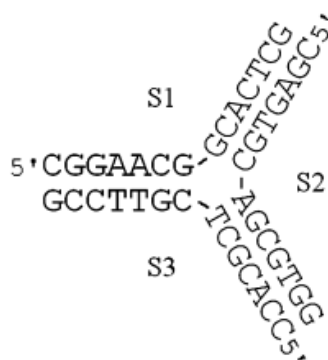
Figure 2.4 – 3 oligonucleotides that assemble to form a synthetic 3WJ. Taken from reference 16.

By radiolabelling the oligonucleotide S3, the structure can be tracked easily in the gel with high sensitivity (~500 pM) which won't be affected by cylinder binding which could prevent

other visualising stains from binding to the DNA such as ethidium bromide. Figure 2.5 shows a native PAGE experiment where the 3 oligos are run with and without the iron cylinder at room temperature, clearly illustrating the band migration shift when the 3WJ is formed and when it is not.
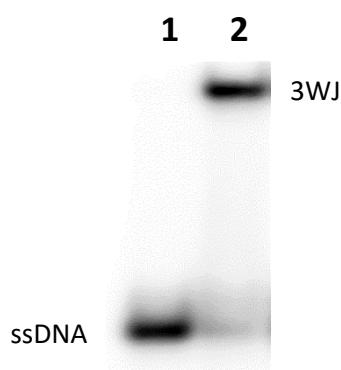
Figure 2.5 – Autoradiogram of a 15% non-denaturing PAGE. Lane 1 containing the 3 oligos required for the 3WJ, unbound as ssDNA. One of which has been radiolabelled for visualisation. Lane 2 contains the oligos with the iron cylinder at 1:1 ratio, forming the 3WJ, causing the band shift.

With this positive control in place, a range of DNA structures were mixed with the iron cylinder and the 3WJ DNA to establish whether cylinder would preferentially bind to the 3WJ or to the competitor, evidenced by a drop in intensity of the 3WJ band in a gel. The experimental design was to first mix and incubate 3WJ DNA and cylinder at a ratio of 1 cylinder per 3WJ (1 hour incubation time). Competing DNA structures were then added at a 1:1 ratio (30 min incubation time) and the samples run on a 15% native PAGE to quantify the proportion of intact 3WJ. The second experimental design was to add 3WJ DNA and competition DNA together prior to cylinder addition. Thus the cylinder has a choice of which structure to bind to and is not pre-bound in the 3WJ. Finally, in the third experimental design, cylinder was incubated with the competitor DNA before 3WJ DNA was added. Here the experiment probes the ability of 3WJ to pull cylinder away from another DNA structure to which it is bound. This range of experiments should give a clear view of cylinder-DNA

structural binding preferences. Figure 2.6 shows the gel electrophoresis results obtained from these experiments (A, B and C).
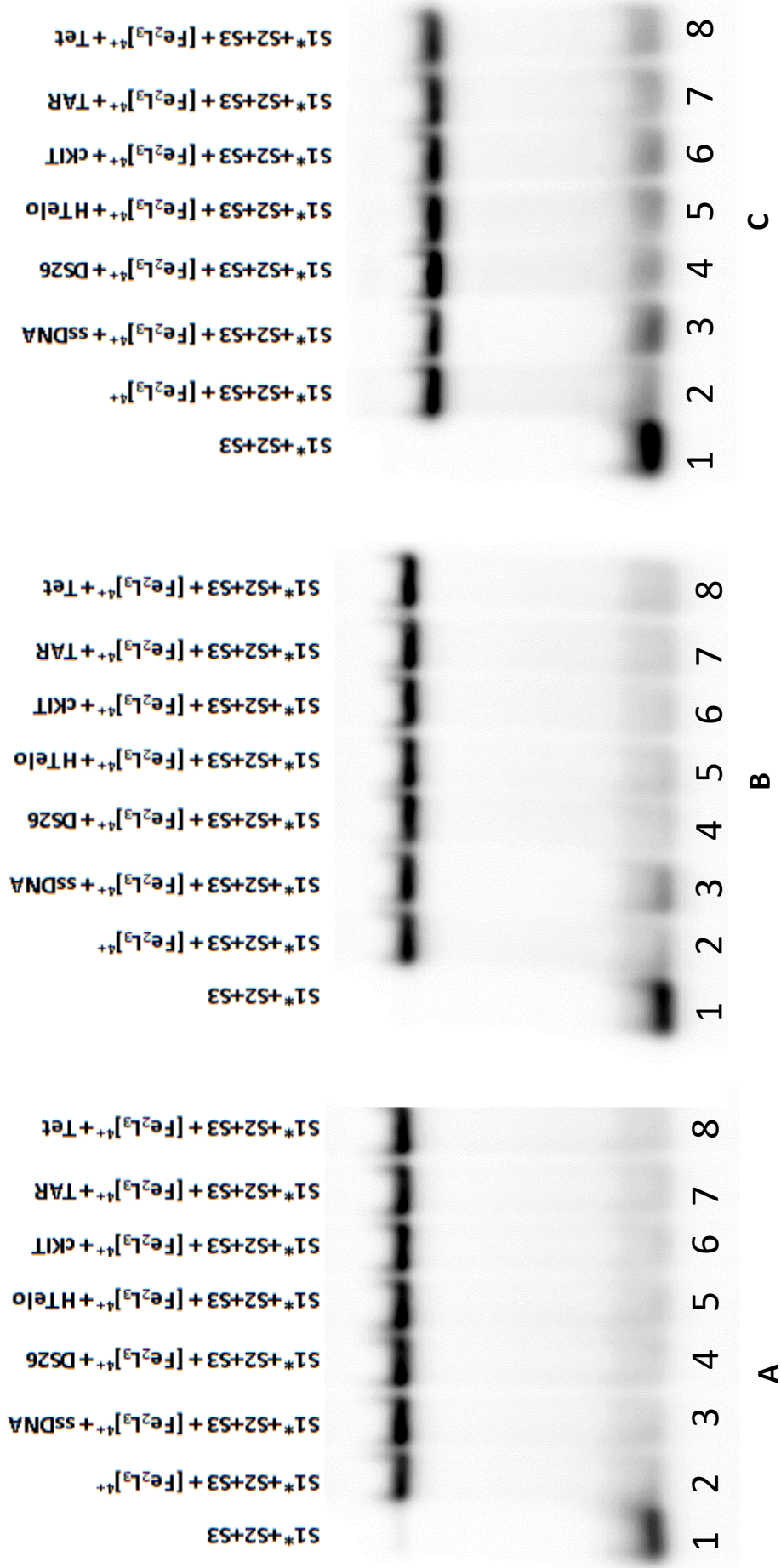
Figure 2.6 – Autoradiograms of competition assays for iron cylinder binding between a 3WJ and other DNA structures. The competitors were a 55-mer single strand of DNA, ssDNA (lane 3), a 26 bp double stranded piece of DNA, DS26 (lane 4), a G-quadruplex from the telemetric region, HTelo (lane 5), a G-quadruplex from a cancer promoting genomic region, cKIT (lane 6), A 31-mer looped piece of RNA found in the HIV virus, TAR (lane 7) and the DNA tetrahedron, Tet (lane 8). Gel A incubated the 3WJ DNA with the cylinder before adding competitor. Gel B incubated the 3WJ DNA and the competitor DNA together before adding the cylinder. Gel C incubated the competitor DNA together with the cylinder before adding 3WJ DNA. All were 15% native PAGE. Ratios were all 1:1:1 referring to 1 cylinder to 1 full 3WJ to 1 full competitor structure (structures illustrated in experimental section.)

Gel A
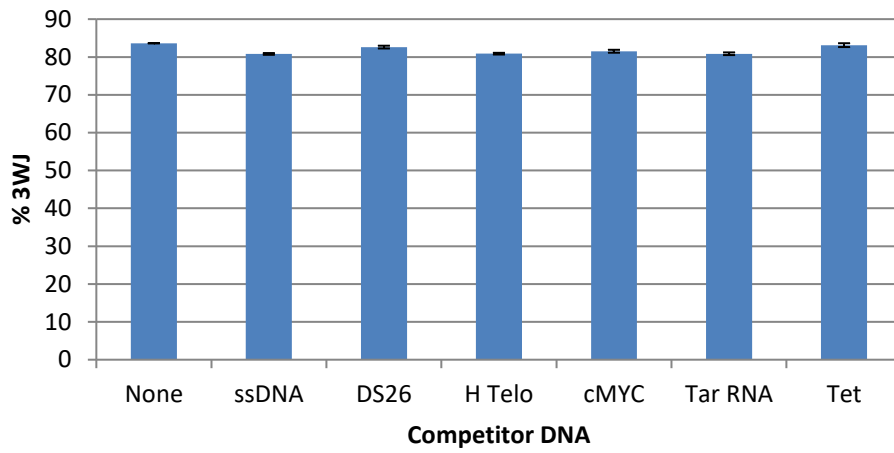
Gel B
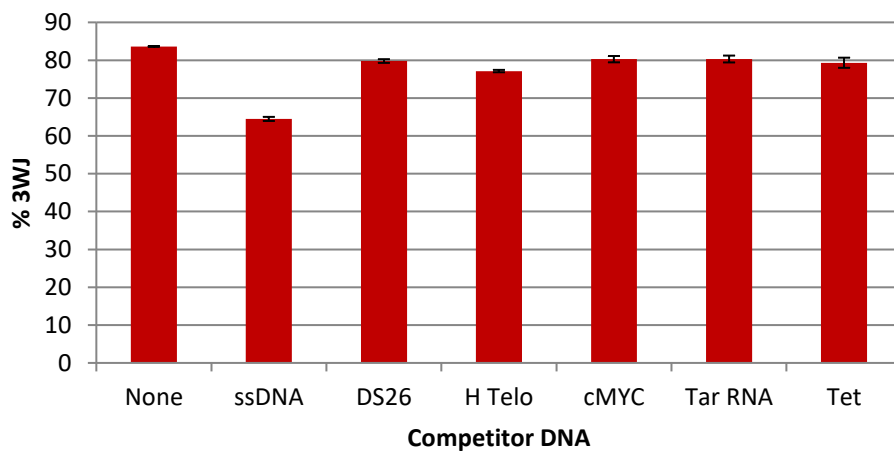
Gel C
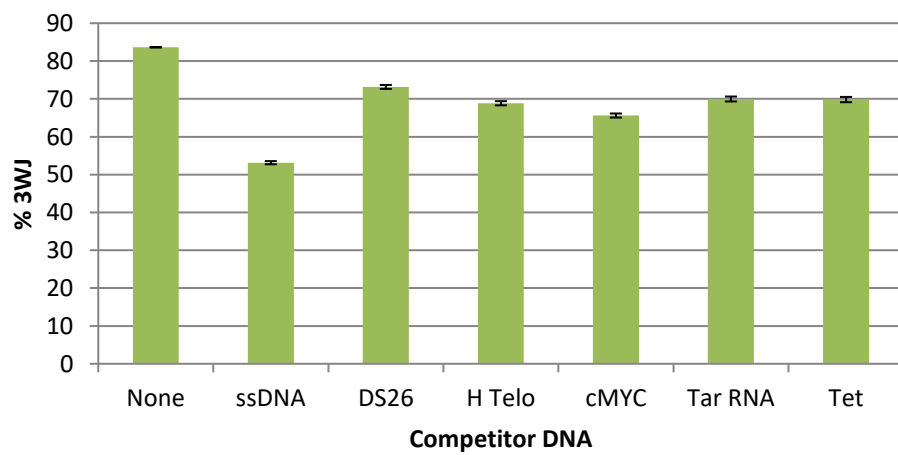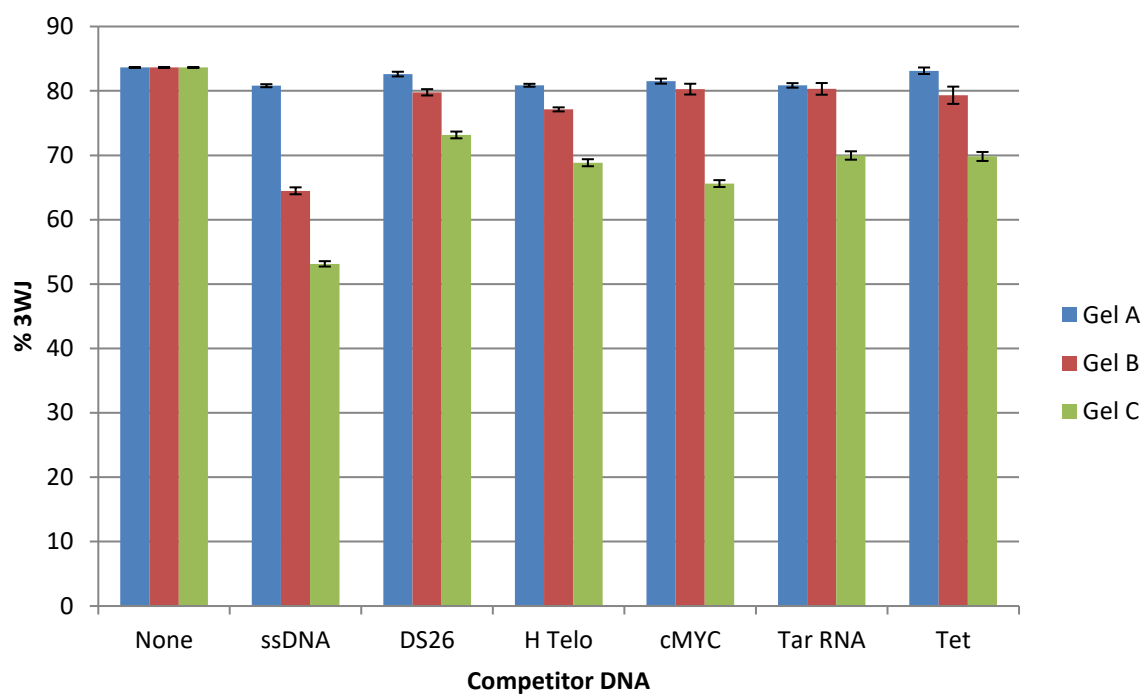
Figure 2.7 – Graphical quantification of gels, showing the % of the 3WJ formed in each of the experimental conditions. Bottom showing all three graphs compared. Error bars show standard error of n=2 experiments.

It is clear that regardless of which DNA structure the cylinder is allowed to bind to initially, the cylinder overwhelmingly prefers to bind and thus stabilise the 3WJ. This was anticipated in gel A where the cylinder had already assembled and bound to the 3WJ and does not shift binding once competitor DNA was added. It was surprising however, that when the cylinder was bound to competitor DNA initially, in gel C; the cylinder still preferentially brought the 3 oligos together to form the 3WJ. This shows that the binding constant is higher for the 3WJ than any of the other structures. The bottom graph of Figure 2.7 shows that the earlier the competitor DNA is added (from gel A-C), allows it to compete more, but only slightly in most cases. The ssDNA was the strongest competitor - in gel C only 53% of 3WJ was present. Whilst it is known that the cylinder can bind ssDNA, the reason for this competition is more likely from the ssDNA pairing with the unpaired oligos so that the DNA for the 3WJ is no longer available for the cylinder; rather than the cylinder binding directly to that 55-mer oligo. Further testing would be required to confirm this as a second band attributed to the radiolabelled strand binding to the ssDNA was not observed. This would be consistent with one (or both) of the other 2 strands binding to the ssDNA, but not the radiolabelled strand.

Also, surprisingly, it was expected that the DNA tetrahedron would be able to compete well with the 3WJ for cylinder, considering that the structure itself contains four 3WJ-like structures. The angled nature of the junctions involved in the tetrahedron seems to be able to cause enough distortion to affect cylinder binding adversely. This in turn meant that little or no competition with the 3WJ was observed and it could be suggested that tetrahedron binding is at least 10 times weaker than 3WJ binding. The interaction with this interesting structure will still be studied in depth later in the chapter.

From these experiments, it can be seen that the cylinder has considerable binding preference for the 3WJ over a variety of other structures at a 1:1 ratio. Physiologically however, 3WJs

are heavily outnumbered by duplex DNA base pairs. To begin to test this, an initial experiment was carried out to test the competition between the 3WJ and large excesses of plasmid DNA for the cylinder. The experiment was very similar to the previous competition gels, but the competition would be against the plasmid PuC19, up to a ratio of 5000 base pairs per 3WJ. Figure 2.8 shows the results of this experiment.
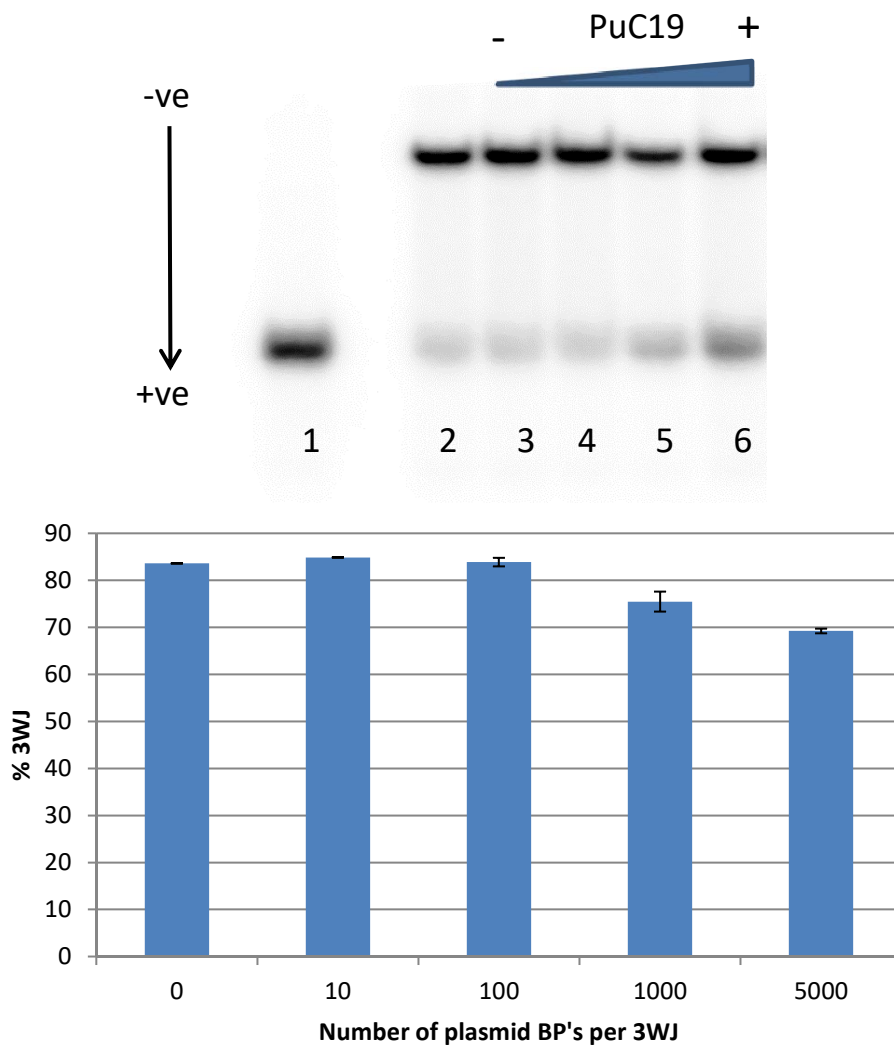
Figure 2.8 – Top: 15% PAGE showing the effect of increasing concentration of PuC19 plasmid on cylinder-3WJ binding. Lane 1 containing all 3 strands for the 3WJ. Lane 2 containing iron cylinder 3WJ at 1:1 ratio (0.4μM), lanes 3-6 containing lane 2 components with plasmid concentrations of 0.0015μM, 0.015μM, 0.15μM and 0.75μM respectively. Bottom: Bar Chart showing the percentage of 3WJ intact when compared to the single stranded band from the gel, each bar corresponding to lanes 2-6. Error bars show the standard error of the mean where n=2 (n = number of repeats).

This initial experiment was designed in the same way as experiment A, where the cylinder and 3WJ DNA were incubated together for 1 hour at RT, followed by addition of the plasmid DNA and an incubation of 30 minutes at RT. The experiment shows that by 5000 bp to 1 3WJ, the proportion of 3WJ present is decreased by approximately 18% compared to the control. This result again confirms that the cylinder has a higher affinity to the 3WJ than duplex DNA. However, it must be noted that the plasmid was in a supercoiled state. With further experimentation, it would be interesting to use linear plasmid DNA that would provide large excesses of duplex DNA in a relaxed state as supercoiled DNA may be less accessible for cylinder binding.

2.2.2 Part 2a – Cylinder – DNA tetrahedron interaction

2.2.2.1 Tetrahedron Synthesis and Characterisation

The method used for the synthesis of the tetrahedron was replicated from a previous publication from Turberfield.[13] Briefly, 4 synthetic strands of the correct sequences (see experimental) of DNA were purchased (Eurofins Operon) which had been HPLC purified. These strands were then annealed in TM buffer (10 mM Tris, 5 mM $MgCl_2$ pH 8.0) by heating to 95°C for 5 minutes and cooling on ice for 10 minutes. The tetrahedron was then purified by passing through a 30K MWCO filter (Pierce) which retained the fully formed tetrahedron, whilst any unincorporated single strands which are smaller than 30k MW in size, were collected in the filtrate and disposed of. The purified tetrahedron could then be diluted to the desired concentration. No further purification was performed and the tetrahedron was stored in TM buffer unless otherwise stated.

2.2.2.2 Polyacrylamide Gel Electrophoresis (PAGE)

The tetrahedron was characterised by a number of methods. The first was gel electrophoresis, using native PAGE to examine and confirm the construction of the DNA tetrahedron.

Figure 2.9 shows a native PAGE experiment illustrating the construction of the DNA tetrahedron. Lane 1 contains just 1 strand alone, lane 2 contains 2 of the strands, lane 3 with 3 strands and lane 4, the fully annealed tetrahedron. Each of the migrations were in agreement with previously reported strand migrations.[13] The absence of any secondary bands demonstrates the effectiveness of the synthesis; other bands in each lane would suggest secondary structures being formed. The approximate yield of the completed tetrahedron is estimated to be >95% by gel electrophoresis studies.[13]
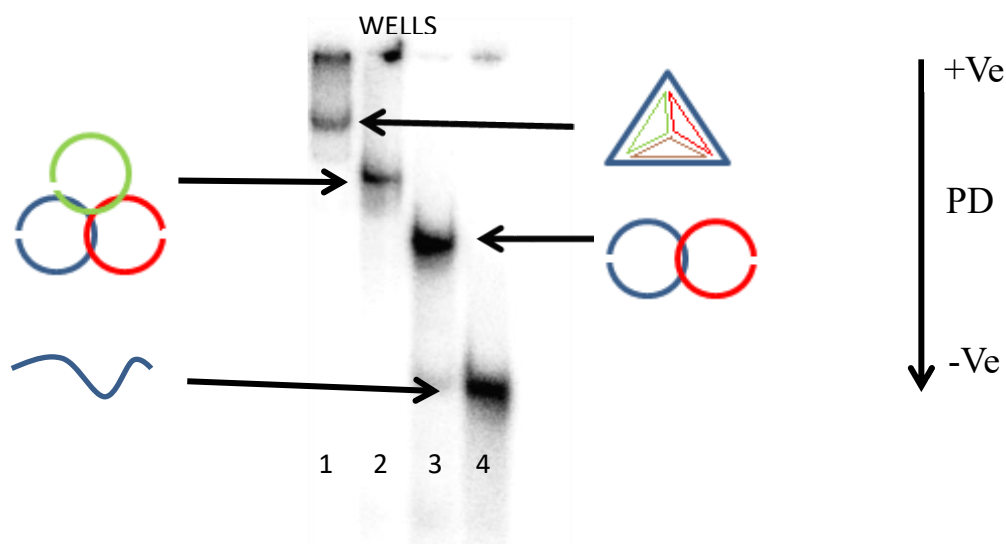
Figure 2.9 – Autoradiogram showing the construction of the DNA tetrahedron on 10% native PAGE. Lane 4: strand 1 only. Lane 3: strands 1 and 2. Lane 2: strands 1, 2 and 3 and finally lane 1 containing all 4 construction strands to form the full tetrahedron. (Appendix fig.1)

2.2.2.3 Dynamic Light Scattering (DLS)

Another method of characterisation used was dynamic light scattering (DLS also known as Photon Correlation Spectroscopy or Quasi-Elastic Light Scattering). This is a useful technique that can determine the size of particles in a solution down to around 1 nm. Most commonly, it is used to size materials such as nanoparticles, polymers, colliods or proteins. Briefly, a laser is shone through a sample-containing solution at a known angle. The subsequently scattered light as it passes through the sample is then collected by a photon detector. The degree of scattering leads to a final calculation of the size of the particle in solution.

DLS is not as commonly used in the field of DNA nanotechnology as most structures in the field do not have a uniform radius and are often not solid throughout, leading to complications in collecting a uniform scattering index. However, it was found that structures like the tetrahedron could provide sizing data which has allowed some experiments to be performed and some published data produced.[20] The tetrahedron was diluted to 100 nM and scanned on the DLS, giving a hydrodynamic diameter of 13 nm (Figure 2.10). This is larger than previous

DLS experiments on the tetrahedron (9.08 nm).[21] It is also slightly larger than the expected diameter of the tetrahedron, just over 6 nm. The DLS calculations assume that the sample is spherical, which exaggerates the size slightly due to the tetrahedral shape, along with some small instrumental margins of error lead to a figure slightly larger than expected. A hydration layer is also present which contributes to the extra size calculated. Despite these slight inaccuracies, DLS provides useful information as not only does it show particles of the correct region of size, it also shows that only one product is present in solution and no large aggregate or secondary structures are left after synthesis and purification.
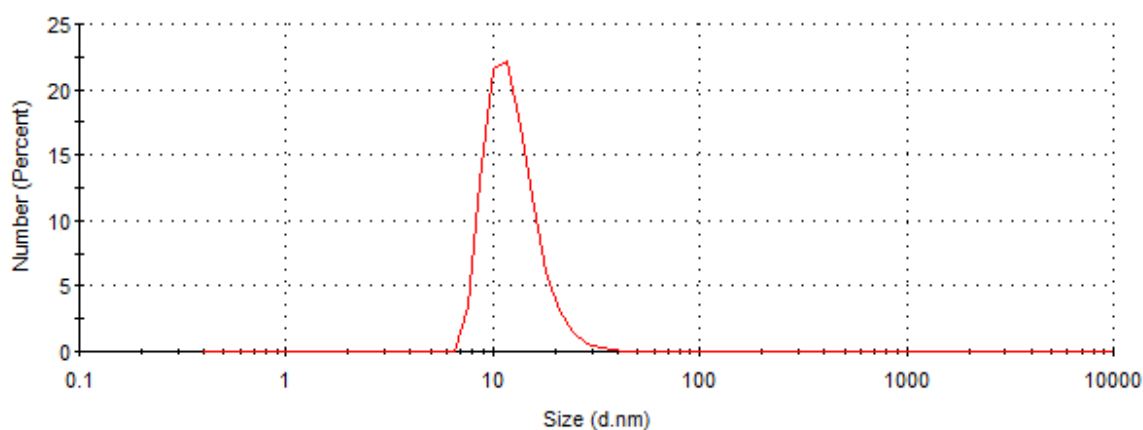
Peak 1:   12.68 d nm / 100%   St.dev : 3.986 nm

Z average (d.nm) : 26.90   PDI   : 0.138   PDI Width : 6.403

**Figure 2.10 -** DLS data of the DNA tetrahedron – showing one species in solution illustrated by the single peak.

2.2.2.4 Atomic Force Microscopy (AFM)

All AFM experiments were completed in the labs of Prof. Shao Fengwei by Dr Wang Liying from the institute of chemical biology, Nanyang Technological University.

Whilst the gel electrophoresis and DLS results give a good idea of the size and amount of base pairs involved, they don't give a full characterisation that the tetrahedron has been formed and it cannot be said with certainty that a tetrahedron is the shape of the structure formed here. Atomic force microscopy (AFM) is the only current method that provides both full structural and mechanical information at high resolution of nanoscale materials.[22] Briefly, AFM works by moving a very fine tip (approximately 2 nm) over a surface. The tip is attached to a sensitive cantilever to which a laser can record any deflections corresponding to any analyte the tip has been dragged over. This builds up a surface topography that can be plotted and imaged computationally.[23] AFM is a powerful tool in analysing biological samples, such as DNA, as it can be performed in an aqueous environment as opposed to drying the sample. Drying a DNA sample can lead to deformations in DNA structure, leading to inaccuracies when establishing structure.

The tetrahedron synthesised here was analysed in collaboration with Dr Wang Liying and Prof. Shao Fengwei at the Nanyang Technological University in Singapore by AFM. Figure 2.11 shows the 3D image created of the sample. The figure shows remarkably clear 3D tetrahedra, all in the size range that was expected. This very positive result fully confirms and characterises the synthesised tetrahedron here. The size calculation, show also in Figure 2.11, of 19.2 ± 1.5 nm is larger than modelling suggests and the DLS result. However, this was not unexpected as AFM measurements also detect the hydration layer surrounding the DNA, along with the added width of the AFM tip of 2 nm leading to a slightly larger value than other methods of measurement. This size figure is included for means of comparison for later on in the chapter.
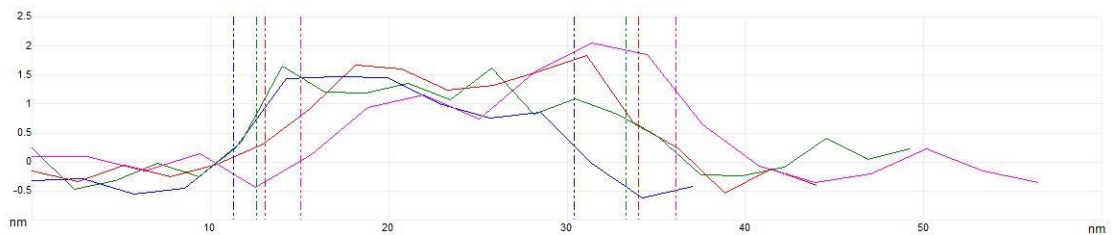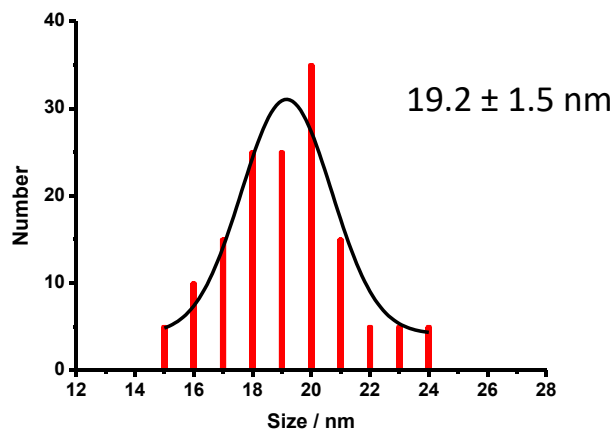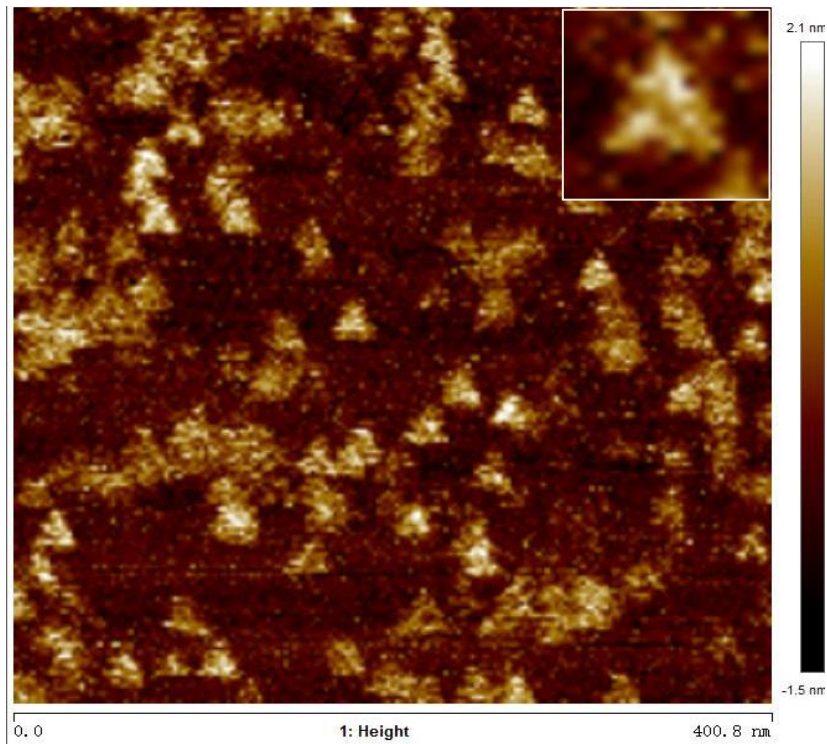
Figure 2.11 – AFM image of the DNA tetrahedron (top), size distribution of tetrahedra (middle). Height profiles of four separate tetrahedra (bottom) Figures produced by Dr Wang Liyang, Nanyang Technological University, Singapore.

2.2.3 Interaction between the cylinder and the Tetrahedron

2.2.3.1 Polyacrylamide Gel electrophoresis

Now the structure of the tetrahedron has been characterised, the interaction between the iron cylinder and the tetrahedron can be studied. The first experiment used was again gel electrophoresis, employed in a similar way to that used to characterise the tetrahedron. Different samples of DNA tetrahedron were incubated with increasing concentrations of iron cylinder at ratios of 0:1, 2:1, 4:1, 6:1, 8:1, 10:1, 0:1 (cylinder to tetrahedron). Figure 2.12 shows the gel image produced. It is shown here that with increasing cylinder concentration, the migration of the DNA tetrahedron is increased, though the effect is small. This is interesting as one would expect the migration to be slowed down with the conjugate becoming bulkier and some of the negative charge of the DNA balanced by the positively charged cylinder. The opposite of the expected trend occurs and this suggests that the cylinder
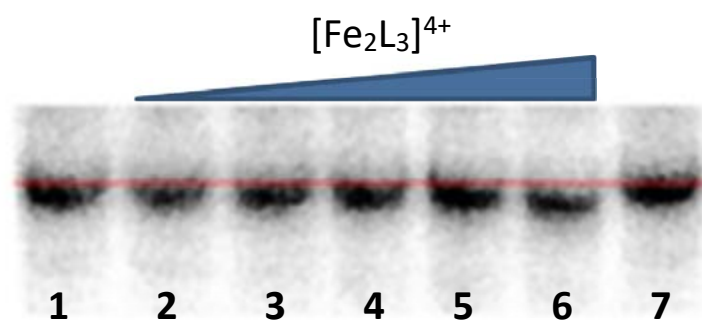
Figure 2.12 – Autoradiogram of a 10% non-denaturing PAGE experiment. Lanes 1 and 7 containing DNA tetrahedron alone as reference (0.5 μM), Lanes 2-6 contain increasing amounts of iron cylinder with the DNA tetrahedron with ratios at 2:1, 4:1, 6:1, 8:1 and 10:1 relating to cylinder concentrations of 1, 2, 3, 4 and 5 μM respectively. Gel was run in 1 x TB buffer (89 mM Tris, 89 mM Boric acid, pH 8.3) at room temperature for 3 hours at 10v/cm.

is binding to the DNA and causing it to compress, becoming a smaller sized structure, speeding the migration through the gel. It could be that the two mentioned effects compete with each other, but the size compression has the overriding effect on the electrophoretic mobility of the tetrahedron.

It is important to prove the cylinder is still intact and bound to the DNA throughout the entire experiment. This was done by running a non-radiolabelled sample of DNA and the band containing the conjugate at a ratio of 5:1 (cylinder: tetrahedron) was excised from the main gel. The conjugate was then liberated from the band using the 'crush and soak' method (see experimental). The resulting solution was then observed using UV-Vis spectroscopy to find the characteristic absorbance at 573 nm attributed to the MLCT band of the iron cylinder (Figure 2.13). This information shows that at least some of the cylinder remains intact, does not break down and that the cylinder is bound to the tetrahedron and migrates with it through the gel
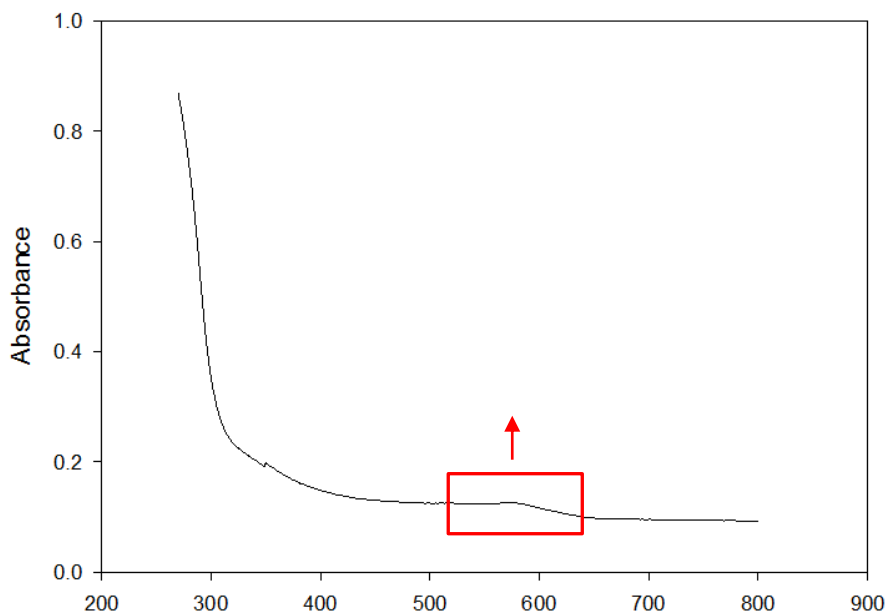
Figure 2.13 – UV Vis spectrum of the excised band showing peak at 573 nm, confirming the presence of the iron cylinder in the band.

2.2.3.2 Dynamic Light Scattering (DLS)

As the first experiment suggested the cylinder compressed the DNA tetrahedron, DLS was used to further explore this hypothesis. As previously discussed, DLS can provide valuable information about a particle in solution and therefore should be able to track any size changes.

Samples of DNA tetrahedron were prepared at 100 nM and iron cylinder solution titrated in to achieve the ratios of DNA tetrahedron to Cylinder of 1:0, 1:2, 1:4, 1:6 and 1:8. At each ratio the sample was scanned on the DLS to find an estimate of the diameter in solution. Figure 2.14 shows a line graph of the results obtained. It is shown that as increasing amounts of cylinder are added, the hydrodynamic diameter decreases (overlay of size distribution shown in Figure 2.23). This result backs up the previous theory that the cylinder's binding forces compression of the DNA into a smaller size. The decrease is by approximately 30% by 8 equivalents of tetrahedron and higher equivalents. DLS remains a useful tool here as it
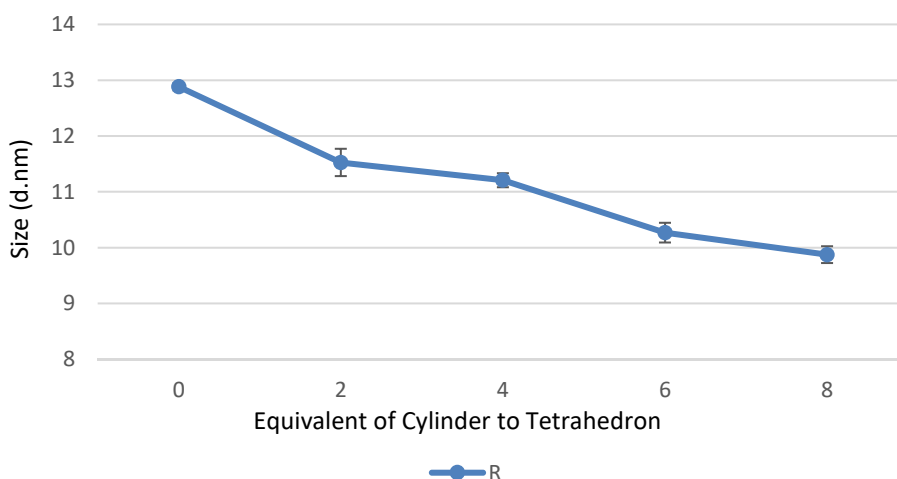
Figure 2.14 – DLS size by number data of the DNA tetrahedron (100nm) as increasing amounts of cylinder is added by ratios of 0, 2,4,6,8 to 1 tetrahedron, relating to concentrations of 0, 200, 400, 600 and 800 nM of cylinder respectively. Error bars show the standard error of the mean size (n=3).

shows the size decreasing comparatively to the tetrahedron alone. This shows that binding of the cylinder to the tetrahedron has a compressing effect on the structure.

2.2.3.3 Atomic Force Microscopy

All AFM experiments were completed in the labs of Prof. Shao Fengwei by Dr Wang Liying from the institute of chemical biology, Nanyang Technological University.

By employing AFM again, it was hoped that the cylinder-tetrahedron size reduction effect would be able to be visualised. Cylinder and tetrahedron were incubated together at a ratio of 4 to 1 before being imaged by AFM. Figure 2.15 shows the image produced by this experiment. The once sharp edges of the tetrahedron are now much less clear and more rounded, suggesting the DNA is been compressed here, possibly by the cylinder binding into the 3WJ and flattening the emerging edges, although AFM cannot reveal where exactly the cylinder is bound. The tetrahedra has also become less defined than before, suggesting the structure as a whole has lost some rigidity and is not fully resisting the AFM tip now, leading to a less sharp reading of the structure. Figure 2.15 shows also the diameter of the resulting conjugate from 19 nm to 12 nm – a decrease of 37% which is a dramatic decrease. When compared with the previous DLS measurement at 4:1, the decrease is just 18%. It is not clear what causes this disparity but the most likely source of difference is instrumental. Overall, it can be concluded that the iron cylinder binds to the DNA tetrahedron and on doing so, causes a deformation in the structure, dramatically reducing its rigidity, size and thus the volume of the central cavity.
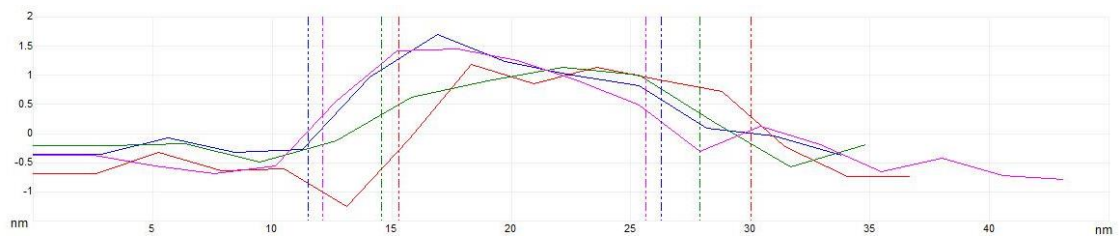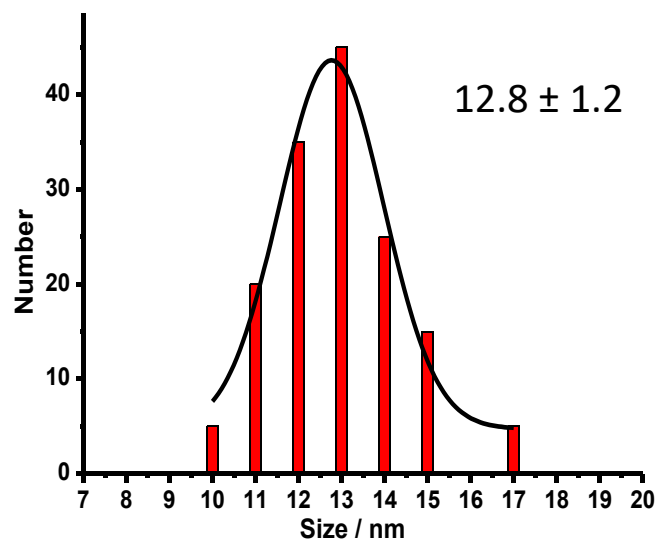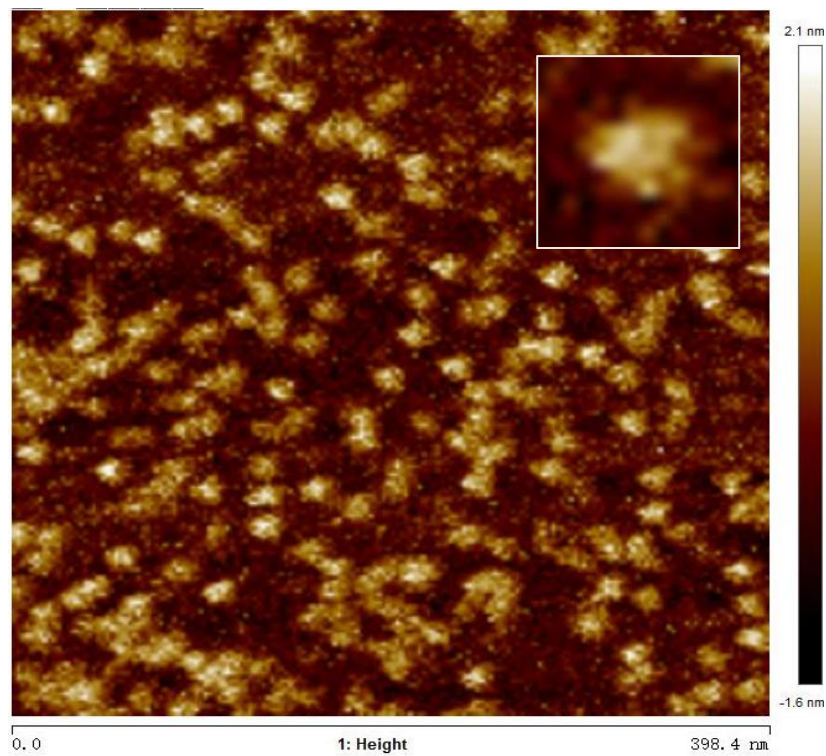
Figure 2.15 – AFM image of the DNA tetrahedron with cylinder bound (1:4) (top), size distribution of tetrahedra-cylinder conjugate (middle). Side size profile of 4 separate tetrahedra (bottom). Figures produced by Dr Wang Liyang, Nanyang Technological University, Singapore.

2.2.3.4 Stabilisation Effect

In solution alone, the cylinder breaks down over time by the ligands becoming liberated from the iron metal. As the cylinder has a unique MLCT absorption band at 573 nm (ϵ = 16900)[11] UV-Vis spectroscopy can be used to monitor the concentration of intact cylinder over time to ascertain the rate of degradation. It would be interesting to see whether, when bound to the tetrahedron, the cylinder would experience enhanced stability in solution. In this regard, two solutions in TM buffer containing identical concentrations of cylinder, one free in solution and the other bound to the DNA tetrahedron were prepared. These solutions were then monitored over time by UV spectroscopy, observing the absorbance at 573 nm. Figure 2.16
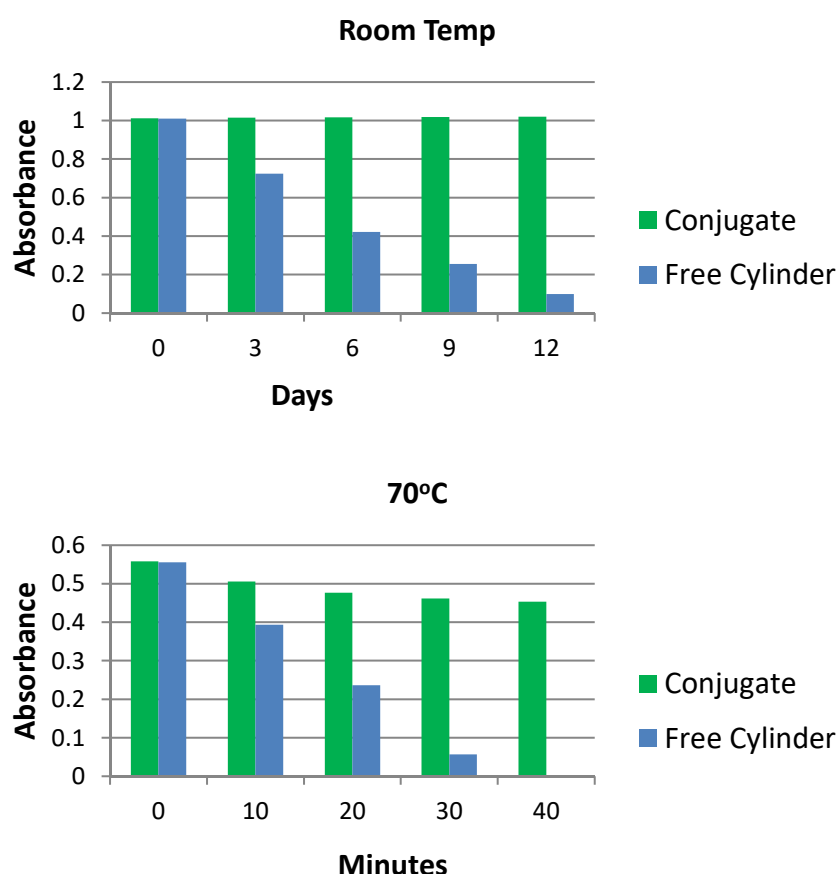
Figure 2.16 – UV-Vis data illustrating the breakdown of the iron cylinder at room temperature (top) and at 70ºC (bottom). Green representing when the cylinder is bound to the tetrahedron and blue representing the free cylinder.

shows the concentration of the two solutions when kept at room temperature and another experiment at 70°C. When bound to the tetrahedron, at room temperature, no degradation is observed at all over 12 days. In fact a very small increase in absorption (<1%) was observed which was attributed to small amounts of water evaporating even though the cuvette had a lid. Free cylinder, however, almost completely degrades in the same time period. At an elevated temperature of 70°C, the free cylinder is fully degraded within 40 minutes, whereas the conjugate has only slight degradation over the same period. The DNA binding helps protect the iron-nitrogen coordination from hydration when in solution. This is particularly useful in biological applications as the cytotoxic cylinder would remain intact for longer at temperatures of 37.5°C *in vivo,* increasing the half-life inside the body and thus increasing potential bio-availability, creating an overall more effective therapeutic.

2.2.4 Part 2a – Assessing different characteristics of Cylinder Enantiomers

2.2.4.1 Separating and characterising the Cylinder Enantiomers

The cylinder is a triple helicate, and therefore is inherently chiral. As discussed earlier, it has two enantiomers in a racemic mixture. These enantiomers are known as M and P, to denote the right and the left handed chiral twists enantiomers. These enantiomers can be separated using column chromatography with cellulose as the stationary phase. Figure 2.17 shows the enantiomers visually separated as two fractions on the column, with the M enantiomer eluting before the P.

Figure 2.17 – Cellulose column showing iron cylinder enantiomer separation. The M enantiomer is eluted first, followed by the P. Eluted with 0.2M NaCl solution.

It is interesting to separate the enantiomers and observe their behaviour as previous reports have suggested that each have differing DNA binding properties. The M enantiomer was reported to have a stronger binding constant with the major groove in DNA than the P and

only the M enantiomer was observed inside 3-way-junction DNA in crystallographic experiments.[11] However, gel studies performed previously in the group show that both the M and P enantiomers can stabilise the DNA 3WJ. This suggests that M enantiomer potentially has a more favourable spatial fit inside 3WJ and major groove DNA than the P enantiomer and therefore could have differing binding strengths to the DNA tetrahedron.

2.2.4.2 Circular Dichroism (CD)

One of the experiments used to test the enantiomer separation and purity of the products was by circular dichroism (CD). Circular dichroism is exhibited as the effect of chiral molecules have on passing circularly polarised light, specifically the differential absorption of left and right handed polarised light.[24] In a racemic mixture of the cylinder, the CD signals of each enantiomer cancel each other out as they are present in equal concentrations. Once separated the enantiomers CD signal can be observed. Pure enantiomers would give exactly the same intensity of CD signal mirrored to each other when overlaid, provided the concentrations of the enantiomers and path length are the same. By scanning exact concentrations of each enantiomer, the resulting absorption spectra should mirror one another in shape and intensity. Figure 2.18 shows close to enantiopure samples of each enantiomer were achieved with each enantiomer mirroring the CD peaks in each of the spectra. Here, the M enantiomer is seen to have a slightly more intense CD peaks than the P. This is explained simply by the eluting order of the enantiomers from the cellulose column. The M enantiomer is eluted first, but the slow moving smearing nature of the eluting band causes some enantiomer to drag behind into the P enantiomer band. Much effort was put into improving enantio-purity by increasing the amount of stationary phase and decreasing sample load to enhance band resolution. To obtain P enantiomer of purity comparable to M enantiomer, it was necessary to run the enantiomer through multiple cellulose columns to remove as much M enantiomer as possible.

During this process, it became apparent that in solution at room temperature, purified enantiomers could re-racemise to form its opposite enantiomer at a slow rate. This was minimised by freeze drying and de-salting the fractions quickly. Through this it was possible to obtain highly pure enantiomers.
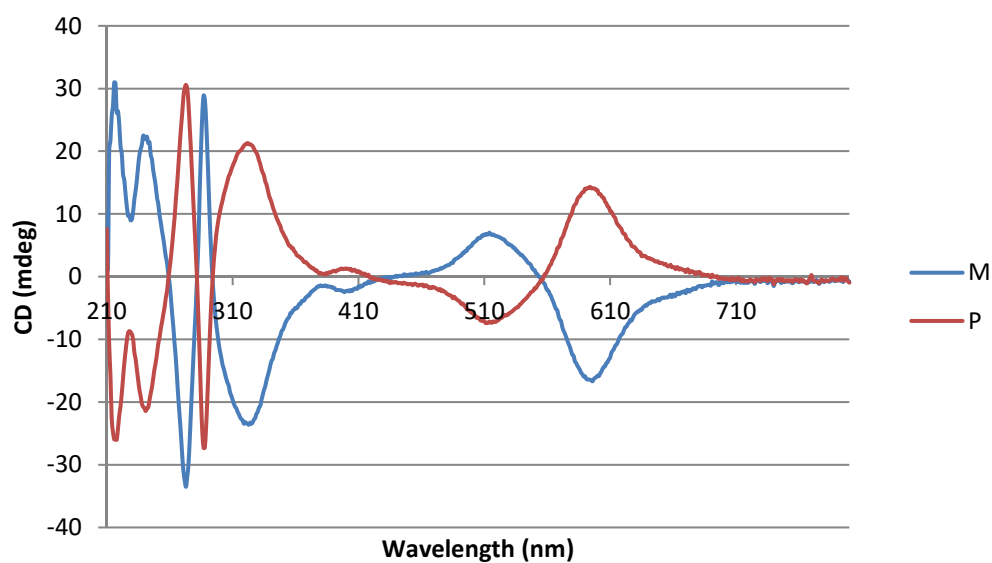
Figure 2.18 – CD data of the M and P enantiomers, illustrating the mirrored nature of the CD signals. Samples were of 15 µM cylinder with a 1 cm path length.

2.2.4.3 Chiral Shift Reagent - Λ-TrisPhat

To fully ascertain whether pure enantiomers where obtained by this method, the chiral shift reagent Λ-TrisPhat tetrabutylammonium salt ([Tetrabutylammonium] [Δ-tris(tetrachloro-1,2-benzenediolato)phosphate(V)]) was used (Figure 2.19). This chiral anion is configurationally stable in solution and can be isolated as either isomer. It has also been shown to be able to form diastereomeric ion pairs with chiral metal-ligand complexes which then exhibit different chemical shifts in ^{1}H NMR spectroscopy.[25]
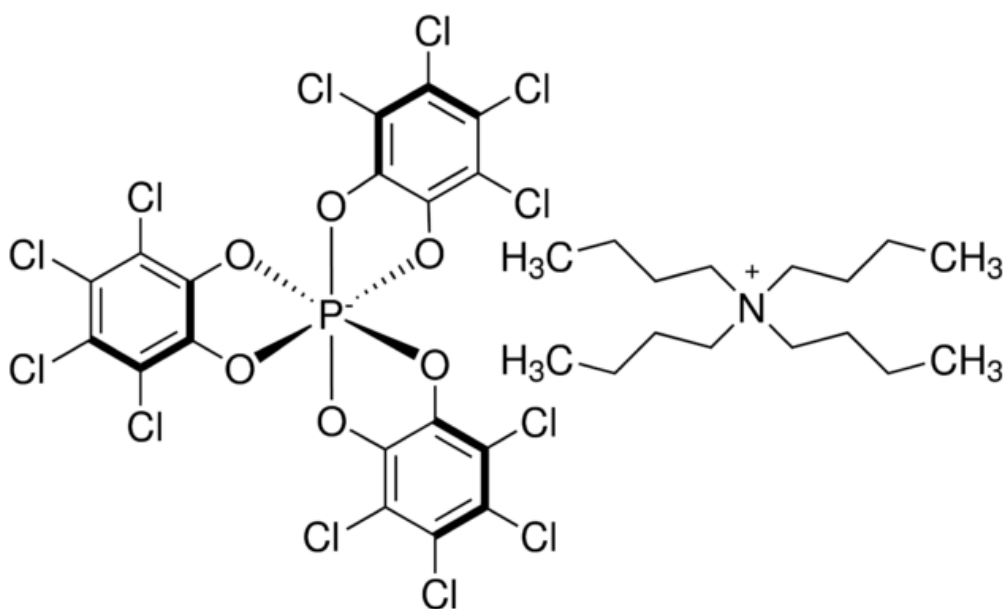
Figure 2.19 - Λ-TrisPhat tetrabutylammonium salt structure, taken from Sigma Aldrich product web page.

By adding Λ-TrisPhat to samples of racemic cylinder and also to sample of the M and P enantiomers, it was found that the anionic counter ion interacts each of the enantiomers differently. Figure 2.20 shows the ^{1}H NMR data of the racemic iron cylinder alone. On addition of the chiral anion, ^{1}H environments CH$_2$, H$_{im}$ and 5py split into two more sets of peaks.
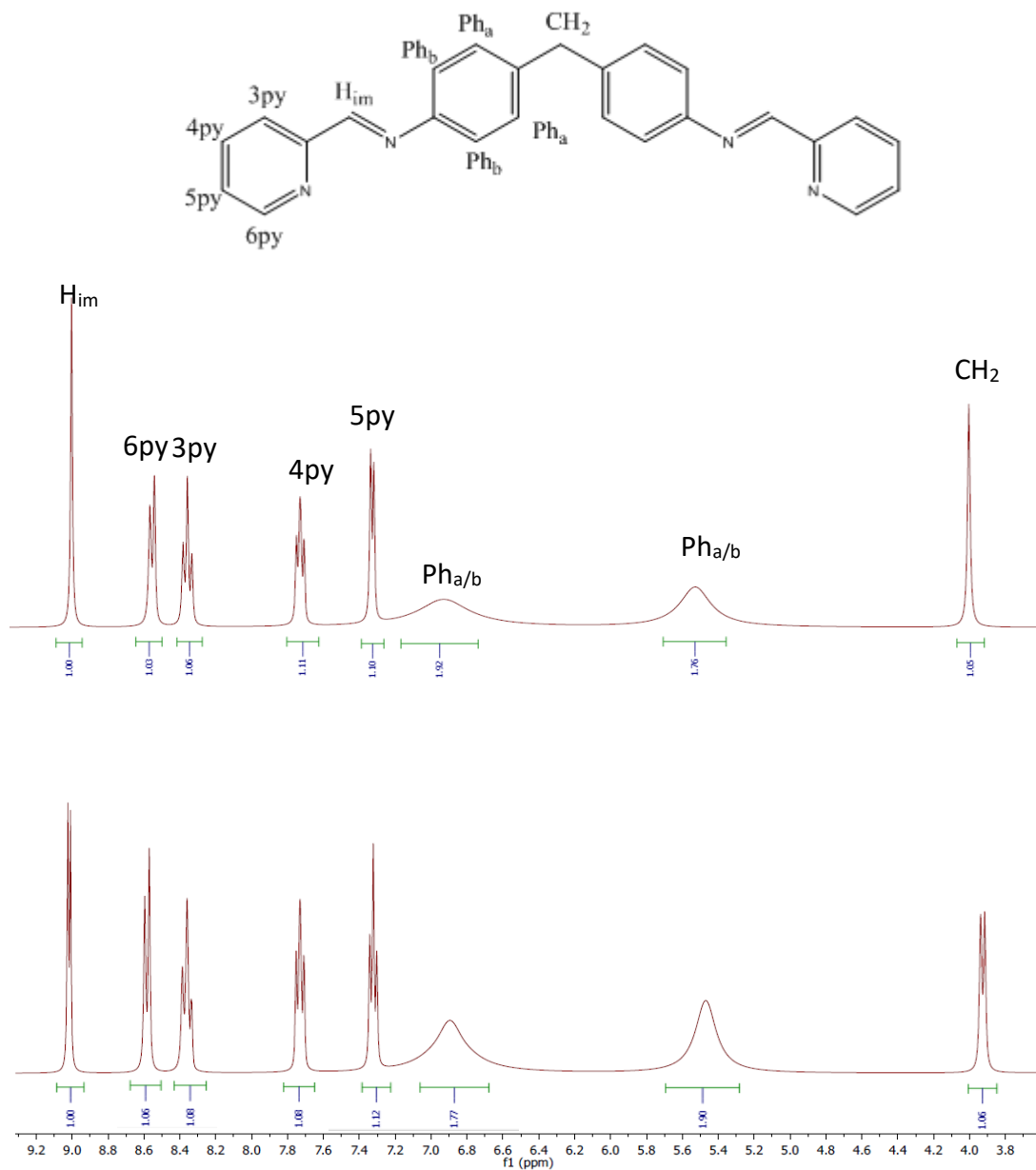
Figure 2.20 – H[1] NMR data of racemic iron cylinder with assignments (top) and racemic cylinder with a 1:1 molar equivalent of Λ-TrisPhat (bottom) illustrating the peak splitting of H_{im}, 5py and CH_2 as the chiral anion interacts with each of the enantiomers differently.

This is due to the anion interacting and binding to each of the cylinder enantiomers differently. This causes the proton environments to change and shifts the signals. The cylinder environments the TrisPhat is interacting with is the central bridging section of the ligand (CH$_2$) and the metal coordination site. Previous work in the group performed by Dr Lucia Cardo has concluded that the up field shift of the new peaks on CH$_2$ is the anion binding to the M enantiomer and the down field shifts of the new peaks at H$_{im}$ and 5py is binding to the
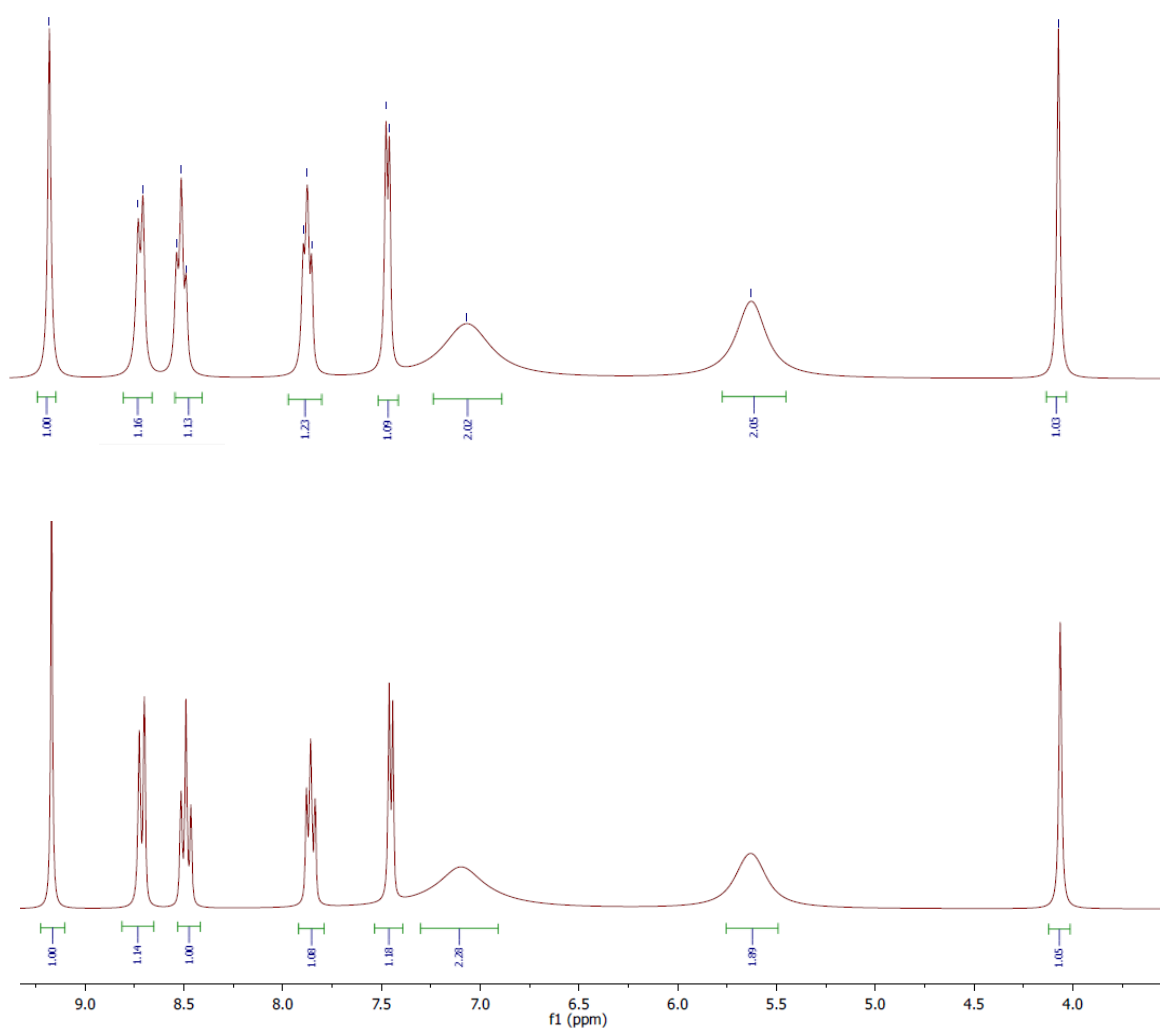
Figure 2.21 – H^1 NMR data M enantiomer of the iron cylinder (top) and P enantiomer of the iron cylinder (bottom) both with a 1:1 molar equivalent of Λ-TrisPhat illustrating the leak of peak splitting.

P enantiomer. This was done by spiking an enantiomer sample with a known amount of the other enantiomer and quantifying the new environment to confirm which enantiomer was responsible for each of the new peaks.

Using this model, Λ-TrisPhat was added to each of the separated enantiomers at a 1:1 molar ratio to look for the presence of any of the opposite enantiomer, which would be evidenced by new peak splitting in small amounts. Figure 2.21 shows the ^{1}H NMR data of this experiment. From this, no peak splitting was observed in the areas of interest. With this information, the cylinder enantiomers could be considered to have an acceptable level of enantiomeric purity (<95%) which could be used for further experimentation.

2.2.5 Part 2b - Differences in the enantiomer effects on the Tetrahedron.

2.2.5.1 Polyacrylamide Gel electrophoresis

As previously highlighted, the M enantiomer has been shown to have a higher binding affinity to the major groove in linear DNA and was the only enantiomer found to bind inside the 3-way-junction in crystallographic experiments, even when racemic cylinder was used. To see the effect the different enantiomers might have on the DNA tetrahedron, a similar gel electrophoresis experiment was performed as before. This time the DNA was incubated with the same concentrations of each enantiomer and the effect of each compound analysed. This experiment backed up previous investigation that the M enantiomer binds more strongly. Figure 2.22 shows that the lanes containing the M enantiomer have a slightly greater effect of speeding migration through the gel than the P enantiomer. This suggests that the stronger the binding of the cylinder, the stronger the deformation of the rigid tetrahedron structure into a

smaller, faster migrating conjugate. Another explanation could be that both enantiomers bind equally well, but the binding of the M enantiomer has a bigger structural effect than the P enantiomer.
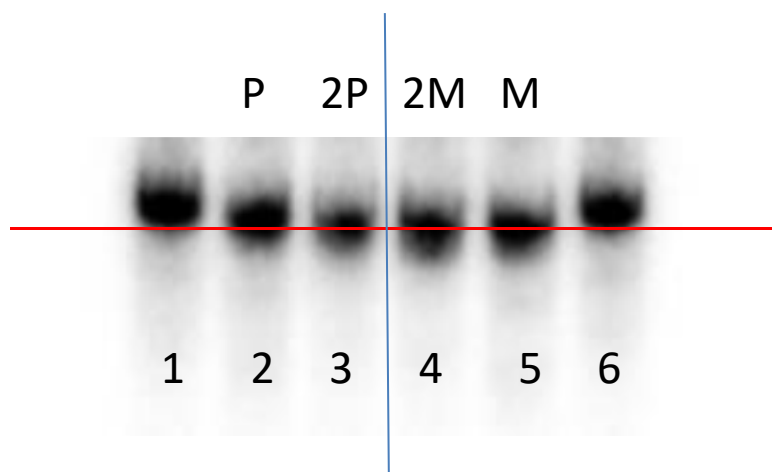
Figure 2.22 – Autoradiogram of a 10% non-denaturing PAGE experiment. Lane 1 and 6 consisting of DNA tetrahedron only (1μM), lane 2 and 3 containing tetrahedron with P enantiomer and tetrahedron at ratios of 5:1 and 10:1 respectively, with cylinder corresponding cylinder concentration of 5μM and 10μM respectively. Lanes 4 and 5 containing tetrahedron with P enantiomer and tetrahedron at ratios of 5:1 and 10:1 respectively, with cylinder corresponding cylinder concentrations of 5μM and 10μM respectively.

2.2.5.2 DLS

The earlier DLS experiment in which racemic cylinder was titrated into tetrahedron was now repeated with each of the enantiomers. This was done to attempt to quantify the earlier gel electrophoresis result in the expectation that the M enantiomer would decrease the overall size of the DNA tetrahedron more effectively than the P enantiomer. Figure 2.23 shows the DLS data obtained from this experiment, with the previous racemic experiment data overlaid for comparison. From the scatter graph, it can be seen that the expected trend is very neatly

illustrated, with the M enantiomer having the most effect on the tetrahedron, with the P enantiomer having the least. In comparison, the racemic cylinder sits between two. The difference is very subtle as previously shown by the gel electrophoresis.
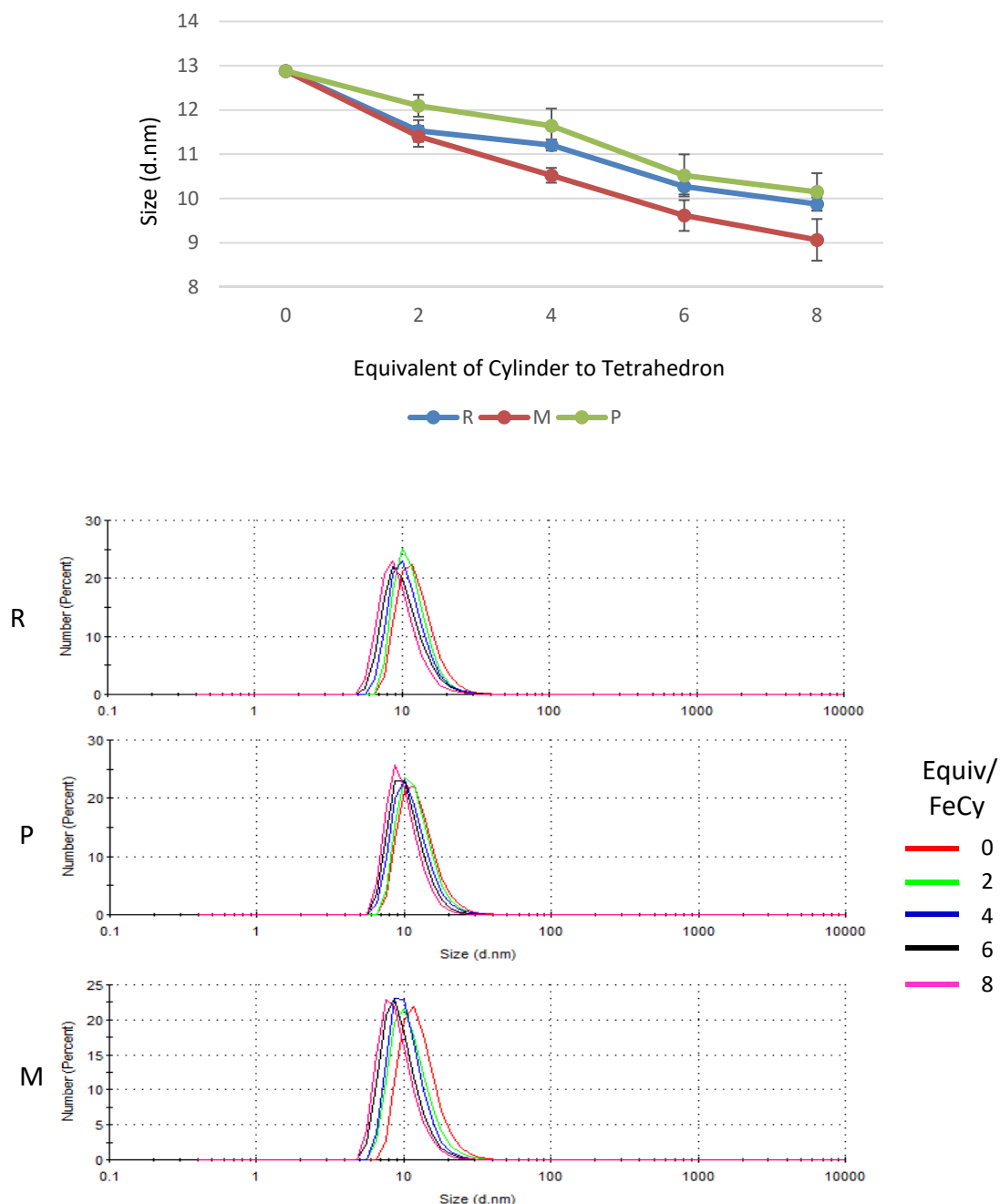
Figure 2.23 – Top) DLS size data of the DNA tetrahedron (100 nM) as increasing amounts of different enantiomers of iron cylinder are added to create ratios of 0,2,4,6,8 to 1 tetrahedron, relating to concentrations of 0, 200, 400, 600, 800 nM of cylinder respectively. R = racemic mixture of cylinder enantiomers. M = M enantiomer. P = P enantiomer. Error bars show the standard error were n=3. Bottom) Overlays of an experiment of separate titrations showing the decrease in size.

It is worth noting the range in the distribution of the size is wide, and this is probably due to the none-spherical and none solid structure of the tetrahedron causing a range of scattering. From the overlays, however, it is clear the entire range can be seen to shift to the left on increasing cylinder, showing an overall decrease in size.

2.3 Conclusions

Overall, in the initial parts of this chapter, it was shown that the iron cylinder has very high affinity to a synthetic DNA 3WJ and prefers to stabilise this structure over a wide range of other common DNA structures. From this, in part 2a, the cylinder was shown to also bind to a DNA tetrahedron. Further investigation into this binding led to the discovery of a very interesting interaction between the two; that cylinder binding lead to deformation and structural compression of the tetrahedron. This interaction was characterised through various techniques and a similar result obtained through each technique. In part 2b the cylinder enantiomers were separated and characterised successfully, following on from previous group work showing that the M and P enantiomers may behave differently with regards to DNA binding. In this respect, both enantiomers were shown to cause compression on interaction with the tetrahedron, with the M enantiomer shown to be more slightly more effective that the P enantiomer.

The interaction discovered here is a novel one between a small molecule and DNA nanostructure. As DNA nanostructures with hollow central cavities have been widely championed as cargo vessels for drugs, an interaction which would potentially see an internalised cargo pushed out on addition of cylinder is very exciting. The conjugate formed between the iron cylinder and the tetrahedron also has great biological potential which will be studied further in the following chapter.

2.4 Experimental

Materials

All Chemicals were purchased from Sigma Aldrich unless otherwise stated. Pre-mixed Acrylamide / Bisacrylamide Stabilized Solution for gel electrophoresis was purchased from National Diagnostics. ATP-32 was sourced from Perkin Elmer. All oligonucleotides were purchased reverse phase HPLC purified from Eurofins. T4 Polynucleotide kinase was purchased from New England Biolabs.

Synthesis of Parent Ligand (L: $C_{25}H_{20}N_4$)

4,4'Methylenedianiline (1.99g, 0.01 mol) was dissolved in ethanol (10 ml). To this solution, pyridine-2-carboaldehyde (1.90 ml, 0.02 mol) was added. The solution was then left to stir overnight. The yellow precipitate formed was then collected by vacuum filtration. The crude product was then purified by re-crystallisation from ethanol (3.50 g, 93% yield). The product is a pale yellow solid.

Mass Spectrum (ESI): m/z = 399 [M+Na]

^{1}H NMR (300 MHz), CDCl$_3$, 298K): δ 8.71 (2H, d, J = 3.9 Hz, 6py), δ 8.63 (2H, s, J = H$_{im}$), δ 8.22 (2H, d, J = 7.0 Hz 3py), δ 7.82 (2H, td, J = 8.3, 1.9, 0.6 Hz, 4py), δ 7.40 (2H, ddd, J = 7.6, 4.9, 1.2 Hz, 5py), δ 7.30 (8H, m, Ph$_a$ and Ph$_b$), δ 4.08 (2H, s, CH$_2$)

Synthesis of the triple stranded iron helicate [Fe$_2$(L)$_3$]Cl$_4$

Ligand (3.0g, 0.008 mol) was dissolved in methanol (400 ml). Iron (II) chloride tetrahydrate (1.06 g, 0.005 mol) was then added to the solution and the resulting solution was brought to reflux at 65°C for 3 hours. The solution was then taken to dryness *in vacuo*. The crude product was then dissolved in minimal amounts of methanol (10 ml) and excess methanolic ammonium hexafluorophosphate added. The resulting precipitate was collected by filtration and washed with water (2 x 10 ml) and then diethyl ether (5 x 25 ml). The filtrate was then suspended in methanol and stirred with Dowex until the product had dissolved. The Dowex was then filtered off. The filtrate was taken to dryness *in vacuo*, and then redissolved in a minimum amount of methanol. Excess diethyl ether was added until the product precipitates, the final product was filtered and washed with ether and dried (1.65g, 59.7%). The final product was a crystalline purple solid.

Mass Spectrum (ESI): m/z = 425.5 [Fe$_2$L$_3$]Cl^{3+} , 310 [Fe$_2$L$_3$]$^{4+}$

^{1}H NMR (300 MHz), CD$_3$OD, 298K): δ 9.13 (2H, s, H$_{im}$), δ 8.71 (2H, d, J = 7.2 Hz, 6py), δ 8.48 (2H, t, J = 7.8, 3py), δ 7.84 (2H, ddd, J = 5.6, 4py), δ 7.44 (2H, d, J = 5.2, 5py), δ 7.05 (4H, broadened, Ph$_{a/b}$), δ 5.62 (4H, broadened, Ph$_{a/b}$), δ 4.07 (2H, s, CH$_2$)

UV-Vis (H$_2$O), λ$_{max}$ (ε$_{max}$/dm^{3}mol^{-1}cm^{-1}) 584 (16900) nm

Radiolabelling of Oligonucleotides

A mixture of 9.6 µl of MilliQ water, 2 µl of 10x T4 polynucleotide kinase buffer (New England Biolabs), 2 µl of bacteriophage T4 polynucleotide kinase (New England Biolabs) , 2.4 µl of 100 µM of oligonucleotide and 4 µl of ^{32}P ATP (6000 Ci/mmol – Perkin Elmer) was added to a 1.5 mL eppendorf. The mixture was vortexed gently (2secs), centrifuged (3000

rpm, 5 secs) and then incubated at 37 °C for 1 hour. The enzyme was then deactivated by heating to 80 °C for 3 minutes. The labelled oligonucleotide was then purified by adding 200 µl of PNI Buffer (QIAquick nucleotide removal kit) and the total solution transferred to a QIAquick 2 ml spin column. It was then centrifuged at 6000 rpm for one minute. The spin column was transferred to a new collection tube and 500 µl of PE buffer was added. The tube was again spun at 6000 rpm for 1 minute. This wash was repeated followed by centrifugation at 13000 rpm for 1 minute to remove all buffer and pellet the DNA in the tube fully. 24 µl of ultrapure water was added to the tube and left for 5 minutes. The labelled DNA strand was then centrifuged from the tube into an eppendorf at 13000 rpm for 2 minutes to obtain a 10 µM stock solution of radiolabelled oligonucleotide.

Preperation of non-denaturing Polyacrylamide Gel for electrophoresis

Two glass plates for vertical electrophoresis were placed on top of one another, the smaller on top of the larger. The plates were separated with plastic spacers each side. The plates were held together with 4 bulldog clips or set in a Bio Rad casting chamber depending on the size of the plates. The desired percentage of 30% 37.5:1 Acrylamide to Bisacrylamide (National Diagnostics) was created by diluting with TB buffer and deionised water up to 50 mL in a falcon tube (final buffer concentration of 89 mM Tris base, 89 mM Boric acid, pH 8.3). A freshly made 10% ammonium persulphate solution was then added (232 µl), followed by 25 µl of TEMED. The falcon tube was mixed carefully by inversion to disperse any air bubbles. Using a 50 ml pipette and pipette gun, the gel solution was transferred into the glass plates. The gel was left to set fully (approximately 45 mins). The set gel was then wrapped in paper

towel soaked in deionised water and then cling film to prevent the edges of the gel drying out, before being refrigerated until needed.

Competition PAGE Experiment

Three 14-mer reverse phase HPLC purified DNA oligonucleotides (Eurofins) of sequence:

S1: CGGAACGGCACTCG (radiolabelled)

S2: CGAGTGCAGCGTGG

S3: CCACGCTCGTTCCG

were mixed in stoichiometric quantities in TBN buffer (9µl) (89 mM tris base, 89 mM boric acid, 100 mM NaCl, pH 8.0) to a final concentration of 0.4 µM per strand, competition DNA (sequences below) and iron cylinder (1µl) were mixed in also to a final concentration of 0.4 µM (10µl final). The order these were mixed depended on the experiment (A = competition DNA last, B = Cylinder last, C = 3WJ DNA last). Before the final component was added, solutions were incubated for 1 hour and a further 30 mins on addition of final component, all at room temperature. 5 µl of 30% glycerol was then added to each sample to help the sample sink into the gel wells whilst in buffer. Samples were then loaded onto a 15% non-denaturing polyacrylamide gel and run at 11v/cm for 3 hours. The gel was then exposed to a phosphor plate and imaged on a molecular imager and the image quantified using Quantity One software (Bio-Rad).

Competitor DNA sequences (5'-3'):

ssDNA (single stranded DNA – 55 mer):

ACATTCCTAAGTCTGAAACATTACAGCTTGCTACACGAGAAGAGCCGCCATAGTA

DS26 (double stranded DNA – x2 = 26 bp):

CCTTCACGCGAACGTAATCCTAGGATTACGTTCGCGTGAAGG

hTelo (Human telomeric guanine quadruplex – 22 mer):

AGGGTTAGGGTTAGGGTTAGGG

c-MYC (c-MYC promotor guanine quadruplex – 22 mer):

TGAGGGTGGGTAGGGTGGGTAA

TAR RNA (Trans-activation response element RNA in HIV virus – 31 mer):

GGCCAGAUCUGAGCCUGGGAGCUCUCUGGCC

PuC19 Plasmid

Tet (DNA tetrahedron – 220 bp)

Composition of preparation detailed below

All competitor DNA (aside from Tet and Puc19 plasmid) was annealed by heating to 90°C for 5 mins followed by cooling on ice to ensure correct structure. All sequences purchased from Eurofins.

Structures of competitor DNA with secondary structure shown below.

c-MYC[26]:
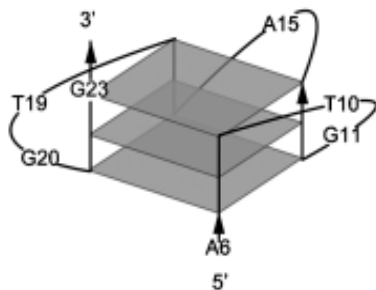
hTelo[27]:
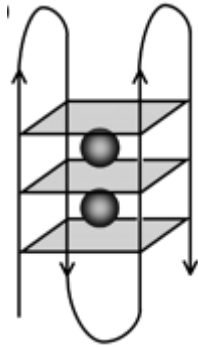
TAR RNA[28]:
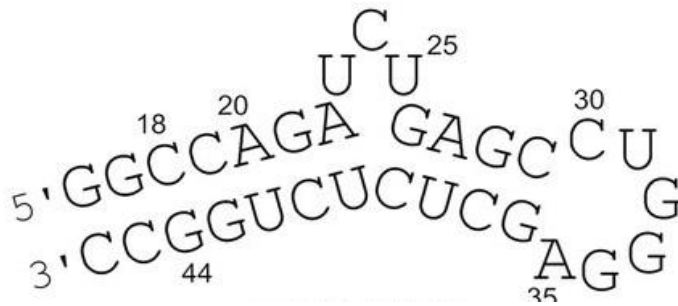
Construction of DNA Tetrahedron

Stoichiometric amounts of each of 4 HPLC purified oligonucleotides (Eurofins) of sequences:

17T1:

ACATTCCTAAGTCTGAAACATTACAGCTTGCTACACGAGAAGAGCCGCCATAGTA

17T2:

TATCACCAGGCAGTTGACAGTGTAGCAAGCTGTAATAGATGCGAGGGTCCAATAC

17T3:

TCAACTGCCTGGTGATAAAACGACACTACGTGGGAATCTACTATGGCGGCTCTTC

17T4:

TTCAGACTTAGGAATGTGCTTCCCACGTAGTGTCGTTTGTATTGGACCCTCGCAT

were mixed in TM buffer (10mM Tris base, 5mM $MgCl_2$, pH 8) (max concentration of 1 µM per strand) in an Eppendorf. The mixture was then heated to 95 °C in a thermal block for 5 minutes. On cooling at room temperature for 30 seconds, the Eppendorf was placed on ice for 5 minutes and then centrifuged for 5 seconds. The product was then purified and concentrated to desired concentration in a 30K MWCO filter (Pierce).

Tetrahedron Gel Electrophoresis

Tetrahedron samples (17T1 radiolabelled) (1 µM) were prepared in 1.5 ml Eppendorfs in 1 x TM Buffer (10mM Tris base, 5mM $MgCl_2$, pH 8) and cylinder added to achieve the desired ratios. The samples were incubated at room temperature for 60 minutes and then on ice for 10 minutes. 5 µl of 30% glycerol was then added to each sample to help the sample sink into the gel wells whilst in buffer. The samples were then loaded into separate lanes on a 10% non-denaturing polyacrylamide gel in the desired order. 10µl of gelpilot™ (Qiagen) was added to the adjacent wells to the samples to track the progress of the experiment. The gels were run at a constant 11V/cm of gel at room temperature for 5 hours. The gel was extracted from the glass plates using a sheet of Whatman paper and wrapped in clingflim. The gel was placed inside a developing cassette with a white phosphor film placed over for 1 hour. The phosphor film was imaged using a molecular imager to produce an autoradiogram.

Dynamic Light Scattering – DLS

DNA tetrahedron samples were prepared and diluted to 100 nm with iron cylinder to achieve ratios of 0:1, 2:1, 4:1, 6:1 and 8:1 relating to concentrations of 0, 200, 400, 600 and 800 nM respectively before being passed through a 1 µM syringe filter (Pall). Samples were incubated

at room temperature for 1 hour and then on ice for 1 mins. The samples (1 ml) were then transferred to separate disposable sizing cuvettes and then scanned on a Malvern Zetasizer nano for a total of 60 runs (3 x 20) to provide a size by number distribution.

Atomic Force Microscopy – AFM

All atomic force microscopy was performed in Singapore by Dr Wang Liyang in the labs of Prof. Shao Fengwei at Nanyang Technological University. AFM images were obtained on a Bruker Multimode 8 SPM equipped with a liquid cell.

Freshly cleaved mica was treated with 0.1 % (v/v) APTES ((3-Aminopropyl) triethoxysilane) aqueous solution for 10 mins to make the surface positively charged, and then washed with 2 mL ultrapure water and dried by compress nitrogen. 35 uL of DNA tetrahedron (or tetrahedron-cylinder conjugate at 1:4) solution was dropped onto the mica surface to incubated for 5 min. Then the sample was ready for measurement under the ScanAsyst in fluid mode with the SNL-10 probe (Bruker).

UV-Vis Stabalisation

Two iron cylinder solution of identical concentration ($60 \mu M$), one alone and one bound to DNA tetrahedron at a ratio of 4:1 cylinder to tetrahedron. Samples were incubated in a 1 cm path length UV cuvette (Starna) at room temperature for 1 hour before the absorbance of each solution was recorded at 573 nm for time point 0. The solutions were then incubated at the temperature for the experiment and the absorption recorded at set time points. All UV-vis experiments were performed in a Varian Cary 5000 spectrometer and elevated temperature runs were also performed in this with a Varian Cary temperature controller.

Seperation of the iron cylinder enantiomers

A slurry of Cellulose powder (Sigma Aldrich – column chromatography grade) (8.00g) and 0.2M NaCl solution (45 mL) was stirred into a beaker before being added to a 2x40 cm sintered glass column. Bellows were used to apply pressure to pack the cellulose in the column. Approximately 20 mL of extra 0.2M NaCl solution was added over the next hour to ensure the cellulose never went dry during the packing process. Once the cellulose was fully packed and the top of the cellulose was exposed. $[Fe_2L_3]^{4+}$ (0.05g) was dissolved in 0.2M NaCl solution (0.75 mL). Using a glass pipette, the sample solution was very carefully loaded onto the cellulose, ensuring no sample was accidently applied to the sides of the glass. Pressure was then applied to push all the sample solution into the cellulose and re-expose the top. Approximately 3 cm of sand was then added to protect the top of the cellulose. 0.2 NaCl solution can then be freely added to fully eluate the column under pressure. Two purple bands could be visibly distinguished and were collected as two separate fractions. The fractions were then freeze dried, re-dissolved in methanol and de-salted separately through a G25 Sephadex column using methanol as the eluent. The samples were then taken to dryness *in vacuo*. Column was repeated until enantiomer samples of sufficient purity were observed by CD and chiral shift reagent NMR

Circular Dichroism of enantiomers

Each enantiomer was dissolved in 50mM Tris.HCl buffer (pH 8.0) to a concentration of 15 μM as established by UV-Vis at 573 nm (ε=16900) and placed inside a 1 cm path length cuvette (starna). A Chirascan plus spectrometer (Applied Photophysics) was then used to scan the cuvette using the following parameters; Mode: Circular Dichroism in millidegrees,

Bandwidth: 1 nm, Response: 1 secs, Temperature: 25°C, accumulations: 4, Wavelength range 200-800 nm. Data was collected and the 4 accumulations averaged to provide the presented spectra.

^{1}H NMR of enantiomers with Δ-TRISPHAT

Enantiomers M and P along with a racemic mixture were dissolved to a concentration of 500 μM in MeOD (0.75 mL, Cambridge isotope labs). Δ-TRISPHAT tetrabutylammonium salt (sigma) (0.38 mgs) was then added to each sample to produce a molar ratio of 1:1. The NMR was run on an AVII-300 300 mHZ NMR.

2.5 References

1.   I. Meistermann, V. Moreno, M.J. Prieto, E. Moldrheim, E. Sletten, S. Khalid, P.M. Rodger, J.C. Peberdy, C.J. Isaac, A. Rodger, and M.J. Hannon, *Intramolecular DNA coiling mediated by metallo-supramolecular cylinders: differential binding of P and M helical enantiomers.* Proceedings of the National Academy of Sciences of the United States of America, 2002. **99**(8): p. 5069-74.

2.   L. Cerasino, M.J. Hannon, and E. Sletten, *DNA Three-Way Junction with a Dinuclear Iron(II) Supramolecular Helicate at the Center: A NMR Structural Study.* Inorganic Chemistry, 2007. **46**(16): p. 6245-6251.

3.   M.J. Hannon, V. Moreno, M.J. Prieto, E. Moldrheim, E. Sletten, I. Meistermann, C.J. Isaac, K.J. Sanders, and A. Rodger, *Intramolecular DNA Coiling Mediated by a Metallo-Supramolecular Cylinder.* Angewandte Chemie, 2001. **113**(5): p. 903-908.

4.   M.J. Hannon, V. Moreno, M.J. Prieto, E. Moldrheim, E. Sletten, I. Meistermann, C.J. Isaac, K.J. Sanders, and A. Rodger, *Intramolecular DNA Coiling Mediated by a Metallo-Supramolecular Cylinder.* Angewandte Chemie International Edition, 2001. **40**(5): p. 879-884.

5.   G.I. Pascu, A.C.G. Hotze, C. Sanchez-Cano, B.M. Kariuki, and M.J. Hannon, *Dinuclear Ruthenium(II) Triple-Stranded Helicates: Luminescent Supramolecular Cylinders That Bind and Coil DNA and Exhibit Activity against Cancer Cell Lines.* Angewandte Chemie, 2007. **119**(23): p. 4452-4456.

6.   A.C.G. Hotze, N.J. Hodges, R.E. Hayden, C. Sanchez-Cano, C. Paines, N. Male, M.-K. Tse, C.M. Bunce, J.K. Chipman, and M.J. Hannon, *Supramolecular Iron Cylinder with Unprecedented DNA Binding Is a Potent Cytostatic and Apoptotic Agent without Exhibiting Genotoxicity.* Chemistry & Biology, 2008. **15**(12): p. 1258-1267.

7.   J. Malina, M.J. Hannon, and V. Brabec, *Interaction of Dinuclear Ruthenium(II) Supramolecular Cylinders with DNA: Sequence-Specific Binding, Unwinding, and Photocleavage.* Chemistry – A European Journal, 2008. **14**(33): p. 10408-10414.

8.   J. Malina, M.J. Hannon, and V. Brabec, *Recognition of DNA bulges by dinuclear iron(II) metallosupramolecular helicates.* FEBS Journal, 2014. **281**(4): p. 987-997.

9.   J.M.C.A. Kerckhoffs, J.C. Peberdy, I. Meistermann, L.J. Childs, C.J. Isaac, C.R. Pearmund, V. Reudegger, S. Khalid, N.W. Alcock, M.J. Hannon, and A. Rodger, *Enantiomeric resolution of supramolecular helicates with different surface topographies.* Dalton Transactions, 2007(7): p. 734-742.

10.   M.J. Hannon, I. Meistermann, C.J. Isaac, C. Blomme, J.R. Aldrich-Wright, and A. Rodger, *Paper: a cheap yet effective chiral stationary phase for chromatographic resolution of metallo-supramolecular helicates.* Chemical Communications, 2001(12): p. 1078-1079.

11.   I. Meistermann, V. Moreno, M.J. Prieto, E. Moldrheim, E. Sletten, S. Khalid, P.M. Rodger, J.C. Peberdy, C.J. Isaac, A. Rodger, and M.J. Hannon, *Intramolecular DNA coiling mediated by metallo-supramolecular cylinders: Differential binding of P and M helical enantiomers.* Proceedings of the National Academy of Sciences of the United States of America, 2002. **99**(8): p. 5069-5074.

12.   A. Oleksi, A.G. Blanco, R. Boer, I. Usón, J. Aymamí, A. Rodger, M.J. Hannon, and M. Coll, *Cover Picture: Molecular Recognition of a Three-Way DNA Junction by a Metallosupramolecular Helicate (Angew. Chem. Int. Ed. 8/2006).* Angewandte Chemie International Edition, 2006. **45**(8): p. 1167-1167.

13.   R.P. Goodman, R.M. Berry, and A.J. Turberfield, *The single-step synthesis of a DNA tetrahedron.* Chemical Communications, 2004(12): p. 1372-1373.

14.   C.M. Erben, R.P. Goodman, and A.J. Turberfield, *Single-molecule protein encapsulation in a rigid DNA cage.* Angewandte Chemie International Edition, 2006. **45**(44): p. 7414-7.

15. A.S. Walsh, H. Yin, C.M. Erben, M.J.A. Wood, and A.J. Turberfield, *DNA Cage Delivery to Mammalian Cells.* ACS Nano, 2011. **5**(7): p. 5427-5432.

16. J. Malina, M.J. Hannon, and V. Brabec, *Recognition of DNA Three-Way Junctions by Metallosupramolecular Cylinders: Gel Electrophoresis Studies.* Chemistry – A European Journal, 2007. **13**(14): p. 3871-3877.

17. A. Rath, M. Glibowicka, V.G. Nadeau, G. Chen, and C.M. Deber, *Detergent binding explains anomalous SDS-PAGE migration of membrane proteins.* Proceedings of the National Academy of Sciences of the United States of America, 2009. **106**(6): p. 1760-5.

18. S.F. Zakharov, H.T. Chang, and A. Chrambach, *Reproducibility of mobility in gel electrophoresis.* Electrophoresis, 1996. **17**(1): p. 84-90.

19. J.L. Kadrmas, A.J. Ravin, and N.B. Leontis, *Relative stabilities of DNA three-way, four-way and five-way junctions (multi-helix junction loops): unpaired nucleotides can be stabilizing or destabilizing.* Nucleic Acids Research, 1995. **23**(12): p. 2212-2222.

20. Y. He, T. Ye, M. Su, C. Zhang, A.E. Ribbe, W. Jiang, and C. Mao, *Hierarchical self-assembly of DNA into symmetric supramolecular polyhedra.* Nature, 2008. **452**(7184): p. 198-201.

21. K.R. Kim, D.R. Kim, T. Lee, J.Y. Yhee, B.S. Kim, I.C. Kwon, and D.R. Ahn, *Drug delivery by a self-assembled DNA tetrahedron for overcoming drug resistance in breast cancer cells.* Chemical Communications, 2013. **49**(20): p. 2010-2012.

22. A. Trache and G.A. Meininger, *Atomic force microscopy (AFM).* Current Protocol Microbiology, 2008. **2**(2).

23. A. Engel, Y. Lyubchenko, and D. Müller, *Atomic force microscopy: a powerful tool to observe biomolecules at work.* Trends in Cell Biology, 1999. **9**(2): p. 77-80.

24. B. Franck, *Optical Circular Dichroism. Principles, Measurements, and Applications. Von L. Velluz, M. Legrand und M. Grosjean, übers. von J. MacCordick. Verlag Chemie GmbH.,*

Weinheim/Bergstr., und Academic Press, New York-London, 1965. XII, 247 S., 149 Abb., 10 Tab., geb. DM 40.–. Angewandte Chemie, 1965. **77**(19): p. 875-875.

25.   J. Lacour, C. Ginglinger, F. Favarger, and S. Torche-Haldimann, *Application of TRISPHAT anion as NMR chiral shift reagent.* Chemical Communications, 1997(23): p. 2285-2286.

26.   T.M. Ou, Y.J. Lu, J.H. Tan, Z.S. Huang, K.Y. Wong, and L.Q. Gu, *G-quadruplexes: Targets in anticancer drug design.* Chemmedchem, 2008. **3**(5): p. 690-713.

27.   J.L. Huppert, *Four-stranded DNA: cancer, gene regulation and drug development.* Philosophical Transactions of the Royal Society A: Mathematical, Physical and Engineering Sciences, 2007. **365**(1861): p. 2969-2984.

28.   J. Malina, M.J. Hannon, and V. Brabec, *Iron(II) supramolecular helicates interfere with the HIV-1 Tat–TAR RNA interaction critical for viral replication.* Scientific Reports, 2016. **6**: p. 29674.

Chapter 3

Biological Activity of the Iron Cylinder-DNA Tetrahedron conjugate

3.1 Introduction

The iron cylinder, with its unprecedented DNA binding, differs dramatically from traditional DNA binders, such as members of the cisplatin drug family; cisplatin carboplatin, oxaliplatin and nedaplatin. These platins are still used today in the clinic despite decades of research in the field,[1] and it is estimated that between 50-70% of all cancer patients will be treated by platinum drugs throughout their therapy.[2] For this reason it was interesting to explore the biological activity of the iron cylinder; to see whether the promising and very different DNA binding would translate to in-vitro cytotoxic effects in cancer cell lines. Research from the Hannon group[3] showed potent action against a range of cell lines (Table 3.1) with comparable IC_{50} values (concentration of compound required to inhibit cellular growth and viability by 50%) to those of cisplatin.

CELL TYPE:	HBL100 (BREAST)	T47D (BREAST)	SKOV3 (OVARIAN)	HL-60 (LEUKEMIA)	MRC5 (LUNG)
IRON CYLINDER (μM)	27 ± 5	52 ± 10	35 ± 5	18 ± 3	19 ± 3
CISPLATIN (μM)	4.9 ± 0.3	28 ± 1.7	6 ± 0.3	7 ± 1	<3

Table 3.1 - Table from reference 3, showing IC_{50} values (μM) at 72 hours on various cell lines for the Iron cylinder compared with cisplatin. ± SD (n=3).

The research also showed that the iron cylinder was non-genotoxic, meaning that is does not cause any DNA strand breaks during its interaction with the cells in a comet assay (Table 3.2).[3] This is important as genotoxic DNA damage, whilst it can contribute to cell apoptosis, can also lead to mutations which can then go on to cause cancer,[4] which if the original aim was to treat the cancer, would be known as secondary cancer and is clearly an undesirable attribute in a potential drug. This is the case with certain current chemotherapy agents such as

cisplatin[5] and gemcitabine (a cytidine analogue).[6] Overall, the iron cylinder was shown to have very interesting biological activity.

IRON CYLINDER (µM)	MRC5 (LUNG)	HBL100 (BREAST)	HL-60 (LEUKEMIA)
0	1.43 ± 0.82	4.89 ± 3.84	0.27 ± 0.15
5	2.18 ± 0.12	8.93 ± 4.07	0.40 ± 0.51
10	2.54 ± 0.47	6.16 ± 4.41	0.39 ± 0.47
15	2.31 ± 0.57	6.29 ± 4.17	0.45 ± 0.39
20	1.86 ± 0.44	6.48 ± 2.46	1.95 ± 2.33
25	2.32 ± 0.22	ND	ND

Table 3.2 - Table from reference 3. The results represent tail DNA % ± SD (n = 3) of three independent experiments. There was no statistically significant effect of cylinder treatment (24 hr) at any of the concentrations investigated in any cell line studied. ND, not determined because 25 µM, 24 hr was toxic to these cell lines.

The previous chapter focussed on the interaction between the iron cylinder and DNA tetrahedron. The tetrahedron itself has also been reported to have interesting biological properties in that it is readily taken up by cells.[7] This led to proposals suggesting that the DNA tetrahedron could be used for drug delivery applications due to its hollow central cavity able to hold a cargo, such as the protein cytochrome c (Figure 3.1A),[8] or a single transcription protein (figure 3.1B).[9] Successful drug delivery of doxorubicin has been reported with the DNA tetrahedron,[10] which was reported to overcome drug resistance due to an altered uptake mechanism which meant developed cellular metabolism resistance was by-passed. With these interesting biological properties, it would be interesting to study the combined biological effects of the cylinder-tetrahedron conjugate.
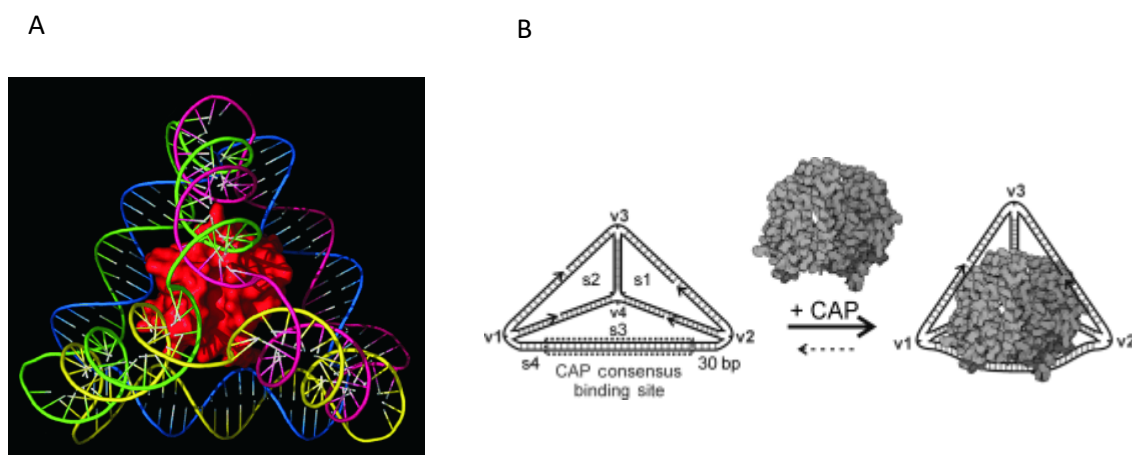
Figure 3.1 - A: DNA tetrahedron containing the protein cytochrome c, covalently bound to the inner cavity. B: catabolite activator protein (CAP) encapsulated non-covalently by using a DNA recognition site for the protein to bind to. A taken from reference 8, B taken from reference 9.

This chapter aims to study the tetrahedron cellular uptake, localisation and toxicity of the cylinder conjugate. The chapter aims to also pave the way for further research using the cylinder binding effect of collapsing the tetrahedron into a smaller structure for triggering the release of an internal cargo by proving the compatibility of the conjugate inside cells.

3.2 Results and Discussion

3.2.1 Cellular Uptake

The iron cylinder enters cells readily[11] to exhibit strong cytotoxic effects across a broad range of cell lines.[3] It is interesting to explore whether the iron cylinder, when bound to the DNA tetrahedron, would still be taken up by cells and whether this uptake would be altered in any way from previous reports of tetrahedron uptake. It would also be interesting to see any changes in the effect of the cylinder on the cells when delivered by the DNA tetrahedron. To study this, the conjugate and the tetrahedron alone were subjected to various in-vitro

experiments on cancer cell lines to determine the behaviour of each and if they differ in any way.

3.2.2 Flow Cytometry

One commonly used technique to observe cellular uptake of a drug is by flow cytometry. For this technique, the drug must be fluorescent for it to be observed inside the cell. The technique itself involves passing a suspension of cells through an electronic cell counter one by one, which excites each cell with a laser at a chosen wavelength so that the emission intensity of the fluorescent complex inside each counted cell can be recorded. This effectively and efficiently produces data on how many treated cells have taken up the analyte. The machine can then go on to sort the cells based on their fluorescent output. Figure 3.2 shows a schematic diagram of a flow cytometer in action.[12]
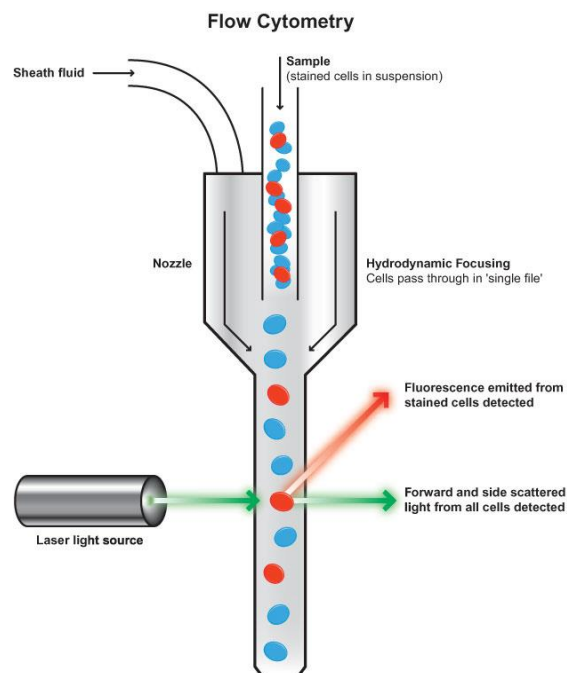

Figure 3.2 – Schematic diagram representing a flow cytometer exciting fluorescently tagged cells via an external light source. Taken from reference 12.

To utilise flow cytometry for cellular uptake, the conjugate would first have to be made fluorescent for it to be observable by the detector. Due to the ease of functionality of DNA, this was achieved by purchasing one of the construction strands of the tetrahedron, labelled with Cyanine-5 (Cy5). Cy5 is a fluorescent dye which emits in the far red end of the spectrum with an emission maximum at 666 nm. The tetrahedron can then be synthesised as before to form a Cy5 labelled tetrahedron, following a previously reported method.[7]

Three samples of HeLa cells were then incubated with the cylinder, labelled tetrahedron, and with the labelled tetrahedron - cylinder conjugate for 24 hours and analysed using flow cytometry. Figure 3.3 shows the cellular uptake with and without the presence of the cylinder on the tetrahedron by measuring the Cy5 emission of each cell at 670 nm. Three identical separate repeats of this experiment were performed, counting 10,000 cells in each sample cycle. The forward and side scatter of a control sample of HeLa cells in each repeat experiment was manually gated and this gate applied to all subsequent fluorescent measurements of that repeat set to remove any dead cells or large material that will pass through the flow cytometer that should not be included in the data interpretation as they cannot be considered viable cells.

From this, it can be seen that the uptake of the tetrahedron over 24 hours is extensive with 94% of the gated cells emitting a Cy5 signal when treated with the Cy5 tetrahedron. 95% of cells emitted a Cy5 signal when treated with the Cy5-conjugate, showing there is no statistically significant difference between the two. Both the no treatment control and the cells treated with just cylinder resulted in a very low amount of emission in this window, which is expected and has been attributed to auto-fluorescence from the cell. Interestingly, the uptake is almost identical for the tetrahedron with or without the cylinder bound to it. It might have been anticipated that the positively charged cylinder would negate some of the negative

charge on the DNA and help the conjugate pass through the negatively charged cell membrane. This is not the case, however, initially suggesting that the tetrahedron is actively up-taken through endocytosis as previously proposed, as it seems unlikely that this amount of tetrahedron would be able to enter the cells by passive diffusion due to the negative charge on DNA with is consistent with previous research.[13] The intensity of the Cy5 peak of the histograms of the treated cells is also very similar. This suggests that roughly an equal amount of the tetrahedra are taken up, regardless of cylinder presence. Whilst this experiment shows a good indicator of overall cellular uptake, it does not give any idea of cellular localisation.
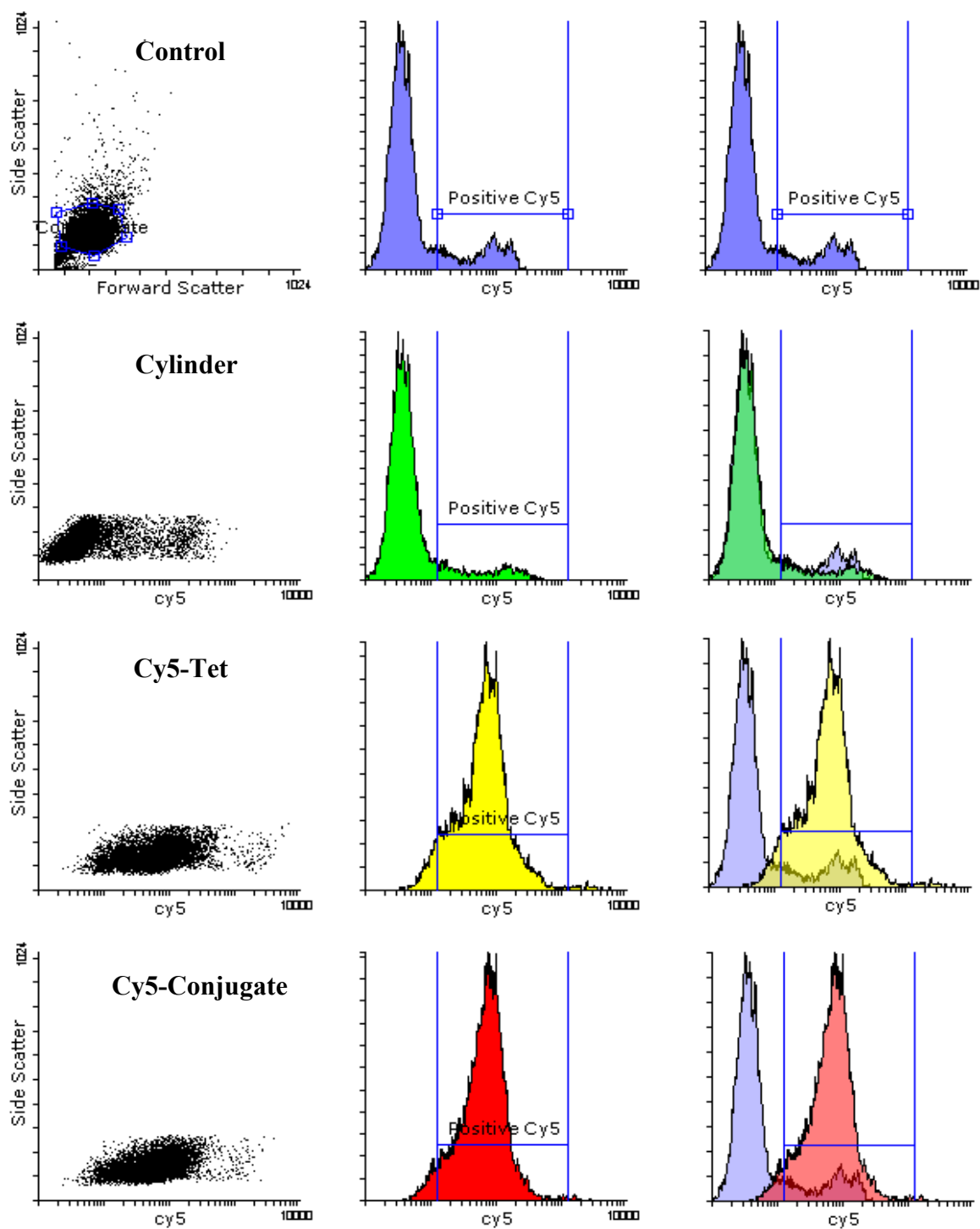
|	CY5 POSITIVE: %
CONTROL	17.0
CYLINDER	13.0
CY5-TETRAHEDRON	93.7
CY5-CONJUGATE	94.8

Figure 3.3 - Flow cytometry data, left column showing dot plots of the samples with gated control at the top. Middle column – histogram distributions of Cy5 intensity. Right – Overlap of sample Cy5 intensity and non-treated control sample.

3.2.3 Confocal Microscopy

Exploiting the Cy5 label on the tetrahedron again, fluorescence microscopy can be a very powerful tool in analysing cellular localisation of a substance. Confocal microscopy works by exciting the sample with lasers of a chosen wavelength. A pinhole in the focal plane of the light then filters out the out of focus light, only allowing the image of the current level of focus through to the detector. This allows the user to build up a 3D profile of the analyte by taking snapshots of each level. This can be hugely effective for analysing localised cellular uptake of fluorescently tagged molecules and compounds.

In this experiment, HeLa cells were incubated with a relatively low concentration of Cy5-conjugate (2µM, 1:4 tetrahedron (2µM) : cylinder (8µM)) for time periods of 2 hours and 24 hours. The HeLa cells were then stained with Hoechst nuclear stain, staining the nucleus of the cells blue for visual reference and to help establish localisation of the Cy5. The cells were then fixed onto slides and imaged on a Nikon A1 inverted confocal microscope. Figure 3.4 shows the images obtained.
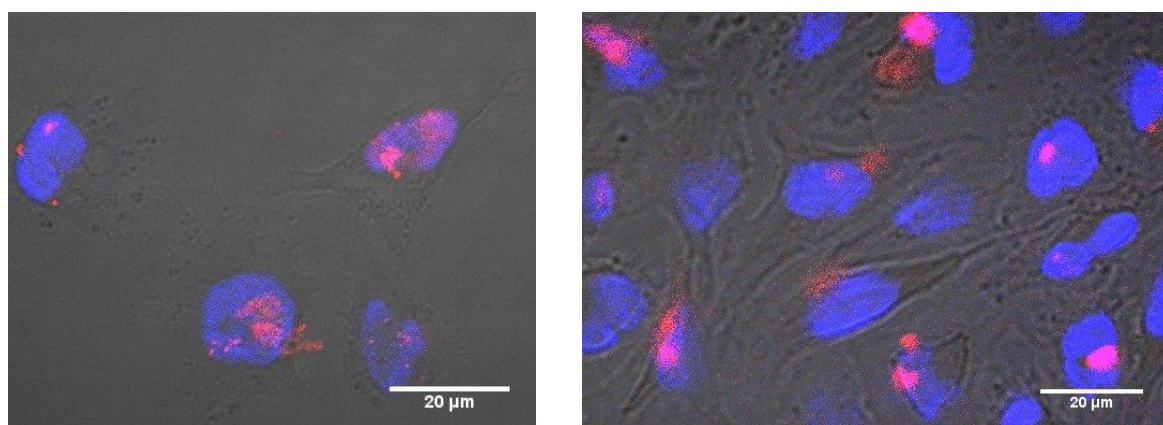

Figure 3.4 - Confocal fixed cell imaging showing cell uptake of Cy5-Conjugate after 2 hours (left) and 24 hours (right).

From this, it is clear to see that even after just 2 hours of incubation, the labelled conjugate is taken up into cells. This backs up previous analysis with flow cytometry that the conjugate is taken up by cells. Accumulation does appear to increase with time but only slightly and not in a linear fashion and further quantification of the fluorescent images would be needed to confirm this.

Attempting to distinguish localisation of the conjugate inside the cells from these images was challenging as it appears to be in some cell nuclei but not in others. To attempt to assess this, live cell imaging was performed to analyse localisation in cells in their natural state. Live cell imaging is useful here since fixing cells with formaldehyde could lead to analyte compound leaching through breached membranes that have become so during fixation, causing uncertainty as to original accumulation and localisation.

Cells were incubated in 3 cm Matek dishes with compound incubation times kept at 3 hours for all samples. Figure 3.5 shows the results obtained. By staining the cells with Hoechst nuclear stain, it was hoped that the degree of localisation in the nucleus could be quantified by a co-localisation calculation. However, the conjugate mainly accumulates in the cytoplasm and doesn't appear to be in specific areas here. Figure 3.5 is also in agreement with the previous flow cytometry experiment showing the uptake is largely unaffected whether the cylinder is present on the tetrahedron or not. To ascertain the localisation by confocal microscopy, further experimentation with different structural stains to see if significant co-localisation could be seen.
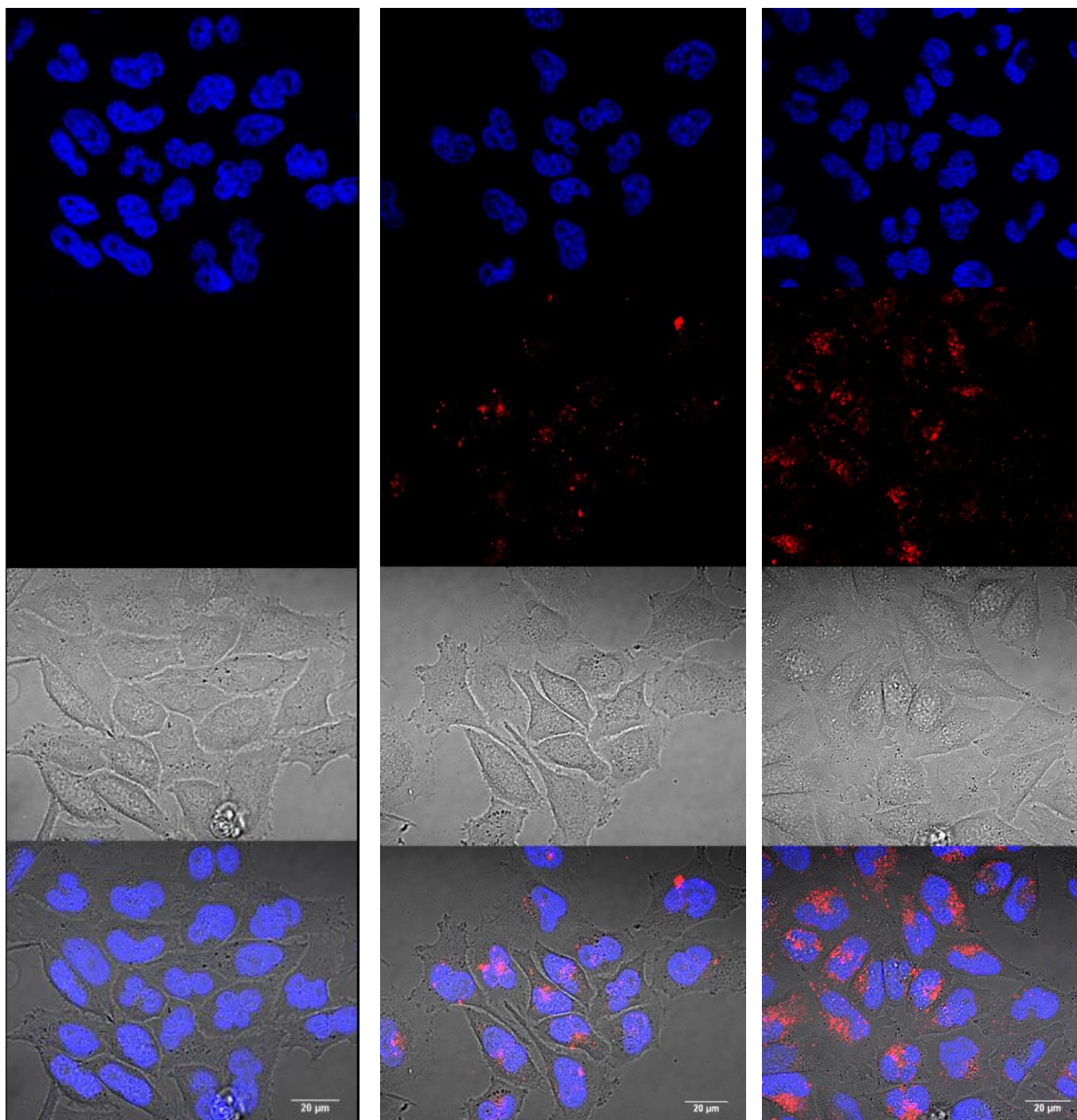
Figure 3.5 – Confocal image montages, Left, HeLa cells incubated with [Fe2L3]Cl4 (8 µM) and stained with Hoechst 33258 to visualise the blue nucleus. Centre, HeLa cells incubated with Cy5-Tetrahedron (2 µM) and stained again with Hoechst. Right, HeLa cells incubated with Cy5-Conjugate (4:1 cylinders to tetrahedron corresponding to 8 µM : 2 µM).

Another advantage of confocal microscopy is the ability to build up a 3D image of the cells. As the focal plane can be adjusted throughout a cell, images can be taken for each slice. This

helps to illustrate the complex is not simply accumulating on-top of the cell membrane instead of inside the cell. Combining the slices produces a Z-stack which builds up a 3D profile. Figure 3.6 illustrates this, presenting Cy5 signal throughout the cell and confirming complex presence inside the cell.
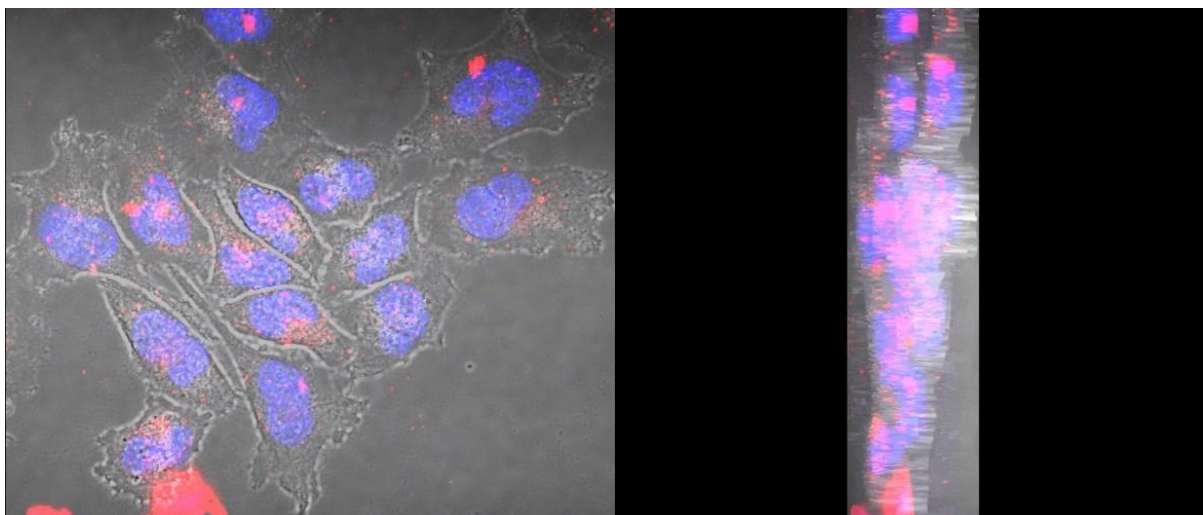
Figure 3.6 – Z-stack images combined to produce a 3D image showing red Cy5 inside the cell. Left – Front on view. Right – Side on view.

3.2.4 ICP-MS analysis

A further useful technique that can be utilised to ascertain cellular localisation is inductively coupled plasma mass spectrometry (ICP-MS). This technique is a quantitative variation of mass spectrometry which involves atomising a sample using an inductively coupled plasma created with Argon gas. The ionised sample is then separated into elements using quadrupoles and quantified in a connected mass spectrometer. This technique is highly sensitive and can detect elements (mainly metals) in a sample down to ppb quantities.[14]

This technique is useful as biological samples can be digested and analysed by ICP-MS. By separating the major structures of cellular samples, a process known as cell fractionation, it is

possible to analyse each fraction for presence of certain analyte metal ions and quantify them. Through this, it would be possible to quantify and compare cellular accumulation in the nucleus and the cytoplasm of the cell. Unfortunately, the presence of natural iron inside cells prevents quantitative iron analysis here, as it gives too high a background reading for accurate measurement. To get around this, the central metal ions in the cylinder need to be replaced. If the new cylinder binds in a similar fashion to the DNA tetrahedron, it could provide a similar model for cell accumulation that could be quantified with ICP-MS.

A cylinder with the same ligand structure, shape and size but with two ruthenium(II) ions in place of the iron was reported in the Hannon group in 2007.[15] Figure 3.7 shows the crystal structure obtained of the iron cylinder and the ruthenium cylinders (RuCy), illustrating the close-to-identical size and shape of the two molecules.[15,16,17]
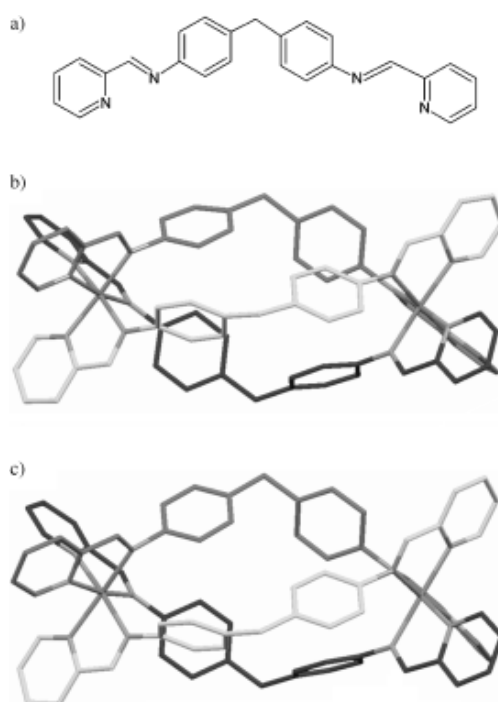
Figure 3.7 - A – The ligand (L) in the cylinders. B – Crystal structure of the iron cylinder $[Fe_2L_3]^{4+}$ and C – Crystal structure of the ruthenium cylinder $[Ru_2L_3]^{4+}$, Taken from reference 15.

The RuCy also shows very similar binding to the iron cylinder to DNA, causing supercoiling in linearized plasmid DNA.[15] To show the RuCy has similar binding to the tetrahedron and its building blocks, a PAGE gel was carried out, running iron cylinder with DNA tetrahedron building strands next to ruthenium cylinder and building strands. Figure 3.8 shows identical band shifts between the iron and the ruthenium, illustrating that the similar size and shape of the complexes shown by x-ray crystallography translates to similar binding to the tetrahedron. This indicates that the conjugates should be similar and therefore cylinder uptake into cells might be quantified by ICP-MS, scanning for ruthenium content.
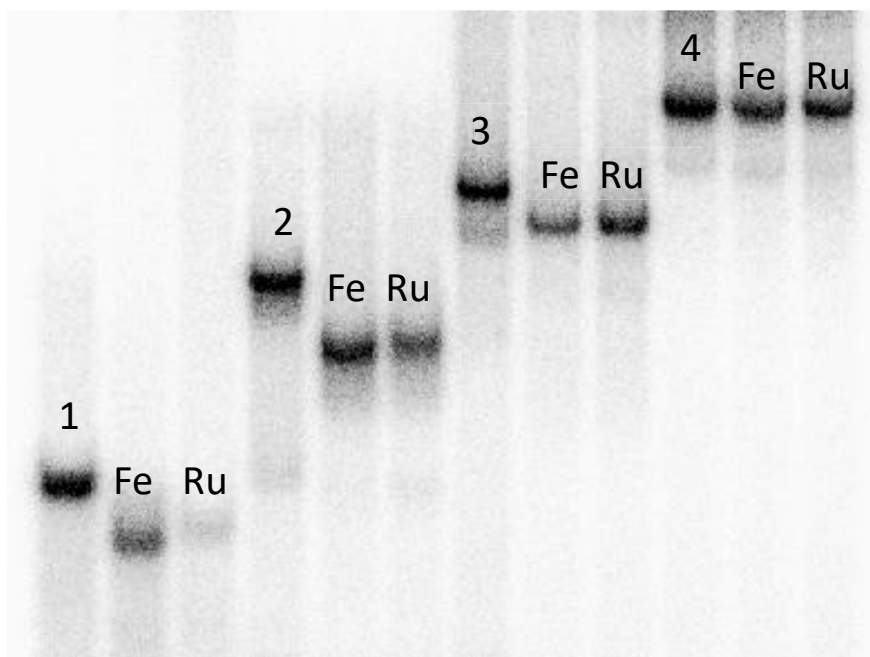
Figure 3.8 – Autoradiogram showing the building blocks of the DNA tetrahedron: lane 1 – strand 1 only, lane 2 – strands 1+2, lane 3 – strand 1+2+3, lane 4 – complete tetrahedron. Adjacent to each numbered lane is identical DNA incubated with iron or ruthenium cylinder as indicated.

HeLa cells were incubated with RuCy and RuCy-conjugate, followed by fractionation of the cells into nuclear and cytoplasmic fractions. ICP-MS was then use to ascertain the levels of ruthenium metal in each of the fractions and also be compared to a whole cell sample gathered. Figure 3.9 shows the results obtained from this ICP-MS experiment. The control cells show the base level of no ruthenium atoms detected in all fractions (a background). The cells treated with RuCy alone showed a positive amount of ruthenium in the whole cell fraction. It also showed that around a third of the RuCy is accumulated in the nuclear fraction whilst the rest is found in the cytoplasm. These results are encouraging as it shows that some of the cylinder is able to pass into the nucleus, the target for DNA binding drugs. The cells treated by the RuCy-tetrahedron conjugate showed a dramatic increase in Ruthenium content in the whole cell sample. This was a very positive result as it suggests that the cells, when actively up taking the tetrahedron, do so more effectively than the RuCy up take alone. This further champions the tetrahedrons case as a drug delivery vessel.
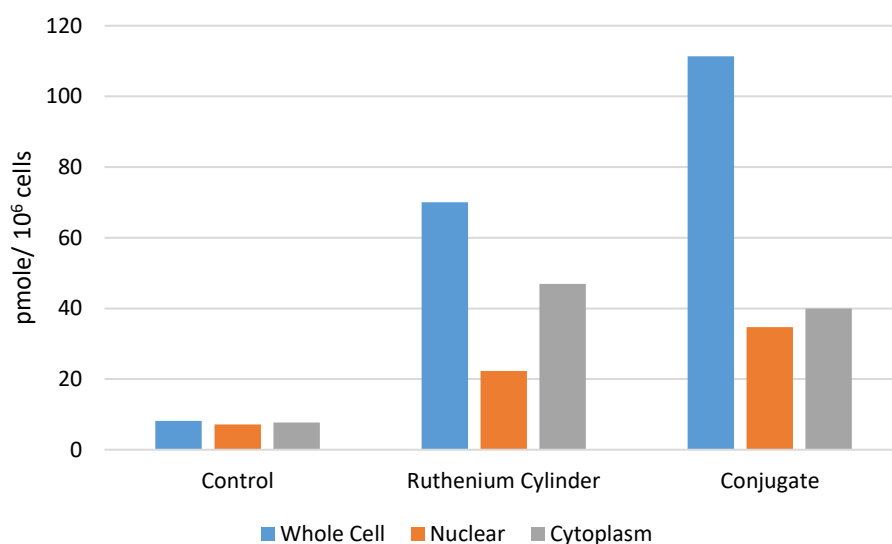
Figure 3.9 – ICP-MS data presenting Ruthenium content accumulated in whole cell, nuclear and cytoplasmic fractions when HeLa cells have been treated with Ruthenium cylinder with and with DNA tetrahedron.

Figure 3.9 also shows the nuclear accumulation is also increased by 75% from approximately 20 pmole/ 10^6 cells to approximately 35 pmole/ 10^6 cells. This must again be down to differing cellular uptake pathways and cell metabolism of the conjugate. A slightly unexpected result came from the cytoplasmic fraction which showed a decrease from the RuCy alone. This meant that the combined nuclear and cytoplasmic ruthenium content did not equal the whole cell sample. It could be suggested that the remaining ruthenium remains on the membrane of the cell, which would be in agreement with the endocytosis uptake of the conjugate as some would still be stuck on the membrane in this case. Further repeats of this experiment and analysis of the membrane fraction are required to fully come to this conclusion.

3.2.5 Cell Toxicity – MTT Assay

As discussed in the introduction, the cytotoxicity of the iron cylinder has been studied in depth.[3] Now that the cellular uptake of the cylinder-tetrahedron conjugate has been studied, it is important to see whether the cylinder's toxicity is maintained when delivered by tetrahedron. It is possible, as observed by other research groups, that the uptake mechanism can alter drug localisation and therefore cause an altered toxicity effect.[10] To study this, a very commonly used cell viability assay known as an MTT assay was employed. An MTT assay works by treating cells, post drug treatment, with a tetrazolium dye MTT (3-(4,5-dimethylthiazol-2-yl)-2,5-diphenyltetrazolium bromide) (Figure 12). The MTT salt, when inside the cell is reduced by NAD(P)H dependant oxidoreductase enzymes, located in cell mitochondria, to insoluble formazan (Figure 3.10). This formazan is deep purple in colour which is then dissolved in DMSO to produce a quantifiable purple solution that is then read by a spectrophotometer / plate reader.[18] This gives an indication of cell viability as more cells

produce more formazan which gives a higher absorption reading on the plate reader and vice-versa. This assay also allows for the calculation of the IC_{50} value.

(MTT: (3-(4,5-dimethylthiazol-2-yl)-2,5-diphenyltetrazolium bromide))

(2*E*,4*Z*)-(4,5-Dimethylthiazol-2-yl)-3,5-diphenylformazan

l_{max} 560 nm
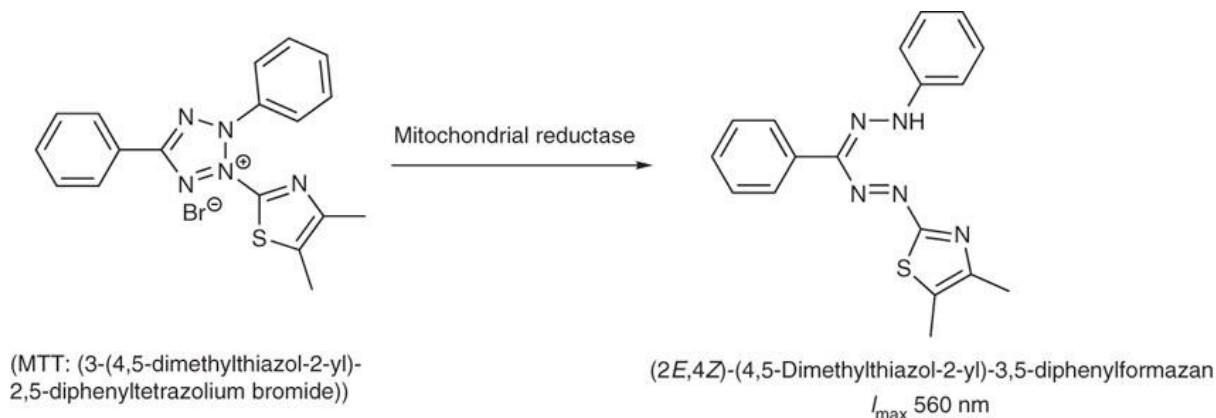
Figure 3.10 - Reaction scheme illustrating the reduction of MTT to form purple formazan. Taken from reference 18.

It is worth noting that there can be some doubt about the effectiveness of the MTT assay as a tool for assessing cell death. This is mainly because low mitochondrial activity doesn't necessarily confirm cell death; some cell lines exhibit low metabolism and thus low levels of mitochondrial activity and so would appear as 'non-viable' in the assay. In this case however, the control cells give a comparative reference of activity to the treated cells and the cell lines have been selected to ensure that the cell metabolism is high enough to be accurately measured in this assay.

Two cell lines were selected, HeLa, a cervical cancer cell line used throughout this chapter, and A2780, an ovarian cancer cell line; these cells were then treated with increasing concentrations of free cylinder and cylinder-tetrahedron conjugate. Cisplatin was also included in the treatments as a positive control as it is still considered to be the 'gold-standard' of chemotherapy drugs in use today.

Figure 3.11 shows the results obtained. In both cell lines, it is clear that the conjugate has a diminished toxicity when compared to free cylinder, though this is more dramatic in A2780 cells than in HeLa cells. This was not a totally surprising result as the cylinder is bound to DNA when on the tetrahedron, and so cellular DNA will have to compete with the tetrahedron for cylinder binding. This therefore means that less overall cylinder will be immediately available to bind to cellular DNA and cause apoptosis. Overall, the conjugate still maintained a potent amount of cell toxicity.

It is assumed that the cylinder, when bound to the tetrahedron, simply preferentially binds to cellular DNA due to its abundance. However, another hypothesis could be that the cylinder is not released to bind to genomic DNA until the tetrahedron is digested inside the cells. To test this, a tetrahedron was synthesised which was less susceptible to digestion. The full details of this will be discussed in chapter 4, but follows a previously reported protocol by Goodman *et al.*[19] Briefly, it involves phosphorylating all the construction oligos and ligating them together to form a tetrahedron with no nicks in the backbone. This makes it more resistant to digestion as many cellular enzymes can only initiate on the 5' or 3' end of DNA or DNA blunt ends.[20] As the ligated tetrahedron would have none, this should make it more resistant to digestion once inside the cell. If cell toxicity was further decreased when the cylinder was delivered by the ligated tetrahedron, it would indicate that cylinder is being released upon digestion of the tetrahedron and it is not delivered simply by shifting to a more preferential target amongst the cellular DNA. Figure 3.12 shows the MTT assay obtained when treating with the same cylinder concentration (25 μM) delivered by the original nicked tetrahedron and with the ligated un-nicked tetrahedron. From this, it can be seen that the cell viability post-treatment of both is identical and therefore cellular digestion of the tetrahedron is unlikely to be the mechanism of drug delivery in this case.

A2780
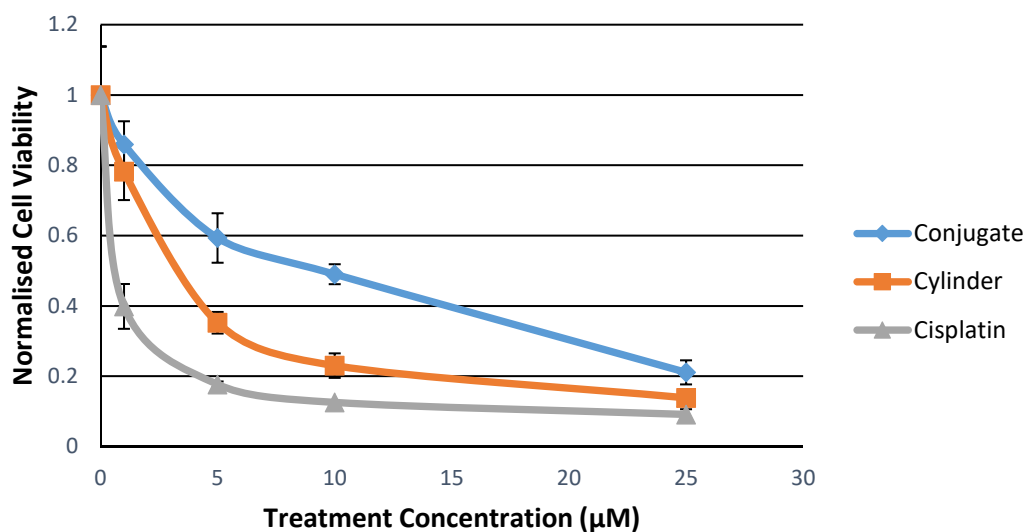
HeLa
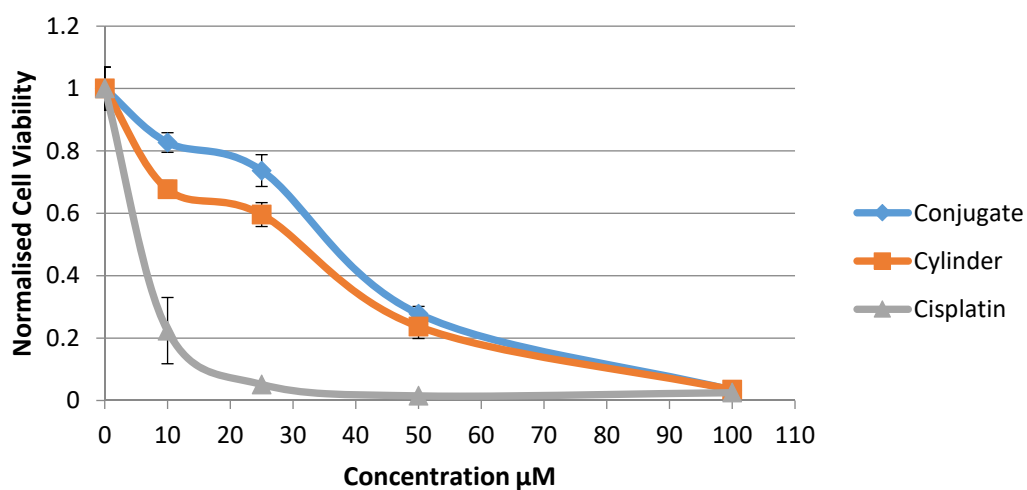
	HELA	A2780
IRON CYLINDER	37 ± 3	4.3 ± 0.7
CISPLATIN	5.6 ± 0.8	1.2 ± 0.3
CONJUGATE	39.7 ± 4.4	10.8 ± 2.4

Figure 3.11 - MTT assay results from 72 hours of indicated drug concentration treatment. Top – A2780 cell line, Bottom – HeLa cell line, table below presenting IC50 values in μM. Error bars correspond to the standard error of the mean result of n=3 repeats

MTT Assay, 72h, A2780
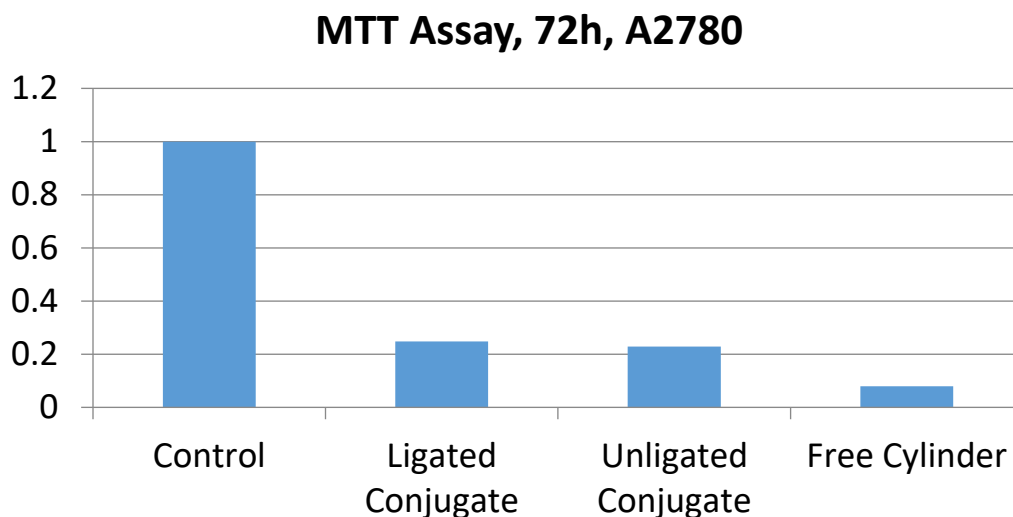
Figure 3.12 – MTT assay comparing toxicity of 25 µM of cylinder when delivered by ligated tetrahedron and un-ligated tetrahedron with free cylinder as a positive control.

3.3 Conclusions

This chapter set out to investigate the potential biological compatibility of the DNA tetrahedron as a drug delivery vessel. By testing the cellular uptake through various means, it can be concluded that the tetrahedron is very compatible and is readily taken up by cancer cells in an *in vitro* environment. It is also shown that both the iron cylinder and the ruthenium cylinder could be delivered by the tetrahedron to cells. Once delivered, it was shown that the toxicity of the iron cylinder was maintained, although at a diminished level. Although ICP-MS studies gave insight as to where the cylinders end up once delivered to cells, further experimentation is needed to fully ascertain the localisation of the tetrahedron in the cell, for example, by staining alternative cell structures to find co-localisation in a confocal microscopy experiment.

The question of whether the conjugate remains intact when entering the cell or whether the cylinder separates before uptake is a pertinent one. For this question to be answered, it must first be possible to visualise the cylinder inside the cell. Currently the Hannon group is still attempting to synthesise a cylinder possessing a fluorescent tag which would enable simultaneous visualisation of the cylinder and the tetrahedron inside the cell, allowing FRET studies to be carried out. This would be crucial to understanding the state of the conjugate at this stage. Unfortunately, this continues to be a very challenging goal. However, evidence of increased cylinder uptake when delivered by tetrahedron and diminished toxicity both point strongly to the fact that the conjugate is initially intact inside the cell.

3.4 Experimental

Materials: Enzymes T4 Ligase and Kinase were purchased from New England Biolabs. All chemicals were purchased from Sigma Aldrich unless otherwise stated. DNA oligonucleotides were purchased HPLC purified from Eurofins. DMEM medium (high glucose) was purchased from sigma. RPMI medium was purchased from life technologies. Cell culture equipment was purchased from Corning.

Flow Cytometry: HeLa cells were seeded into a 24-well plate at 35,000 cells per well, counted using a Haemocytometer. Cells were supplemented with DMEM medium (1ml) and left to incubate in the wells for 48 hours at 37°C to allow them to adhere fully to the well. Leaving control wells, separate wells were treated with cylinder alone, Cy5-Tetrahedron and Cy5-Conjugate to final concentrations of 20 µM of cylinder and 10 µM of DNA tetrahedron, corresponding to a ratio of 2:1 cylinder : tetrahedron in the Cy5-Conjugate sample well (400µl). Samples were then incubated overnight. Samples were then trypsinised (5mins) and re-suspended in PBS solution (2ml). They were then added to separate FACS tubes and each sample run on a BD FACscaliber flow cytometer with a Cy5 excitation laser. For each sample 10,000 cells were counted for a total of three repeat experiments.

Fixed Cell Confocal imaging: HeLa cells were seeded at 50,000 cells per well inside a 24 well plate containing a sterilised glass coverslip and supplemented with DMEM. Cells were left to adhere to coverslip for 24 hours. Cells were then incubated with Cy5 containing compounds (5 µM) for either 2 or 24 hours. Media was then aspirated and cells washed with thoroughly with PBS solution to remove any non-internalised compound. Cells were then

stained with Hoechst 33258 in DMEM (25 µg/mL) (500µl) for 30 min. The solution was again aspirated and cells washed 3 times with PBS (3 x 300 µL per well) and 4% formalin solution (500µl) was then added and left for 10 min. The formalin solution was then removed via pipette and cells washed with PBS (2 x 300 µl). The Glass coverslips were then removed from the wells, using a needle tip and tweezers, and washed in a PBS bath followed by a pure water bath by dipping. Coverslips were then placed face down onto a microscope slide which had been spotted with oil. The slide was then imaged on a Nikon A1 confocal microscope.

Live Cell Confocal imaging: HeLa cells were seeded into Matek dishes at 300,000 cells per dish as counted with a Haemocytometer, and left to incubate at 37°C for 48 hours in DMEM media (3ml) to allow them to adhere fully to the cover slip. Media was then removed and the cells washed with PBS (5ml). The cells were then treated with cylinder / Cy5 labelled DNA to a final concentration of 8 µM of cylinder and 2 µM of Cy5-Tetrahedron, corresponding to a ratio of 4:1 cylinder : tetrahedron in the Cy5-Conjugate sample well (1ml). The dishes were incubated for pre-determined times before the solutions were aspirated and the cells washed thoroughly with PBS (3 x 5 ml). The cells were then stained with Hoechst 33258 nuclear stain by incubating the cells with 2mL of 25µg/mL Hoechst in DMEM media for 30 mins. The stain was aspirated and cells washed again with PBS (3 x 5 ml). Clear imaging medium (life technologies) was then added to the dishes and the cells imaged on a Nikon-A1 confocal microscope.

Cell Toxicity Assay – MTT Assay: Cells of cell lines A2780 or HeLa were seeded into 96 well plates at 13,000 cells per well as counted by a Haemocytometer and left overnight in 100

μL per well of RPMI (A2780) or DMEM (HeLA) media to adhere and settle in the plate. 50 μL of compound solutions were added to each well to achieve treatment final concentrations. All wells in both plates were then topped up to a final volume of 200 μL with DMEM/RPMI media. The plates were then incubated for 72 hours. After incubation, all media was removed by pipette and each well washed with PBS solution (2 x 200 μl). 180 μL of DMEM/RPMI media was added to each well followed by 20 μL of MTT solution (7.5 mg in 1.5 mL) and mixed well by pipette. The plate was then incubated for 2 hours and then all media removed from the wells via pipette. 200 μL of DMSO was added to each well and incubated for a further 30 minutes. After being placed on a rocker for 5 minutes, the absorbance at 570nm of each well was recorded on a Tecan infinite F200 PRO plate reader. Each concentration was replicated in 4 wells on the same plate and each full experiment was repeated separately 3 times (n=3)

Synthesis of Parent Ligand (L: $C_{25}H_{20}N_4$)

4,4'Methylenedianiline (1.99g, 0.01 mol) was dissolved in ethanol (10 ml). To this solution, pyridine-2-carboaldehyde (1.90 ml, 0.02 mol) was added. The solution was then left to stir overnight. The yellow precipitate formed was then collected by vacuum filtration. The crude product was then purified by re-crystallisation from ethanol (3.50 g, 93% yield). The product is a pale yellow solid.

Mass Spectrum (ESI): m/z = 399 {M+Na}

^{1}H NMR (300 MHz), CDCl$_3$, 298K: δ 8.71 (2H, d, J = 3.9 Hz, 6py), δ 8.63 (2H, s, J = H$_{im}$), δ 8.22 (2H, d, J = 7.0 Hz 3py), δ 7.82 (2H, td, J = 8.3, 1.9, 0.6 Hz, 4py), δ 7.40 (2H, ddd, J = 7.6, 4.9, 1.2 Hz, 5py), δ 7.30 (8H, m, Ph$_a$ and Ph$_b$), δ 4.08 (2H, s, CH$_2$)

Synthesis of Ruthenium Cylinder, **[Ru$_2$(L)$_3$](PF$_6$)$_4$:** RuCl$_3$ (3g, 14.5 mmol) was dissolved in 15 mL of DMSO and heated under reflux at 195°C for 5 minutes. The solution was reduced *in vacuo* to concentrate the solution down to 1 mL. Excess cold acetone was then added to precipitate a yellow solid. The yellow precipitate was then filtered and washed with cold acetone to furnish the yellow solid Ru(DMSO)$_4$Cl$_2$.

Ru(DMSO)$_4$Cl$_2$ (0.988 g, 2.04 mmol) and parent ligand (1.150 g, 3.06 mmol) were added to degassed Ethylene glycol (50 ml) and heated to reflux under argon at 200°C for 5 days. The mixture was allowed to cool and an excess saturated methanolic solution of ammonium hexaflourophosphate was added. The suspension was cooled on ice before the precipitate was filtered and washed with methanol (2 x 40 ml) and dried with ether (3 x 100 ml). The dark brown product was purified by column chromatography on alumina using 20:1:1 MeCN/H$_2$O/ KNO$_{3(aq)}$ solution as eluent to yield the product as an orange solid (11 mg, 0.6% yield).

Mass Spectrum Positive ion ESI: m/z = 666 [M-(PF$_6$)$_4$]$^{2+}$, 444 [M-(PF$_6$)]$^{3+}$, 333.2 [M-(PF$_6$)$^{4+}$

^{1}H NMR (300MHz), CD$_3$CN, 298K : δ = 8.7 (2H, s, H$_{im}$), 8.45 (2H, d, J = 7.6 Hz, 6py), 8.35 (2H, td, J = 7.78 Hz, 5.0 Hz, 3py), 7.65 (2H, d, J = 6.0 Hz, 4py), 7.65 (2H, d, J = 6.0 Hz, 5py), 7.0 (4H, d, J = 8.4 Hz, Ph$_{a/b}$), 5.7 (4H, d, J = 8.3 Hz, Ph$_{a/b}$), 4.1 (2H, s, CH$_2$)

UV-Vis (CH$_3$CN) : λ$_{max}$ (ε / dm^3 mol^{-1} cm^{-1}) 485 (24200)

ICP-MS Cell uptake analysis: 3 separate T75 flasks were seeded with HeLa cells and incubated in DMEM media until fully confluent. Medium was aspirated from the flasks and the cells washed with PBS. To one flask was added 5 mL of medium, to be used as a control. To another, 5 mL of medium containing 2 μM final concentration of Ru cylinder was added and to the final 5 mL of medium containing 4:1 Ru cylinder – Tetrahedron conjugate (0.5 μM : 2 μM) final concentration was added. The flasks were left to incubate for 24 hours at 37°C before the cells were collected and pelleted. Two samples of 2 million cells were taken from each pellet. One sample was then fractionated into a nuclear fraction and a cytoplasmic fraction whilst the other was kept as a whole cell sample. The fractionation procedure was carried out using a Nuclear/Cytosol fractionating kit (BioVision) following the provided protocol. All samples were then digested using 500 μL concentrated ultra-pure HNO_3 (Fluka) at 80°C for 16 hrs in glass vials. Samples were diluted to 5% HNO_3 solution with ultra-pure water to 5 ml and analysed. The Ruthenium content of each sample was then analysed on an Agilent 7500CX ICP-MS.

3.5 References

1. M.J. Hannon, *Metal-based anticancer drugs: From a past anchored in platinum chemistry to a post-genomic future of diverse chemistry and biology.* Pure and Applied Chemistry, 2007. **79**(12): p. 2243-2261.

2. S.J. Lippard and J.M. Berg, Principles of Bioinorganic Chemistry, 1994. **23** (2): p. 115

3. A.C.G. Hotze, N.J. Hodges, R.E. Hayden, C. Sanchez-Cano, C. Paines, N. Male, M.-K. Tse, C.M. Bunce, J.K. Chipman, and M.J. Hannon, *Supramolecular Iron Cylinder with Unprecedented DNA Binding Is a Potent Cytostatic and Apoptotic Agent without Exhibiting Genotoxicity.* Chemistry & Biology, 2008. **15**(12): p. 1258-1267.

4. S.J. Lee, Y.N. Yum, S.C. Kim, Y. Kim, J. Lim, W.J. Lee, K.H. Koo, J.H. Kim, J.E. Kim, W.S. Lee, S. Sohn, S.N. Park, J.H. Park, J. Lee, and S.W. Kwon, *Distinguishing between genotoxic and non-genotoxic hepatocarcinogens by gene expression profiling and bioinformatic pathway analysis.* Scientific Reports, 2013. **3**: p. 2783.

5. D. Khynriam and S.B. Prasad, *Cisplatin-induced genotoxic effects and endogenous glutathione levels in mice bearing ascites Dalton's lymphoma.* Mutation Research, 2003. **526**(1-2): p. 9-18.

6. N. Aydemir and R. Bilaloglu, *Genotoxicity of two anticancer drugs, gemcitabine and topotecan, in mouse bone marrow in vivo.* Mutatation Research, 2003. **537**(1): p. 43-51.

7. A.S. Walsh, H. Yin, C.M. Erben, M.J.A. Wood, and A.J. Turberfield, *DNA Cage Delivery to Mammalian Cells.* ACS Nano, 2011. **5**(7): p. 5427-5432.

8. C.M. Erben, R.P. Goodman, and A.J. Turberfield, *Single-molecule protein encapsulation in a rigid DNA cage.* Angewante Chemie International Edition English, 2006. **45**(44): p. 7414-7.

9. R. Crawford, C.M. Erben, J. Periz, L.M. Hall, T. Brown, A.J. Turberfield, and A.N. Kapanidis, *Non-covalent Single Transcription Factor Encapsulation Inside a DNA Cage.* Angewandte Chemie-International Edition, 2013. **52**(8): p. 2284-2288.

10. K.R. Kim, D.R. Kim, T. Lee, J.Y. Yhee, B.S. Kim, I.C. Kwon, and D.R. Ahn, *Drug delivery by a self-assembled DNA tetrahedron for overcoming drug resistance in breast cancer cells.* Chemical Communications, 2013. **49**(20): p. 2010-2012.

11. A.J. Pope, C. Bruce, B. Kysela, and M.J. Hannon, *Issues surrounding standard cytotoxicity testing for assessing activity of non-covalent DNA-binding metallo-drugs.* Dalton Transactions, 2010. **39**(11): p. 2772-2774.

12. A. Reiger, *Flow cytommetry at the faculty of medicine and destistry.* [online] University of Alberta, April 2017, January 2017 https://flowcytometry.med.ualberta.ca/author/aja/

13. L. Liang, J. Li, Q. Li, Q. Huang, J.Y. Shi, H. Yan, and C.H. Fan, *Single-Particle Tracking and Modulation of Cell Entry Pathways of a Tetrahedral DNA Nanostructure in Live Cells.* Angewandte Chemie-International Edition, 2014. **53**(30): p. 7745-7750.

14. J.E. O'Sullivan, R.J. Watson, and E.C. Butler, *An ICP-MS procedure to determine Cd, Co, Cu, Ni, Pb and Zn in oceanic waters using in-line flow-injection with solid-phase extraction for preconcentration.* Talanta, 2013. **115**: p. 999-1010.

15. G.I. Pascu, A.C.G. Hotze, C. Sanchez-Cano, B.M. Kariuki, and M.J. Hannon, *Dinuclear Ruthenium(II) Triple-Stranded Helicates: Luminescent Supramolecular Cylinders That Bind and Coil DNA and Exhibit Activity against Cancer Cell Lines.* Angewandte Chemie, 2007. **119**(23): p. 4452-4456.

16. J.M.C.A. Kerckhoffs, J.C. Peberdy, I. Meistermann, L.J. Childs, C.J. Isaac, C.R. Pearmund, V. Reudegger, S. Khalid, N.W. Alcock, M.J. Hannon, and A. Rodger, *Enantiomeric resolution of supramolecular helicates with different surface topographies.* Dalton Transactions, 2007(7): p. 734-742.

17. J. Malina, M.J. Hannon, and V. Brabec, *Interaction of Dinuclear Ruthenium(II) Supramolecular Cylinders with DNA: Sequence-Specific Binding, Unwinding, and Photocleavage.* Chemistry – A European Journal, 2008. **14**(33): p. 10408-10414.

18.   J. van Meerloo, G.J. Kaspers, and J. Cloos, *Cell sensitivity assays: the MTT assay.* Methods in Molecular Biology, 2011. **731**: p. 237-45.

19.   R.P. Goodman, I.A.T. Schaap, C.F. Tardin, C.M. Erben, R.M. Berry, C.F. Schmidt, and A.J. Turberfield, *Rapid Chiral Assembly of Rigid DNA Building Blocks for Molecular Nanofabrication.* Science, 2005. **310**(5754): p. 1661-1665.

20.   K.D. Bloch and B. Grossmann, *Digestion of DNA with restriction endonucleases.* Current Protocols in Molecular Biology, 2001. **3**(1).

Chapter 4:

DNA Photocleavage with a Ruthenium Cylinder

4.1 Introduction

Ruthenium complexes capable of inducing DNA photocleavage have been studied extensively over recent years with the main examples centred around [Ru(bpy)$_3$]$^{2+}$ (figure 4.1a).[1] The interest in ruthenium complexes in regard to DNA photocleavage is due to their extensive and variable photophysical, photochemical, and redox properties.[2] Ru(II) DNA photocleavage agents must first be able to bind to DNA to provide a platform for the various energy transfer mechanisms that lead to photocleavage. Various ligand choices can lead to differing binding modes or structural preferences, with intercalation a popular choice, notably the DNA 'light switch' molecule [Ru(bpy)$_2$(dppz)]$^{2+}$ (figure 4.1b) which revolutionised research in this area.[3] In recent times binding to DNA from these octahedral Ru(II) complexes is agreed to be a combination of electrostatic interactions between the positive complexes and the negatively charged phosphosugar backbone of DNA[4], surface binding into the major / minor grooves in the DNA[5], along with the fore-mentioned ligand intercalations.
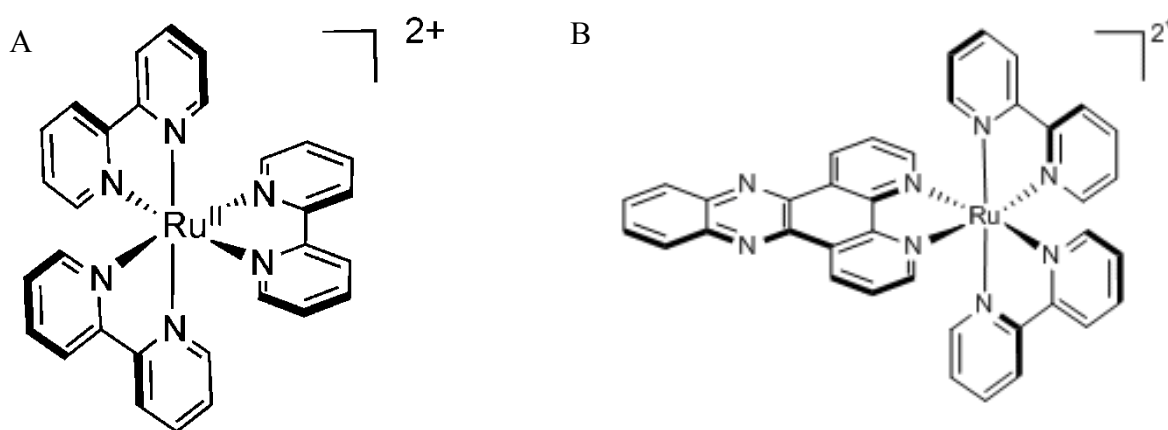

Figure 4.1 – A) Structure of [Ru(bpy)$_3$]$^{2+}$ (taken from 8), B – Structure of [Ru(bpy)$_2$(dppz)]$^{2+}$. Taken from ref 5.

Photocleavage agents also need to possess certain photophysical properties to facilitate the cleavage. In Ru(II) complexes, this usually involves having a ^{3}MLCT excited state as a platform for energy transfer. Cleavage can then progress through production of a singlet oxygen excited state ($^1O_2$), which is generated by exciting an election to the lowest-lying triplet excited state in the ^{3}MLCT state which then transfers energy to the $^3O_2$ ground state to produce $^1O_2$.[7]

Another similar photocleavage pathway follows the same initial excitation to the ^{3}MLCT, but this then transfers an electron to O_2 to form a superoxide anion (O_2^-) which can react with water to from a hydroxyl radical ($\cdot$OH).[8] This hydroxyl radical can then go on to cleave DNA through a nucleophilic addition-elimination on the DNA phosphosugar backbone. Both of these mechanism pathways require the presence of O_2 to proceed.

Alternatively, some reported Ru(II) complexes have been designed to cleave in a completely different fashion, by incorporating electron deficient ligands with Ru(II) (Figure 4.2) which can directly abstract DNA base electrons into their deficient ^{3}MLCT state and cause cleavage through that fashion.[9] Two example ligands which proceed through this mechanism[9] when complexed to Ru(II) are *tap* (1,4,5,8-tetraazaphenanthrene) and *hat* (1,4,5,8,9,12-
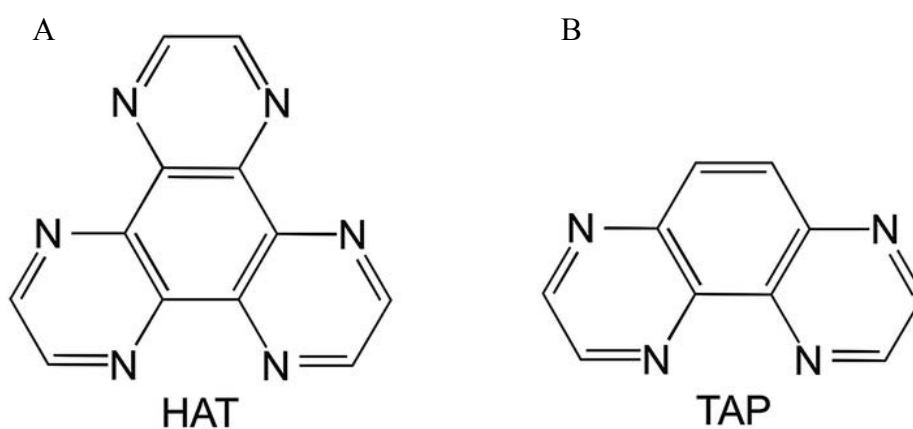

Figure 4.2 – **A)** Structure of HAT, **B)** – Structure of TAP. (Image taken from ref 11).

hexaazatriphenylene) (figure 4.2a and b).[10]

In a similar mechanism, Ru(II) complexes have also been synthesised that can be oxidised to Ru(III) through photo irradiation. These highly oxidising Ru(III) species can then abstract electrons from the DNA bases to induce cleavage.[11,12] These last two mentioned mechanisms differ from the earlier two as they are considered to be anaerobic and do not require the presence of O_2. This has been considered an advantage in certain applications such as photodynamic therapy for treating cancer as tumours in general terms are considered to be quite hypoxic, lacking oxygen due to sporadic blood circulation.
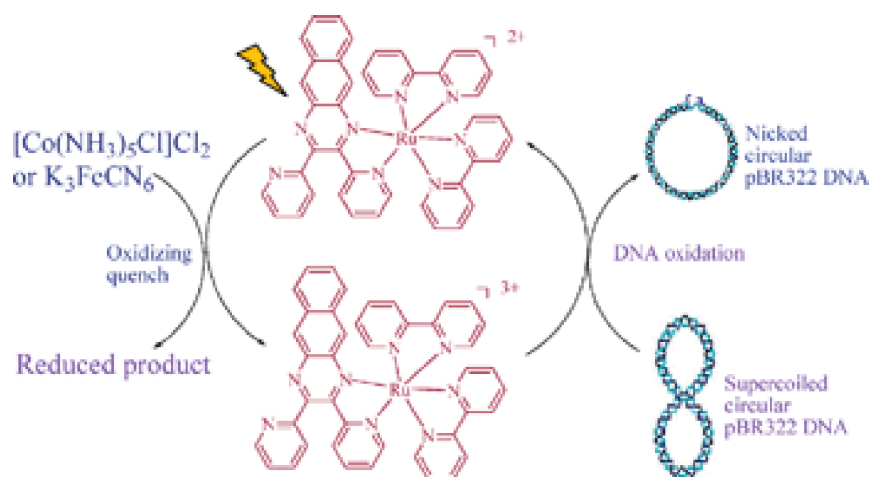
Figure 4.4 - Schematic diagram illustrating anaerobic DNA photocleavage through a Ru(III) intermediate. Taken from ref 12

One of the main applications of these DNA photocleavage agents has been for use in treating cancer with photodynamic therapy (PDT).[13] PDT involves first treating the patient with a photosensitizer drug which can then locate to the sites of a tumour. The drug in this case is usually inactive and non-toxic at this stage.[14] Light can then be shone on the tumour site,

exciting the complex and beginning the DNA damage mechanisms which can lead to various cell death pathways. These are usually from cellular apoptosis from DNA damage, damaging blood vessels around the tumour which resists blood supply, and more recently thought to activate some immune responses.[15]

Currently the only photosensitizer drug licensed in the clinic for treatment of internal cancers is Photofrin®, also known as Porfimer sodium[16] (Figure 4.4). After administration, Photofrin is excited by a strong red laser at 630 nm internally using a fibre optic probe. It is currently used to treat bladder, oesophageal and non-small cell lung cancers.[17] Limitations of PDT, disregarding the usual adverse side effects experiences by most forms of chemotherapy, include treatment area being limited to areas which can be accessed by the laser probe. Also, as the drug requires strong laser excitation, tissue damage directly from the laser is common. The depth at which the laser can penetrate through tissue and maintain the level of energy required to initiate $^1O_2$ production can also be limited depending on the tissue involved.[17]
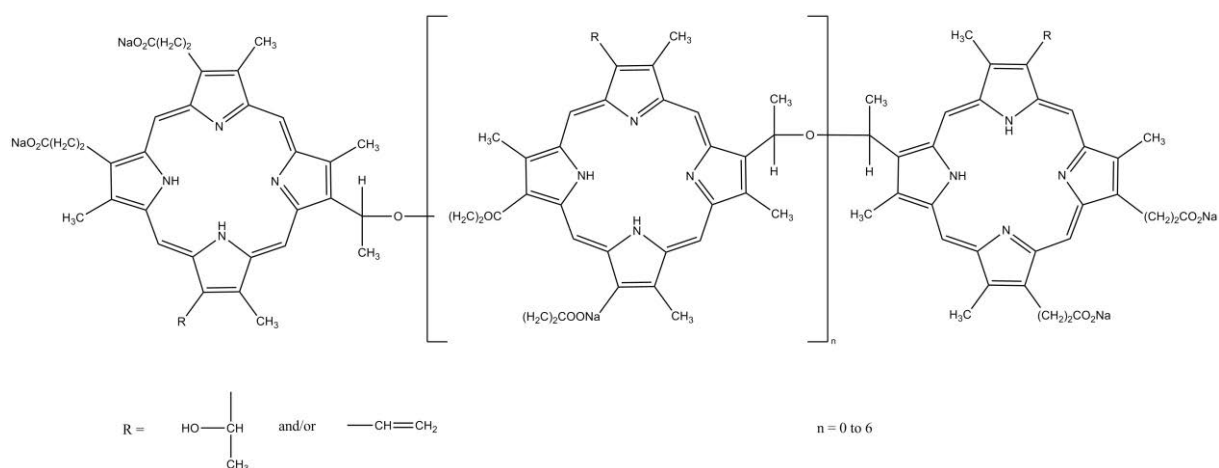
Figure 4.4 - Structure of Photofrin® taken from 18.

Our group reported that the ruthenium cylinder had the capability to photocleave DNA.[19] Following on from the previous chapters, detailing cylinder binding to the DNA tetrahedron, this chapter aims to explore the photocleavage capabilities further. By applying it in context to the DNA tetrahedron, it was hoped to take a different angle on possible applications of PDT by 'breaking open' a DNA nanostructure with an external light trigger (Figure 4.5). This would be done with a view to release a possible internalised cargo and the first time DNA nanotechnology and a photosensitizer of this sort are combined in this application.
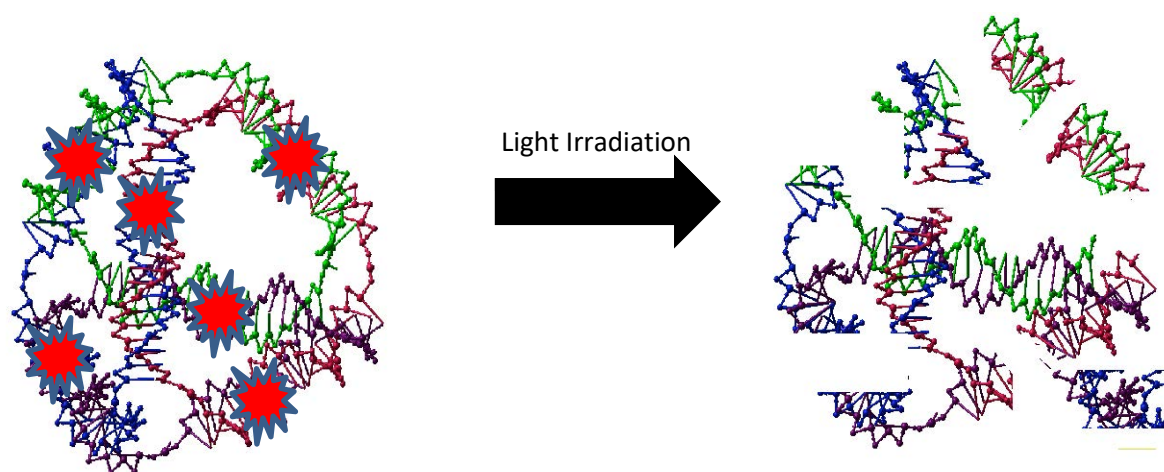

Figure 4.5 - Illustration of utilising photo-cleavage to break apart a DNA tetrahedron

4.2 Results and Discussion

4.2.1 Plasmid Photocleavage

Firstly, to establish the conditions of photocleavage, a positive control experiment was. As discussed, the ruthenium cylinder has proven capable of DNA photocleavage[19], although not

in conjunction with DNA nanostructures or with the low powered LED bulbs planned for this experiment. Tracking DNA plasmid photocleavage with agarose gel electrophoresis provides a very clear and quantifiable result that has been used in many publications over the years.[20] This is because it provides a very clear indication of positive photocleavage with a large band shift and also gives indication of the nature of photocleavage – whether a single or double strand break has occurred.[21] Figure 4.6 shows a typical agarose gel result obtained, illustrating both when a single strand cleavage has occurred, and when a double stand cleavage occurs.
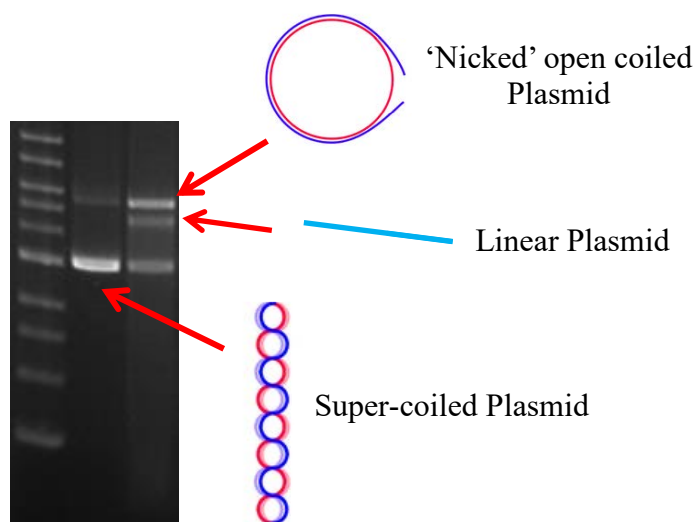
Figure 4.6 - Agarose gel showing a pBR322 plasmid band in its natural supercoiled form and with cleavage to form non-coiled (single strand break) and linear plasmid (double strand break).Taken and illustrated from 21

With a positive control experiment proposed, the plasmid pUC19 was used for the experiments. This plasmid is readily available and tends to produce sharp clear bands in gel electrophoresis with the majority of the plasmid in the natural supercoiled form as desired here. Figure 4.7 shows PuC19 run after being deliberately damaged with a strong UV light for

10 mins to initiate strand cleavage. This was done to establish where the cleavage band would migrate in relation to the DNA ladder used.

It is desirable for the ruthenium cylinder to photocleave DNA using low power LED bulbs that produced minimal heat. This is because a low level light would maximise possible medical applications - high powered lasers and bulbs can cause tissue damage in
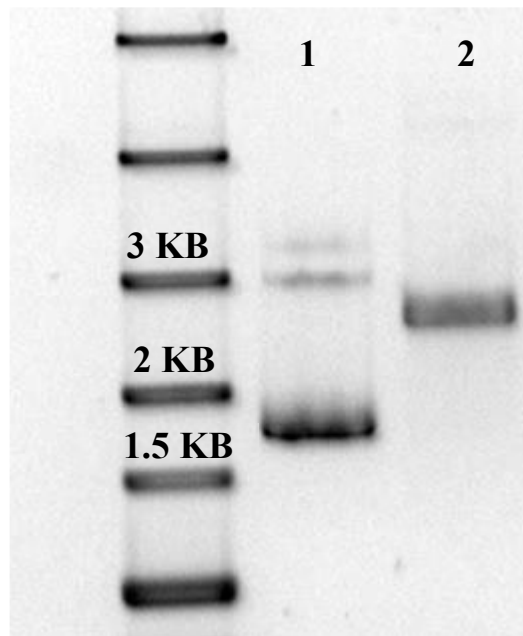
Figure 4.7 - 1% Agarose gel run in 1 x TAE Buffer. Left lane - reference DNA ladder, Lane 1 – pUC19 plasmid unchanged, Lane 2 – pUC19 treated with 10 minutes to UV light to initiate strand breakage to a linear form.

phototherapy applications. To begin the experiments, a 1W white LED bulb was used. This would give a broad range of emission for the ruthenium to absorb from and thus transfer energy to initiate the photocleavage mechanism. Figure 4.8 shows the agarose gel of pUC19
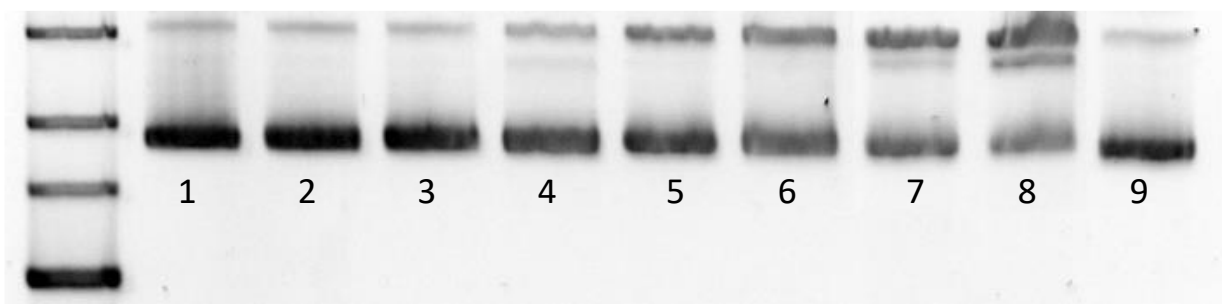
Figure 4.8 - 1% Agarose gel run in 1 x TAE Buffer. Lanes 1 and 9 – control containing pUC19 plasmid. Lane 2 – Plasmid under 24 hours of illumination (1W, white light). Lane 3 – Plasmid with RuCy (100 bp:1 RuCy) with no illumination. Lanes 4-8 – Plasmid with Rucy with 2, 4, 6, 8 and 10 hours 1W white light illumination respectively.

plasmid. From this gel, it is clear that over the 10 hour period of the experiment; only a small amount of strand breakage was detected. At 10 hours, still 55% of the plasmid remains in the unbroken supercoiled state. The majority of the cleavage was single stranded with 35% of the
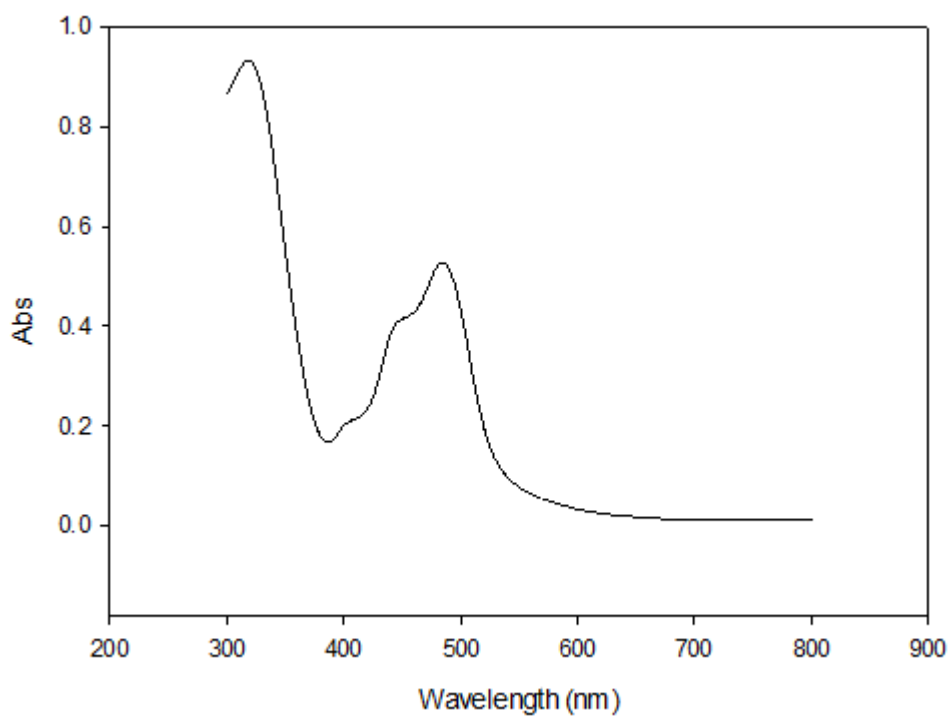
Figure 4.9 - UV-Vis absorption spectrum of the RuCy.

DNA in the lane in the nicked uncoiled form. Interestingly 10% of the DNA in the lane was of the linear form, showing that some double strand breaks occur. As this band only appears in the later lanes of prolonged illumination, it seems unlikely that the RuCy causes double strand breaks and the presence of the linear plasmid band is simply the result of two single strand breaks occurring together. This is expected as the RuCy is expected to form a y-shaped structure following a single strand break. During repeats, it was clear that a longer run time and stronger light could increase the degree of photocleavage, however, this was not desirable as more powerful bulbs create heat and longer exposure times become impractical, as 10 hours is already an extensive amount of time. Instead, another experiment was done to look to increase the specificity of the energy absorbed to hopefully increase the degree of photocleavage. By looking at the absorption spectrum of the RuCy (Figure 4.9) the λ_{max} occurs at 485 nm. By purchasing a 1W blue LED with a λ_{max} emission at 474 nm, it was hoped that the degree of photocleavage would be enhanced without increasing the power output by simply concentrating the power into the wavelength range the RuCy absorbs. Figure 4.10 shows example emission spectra of the two bulbs, illustrating the concentration of emission in the relevant region in the blue bulb compared to the white.
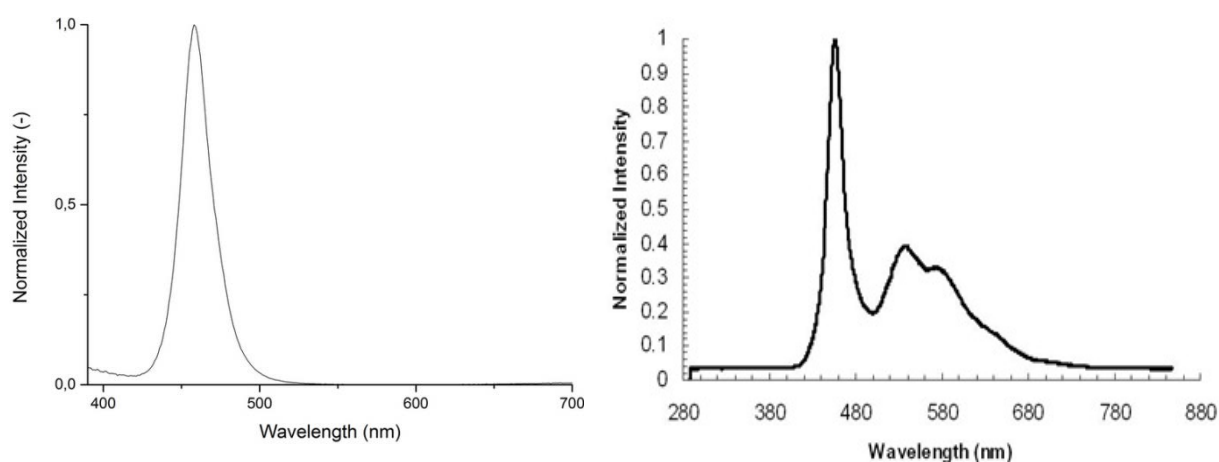
Figure 4.10 - Emission spectra of a blue LED (left) and a white LED (right).

With this in mind, the experiment was repeated with a 1W blue LED this time, the gel image obtained (Figure 4.11) shows that the earlier hypothesis was correct. The degree of DNA cleavage was significantly increased over the same time period with only 10% of the plasmid remaining undamaged. The amount of plasmid in the linear form also increased significantly showing move extensive double strand breaks; with the linear band starting to appear at around 4 hours into the experiment whereas the white light run only exhibited a small band around the 8 hour mark. The difference is illustrated clearly in the line graph in figure 4.12.
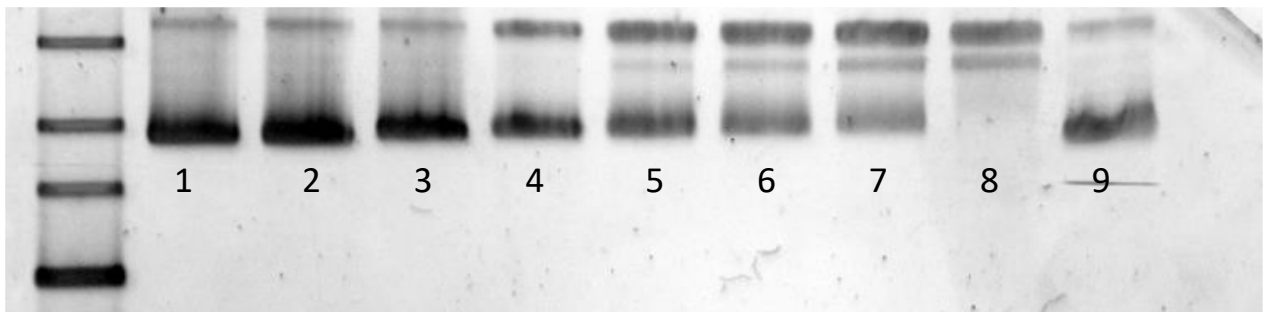
Figure 4.11 - 1% Agarose gel run in 1 x TAE Buffer. Lanes 1 and 9 – control containing PuC19 plasmid. Lane 2 – Plasmid under 24 hours of illumination. Lane 3 – Plasmid with RuCy (100 bp:1 RuCy) with no illumination. Lanes 4-8 – Plasmid with Rucy with 2, 4, 6, 8 and 10 hours 1W blue light illumination respectively.
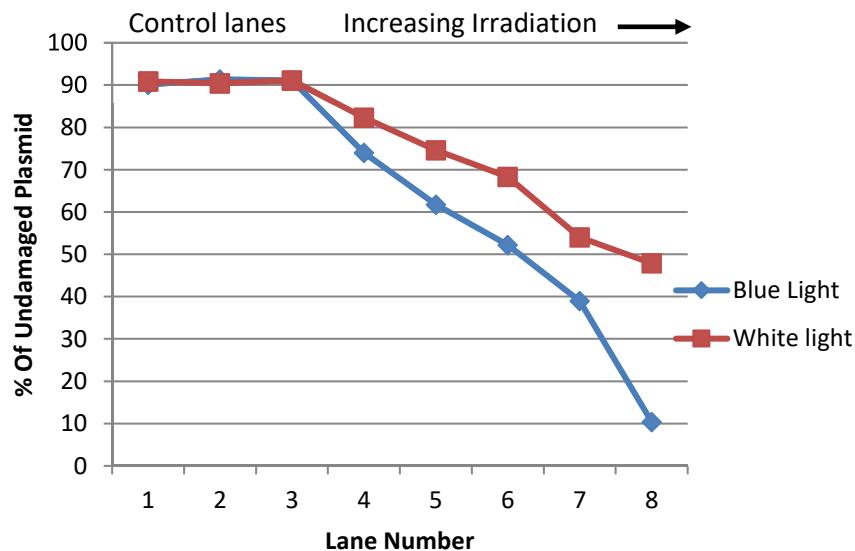
Figure 4.12 - Line graph illustrating the difference in photocleavage between wavelengths.

4.2.2 Photocleavage Mechanism

Whilst a positive control experiment was firmly established, the energy mechanism of how the RuCy initiates photocleavage on the DNA was unclear. As discussed in the introduction, establishing the mechanism of photocleavage is important in the field of photodynamic therapy. Referring to the possible paths of photocleavage in the introduction to this chapter, it is possible to introduce inhibiting or enhancing substances to the reaction mixture, that if successfully alters the rate of photocleavage, should indicate the likely pathway. Some of these substances are well established in the literature for this purpose.[22] One of these is sodium azide (10 mM in this experiment), an excellent quencher of $^1O_2$ (singlet oxygen radicals).[23] Another is to perform the experiment in D_2O in place of H_2O (50%). This is known to increase the lifetime of the $^1O_2$ and thus if rate of cleavage is increased in the presence of D_2O then this pathway is likely.[24] Finally, the presence of DMSO (10%), which is a hydroxyl radical scavenger,[25] was assessed.

The experiments were repeated as before, Figure 4.13 shows the effect of sodium azide and D_2O on the reaction mixture in comparison to the control gel in Figure 4.11. It can be seen that sodium azide inhibits photocleavage by a small amount, suggesting that the mechanism proceeds through the $^1O_2$ pathway. To back this up, the reaction performed in D_2O also showed enhanced cleavage, showing the increased lifetime of the $^1O_2$ is beneficial to the reaction. Other pathways such as through the production of a hydroxyl radial can also be ruled out as DMSO had no effect on the rate of cleavage compared to a tandem no DMSO sample. Through this information we can be confident that the mechanism proceeds through the singlet oxygen radical pathway which is in agreement with previous photocleavage studies on the RuCy.[19]
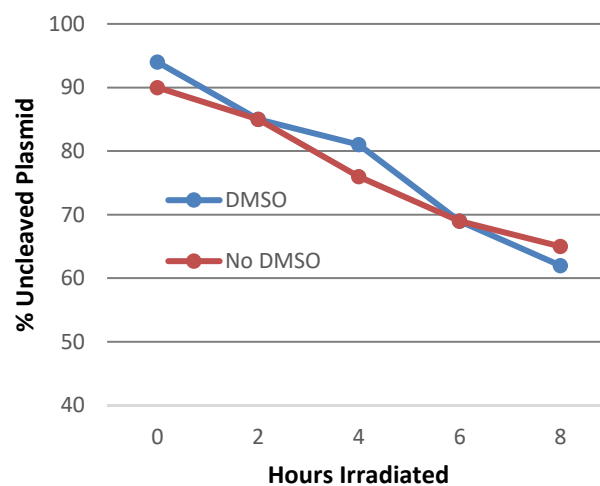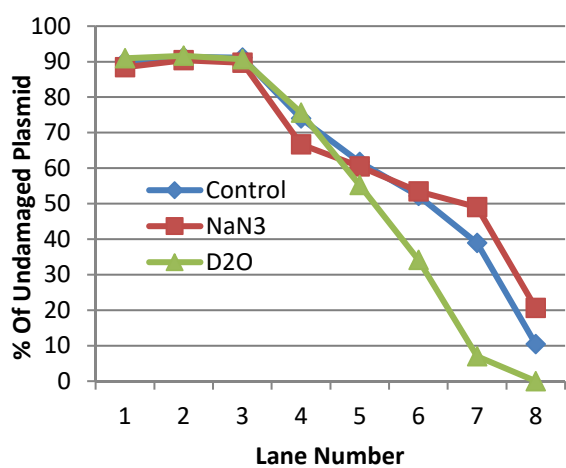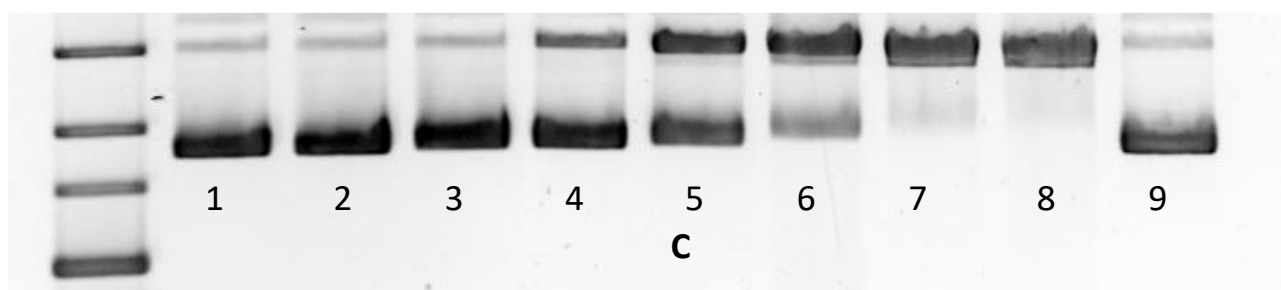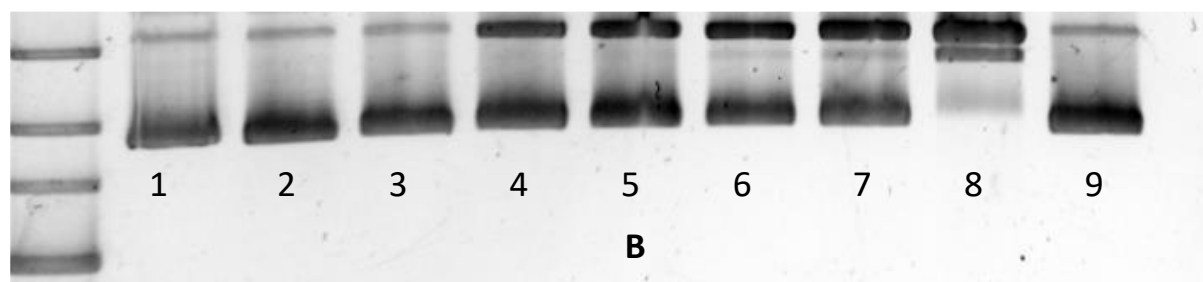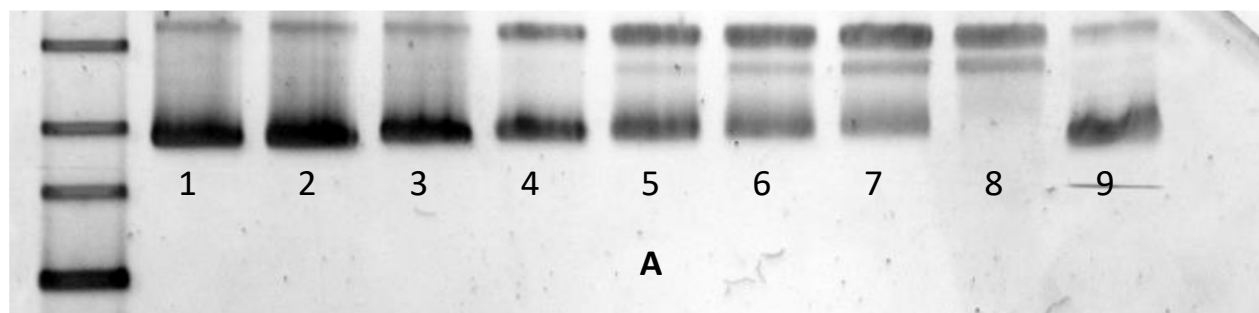
Figure 4.13 - Gel A – Control gel, Gel B – Sodium Azide treated samples, Gel C – D$_2$O treated samples. Left hand graph) graphical quantification of gels A, B and C, performed at 100:1 BP:RuCy Right hand graph) quantification of a separate experiment testing the effects of DMSO on cleavage. Performed at 200:1 BP:RuCy).

4.2.3 Photocleaving the DNA Tetrahedron

Translating this working model onto the DNA tetrahedron required a different approach to visualise and quantify strand breaks in the experiment. This was because the nicked tetrahedron did not produce an obvious band shift like the plasmid in gel electrophoresis. In non-denaturing PAGE gels therefore, single strand breaks were found to produce bands that looked identical to intact tetrahedron. Two different experiments were carried out to try to observe the cleavage.

The first involved forming a 'ligated tetrahedron', the formation of which was first outlined by Turberfield *et al.*[26] This involves using a DNA ligase enzyme to close off nicks in the phosphosugar backbone on the edges of the DNA tetrahedron (Figure 4.14).
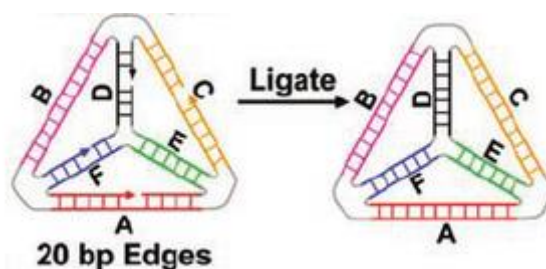
Figure 4.14 - Illustration of the formation of the ligated tetrahedron (Taken from 26)

By doing this after the tetrahedron has been formed, the strands become catenated together and when the DNA is denatured, four joint loops remain. This is advantageous as an undamaged ligated tetrahedron, when run on a denaturing gel, would produce a band containing all 4 undamaged strands. Any single strand breaks would release the damaged loop

from the catenated structure which would decrease the intensity of the undamaged band, allowing photocleavage to be observed. Figure 4.15 shows the resulting gel obtained.
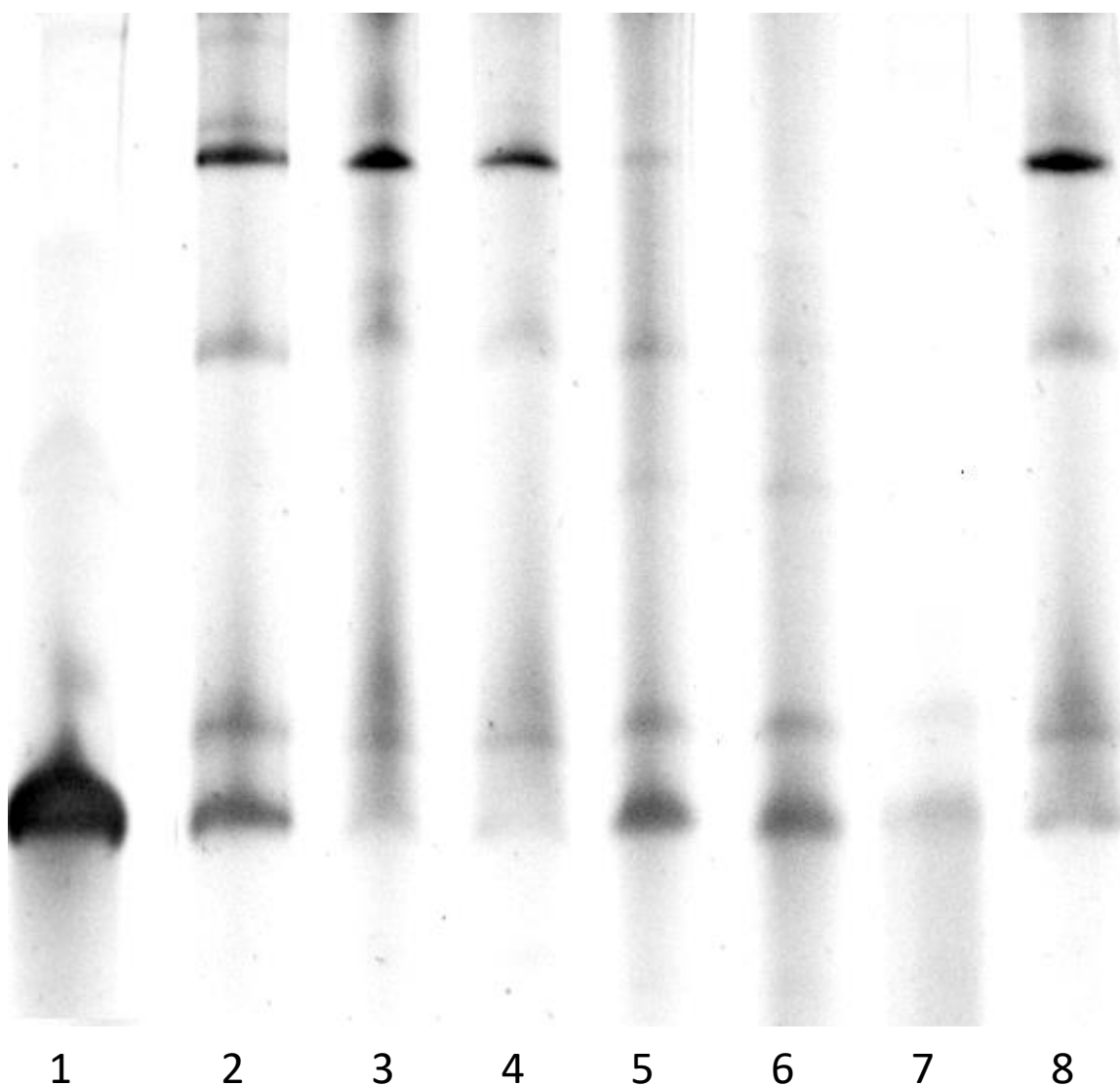
Figure 4.15 – Photo illumination image of a 10% Denaturing Page Gel. Lane 1: Non-Ligated tet. Lane 2: Lig Tet. Lane 3: Lig tet after 5 hours blue light irradiation. Lane 4-8: Lig tet with RuCy (2:1) irradiated with 0, 1,3,5 and 0 hours blue light

The first lane shows the unligated tetrahedron denaturing into 4 building block strands in the denaturing Urea conditions of the gel. Lane 2 shows successful ligation of the tetrahedron

forming 4 single stranded DNA loops that cannot be separated by denaturation. Underneath the main band at the top, there are three fainter bands; these are products of incomplete ligation, corresponding to a 3 single stranded loop, 2 stranded loop, and 1 strand alone at the bottom, equal in migration to the deconstructed unligated tetrahedron in lane 1, confirming identity of the band. It is unclear as to why the ligation is not 100% effective. In previous similar experiments to this gel, ligation was left to proceed for 4 hours as per manufacture protocol and much less ligation efficiency was observed. Extended overnight ligation and excess T4 DNA ligase enzyme as shown here improved ligation efficiency to the point seen here, but total ligation was never achieved. This could be due to phosphorylation inefficiencies and due to the short sides of the tetrahedron not allowing enough space/DNA turns for the enzyme to initiate to full effect. Lanes 2 and 8 show that without RuCy, the blue light does not cause any damage to the DNA. As the duration of light irradiation increases, the tetrahedron is broken down until no intact DNA is left in lane 7. In lanes 5 and 6, it can be observed that bands attributed to the smaller structures increase in intensity. This gave some insight that the RuCy is cleaving initially at some point on one strand. Future work is currently planned to attempt to excise these photocleavage product bands and sequence them to try to see if the RuCy's original binding and subsequent cleavage position on the tetrahedron can be found by analysing the starting sequences of the cleaved product and comparing them to the original construction strands. As irradiation continues, it is possible that the RuCy cleaves and can then re bind to resulting DNA and cause further cleavage; almost no observed DNA bands have been stained in lane 7, leaving only a smear low down the lane. Alternatively, the RuCy could remain bound inside a vertex and continues cleaving sequentially. This suggests only very small randomly sized fragments remain as the SYBR gold stain could not be used to visualise them as they are so low in concentration. Overall,

this experiment was successful in proving that the DNA tetrahedron can be broken down with photocleavage from the ruthenium cylinder.

The second visualisation method explored involved the ligated tetrahedron, but utilised another enzyme. Exonuclease III catalyses stepwise removal of nucleotides on a strand of DNA from the 3' end, effectively digesting it.[27] As the enzyme can only initiate on the end of DNA strands, if there are none, as with the ligated tetrahedron, no digestion should occur. If strand breaks are formed, however, the enzyme should be able to initiate and cause a decrease in the intact band intensity. In Figure 4.16 it can be seen that photocleavage has been a success. Initially, the construction of the tetrahedron can be easily tracked in lanes 1-4. Lane 5 gave further evidence that ligation is not 100% efficient as the exonuclease was able to produce two digestion products, most likely the removal of 1 and 2 strands respectively leaving single stranded gaps in the tetrahedron structure. However, the migrations of these products do not match the ligated 2 and 3 stranded products presented in lanes 2 and 3. They are in fact slower. This could be due to incomplete removal of the strand, leaving the junctions intact. This would lead to a more rigid structure which would have decreased electrophoretic mobility and as such explain the slower migration. On irradiation, the RuCy can be seen to produce many more strand breakages which lead to easier digestion by the enzyme. Again, after 5 hours irradiation in lane 9, no bands are visible, showing the enzyme has broken all the DNA down into single nucleotides and short, unstainable strands.

Through both of these experiments, it is clear much less time is needed to photocleave the tetrahedron when compared to the plasmid DNA. One reason could be that the RuCy binds much more strongly to the tetrahedron than it does to plasmid DNA, facilitating quicker cleavage. This could be due to both the presence of 3WJs on the tetrahedron and the fact that plasmid DNA is supercoiled and could therefore be less accessible for the cylinder.
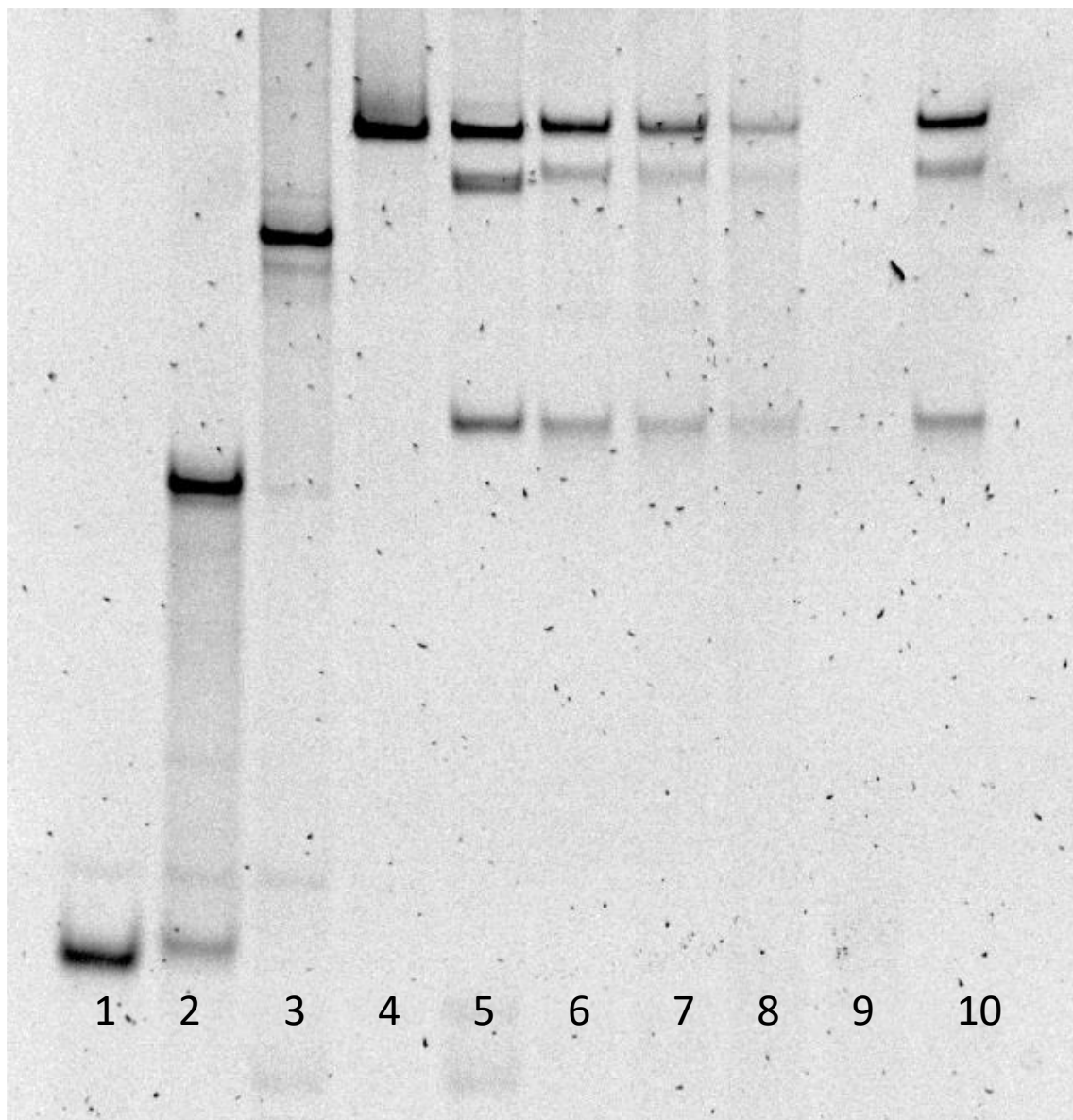
Figure 4.16 – Photo illumination picture 10% Non-denaturing PAGE gel. Lane 1: Strand 1 ligated, Lane 2: Strands 1 + 2 ligated, Lane 3: Strands 1 + 2 + 3 ligated, Lane 4: Full Ligated tetrahedron. Lane 5: Lig-tet exposed to Exonuclease III for 30 mins after no light irradiation. Lane 6: Lig-tet with 2:1 RuCy and no light with Exonuclease III. Lanes 7-9, same as lane 6 but with 1, 3, 5 hours of 1W Blue LED illumination respectively. Lane 10: Control Lig-Tet only with 5 hours light and digestion. Gel stained with SYBR-Gold nucleic acid stain.

4.2.4 Initial Photodynamic Therapy Testing

Ruthenium cylinder for this section was kindly provided by Dr Lucia Cardo

With positive results obtained with the RuCy as a photocleavage agent, some initial *in vitro* testing was carried out to test whether the RuCy and RuCy-tetrahedron conjugate could enter cells, bind to cellular DNA and on excitation with blue light cause damage that triggers cell apoptosis. The focus now would be using the DNA tetrahedron as a delivery agent and targeting nuclear DNA for photocleavage. There are some key questions that it was hoped the testing would address. Firstly, confirmation was sought that extensive illumination with the blue light would not be harmful to cells alone. This would be desirable as current PDT therapies often use powerful lasers or strong fibre optic lights that produce excess heat and causes tissue damage in patients in the treatment area.[13] From the start of this section it was the aim to be able to cause DNA damage with a bulb that does not cause excess heat or at a wavelength that damages DNA alone.

A second aim was that without light excitation, the complexes would not be toxic to cells at doses shown to be active upon photo activation. This is important as low toxicity *in vitro* would suggest low side effects outside of the irradiated area and provide a large therapeutic window which would be advantageous relative to current cancer therapeutics.

Finally, as ICP-MS results shown in chapter 3, it was hoped that the increased cellular accumulation of RuCy when delivered by the tetrahedron as opposed to cylinder alone would cause an enhanced effect of photo activated toxicity in cells. A decrease in activity is also possible as some of the RuCy may remain bound to the tetrahedron and instead cause strand breaks to it. This decrease in activity was observed in MTT assays shown in chapter 3 also when delivering FeCy with tetrahedron.

The initial experiment involved a crude set up using a desk lamp fitted with the same LED bulb used throughout the chapter. 96-well plates could then be fitted to the lamp at a measured distance. Only wells directly above the bulb were used in an attempt to make each well receive the same intensity of light. The set-up, however, will need to be optimised in future to guarantee this. Two 96-well plates were seeded with HeLa cells and following treatment with the complexes, one plate was irradiated with the lamp. The other dark control plate was also left out of the incubator and kept in darkness. It was kept outside of the incubator as it proved impossible to set up the lamp inside a temperature controlled incubator and so to ensure cell death contributed to by 2 hours of room temperature exposure, the control was kept in the same conditions.

After irradiation, the cells were incubated for 24 hours to allow the apoptosis mechanisms to initiate in response to any possible DNA damage caused. Following this a standard MTT assay was performed to establish cell viability for each of the samples. Figure 4.17 shows the results of this experiment.

From these results, it can be seen that the first aim of the experiment has been achieved to a large extent. The blue light has only a small effect on the cell viability (~15%) in comparison to the dark control in the absence of any complexes. The data is noisy but it is worth noting that these are still preliminary experiments and more repeats of this experiment will need to be performed before it is statistically significant.

The second aim of the experiment was to show the complexes are non-toxic to a large extent without light irradiation. Here it can be seen that the RuCy reduces cell viability to 50% by 10 μM treatment. This was surprising as previous unpublished work within the Hannon group on RuCy show the toxicity to be lower than seen here. However, at concentrations of 1 and 2

µM, the cell viability is much more acceptable at 85% and 75% respectively. The RuCy-tetrahedron conjugate exhibited similar behaviour to the MTT assays in chapter 3 in that the cylinder toxicity was reduced. This result could suggest the tetrahedron could have applications guarding against cell toxicity when it is not desired such as in this case.

When observing the cell viability after light irradiation, the RuCy exhibited very high activity. At 2 µM almost no cells were viable, which is significantly different from the dark treatment at the same concentration. The RuCy-tetrahedron conjugate, however, exhibited disappointing toxicity on light irradiation. At 2 µM cell viability is at 55% which is more toxic than the dark control, but considerably less than free cylinder. The toxicity does not change much at all with increase in concentration to 10 µM. This could be because at 2 µM and above, the cylinder and the tetrahedron don't readily dissociate and instead the irradiation simply photo cleaves the tetrahedron instead of cellular DNA. This effect could be advantageous as cleavage could be limited to the tetrahedron to release an internal cargo without causing a toxic effect. Alternatively, addition irradiation time could cleave the tetrahedron, releasing RuCy to then bind cellular DNA and perform secondary cleavage. As observed before, the tetrahedron alone does not have any toxicity and on irradiation, this also remains the case.

Whilst these experiments need more repeats, future experiments could optimise the treatment. Decreasing the treatment time before irradiation from 24 hours could reduce toxicity from the complexes in the dark control. It may also be possible to reduce the irradiation time to make the treatment more practical as the RuCy could have potent activity at far less irradiation time than 2 hours.
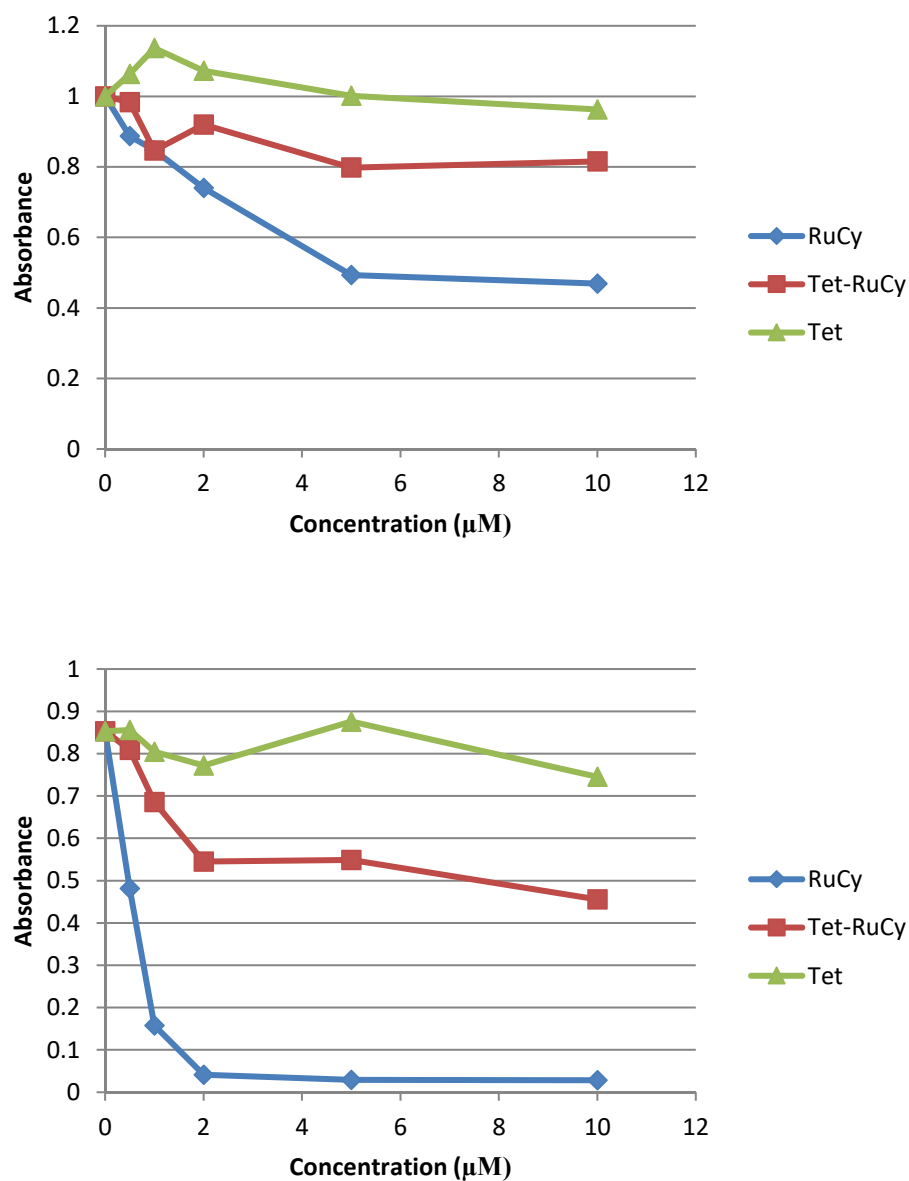
Figure 4.17 – MTT assays of HeLa cells (Cervical) N=1 with data points performed in duplicate. Top) Cell viability when cells have been treated and kept in the dark. Bottom) Cell viability after 2 hour irradiation with blue light. Absorbance has been normalised to the dark 0 µM data to offer easy comparison.

4.3 Conclusions

Overall, the RuCy was shown to be able to bind to DNA and act as a photosensitizer leading to DNA damage. This was shown to be possible even using a weak light source. This opens up further possible research into the area of photodynamic therapy.

When bound to the DNA tetrahedron, the RuCy was shown to break down the structure in two different experiments. This was especially interesting as it is the first time to our knowledge that a photosensitizer has been used in the fashion. In terms of future research, it could be possible to encapsulate a cargo that would be then released following light irradiation. As the tetrahedron-cylinder conjugate has already been shown to enter cells, internal cargo such as cytotoxic viruses[28] or peptides, the latter of which often are degraded by proteolysis before it makes it to cells[29], could be carried into cells in the body and then activated in that area using light.

In initial PDT testing in vitro, the RuCy was shown to have extremely potent cytotoxic activity on irradiation with blue light. (More repeats needed but impossible at the time due to lack of RuCy due to the problematic synthesis). The effect is diminished with the RuCy-tetrahedron conjugate, but this could provide an opportunity to use the conjugate to deliver a different internalised cargo. It is also worth noting that translating these positive results to an in vivo model could be problematic, this is because light in the red region of the spectrum has the best tissue penetration, able to activate effectively around 3 mm deep. Blue light however, can only activate compounds to a depth of 1 mm.[30] Medical devices and light sources for this exact purpose however, are being improved at rapid pace which could minimise this decrease in efficiency.

4.4 Experimental

Materials: Plasmid DNA and enzymes T4 polynucleotide Ligase, T4 polynucleotide Kinase and Exonuclease III were purchased from New England Biolabs. All chemicals were purchased from Sigma Aldrich unless otherwise stated. DNA oligonucleotides were purchased from Eurofins reverse phase HPLC purified. Pre-mixed Acrylamide / Bisacrylamide Stabilized Solution for gel electrophoresis was purchased from National Diagnostics. ATP-32 was sourced from Perkin Elmer. Molecular grade agarose powder was sourced from Bioline. SyBr Gold nucleic acid stain was purchased from Life Technologies. The blue and white LED bulbs used for photoactivation was purchased from electrical world with a GU10 fitting.

Synthesis of Parent Ligand (L: $C_{25}H_{20}N_4$)

4,4'Methylenedianiline (1.99g, 0.01 mol) was dissolved in ethanol (10 ml). To this solution, pyridine-2-carboaldehyde (1.90 ml, 0.02 mol) was added. The solution was then left to stir overnight. The yellow precipitate formed was then collected by vacuum filtration. The crude product was then purified by re-crystallisation from ethanol (3.50 g, 93% yield). The product is a pale yellow solid.

Mass Spectrum (ESI): m/z = 399 {M+Na}

^{1}H NMR (300 MHz), CDCl$_3$, 298K): δ 8.71 (2H, d, J = 3.9 Hz, 6py), δ 8.63 (2H, s, J = H$_{im}$), δ 8.22 (2H, d, J = 7.0 Hz 3py), δ 7.82 (2H, td, J = 8.3, 1.9, 0.6 Hz, 4py), δ 7.40 (2H, ddd, J = 7.6, 4.9, 1.2 Hz, 5py), δ 7.30 (8H, m, Ph$_a$ and Ph$_b$), δ 4.08 (2H, s, CH$_2$)

Synthesis of Ruthenium Cylinder, **[Ru$_2$(L)$_3$](PF$_6$)$_4$:** RuCl$_3$ (3g, 14.5 mmol) was dissolved in 15 mL of DMSO and heated under reflux at 195°C for 5 minutes. The solution was reduced *in vacuo* to concentrate the solution down to 1 mL. Excess cold acetone was then added to precipitate a yellow solid. The yellow precipitate was then filtered and washed with cold acetone to furnish the yellow solid Ru(DMSO)$_4$Cl$_2$.

Ru(DMSO)$_4$Cl$_2$ (0.988 g, 2.04 mmol) and parent ligand (1.150 g, 3.06 mmol) were added to degassed Ethylene glycol (50 ml) and heated to reflux under argon at 200°C for 5 days. The mixture was allowed to cool and an excess saturated methanolic solution of ammonium hexaflourophosphate was added. The suspension was cooled on ice before the precipitate was filtered and washed with methanol (2 x 40 ml) and dried with ether (3 x 100 ml). The dark brown product was purified by column chromatography on alumina using 20:1:1 MeCN/H$_2$O/ KNO$_{3(aq)}$ solution as eluent to yield the product as an orange solid (11 mg, 0.6% yield). The chloride complex could be formed by anion metathesis.

Mass Spectrum Positive ion ESI: m/z = 666 [M-(PF$_6$)$_4$]$^{2+}$, 444 [M-(PF$_6$)]$^{3+}$, 333.2 [M-(PF$_6$)$^{4+}$

^{1}H NMR (300MHz), CD$_3$CN, 298K : δ = 8.7 (2H, s, H$_{im}$), 8.45 (2H, d, J = 7.6 Hz, 6py), 8.35 (2H, td, J = 7.78 Hz, 5.0 Hz, 3py), 7.65 (2H, d, J = 6.0 Hz, 4py), 7.65 (2H, d, J = 6.0 Hz, 5py), 7.0 (4H, d, J = 8.4 Hz, Ph$_{a/b}$), 5.7 (4H, d, J = 8.3 Hz, Ph$_{a/b}$), 4.1 (2H, s, CH$_2$)

UV-Vis (CH$_3$CN) : λ$_{max}$ (ε / dm^3 mol^{-1} cm^{-1}) 485 (24200)

Plasmid Photocleavage: PuC19 plasmid (200 ng per sample) in Tris.HCl buffer (50mM pH 8.0) was incubated with RuCy (0.33 µM) to a final volume of 10 µL for 1 hour in the dark in 0.5 mL Eppendorfs. Samples were then illuminated for the allotted time over either a 1W blue or 1W white LED bulb. Samples not requiring illumination were then kept at 4°C in the dark.

Agarose Gel Electrophoresis: 1% agarose gel was prepared by mixing 0.9 g agarose in 1 X TAE buffer (40mM Tris, 20mM Acetic Acid, 1mM EDTA, pH 8.5) and heated in a microwave until fully dissolved. The gel was allowed to cool to around 60°C before being poured into a 20x15 cm gel cassette in a casting tray, ensuring any bubbles created were removed with a spatula. The gel was allowed to cool and set fully for 60 mins. Once set the gel was placed inside the buffer tank and immersed in 1 x TAE buffer. Samples were then loaded into the wells, using purple gel loading dye (New England Biolabs) to aid in visualisation and to help the samples settle in the well. The gel was then run at 4V/cm for 120 mins. The gel cassette was then removed from the tank and stained using SYBR gold nuclear acid gel stain (Invitrogen) for 30 mins. The gel was then photographed and analysed using a UV transilluminator (AlphaImager HP, ProteinSimple).

Ligated Tetrahedron Construction: Four oligonucleotides were purchased from Eurofins, each of 63 bases in length. The sequences were as follows:

1: AGGCAGTTGAGACGAACATTCCTAAGTCTGAAATTTATCACCCGCCATAGTAGACGTATCACC

2: CTTGCTACACGATTCAGACTTAGGAATGTTCGACATGCGAGGGTCCAATACCGACGATTACAG

3: GGTGATAAAACGTGTAGCAAGCTGTAATCGACGGGAAGAGCATGCCCATCCACTACTATGGCG

4: CCTCGCATGACTCAACTGCCTGGTGATACGAGGATGGGCATGCTCTTCCCGACGGTATTGGAC

All strands were reverse-phase HPLC purified. Each strand was then phosphorylated by mixing 2.4 µl of 100 µM of the oligonucleotide with 9.6 µl of MilliQ water, 2 µl of 10 x T4 polynucleotide kinase buffer, 2 µl of bacteriophage T4 polynucleotide kinase and 4 µl of ATP in an Eppendorf and leaving to incubate at 37°C for an hour before heat inactivation at 80°C. Each phosphorylated strand was then purified using a QIAquick nucleotide removal kit following a previously discussed protocol in chapter 2. Stoichiometric quantities of each phosphorylated strand were mixed in TM buffer (10mM Tris base, 5mM MgCl$_2$, pH 8) and heated to 95 $^{\circ}$C in a thermal block for 5 minutes. On cooling at room temperature for 30 seconds, the eppendorf was placed on ice for 5 minutes and then centrifuged for 5 seconds. 10mM DTT and 1 µL per 10 µL of reaction mixture of T4 DNA ligase enzyme was added and the resulting mixture left to incubate for 24 hours at room temperature. The enzyme was once again heat inactivated at 70°C for 10 mins and the resulting DNA product purified on a 10% denaturing PAGE gel and the excised DNA concentration check by UV-Vis.

Ligated Tetrahedron Photocleavage: 5 µL of LigTet was mixed with 0.75 mL of 10 µM RuCy and 4.25 µL of MilliQ H$_2$O. The sample was then irradiated under 1W Blue LED light for the allotted time before being stored at 4°C in the dark.

DNA digestion: Samples to be digested were first bufferd to 1x concentration using 10x NEBuffer 1 (New England Biolabs). 1 µL of Exonuclease III (New England Biolabs) per 10 µL of reaction mixture was then added. The mixture was incubated for 30 mins and heat inactivated at 70°C for 10 mins.

Denaturing Gel Electrophoresis: 10% denaturing polyacrylamide gel was prepared by mixing 17 mL 30% 29:1 acrylamide/bis-acrylamide, 5 mL 10x TB buffer, 24g Urea, 25 µL

TEMED, 230 µL 10% ammonium persulfate solution and topped up to 50 mL with dd H_2O and leaving to set between two glass plates with a comb for 60 mins. The samples where then loaded and run at 11V /cm of gel for 180 mins. The gel was then removed from the plates and stained with SYBR gold nucleic acid get stain for 30 mins before being visualised and photographed under a UV transilluminator.

Native Polyacrylamide Gel Electrophoresis: 10% Native gel was prepared by mixing 17 mL 30% 29:1 acrylamide/bis-acrylamide, 5 mL 10x TB buffer, 25 µL TEMED, 230 µL 10% ammonium persulfate solution and topped up to 50 mL with dd H_2O and leaving to set between two glass plates with a comb for 60 mins. The samples were then loaded and run at 11V /cm of gel for 180 mins. The gel was then removed from the plates and stained with SYBR gold nucleic acid get stain for 30 mins before being visualised and photographed under a UV transilluminator.

Photodynamic Therapy MTT

HeLa cells were seeded into two 96-well plates at 5000 cells per well, each well containing 200 µL of DMEM. This plates were left for 24 hours before being treated with the complexes to the final concentrations indicated to a volume of 100 µL in DMEM. Cells were incubated for a further 24 hours with the complexes. One plate was then irradiated with a 574 nm blue LED bulb for 1 hour before being placed back inside the incubator for 15 minutes to retain a temperature of 37ºC before another hour of irradiation. Following this, cells were then incubated for a further 24 hours before cell viability was checked through a standard MTT assay described above.

4.5 References

1. Y. Sun, L.E. Joyce, N.M. Dickson, and C. Turro, *Efficient DNA photocleavage by [Ru(bpy)2(dppn)]2+ with visible light.* Chemical Communications, 2010. **46**(14): p. 2426-2428.

2. M.J. Clarke, *Ruthenium metallopharmaceuticals.* Coordination Chemistry Reviews, 2003. **236**(1–2): p. 209-233.

3. A.E. Friedman, J.C. Chambron, J.P. Sauvage, N.J. Turro, and J.K. Barton, *A molecular light switch for DNA: Ru(bpy)2(dppz)2+.* Journal of the American Chemical Society, 1990. **112**(12): p. 4960-4962.

4. J.K. Barton, *Metals and DNA: molecular left-handed complements.* Science, 1986. **233**(4765): p. 727-34.

5. N.J. Turro, J.K. Barton, and D.A. Tomalia, *Molecular recognition and chemistry in restricted reaction spaces. Photophysics and photoinduced electron transfer on the surfaces of micelles, dendrimers, and DNA.* Accounts of Chemical Research, 1991. **24**(11): p. 332-340.

6. L. Troian-Gautier and C. Moucheron, *RutheniumII Complexes bearing Fused Polycyclic Ligands: From Fundamental Aspects to Potential Applications.* Molecules, 2014. **19**(4): p. 5028.

7. R. Lincoln, L. Kohler, S. Monro, H. Yin, M. Stephenson, R. Zong, A. Chouai, C. Dorsey, R. Hennigar, R.P. Thummel, and S.A. McFarland, *Exploitation of Long-Lived 3IL Excited States for Metal–Organic Photodynamic Therapy: Verification in a Metastatic Melanoma Model.* Journal of the American Chemical Society, 2013. **135**(45): p. 17161-17175.

8. Y. Zhang, Q. Zhou, Y. Zheng, K. Li, G. Jiang, Y. Hou, B. Zhang, and X. Wang, *DNA Photocleavage by Non-innocent Ligand-Based Ru(II) Complexes.* Inorganic Chemistry, 2016. **55**(9): p. 4296-4300.

9.   J.-P. Lecomte, A. Kirsch-De Mesmaeker, M.M. Feeney, and J.M. Kelly, *Ruthenium(II) Complexes with 1,4,5,8,9,12-Hexaazatriphenylene and 1,4,5,8-Tetraazaphenanthrene Ligands: Key Role Played by the Photoelectron Transfer in DNA Cleavage and Adduct Formation.* Inorganic Chemistry, 1995. **34**(26): p. 6481-6491.

10.   T. Romero-Morcillo, F.J. Valverde-Munoz, M.C. Munoz, J.M. Herrera, E. Colacio, and J.A. Real, *Two-step spin crossover behaviour in the chiral one-dimensional coordination polymer [Fe(HAT)(NCS)2][infinity].* RSC Advances, 2015. **5**(85): p. 69782-69789.

11.   Q.-X. Zhou, W.-H. Lei, C. Li, Y.-J. Hou, X.-S. Wang, and B.-W. Zhang, *DNA photocleavage in anaerobic conditions by a Ru(ii) polypyridyl complex with long wavelength MLCT absorption.* New Journal of Chemistry, 2010. **34**(1): p. 137-140.

12.   J. Wang, D.F. Zigler, N. Hurst, H. Othee, B.S.J. Winkel, and K.J. Brewer, *A new, bioactive structural motif: Visible light induced DNA photobinding and oxygen independent photocleavage by RuII, RhIII bimetallics.* Journal of Inorganic Biochemistry, 2012. **116**: p. 135-139.

13.   D.E. Dolmans, D. Fukumura, and R.K. Jain, *Photodynamic therapy for cancer.* Nature Review Cancer, 2003. **3**(5): p. 380-7.

14.   B.C. Wilson, *Photodynamic therapy for cancer: principles.* Canadian Journal Gastroenterol and Hepatology, 2002. **16**(6): p. 393-6.

15.   T.J. Dougherty, C.J. Gomer, B.W. Henderson, G. Jori, D. Kessel, M. Korbelik, J. Moan, and Q. Peng, *Photodynamic therapy.* Journal of the National Cancer Institute, 1998. **90**(12): p. 889-905.

16.   S. Tsukagoshi, *[Porfimer sodium (Photofrin-II)].* Gan To Kagaku Ryoho, 1995. **22**(9): p. 1271-8.

17.   E.F. Gudgin Dickson, R.L. Goyan, and R.H. Pottier, *New directions in photodynamic therapy.* Cell Molecular Biology, 2002. **48**(8): p. 939-54.

18.   R. Shi, C. Li, Z. Jiang, W. Li, A. Wang, and J. Wei, *Preclinical Study of Antineoplastic Sinoporphyrin Sodium-PDT via In Vitro and In Vivo Models.* Molecules, 2017. **22**(1): p. 112.

19.   J. Malina, M.J. Hannon, and V. Brabec, *Interaction of Dinuclear Ruthenium(II) Supramolecular Cylinders with DNA: Sequence-Specific Binding, Unwinding, and Photocleavage.* Chemistry – A European Journal, 2008. **14**(33): p. 10408-10414.

20.   S.R. Chatterjee, S.J. Shetty, T.P.A. Devasagayam, and T.S. Srivastava, *Photocleavage of plasmid DNA by the prophyrin meso-tetrakis[4-(carboxymethyleneoxy)phenyl]porphyrin.* Journal of Photochemistry and Photobiology B: Biology, 1997. **41**(1): p. 128-135.

21.   Q.-X. Zhou, W.-H. Lei, Y. Sun, J.-R. Chen, C. Li, Y.-J. Hou, X.-S. Wang, and B.-W. Zhang, *[Ru(bpy)3−n(dpb)n]2+: Unusual Photophysical Property and Efficient DNA Photocleavage Activity.* Inorganic Chemistry, 2010. **49**(11): p. 4729-4731.

22.   S.R. Chatterjee, S.J. Shetty, T.P. Devasagayam, and T.S. Srivastava, *Photocleavage of plasmid DNA by the prophyrin meso-tetrakis[4-(carboxymethyleneoxy)phenyl]porphyrin.* Journal of Photochemistry and Photobiology B, 1997. **41**(1-2): p. 128-35.

23.   S. Mashiko, N. Suzuki, S. Koga, M. Nakano, T. Goto, T. Ashino, I. Mizumoto, and H. Inaba, *Measurement of rate constants for quenching singlet oxygen with a Cypridina luciferin analog (2-methyl-6-[p-methoxyphenyl]-3,7-dihydroimidazo[1,2-a]pyrazin-3-one) and sodium azide.* Journal of Bioluminescence and Chemiluminescence, 1991. **6**(2): p. 69-72.

24.   C. Kanony, A.-S. Fabiano-Tixier, J.-L. Ravanat, P. Vicendo, and N. Paillous, *Photosensitization of DNA Damage by a New Cationic Pyropheophorbide Derivative: Sequence-specific Formation of a Frank Scission.* Photochemistry and Photobiology, 2003. **77**(6): p. 659-667.

25.   B. Armitage, *Photocleavage of Nucleic Acids.* Chemical Reviews, 1998. **98**(3): p. 1171-1200.

26.   R.P. Goodman, I.A.T. Schaap, C.F. Tardin, C.M. Erben, R.M. Berry, C.F. Schmidt, and A.J. Turberfield, *Rapid Chiral Assembly of Rigid DNA Building Blocks for Molecular Nanofabrication.* Science, 2005. **310**(5754): p. 1661-1665.

27. C.D. Mol, C.-F. Kuo, M.M. Thayer, R.P. Cunningham, and J.A. Tainer, *Structure and function of the multifunctional DNA-repair enzyme exonuclease III.* Nature, 1995. **374**(6520): p. 381-386.

28. K.P. Garnock-Jones, *Talimogene Laherparepvec: A Review in Unresectable Metastatic Melanoma.* BioDrugs, 2016. **30**(5): p. 461-468.

29. J. Thundimadathil, *Cancer Treatment Using Peptides: Current Therapies and Future Prospects.* Journal of Amino Acids, 2012. **2012**: p. 13.

30. M.C.A. Issa and M. Manela-Azulay, *Terapia fotodinâmica: revisão da literatura e documentação iconográfica.* Anais Brasileiros de Dermatologia, 2010. **85**: p. 501-511.

Chapter 5

Targeting the trans-activating response element (TAR) in the HIV Virus to prevent replication

5.1 Introduction

The human immunodeficiency virus (HIV) is a lentivirus which is a part of a larger group of viruses known as retroviruses.[1] The virus once inside human cells causes acquired immunodeficiency syndrome which is characterised as a total failure of the human immune system. Without an immune system, patients become very vulnerable to many illnesses and diseases which invariably are fatal. Without treatment, a person infected with HIV can expect to live around 9-11 years.[2] HIV is spread through sharing of many types of bodily fluids, mainly blood and genital fluids and it is estimated, as of 2015, 36.7 million people were infected with HIV and in the same year 1.1 million people died due to illnesses and diseases caused by AIDs.[3] Whilst many drugs have been developed over recent years that have been able to manage the disease, a cure still remains elusive.

The HIV viron itself is a spherical structure of about 120 nm in diameter and Figure 5.1 shows a basic overall structure.[4] The main features include the 2 single strands of RNA which
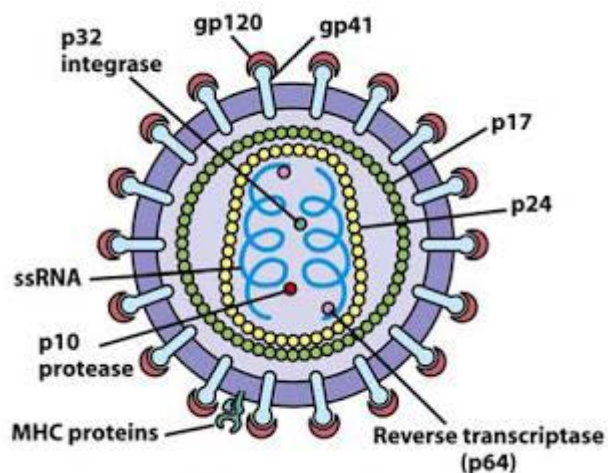
Figure 5.1 - Schematic diagram of the HIV virus. Taken from 4.

hold the sequences of the 9 genes of HIV needed to replicate inside the host cell. These are joined inside the central capsid by the enzymes key to the replication cycle: protease, integrase, ribonuclease and reverse transcriptase.[5] This internal capsid is all enclosed by the viral protein for integrity. Around this capsid is a viral envelope, comprised of a lipid bilayer, which on the surface contains two key proteins, glycoprotein (gp) 120 and gp 41.[6] These two proteins are key to enabling the virus to attach and merge into host cells.

The lifecycle of the virus has been important to drug development as targeting different stages of the cycle has led to key breakthroughs in the field. Figure 5.2 illustrates the major steps of the cycle of HIV.[7] It begins with the glycoproteins on the virus binding to CD4 receptors on the membrane of a host cell. These types of cells tend to be macrophages and T cells. Once bound, the virus can then fuse with the host cell and release the internal RNA and enzymes
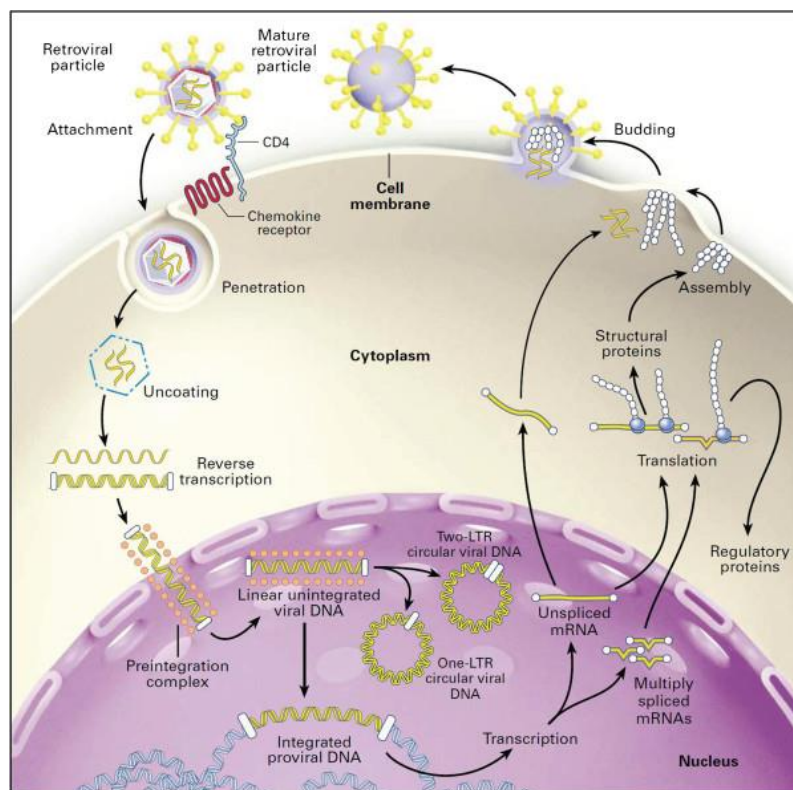
Figure 5.2 - The life cycle of the HIV virus. Taken from 7.

into the cell. The ssRNA then undergoes reverse transcription to form dsDNA which is then localised to the cell nucleus. The enzyme integrase can then integrate this viral DNA into the host cell genome. This DNA codes for the cell to produce new ssRNA and mRNA, which produces key viral proteins, all to form new virons. These 'bud' together at the host cell membrane to form new virus capsules which then exit the cell.[8]

This step-wise cycle provides very clear targets for drug design and has led to five major anti-viral drug families. Entry inhibitors target the binding between the CD4 receptors on the host
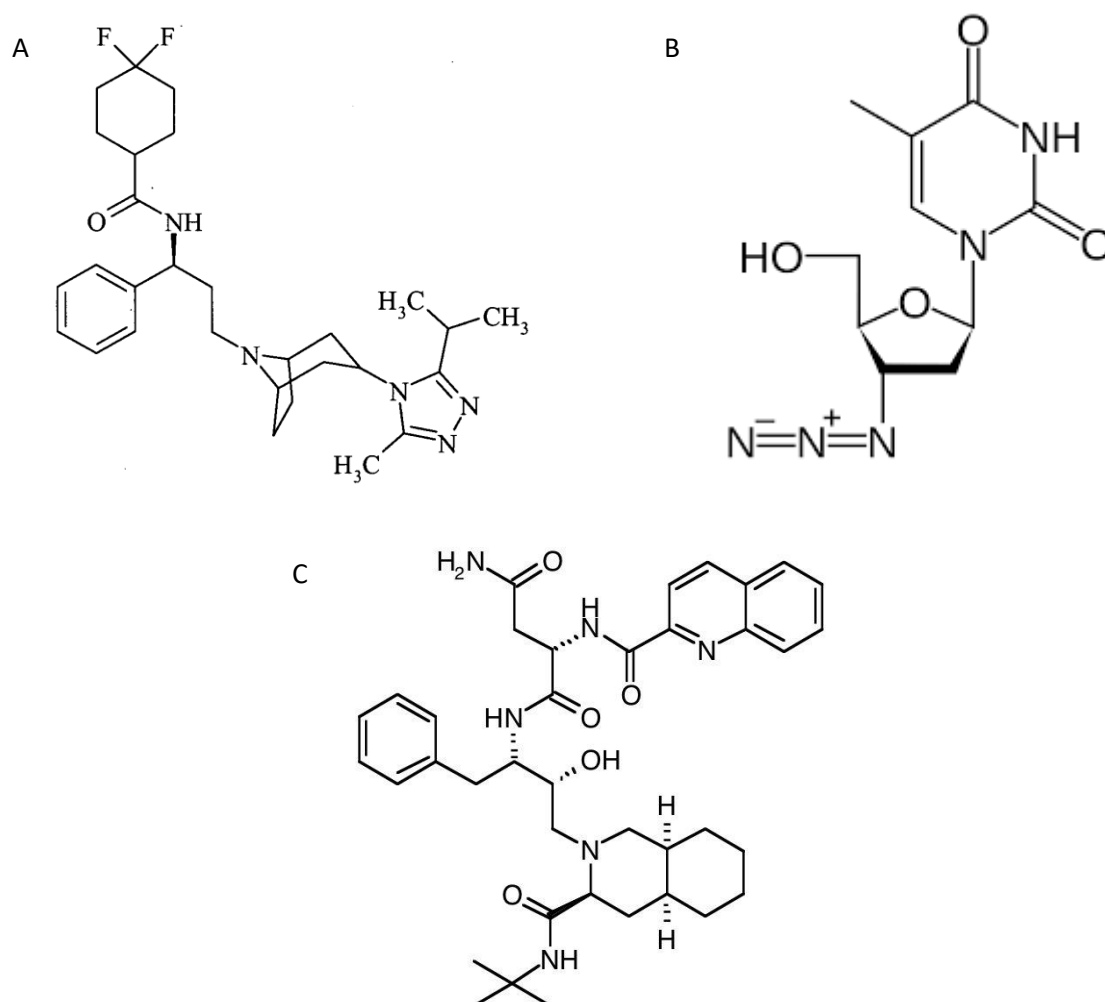
Figure 5.3 – A) Structure of Maraviroc, B) structure of Zidovudine, C) structure of Saquinavir. Taken from refs 9, 12 and 19 respectively.

cell and the GP120 on the viron in the very first stage of the cycle. Maraviroc (figure 5.3a) is one such inhibitor.[9] Fusion inhibitors work in a similar fashion, but target the GP41 on the virus membrane which is responsible for fusing the virus with the host cell membrane. Enfuritide is a licensed drug that does exactly this, by binding to GP41, it prevents entry to host cells.[10]

Reverse transcriptase inihibitors (RTIs) work by preventing the transcription of the HIV ssRNA to dsDNA, they do this by acting as a DNA base, but lacking a phosphate group which renders the transcriptase unable to continue once it has paired an RTI into the duplex.[11] The class contains the most available drugs and the first ever licensed HIV drug, Zidovudine (figure 5.3b).[12] Integrase inhibitors work by preventing the transfer and integration of the dsDNA into the host cell nuclear DNA. There are many possible ways in which this can happen, but the main focus of research and development has been to prevent the initial binding of the viral DNA to the integrase enzyme before the transfer to the cell nucleus.[13] This is done by exploiting two features on the enzyme, a small hydrophobic pocket and two divalent Mg^{2+} sitting inside the enzymes active site.[14] Successful drugs such as Raltigravir and Elvitegravir (Figure 5.4) show the consensus functional groups necessary for strong enzyme binding and potent integrase inhibition. A hydrophobic flouro-benzyl moiety, for the
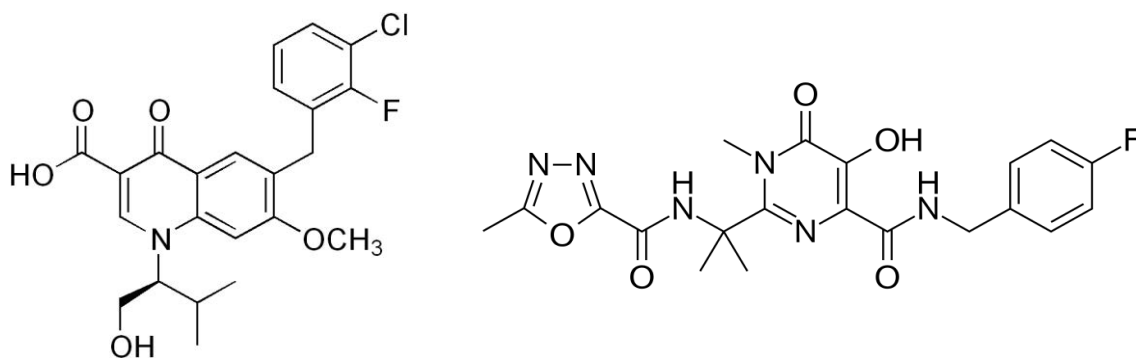

Figure 5.4 - Integrase inhibitors Elvitegravir (left) and Raltegravir (right)

hydrophobic pocket, and the hydroxyl-benzyl group flanked by 2 carbonyl groups to form a suitable chelation point for the two Mg^{2+} ions. [15,16] This actively outcompetes in binding with the HIV DNA and stops the cycle.

The final class of drugs are known as protease inhibitors. These work by targeting the enzyme HIV1-protease, which works on newly released HIV virons. When initially released, the virus contains large proteins which must be broken down to form key structural parts of the virus and the internal enzymes. During this stage the virus is considered 'immature' and cannot infect new host cells.[17] HIV1-protease breaks down these large proteins to mature the cell into the infective form. Peptide-like drugs have been developed which can bind to this protease, but contain an un-cleavable hydroxyethylen group which blocks enzyme action.[18] The first drug of its class, Saquinavir (figure 5.3c) illustrates this functionality.[19]

These five families of drugs have led to very effective multi-drug therapies which can keep levels of HIV virus in the body at very low, sometimes undetectable levels.[20] Unfortunately, this drug regime does not fully eliminate the HIV virus from the body and if medication is ceased, a rapid increase of virus levels is observed.[20] Whilst there is strong debate over the possible reservoirs harbouring virus, one theory for the survivability in the body is the role of the trans-activating regulatory (tat) protein. Tat protein is a small protein between 86 and 101 amino acids long which regulates the transcription of the integrated HIV DNA by polymerase to produce full length HIV RNA transcripts.[21] It does that by binding to a short looped piece of HIV RNA in a region called the trans-activator region (TAR).[21] TAR and Tat bring together the positive transcription elongation complex (P-TEFb) and cyclin T1, Which facilitate the production of full-length viral RNA (Figure 5.5).[23] In the absence of Tat, non-complete strands of HIV RNA are produced which code for mRNA to produce tat protein to begin the cycle instead of full virons.[24] This self-sustaining process leads to exponential

increase or 'explosive' increase in virus levels.[24] Tat is released into the bloodstream to encourage further replication and also has apoptotic action against T-cells, protecting infected host cells from immune response.[25] It is theorised that under current anti-retroviral regimes, tat protein is still secreted into the blood stream.[26] This greatly assists the dormant, low population HIV reservoirs to repopulate rapidly if anti-retro viral therapy is ceased.[27] Clearly this is an attractive target for a new family of anti-viral drugs.
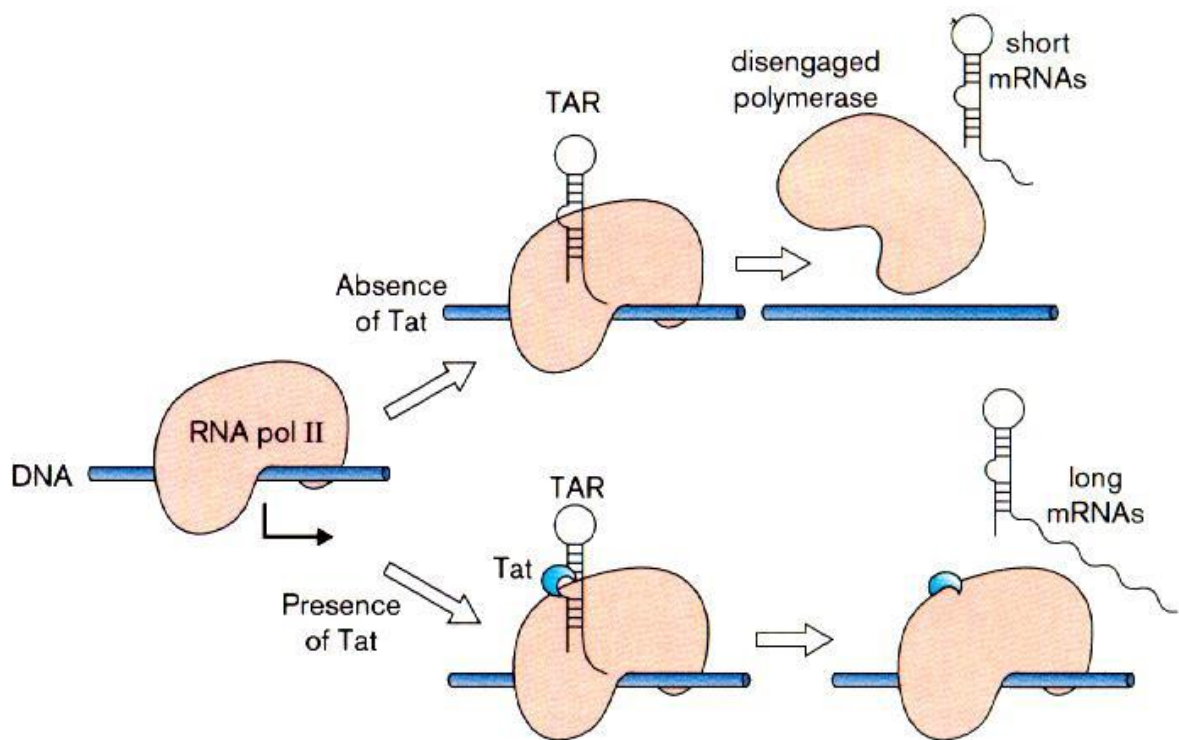
Figure 5.5 - A schematic diagram illustrating the binding location of TAR RNA and Tat protein on RNA polymerase and the products of binding. Taken from 21.

In 1993 Churcher *et al*. identified and characterised the TAR-TAT interaction *in vitro* by gel electrophoresis using synthetic RNA to mimic the looped region (Figure 5.6).[28] Since then there have been some attempts to target this interaction, such as with peptides that

competitively bind the TAR RNA.[29] However, no attempts have yet made it to the clinic. Previous studies in our group on cylinders have shown the ability of the iron cylinder to bind to DNA bulged regions.[30] Following on from this, it was shown that the iron cylinder could bind to the 3-base bulge on TAR RNA.[31] This chapter aims to assess the binding capabilities of both the ruthenium cylinder and a nickel cylinder to TAR RNA, the potential inhibition of tat binding and subsequent anti-viral activity.
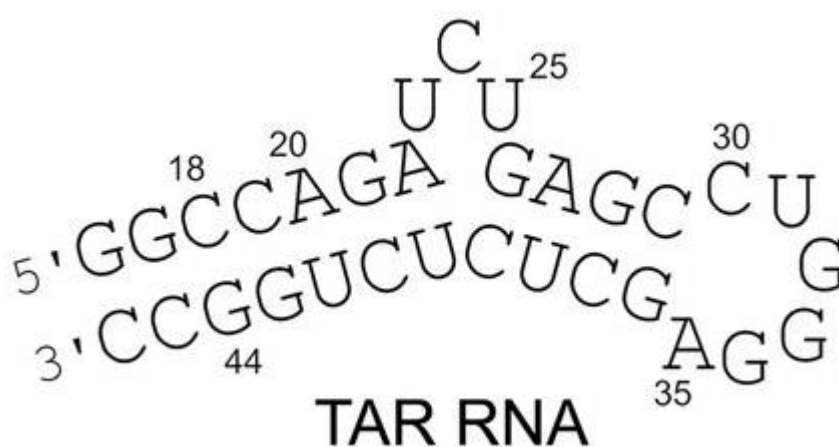
Figure 5.6 - Structure of the looped region of TAR RNA, showing the 3 base UCU bulge where both cylinder and Tat protein bind. Taken from 31.

5.2 Results and Discussion

5.2.1 Gel Electrophoresis

Nickel and ruthenium cylinders for this section were kindly provided by Dr Lucia Cardo.

After observing the potent anti-viral activity possessed by the cylinders. It is important to verify whether the activity is due to the inhibition of Tat protein binding to the TAR RNA looped region. To do this, a 31-mer RNA strand was synthesised (Integrated DNA

Technologies) (Figure 5.6). Samples of the RNA were then incubated with each of the cylinders and run on a non-denaturing gel. Figure 5.7 shows the gels obtained. With increasing concentration of each of the cylinders, the RNA band migration is slowed. This is indicative that all the cylinders, iron, nickel and ruthenium all have an affinity for the RNA loop. This is due to the bulky nature of the cylinders creating a larger overall complex which migrates more slowly through the gel. The positive charge on the cylinders also negates some of the negative charge on the RNA, which in turn means the cathode has less of a negative charge to attract through the gel. It is difficult to see here if any of the cylinders have more of an effect each other and any differences would be subtle anyway, but it is certain that they all bind.

By designing the synthetic RNA to be as short as possible, cylinder binding to duplex DNA was unlikely in the tail regions, making bulge binding the most probable mode. Although efforts continue to obtain a crystal structure of this, it remains elusive to fully confirm the cylinder binding position. At this point however, it is the most likely binding position.
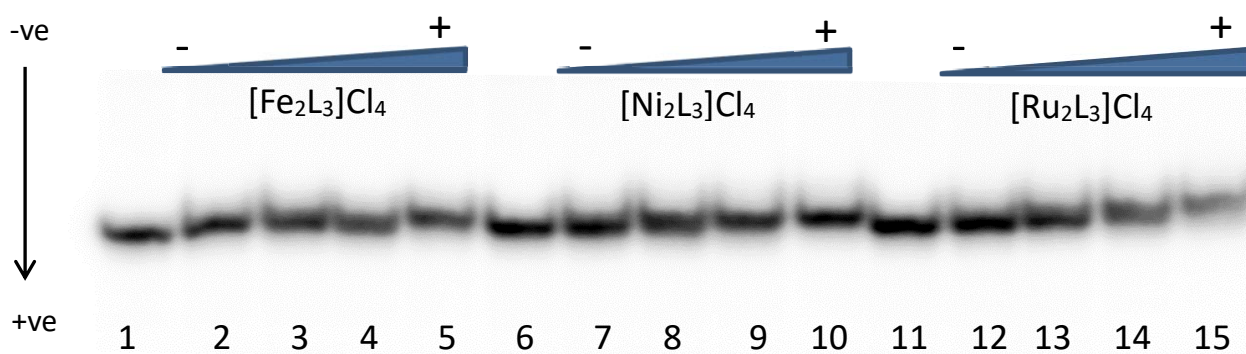
Figure 5.7 – Autoradiogram showing the effect of the cylinders on the TAR RNA (2 μM). Control wells 1, 6 and 10 containing RNA only. Wells 2-5 containing increasing concentrations of iron cylinder (1, 2, 3 and 4 μM respectively); Wells 7-10 containing increasing concentrations of nickel cylinder (1, 2, 3 and 4 μM respectively) and wells 12-15 containing increasing concentrations of ruthenium cylinder (1, 2, 3 and 4 μM respectively).

5.2.2 ADP-1 Binding

The next step in the investigation was to observe binding between the TAR RNA and Tat protein. However, by utilising a short fragment of TAR, binding to the full HIV-1 tat protein proved very difficult to replicate in-vitro with this particular sequence. Instead, Churcher *et al.* had reported the main regions of the 101-amino acid recombinant tat protein for binding to TAR.[28] By synthesising the polypeptide ADP-1, containing amino acid residues 37-72 with a sequence of SFTTKALGISYGRKKRRQRRRPPQGSQTHQVSLSKQ with serine replacing cysteine in position one to reduce oxidation probability[31] it was possible to create an in-vitro model of the binding interaction. Figure 5.8 illustrates by form of gel electrophoresis the complex band formed when ADP-1 peptide is added in increasing concentrations to a radiolabelled sample of TAR RNA.
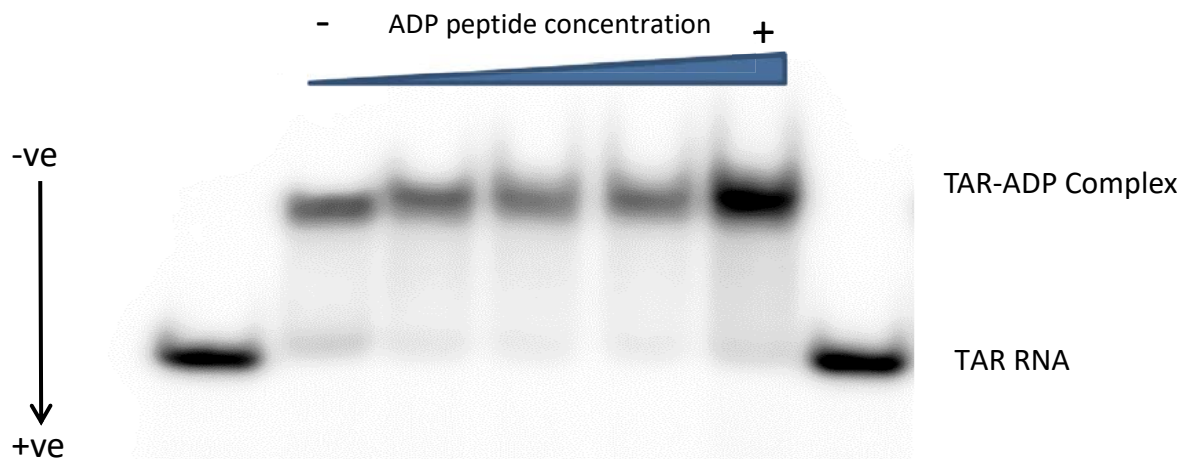
Figure 5.8 – Autoradiogram illustrating the complex formed between TAR RNA (0.1 μM) and the ADP-1 peptide. With increasing peptide concentration (0.2 – 1.0 μM) the band intensity corresponding to complex increases.

5.2.3 Inhibition of binding using a range of Cylinders

With a positive control established, the extent of the ability of the cylinders to inhibit RNA-peptide binding could be assessed. This would also confirm that anti-viral activity observed is in fact partly due to this action. Figure 5.9 shows representative polyacrylamide gels of three identical repeat experiments involving the iron, nickel and ruthenium cylinders. Each gel shows the band corresponding to RNA-peptide binding as before. With increasing cylinder concentration, the intensity of this band diminishes. This is due to cylinder competitively binding with the RNA bulge, blocking binding action of the peptide. All three cylinders clearly exhibit this action. Another feature of the gels on figure 5.9 is the retardation of the RNA band upon cylinder binding that is also observed in figure 5.7. This further confirms cylinder competitively binding RNA and blocking peptide binding.

By quantifying the RNA-peptide band, an attempt can be made to compare the inhibition action of each of the cylinders. Figure 5.10 shows raw data of the percentage of RNA-peptide complex against concentration of cylinder (average data of 3 repeat experiments for each cylinder). The nickel cylinder immediately appears to be most active in blocking complex formation.

The iron and ruthenium both have similar activity within the error bars on the graph, but the nickel cylinder has consistently the most potent action, followed by the iron cylinder and then the ruthenium. This cause of this trend is hard to confirm. With regards to aqueous stability, the ruthenium cylinder is the most stable, followed by the NiCy with the FeCy the least stable. *In vitro* cell toxicity trends to run the opposite way, showing the FeCy the most active and RuCy the least. The crystal structures of the cylinders show the size and shape of all three are very comparable, it is possible however, that subtle changes in ligand orientation amongst the
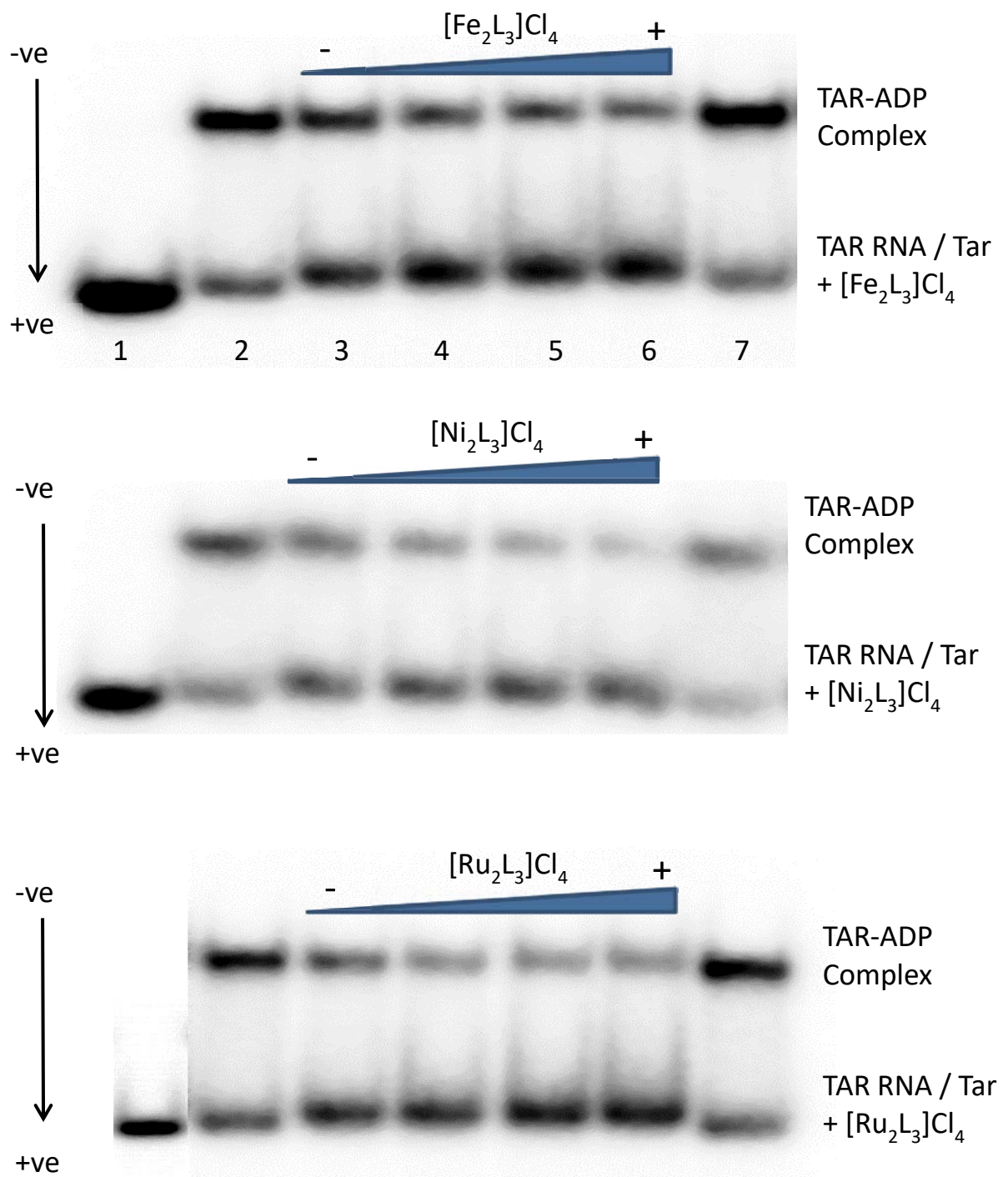
Figure 5.9 - Autoradiograms illustrating the inhibition of the formation of the ADP peptide (300 nM) – TAR RNA (100 nM) complex, with increasing cylinder concentration (0.2 μM – 1.6 μM), less complex is able to form due to cylinder binding to RNA. Retardation of RNA band is observed confirming cylinder binding. Each gel image is one representative of three identical repeat PAGE experiments.

metals could be responsible for the difference in the binding strength to this specific RNA loop. Further experimentation is needed to fully confirm this trend such as NMR or X-ray crystallography of the cylinders-RNA complex.
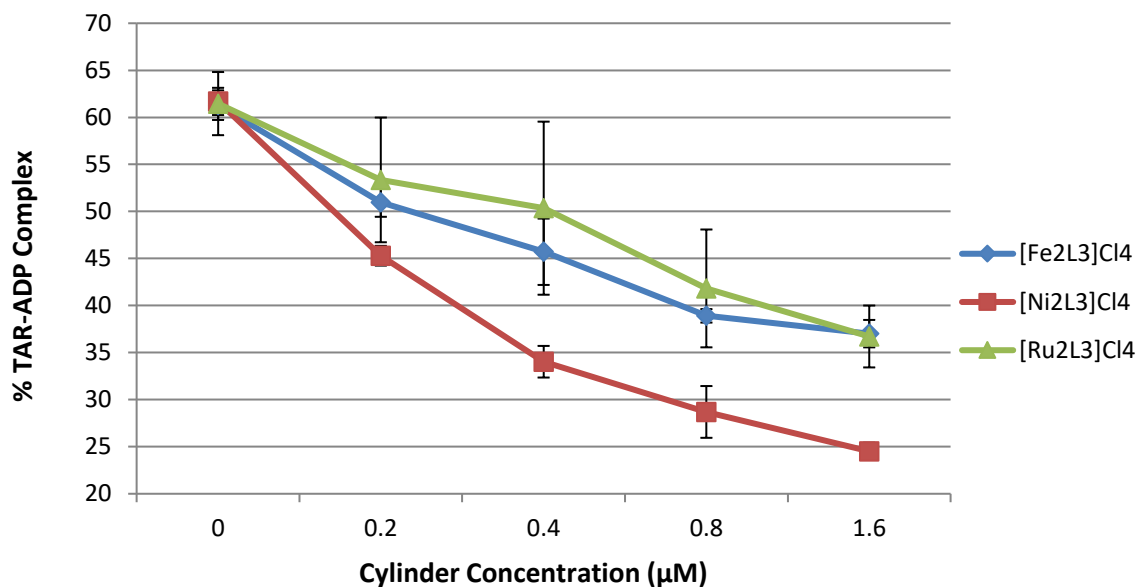
Figure 5.10 – Line graph illustrating the inhibition of RNA (100 nM) – ADP-1 (300 nM) binding through addition of increasing concentrations of cylinder from 0-1.6 µM. Error bars show the standard error of the mean where n=3.

5.3 Conclusions

From these experiments, iron, nickel and ruthenium cylinders were shown to be able to inhibit TAR-ADP-1 complex formation by binding to the TAR RNA looped region. Follow on experiments in collaboration with Dr Lucia Cardo and Dr Isabel Nawroth have shown that the cylinders can inhibit HIV replication *in cellulo* in mammalian HIV infected cell lines, With the RuCy proving particularly effective. To further prove the effectiveness of these cylinders, the cytotoxicity of each of the cylinders was tested against the same cell lines, showing the nickel cylinder to have minimal cytotoxicity during anti-viral treatment whilst the ruthenium had a modest cytotoxic effect. The iron cylinder, however, proved to be too cytotoxic to be considered useful as an anti-viral agent.

This new class of anti-viral agents is particularly interesting as many viruses can mutate viral sequences and vary RNA bulge shapes to develop sequence specific drug resistance.[32] However, the TAR RNA bulge appears to be essential to TAT recognition and therefore HIV replication. This means the only mutations the virus has been observed exhibiting here have been sequence changes within the bulge sequence rather that structural. As the cylinder binds the bulge structure and not the sequence, the cylinder would not be affected by such viral mutations. The cylinder has also been shown to be able to bind to a wide variety of bulge structures, not just this one,[30] which provides further advantage against any possible viral structural mutations.

Therefore, these experiments have shown that targeting RNA structures which are prevalent in a wide variety of viruses[33] is an effective new approach to anti-viral research.

5.4 Experimental

Ruthenium and nickel cylinders were provided by Dr Lucia Cardo and were synthesised by following previously reported synthesis.[34, 35] The synthetic oligoribonucleotide (TAR) (Figure 5.6) was purchased from Integrated DNA technologies ready reverse phase HPLC purified. ADP peptide was purchased from Schafer-N (Copenhagen, Denmark). Pre-mixed Acrylamide / Bisacrylamide Stabilized Solution for gel electrophoresis was purchased from National Diagnostics. ATP-32 was sourced from Perkin Elmer. T4 Polynucleotide kinase was purchased from New England Biolabs.

Synthesis of Parent Ligand (L: $C_{25}H_{20}N_4$)

4,4'Methylenedianiline (1.99g, 0.01 mol) was dissolved in ethanol (10 ml). To this solution, pyridine-2-carboaldehyde (1.90 ml, 0.02 mol) was added. The solution was then left to stir overnight. The yellow precipitate formed was then collected by vacuum filtration. The crude product was then purified by re-crystallisation from ethanol (3.50 g, 93% yield). The product is a pale yellow solid.

Mass Spectrum (ESI): m/z = 399 [M+Na]

^{1}H NMR (300 MHz), CDCl$_3$, 298K): δ 8.71 (2H, d, J = 3.9 Hz, 6py), δ 8.63 (2H, s, J = H$_{im}$), δ 8.22 (2H, d, J = 7.0 Hz 3py), δ 7.82 (2H, td, J = 8.3, 1.9, 0.6 Hz, 4py), δ 7.40 (2H, ddd, J = 7.6, 4.9, 1.2 Hz, 5py), δ 7.30 (8H, m, Ph$_a$ and Ph$_b$), δ 4.08 (2H, s, CH$_2$)

Synthesis of the triple stranded iron helicate [Fe$_2$(L)$_3$]Cl$_4$

Ligand (3.0g, 0.008 mol) was dissolved in methanol (400 ml). Iron (II) chloride tetrahydrate (1.06 g, 0.005 mol) was then added to the solution and the resulting solution was brought to reflux at 65°C for 3 hours. The solution was then taken to dryness *in vacuo*. The crude product was then dissolved in minimal amounts of methanol (10 ml) and excess methanolic ammonium hexafluorophosphate added. The resulting precipitate was collected by filtration and washed with water (2 x 10 ml) and then diethyl ether (5 x 25 ml). The filtrate was then suspended in methanol and stirred with Dowex until the product had dissolved. The Dowex was then filtered off. The filtrate was taken to dryness *in vacuo*, and then redissolved in a minimum amount of methanol. Excess diethyl ether was added until the product precipitates, the final product was filtered and washed with ether and dried (1.65g, 59.7%). The final product was a crystalline purple solid.

Mass Spectrum (ESI): m/z = 425.5 [Fe$_2$L$_3$]Cl^{3+} , 310 [Fe$_2$L$_3$]$^{4+}$

^{1}H NMR (300 MHz), CD$_3$OD, 298K): δ 9.13 (2H, s, H$_{im}$), δ 8.71 (2H, d, J = 7.2 Hz, 6py), δ 8.48 (2H, t, J = 7.8, 3py), δ 7.84 (2H, ddd, J = 5.6, 4py), δ 7.44 (2H, d, J = 5.2, 5py), δ 7.05 (4H, broadened, Ph$_{a/b}$), δ 5.62 (4H, broadened, Ph$_{a/b}$), δ 4.07 (2H, s, CH$_2$)

UV-Vis (H$_2$O), λ$_{max}$ (ε$_{max}$/dm^{3}mol^{-1}cm^{-1}) 584 (16900) nm

Cylinder - TAR RNA binding – A synthetic 31 base RNA strand of sequence 5' GGCCAGAUCUGAGCCUGGGAGCUCUCUGGCC 3' was purchased from Integrated DNA Technologies (IDT) HPLC purified. RNA was radiolabelled at the 5' end using T4 polynucleotide kinase and [γ-^{32}P]ATP. RNA was then annealed in 50 mM Tris HCl (pH 8.0) at 80°C for 5 min and then 10 min at 4°C on ice. RNA samples (2 μM) were incubated with increasing cylinder concentrations (1-4 μM, relating to ratios of 0.5, 1, 1.5 and 2 cylinders per RNA strand) of cylinder in TK buffer; Tris HCl (50 mM, pH 8.0), KCl (100 mM) to a final volume of 10 μL for 30 min at RT and then on ice for 10 min. Samples were then run on a 15% non-denaturing polyacrylamide gel in 0.5 x TB buffer; Tris.HCl (40mM), Boric acid (45 mM), pH 8.3 at 11 v/cm and 4°C for 5 hours. Gel was imaged by developing on a white phosphor screen and scanned using a Bio-Rad personal molecular imager (PMI).

ADP-RNA binding inhibition – The TAR RNA was radiolabelled and annealed as before. 10 μL sample solutions containing final concentrations of TAR RNA (100 nM) DTT (100 mM) ADP peptide (300 nM), 0.1% Triton X-100, Tris.HCl (50 mM pH 8.0) and cylinder (Fe, Ni or Ru at 0.2, 0.4, 0.8 and 1.6 μM, corresponding to ratios of 2, 4, 8 and 16 cylinders per RNA strand) were prepared and incubated at RT for 30 min and then on ice for 10 min. Samples were run on a 10% non-denaturing polyacrylamide gel at 4°C for 2.5 hours at 11v/cm. Gel was imaged by developing on a white phosphor screen and scanned using a Bio-Rad personal molecular imager (PMI).

5.5 References

1. R. Weiss, *How does HIV cause AIDS?* Science, 1993. **260**(5112): p. 1273-1279.

2. G. Maartens, C. Celum, and S.R. Lewin, *HIV infection: epidemiology, pathogenesis, treatment, and prevention.* The Lancet. **384**(9939): p. 258-271.

3. UNAids.org, *Fact sheet November 2016.* 2016.

4. T. Acharya, *MCQ in microbiology and microbiology classnotes [online], blogspot, April* 2010 , Febuary 2017 (http://edusanjalmicro.blogspot.co.uk/2010_04_01_archive.html).

5. D.C. Chan, D. Fass, J.M. Berger, and P.S. Kim, *Core Structure of gp41 from the HIV Envelope Glycoprotein.* Cell, 1997. **89**(2): p. 263-273.

6. J.S. Klein and P.J. Bjorkman, *Few and Far Between: How HIV May Be Evading Antibody Avidity.* PLOS Pathogens, 2010. **6**(5): p. e1000908.

7. A.O. Pasternak, V.V. Lukashov, and B. Berkhout, *Cell-associated HIV RNA: a dynamic biomarker of viral persistence.* Retrovirology, 2013. **10**(41): p. 1742-4690.

8. F. Barre-Sinoussi, A.L. Ross, and J.-F. Delfraissy, *Past, present and future: 30 years of HIV research.* Nature Reviews Microbiology, 2013. **11**(12): p. 877-883.

9. P. Pugach, T.J. Ketas, E. Michael, and J.P. Moore, *Neutralizing antibody and anti-retroviral drug sensitivities of HIV-1 isolates resistant to small molecule CCR5 inhibitors.* Virology, 2008. **377**(2): p. 401-407.

10. J.P. Lalezari, J.J. Eron, M. Carlson, C. Cohen, E. DeJesus, R.C. Arduino, J.E. Gallant, P. Volberding, R.L. Murphy, F. Valentine, E.L. Nelson, P.R. Sista, A. Dusek, and J.M. Kilby, *A phase II clinical study of the long-term safety and antiviral activity of enfuvirtide-based antiretroviral therapy.* Aids, 2003. **17**(5): p. 691-8.

11. V. Goldschmidt and R. Marquet, *Primer unblocking by HIV-1 reverse transcriptase and resistance to nucleoside RT inhibitors (NRTIs).* The International Journal of Biochemistry & Cell Biology, 2004. **36**(9): p. 1687-1705.

12. R. Sperling, *Zidovudine.* Infectious Diseases in Obstetrics and Gynecology, 1998. **6**(5): p. 197-203.

13. X. Fan, F.-H. Zhang, R.I. Al-Safi, L.-F. Zeng, Y. Shabaik, B. Debnath, T.W. Sanchez, S. Odde, N. Neamati, and Y.-Q. Long, *Design of HIV-1 integrase inhibitors targeting the catalytic domain as well as its interaction with LEDGF/p75: A scaffold hopping approach using salicylate and catechol groups.* Bioorganic & Medicinal Chemistry, 2011. **19**(16): p. 4935-4952.

14. A. Pendri, N.A. Meanwell, K.M. Peese, and M.A. Walker, *New first and second generation inhibitors of human immunodeficiency virus-1 integrase.* Expert Opinion on Therapeutic Patents, 2011. **21**(8): p. 1173-1189.

15. M.M. Dąbrowska and A. Wiercińska-Drapało, *Integrase inhibitors as a new class of ARV treatment.* HIV & AIDS Review, 2007. **6**(4): p. 10-14.

16. Z. Wang, J. Tang, C.E. Salomon, C.D. Dreis, and R. Vince, *Pharmacophore and structure–activity relationships of integrase inhibition within a dual inhibitor scaffold of HIV reverse transcriptase and integrase.* Bioorganic & Medicinal Chemistry, 2010. **18**(12): p. 4202-4211.

17. E.T. Brower, U.M. Bacha, Y. Kawasaki, and E. Freire, *Inhibition of HIV-2 Protease by HIV-1 Protease Inhibitors in Clinical Use.* Chemical Biology & Drug Design, 2008. **71**(4): p. 298-305.

18. B. Turk, *Targeting proteases: successes, failures and future prospects.* Nature Reviews Drug Discovery, 2006. **5**(9): p. 785-799.

19. G.L. Plosker and L.J. Scott, *Saquinavir: a review of its use in boosted regimens for treating HIV infection.* Drugs, 2003. **63**(12): p. 1299-324.

20. E.J. Arts and D.J. Hazuda, *HIV-1 Antiretroviral Drug Therapy.* Cold Spring Harbor Perspectives in Medicine, 2012. **2**(4): p. a007161.

21. S. Debaisieux, F. Rayne, H. Yezid, and B. Beaumelle, *The Ins and Outs of HIV-1 Tat.* Traffic, 2012. **13**(3): p. 355-363.

22. N.L. Greenbaum, *How Tat targets TAR: structure of the BIV peptide–RNA complex.* Structure, 1996. **4**(1): p. 5-9.

23. R.S. Doherty, T. De Oliveira, C. Seebregts, S. Danaviah, M. Gordon, and S. Cassol, *BioAfrica's HIV-1 proteomics resource: combining protein data with bioinformatics tools.* Retrovirology, 2005. **2**: p. 18.

24. C. Zhou and T.M. Rana, *A Bimolecular Mechanism of HIV-1 Tat Protein Interaction with RNA Polymerase II Transcription Elongation Complexes.* Journal of Molecular Biology, 2002. **320**(5): p. 925-942.

25. G.R. Campbell, E. Pasquier, J. Watkins, V. Bourgarel-Rey, V. Peyrot, D. Esquieu, P. Barbier, J. de Mareuil, D. Braguer, P. Kaleebu, D.L. Yirrell, and E.P. Loret, *The glutamine-rich region of the HIV-1 Tat protein is involved in T-cell apoptosis.* Journal of Biological Chemistry, 2004. **279**(46): p. 48197-204.

26. E. Loret, *HIV extracellular Tat: myth or reality?* Current HIV Research, 2015. **13**(2): p. 90-7.

27. E.P. Loret, A. Darque, E. Jouve, E.A. Loret, C. Nicolino-Brunet, S. Morange, E. Castanier, J. Casanova, C. Caloustian, C. Bornet, J. Coussirou, J. Boussetta, V. Couallier, O. Blin, B. Dussol, and I. Ravaux, *Intradermal injection of a Tat Oyi-based therapeutic HIV vaccine reduces of 1.5 log copies/mL the HIV RNA rebound median and no HIV DNA rebound following cART interruption in a phase I/II randomized controlled clinical trial.* Retrovirology, 2016. **13**: p. 21.

28. M.J. Churcher, C. Lamont, F. Hamy, C. Dingwall, S.M. Green, A.D. Lowe, P.J.G. Butler, M.J. Gait, and J. Karn, *High Affinity Binding of TAR RNA by the Human Immunodeficiency Virus Type-1 tat Protein Requires Base-pairs in the RNA Stem and Amino Acid Residues Flanking the Basic Region.* Journal of Molecular Biology, 1993. **230**(1): p. 90-110.

29. F. Hamy, E.R. Felder, G. Heizmann, J. Lazdins, F. Aboul-ela, G. Varani, J. Karn, and T. Klimkait, *An inhibitor of the Tat/TAR RNA interaction that effectively suppresses HIV-1 replication.* Proceedings of the National Academy of Sciences of the United States of America, 1997. **94**(8): p. 3548-3553.

30. J. Malina, M.J. Hannon, and V. Brabec, *Recognition of DNA bulges by dinuclear iron(II) metallosupramolecular helicates.* FEBS Journal, 2014. **281**(4): p. 987-997.

31. J. Malina, M.J. Hannon, and V. Brabec, *Iron(II) supramolecular helicates interfere with the HIV-1 Tat–TAR RNA interaction critical for viral replication.* Scientific Reports, 2016. **6**: p. 29674.

32. B.R. Cullen, *MicroRNAs as mediators of viral evasion of the immune system.* Nature Immunology, 2013. **14**(3): p. 205-210.

33. J. Witteveldt, R. Blundell, J.J. Maarleveld, N. McFadden, D.J. Evans, and P. Simmonds, *The influence of viral RNA secondary structure on interactions with innate host cell defences.* Nucleic Acids Research, 2014. **42**(5): p. 3314-3329.

34. G.I. Pascu, A.C.G. Hotze, C. Sanchez-Cano, B.M. Kariuki, and M.J. Hannon, *Dinuclear Ruthenium(II) Triple-Stranded Helicates: Luminescent Supramolecular Cylinders That Bind and Coil DNA and Exhibit Activity against Cancer Cell Lines.* Angewandte Chemie, 2007. **119**(23): p. 4452-4456.

35. M. J. Hannon, C. L. Painting, A. Jackson, J. Hamblin, and W. Errington, *An inexpensive approach to supramolecular architecture.* Chemical Communications, 1997(18): p. 1807-1808.

Chapter 6

Conclusions and Future work

6.1 Conclusions and Future Work

6.1.1 Conclusions

Overall, this thesis has shown that the iron cylinder and its enantiomers can bind to a DNA tetrahedron and, upon binding, cause the structure to contract, potentially having the effect of decreasing the size of the internal cavity. It was also found that increasing the ratio of cylinder to DNA tetrahedron increases the compression effect on the tetrahedron. However, at high ratios, the positive charge of the cylinder overcomes the negative charge on the DNA and causes the conjugate to precipitate out of solution. Whilst it proved very difficult to ascertain where exactly the cylinder was bound to the tetrahedron, separate gel electrophoresis competition experiments showed the cylinder has a much higher affinity to 3WJ structures over duplex DNA, suggesting the cylinder preferentially binds to the 3WJs on the tetrahedron over the duplex DNA present. Interestingly when the M and P enantiomers were separated and then combined with the tetrahedron, the M enantiomer had a stronger effect than the P enantiomer compressing the tetrahedron. This was interesting as previous experiments showed only the M enantiomer bound inside 3WJs in crystallographic experiments using racemic cylinder, suggesting that the M enantiomer prefers to bind to the 3WJ DNA in the tetrahedron more so than the P enantiomer.

This opens up further research into other DNA nanostructures that cylinders could bind to and effect. Potentially creating DNA nano-machines in conjunction with supramolecular chemistry.

The cylinder-tetrahedron conjugate was also found to be readily taken up by mammalian cells through a variety of experiments. The cytotoxicity of the cylinder, when delivered by tetrahedron was diminished but still remained potent. This was most likely due to an equilibrium of binding for the cylinder between genomic DNA and tetrahedron DNA, reducing

the amount of cylinder available to cause apoptosis through genomic DNA binding. Initial results using an almost identical ruthenium cylinder with ICP-MS suggested that overall uptake of cylinder is increased when delivered by tetrahedron, in the cytoplasm and nucleus. Whilst considerable research has already been published on the merits of DNA nanotechnology as therapeutic carriers; this particular research shows supramolecular chemistry can also play a role in the field.

The ruthenium cylinder has DNA photocleavage capabilities that are most effective in the blue end of the spectrum, centred on its absorption maxima at 474 nm. This was very interesting when combined with the DNA tetrahedron as it was shown that the tetrahedron could be broken down on excitation with a specific wavelength of light, suggesting that potential internalised cargos could be released on excitation with the external light trigger. Ruthenium cylinder and its tetrahedron conjugate were also shown to have potent cytotoxic capabilities when utilised as a photodynamic therapy agent, where the cylinder is delivered to genomic DNA and apoptosis is triggered by photocleavage caused by subsequent excitation with light. By utilising the difference in toxicity with and without tetrahedron, further research into widening the therapeutic window of the RuCy when being used as a PDT agent would be very interesting.

The versatility of the cylinder was also demonstrated by the spatial recognition of a looped structure of RNA. The RNA, known as TAR, is found in the virus HIV-1 and binds to ADP-1 protein to regulate transcription to facilitate viral capsid replication. The competitive binding of the iron, nickel and ruthenium cylinders was able to inhibit binding between TAR and ADP-1 and thus had potential to become a new class of anti-viral agents. This is particularly exciting as the cylinder's action in this chapter was not sequence specific, but more specific to the RNA structure. This makes it less susceptible to common virus adaptations to develop drug

resistance. There is a great deal of opportunity in research for the cylinders as a new class of anti-viral agents due to the large amount of discovered RNA secondary structures in nature.

6.1.2 Future Work

6.1.2.1 Chapter 2

Following from chapter 2, it would be interesting to see the differences between the iron cylinder enantiomers in the 3WJ competition assays. From this thesis it has been seen that the M enantiomer is more effective at compressing the tetrahedron. Therefore its affinity to the synthetic 3WJ could also be different to the P enantiomer when competing with other DNA structures.

Current collaborations are also currently working to establish whether the differences between the M and P enantiomers on the DNA tetrahedron can be seen by atomic force microscopy as previously seen with the racemic mixture by Prof. Shao Fengwei and Dr Liying Wang.

6.1.2.2 Chapter 3

The localisation of the tetrahedron and tetrahedron conjugate inside the cell remains a question. Whilst no significant co-localisation with the Hoechst nuclear stain and the Cy5 labelled tetrahedron was seen, another cell stain could be used to see whether any significant co-localisation could be seen between the two which could confirm the cellular localisation of the complexes. This co-localisation could be quantified and any difference to localisation when cylinder is attached to the tetrahedron or not could be analysed.

Furthermore, the integrity of the cylinder – tetrahedron conjugate whilst inside the cell still must be confirmed. This remains a challenging task, which one solution could be to furnish a

FRET pair between the cylinder and the tetrahedron and analyse the intensity whilst inside the cell. Unfortunately, creating a cylinder with a fluorescent tag remains a long term goal as synthesis often results in insoluble cylinders or cylinders with altered characteristics to the parent cylinder. An alternative proposition could be to use a fluorescent tag on the tetrahedron which is quenched upon cylinder binding. The intensity of this tag would increase on cylinder release and the integrity of the conjugate could be assessed in this fashion.

6.1.2.3 Chapter 4

Very interesting results involving the photocleavage capability of the ruthenium cylinder were observed in chapter 4. One further experiment which would shed light on whether the ruthenium cylinder is a good candidate for PDT would be to measure the amount of singlet oxygen created, when irradiated by light, with Raman spectroscopy.

As seen in figure 4.17, potent cytotoxicity is observed by the ruthenium cylinder. As this was only initial testing, more rigorous experimentation is required to fully explore this, varying irradiation times and concentrations. It would also be interesting to combine an intercalator drug inside the tetrahedron with a view to releasing the drug on light excitation which would then trigger a cytotoxic response from that intercalator drug. Delivery by this method could increase specificity and decrease potential side effects as the tetrahedron could be light activated locally on a patient.

6.1.2.4 Triggered release of an encapsulated cargo

One of the aims of this thesis was to use supramolecular cylinders with DNA nanostructures to trigger the release of a therapeutic cargo. Two ways in which this could be achieved were highlighted in chapter 2 and chapter 4. In chapter 2, the iron cylinder was shown to compress the DNA tetrahedron into a smaller size, which would decrease the size of the internal cavity.

This in turn could cause the cavity to release a cargo which would now be too large to be accommodated by the cavity (Figure 6.1a).

In chapter 4, the tetrahedron was shown to be photo cleaved apart by a ruthenium cylinder on excitation by light. This proposes that an internalised cargo could be released by 'breaking the bars' of the cage through photocleavage, opening up the central cavity (Figure 6.1b).
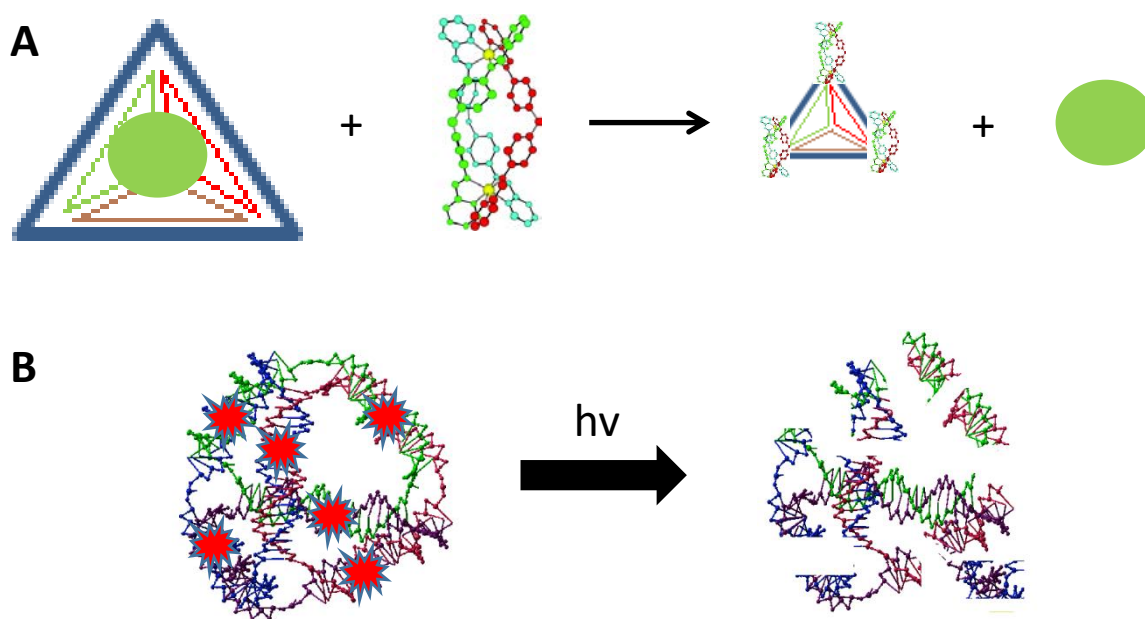

Figure 6.1 – A) Model diagram illustrating cargo released triggered by binding and subsequent compressing of a DNA tetrahedron by the iron cylinder. B) 'Breaking the bars' of a DNA tetrahedron on excitation by light.

For this triggered release to be possible, a cargo must first be internalised. Initial work was completed on one approach. This involved expressing hexa-histidine tagged EGFP (enhanced green fluorescent protein) from *e.coli* (Escherichia coli) bacteria. This protein was then attached to one of the tetrahedron oligonucleotide strands, following a protocol first reported by Shimada *et al.* in 2008.[1] The coupling involves functionalising the oligonucleotide with Nitrilotriacetate (NTA). This was done by purchasing an oligo functionalised with a thiol group at the 5' end

(Eurofins). The oligo was then incubated with tris(2-carboxyethyl)phosphine (TCEP) for 2 hours to reduce and activate the thiol group. Maleimido-C3-NTA (*N*-[5-(3′-maleimidopropylamido)-1-carboxypentyl]iminodiacetic acid, disodium salt, monohydrate (Dojindo) was then added and incubated for 24 hours with shaking to furnish the NTA-functionalised oligo. The remaining three oligos were then added to anneal the tetrahedron in the same manner as previously stated, still filtering with the 30k MWCO filter (Pierce) to remove excess NTA. Excess $NiCl_2$ and His-EGFP were then added and incubated in the fridge overnight. To remove any unbound EGFP, the mixture was added to a Ni-NTA agarose mini column (Thermofisher). The resulting EGFP-tetrahedron was then be analysed on a fluorimeter (PTI MD-50-20). The overall coupling can be seen visually in Figure 6.2.
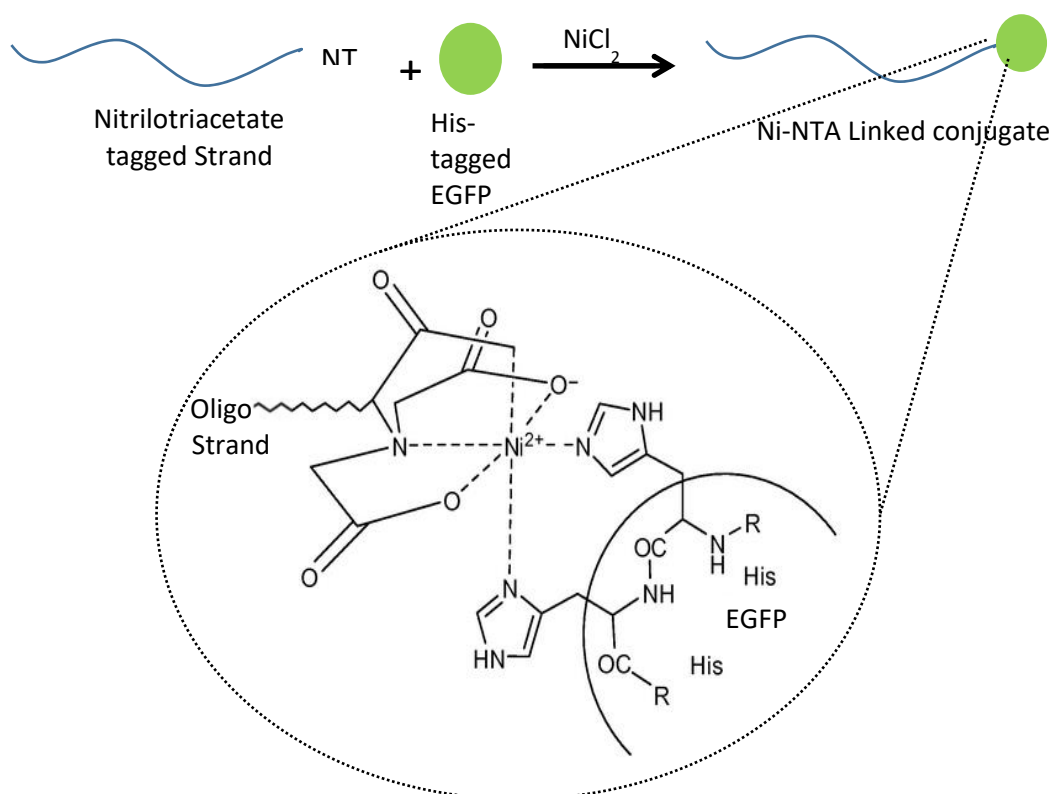
Figure 6.2 – Model diagram illustrating the coupling between His-tagged EGFP and a DNA oligonucleotide.

The orientation of the EGFP could be controlled by following the same method reported by Erben *et al.*[2] By simply selecting the 5' position by ordering the nucleotides corresponding to their helical turn per base (Figure 6.3). Through this, tetrahedra with both EGFP facing directly into the internal cavity and also one facing directly outside the cavity were synthesised but unfortunately never characterised fully.
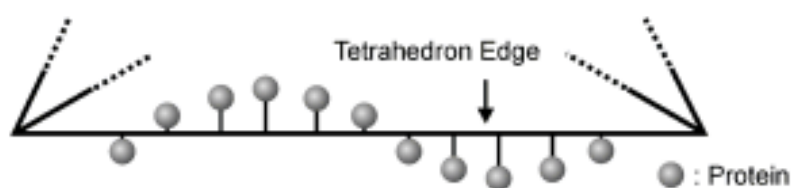
Figure 6.3 – Model diagram showing how protein attachment position can be manipulated by altering the sequence of the functionalised oligonucleotide. Taken from ref 2.

As further work, this protein internalisation needs further characterisation to fully confirm synthesis. Following from this, adding either the iron or ruthenium cylinders for each method of triggered delivery could be tested. Unfortunately in initial testing the blue light required for photocleavage proved to be able to bleach some of the fluorescence from the protein and the iron cylinder also quenched protein fluorescence when bound to the tetrahedron.

Building on this protein encapsulation, alternative cargoes could be found to fully realise the potential for the cylinders releasing an internalised cargo from a DNA nanostructure.

6.2 References

1. J. Shimada, T. Maruyama, T. Hosogi, J. Tominaga, N. Kamiya, and M. Goto, *Conjugation of DNA with protein using His-tag chemistry and its application to the aptamer-based detection system.* Biotechnology Letters, 2008. **30**(11): p. 2001-6.

2. C.M. Erben, R.P. Goodman, and A.J. Turberfield, *Single-molecule protein encapsulation in a rigid DNA cage.* Angewante Chemie International Edition English, 2006. **45**(44): p. 7414-7.